frontiers | Research Topics

Efficient exploration and development of unconventional natural gas

Edited by
Shu Tao, Zhengguang Zhang, Shida Chen,
Yu Jing and Junjian Wang

Published in
Frontiers in Earth Science

ISSN 1664-8714
ISBN 978-2-8325-6916-0
DOI 10.3389/978-2-8325-6916-0

Generative AI statement
Any alternative text (Alt text) provided alongside figures in the articles in this ebook has been generated by Frontiers with the support of artificial intelligence and reasonable efforts have been made to ensure accuracy, including review by the authors wherever possible. If you identify any issues, please contact us.

About Frontiers

Frontiers is more than just an open access publisher of scholarly articles: it is a pioneering approach to the world of academia, radically improving the way scholarly research is managed. The grand vision of Frontiers is a world where all people have an equal opportunity to seek, share and generate knowledge. Frontiers provides immediate and permanent online open access to all its publications, but this alone is not enough to realize our grand goals.

Frontiers journal series

The Frontiers journal series is a multi-tier and interdisciplinary set of open-access, online journals, promising a paradigm shift from the current review, selection and dissemination processes in academic publishing. All Frontiers journals are driven by researchers for researchers; therefore, they constitute a service to the scholarly community. At the same time, the *Frontiers journal series* operates on a revolutionary invention, the tiered publishing system, initially addressing specific communities of scholars, and gradually climbing up to broader public understanding, thus serving the interests of the lay society, too.

Dedication to quality

Each Frontiers article is a landmark of the highest quality, thanks to genuinely collaborative interactions between authors and review editors, who include some of the world's best academicians. Research must be certified by peers before entering a stream of knowledge that may eventually reach the public - and shape society; therefore, Frontiers only applies the most rigorous and unbiased reviews. Frontiers revolutionizes research publishing by freely delivering the most outstanding research, evaluated with no bias from both the academic and social point of view. By applying the most advanced information technologies, Frontiers is catapulting scholarly publishing into a new generation.

What are Frontiers Research Topics?

Frontiers Research Topics are very popular trademarks of the *Frontiers journals series*: they are collections of at least ten articles, all centered on a particular subject. With their unique mix of varied contributions from Original Research to Review Articles, Frontiers Research Topics unify the most influential researchers, the latest key findings and historical advances in a hot research area.

Find out more on how to host your own Frontiers Research Topic or contribute to one as an author by contacting the Frontiers editorial office: frontiersin.org/about/contact

Efficient exploration and development of unconventional natural gas

Topic editors

Shu Tao — China University of Geosciences, China

Zhengguang Zhang — General Prospecting Institute of China National Administration of Coal Geology, China

Shida Chen — China University of Geosciences, China

Yu Jing — University of New South Wales, Australia

Junjian Wang — Independent Researcher, Brisbane, Australia

Citation

Tao, S., Zhang, Z., Chen, S., Jing, Y., Wang, J., eds. (2025). *Efficient exploration and development of unconventional natural gas*. Lausanne: Frontiers Media SA.

doi: 10.3389/978-2-8325-6916-0

Table of contents

frontiers | Frontiers in Earth Science

TYPE Editorial
PUBLISHED 16 September 2025
DOI 10.3389/feart.2025.1660899

OPEN ACCESS

EDITED AND REVIEWED BY:
Valerio Acocella,
Roma Tre University, Italy

*CORRESPONDENCE
Shu Tao,
taoshu@cugb.edu.cn

RECEIVED 07 July 2025
ACCEPTED 01 September 2025
PUBLISHED 16 September 2025

CITATION
Tao S, Zhang Z, Chen S, Jing Y and Wang J (2025) Editorial: Efficient exploration and development of unconventional natural gas. *Front. Earth Sci.* 13:1660899. doi: 10.3389/feart.2025.1660899

Editorial: Efficient exploration and development of unconventional natural gas

Shu Tao[1]*, Zhengguang Zhang[2], Shida Chen[1], Yu Jing[3] and Junjian Wang[4]

[1]School of Energy Resources, China University of Geosciences (Beijing), Beijing, China, [2]General Prospecting Institute of China National Administration of Coal Geology, Beijing, China, [3]University of New South Wales, Sydney, NSW, Australia, [4]EMM Consulting Pty Ltd., Brisbane, QLD, Australia

KEYWORDS

unconventional natural gas, geology–engineering integration, horizontal well optimization, AI-driven approach, efficient development

Editorial on the Research Topic
Efficient exploration and development of unconventional natural gas

1 Introduction

Unconventional natural gas resources—including shale gas, coalbed methane (CBM), and natural gas hydrates—serve as critical drivers of the global low-carbon energy transition, profoundly reshaping conventional exploration and development paradigms (Bocora, 2012; Flores and Moore, 2025; Tao et al., 2019). With sustained progress in the shale gas revolution and breakthroughs in gas hydrate trial production technologies, unconventional resources, such as CBM, tight sandstone gas, and shale gas, are becoming increasingly important components of energy security (Boswell and Collett, 2011; Guo et al., 2025). These resources demonstrate strategic significance in mitigating hydrocarbon supply-demand imbalances and optimizing energy structures. Guided by China's "Dual Carbon" strategy—targeting a national CO_2 emissions peak before 2030 and carbon neutrality by 2060—unconventional natural gas exploration and development are increasingly guided by two interlinked priorities: intelligent target identification and low-carbon process regulation. This aligns with global decarbonization trajectories, where CCUS emerges as a pivotal technology. McLaughlin et al. (2023) provide a sociotechnical synthesis of CCUS's role in industrial decarbonization, outlining both technical challenges and policy implications, while Yusuf and Al-Ansari (2023) highlight how integrating CCUS within natural gas supply chains—particularly in the context of low-carbon hydrogen production—can significantly enhance sectoral sustainability. Together, these international perspectives enrich the framing of China's geology–engineering integration framework within the wider context of global low-carbon transitions.

In conventional natural gas development, enhanced recovery technologies continue to evolve, establishing an engineering framework centered on enhanced hydrocarbon

recovery (EOR), multi–stage hydraulic fracturing, and precision well completion. These techniques have demonstrated robust production stability in low-to-medium permeability reservoirs (Abdulhadi et al., 2025; Akbarabadi et al., 2023; Gomaa et al., 2024; Sambo et al., 2023). Current research priorities are rapidly shifting from conventional to unconventional reservoirs, driving the multidimensional reconstruction of technological approaches. Core efforts focus on optimizing coupled processes in CO_2 displacement mechanisms (Zhou et al., 2024), molecular-level tuning of fracturing fluid structures (Yang et al., 2024), and upgrading intelligent completion systems based on formation response. These innovations address challenges posed by microscopic heterogeneity and thermo–hydro–mechanical–chemical (THMC) coupling complexities in shale, tight sandstone, and coal reservoirs. In field applications, shale gas development addresses nanoscale pore–throat constraints by establishing confined flow control mechanisms centered on chemical stimulation, significantly enhancing capillary-driven flow efficiency. For tight sandstone reservoirs, rock brittleness classification models enable precise fracturing parameter matching and optimized fracture propagation pathways (Wu et al., 2024). The development of CBM utilizes organic matter–fluid interaction mechanisms to formulate fracturing fluids incorporating long-chain alkyl surfactants, which exhibit targeted dissolution behavior and thereby minimize structural disruption while enhancing pore connectivity and methane adsorption capacity (Zhao et al., 2024). Global research trends further indicate a shift toward multi-driver mechanisms in unconventional gas development. Specifically, CO_2/N_2 coinjection demonstrates superior pressure-synergistic effects in coal seams, optimizing gas desorption-production dynamics (Wang et al., 2025); gas hydrate production employs coupled depressurization-displacement mechanisms to enhance methane recovery efficiency and production stability (Kasala et al., 2025). Supported by high-fidelity multiphysics simulations and advanced data-driven algorithms, an intelligent production control paradigm for unconventional reservoirs is emerging. Physics-informed machine learning is increasingly applied to improve interpretability, accuracy, and adaptability of reservoir models, while hybrid frameworks integrating statistical analysis, machine learning, and optimization have enhanced production forecasting and decision-making in shale gas development (Meng et al., 2023). These advances highlight the convergence of mechanistic modeling and data-driven optimization toward digitally enabled, mechanism-driven reservoir management.

Breakthroughs in intelligent low-carbon development technologies for unconventional natural gas have addressed core bottlenecks throughout resource extraction processes. To overcome geological target identification uncertainties, the integrated application of deep learning–based 3D geological modeling and real-time intelligent drilling decision systems has enhanced sweet-spot targeting accuracy and well placement precision (Carpenter, 2023). The development of multimechanism coupled flow models, integrated with digital rock core high-resolution characterization techniques, provides theoretical insights and parameterization support for fracture network design and flow channel optimization under nano-/micro-pore–scale mass transfer constraints (Yu et al., 2019). Amid tightening carbon constraints, lifecycle carbon footprint assessment models pinpoint primary emission sources across process chains, accelerating deployment of clean energy-powered fracturing systems and subsurface carbon capture–production integration systems (Khan et al., 2025). Frontier advancements reveal that integrating multienergy coupled supply systems with closed-loop intelligent carbon management platforms is catalyzing unprecedented deep integration of intelligence, systematization, and carbon neutrality in unconventional gas development (Brown et al., 2017).

This introductory review for the *Frontiers in Earth Science* Research Topic addresses technical challenges in geology–engineering integration for unconventional natural gas development. The Research Topic presents ten representative studies systematically presenting recent advances in intelligent algorithms and low-carbon technologies aimed at high-efficiency unconventional gas development.

2 Review of research presented in This Research Topic

This Research Topic compiles cutting-edge advances in efficient unconventional gas exploration and development, encompassing critical technological pathways including geological target identification, reservoir stimulation mechanisms, and intelligent low-carbon regulation. These contributions span diverse reservoirs—shale gas, CBM, gas hydrates, and tight sandstone—yielding systematic breakthroughs in structural–sedimentary interpretation, flow regulation optimization, and mechanistic-based modeling. Collectively, they highlight a dual-driven technological transition toward enhanced efficiency and emission abatement in unconventional gas development.

2.1 Intelligent exploration and synergistic appraisal

Unconventional natural gas exploration confronts three primary challenges: unpredictability of fracture networks, lack of diagnostic indicators for coexisting critical minerals, and poorly constrained deep sweet-spot positioning. This theme centers on the integration of multi-source geological, logging, and seismic data, promoting the reconstruction of integrated natural gas–critical mineral co-exploration frameworks (Mirzaee Mahmoodabadi and Zahiri, 2023; Mubarak and Koeshidayatullah, 2023; Prochnow et al., 2022). Specifically, Wu et al. integrated surface fracture outcrop distributions with coal seam thickness constraints to reconstruct paleotectonic stress field models, elucidating fracture networks predominantly governed by structural curvature. The Laochang Block, situated in eastern Yunnan Province, China, is a tectonically complex coalbed methane–bearing region characterized by intense multi-phase deformation and heterogeneous stress regimes. Application of this integrated approach markedly improved the accuracy of CBM sweet-spot identification in the block, offering novel geomechanical insights into fracture development and permeability enhancement in structurally intricate reservoirs. Mu et al. employed K-means clustering to extract natural gamma-ray and resistivity responses, establishing logging identification criteria and resource co-evaluation systems for Li-enriched coal

seams. These advances integrated exploration technologies for unconventional gas and critical minerals. Additionally, Zhang et al. applied multifrequency seismic attribute fusion—combining high–frequency amplitude with low-frequency coherence—to jointly characterize sedimentary facies and fault systems. Their methodology elucidates reservoir–controlling mechanisms, establishes intelligent prediction pathways for deep carbonate sweet spots, and facilitates substantial exploration success in the Dengying Formation, located within the Sichuan Basin of southwestern China—one of the country's most prolific hydrocarbon provinces.

2.2 Fracture network stimulation and multiphase flow regulation

Unconventional reservoir development must urgently overcome core bottlenecks in multiphase flow control—including gas–condensate–hydrate multiphase systems, heterogeneity in fracture network stimulation responses to fracture network stimulation, and high flow initiation thresholds. Research presented herein drives the transition of reservoir engineering from experience-driven to mechanism-driven paradigms through mechanistic analysis and modeling innovations (Yuan et al., 2023). Specifically, Wei et al. developed a dynamic depressurization model for marine hydrate extraction, demonstrating that horizontal well development in three-phase zones can simultaneously enhance gas and hydrate recovery efficiency. Their proposed well type–layer matching criterion for multiphase flow regulation guides commercial development in the Shenhu Area, South China Sea. Zhao et al. utilized *in situ* computed tomography (CT) scanning to track cyclic gas injection processes, revealing induced phase transitions of condensate from wavy to slug flow patterns, thereby significantly improving oil–gas phase distribution. The first injection cycle contributed most significantly to saturation reduction, underscoring the dominant role of fracture systems in condensate reservoir recovery mechanisms. Additionally, Ren et al. established a material-balance-driven fracture network propagation model to quantify synergistic controls of natural fracture development and fracturing fluid imbibition on stimulated reservoir volume. They developed a fracturing optimization pathway based on physical response parameters, marking a paradigm shift from experience-based to mechanism-driven fracturing design in tight reservoirs. Li et al. develop a coupled permeability–pressure–water–cut threshold flow initiation equation through physical experiments and regression analysis. Confirming water saturation as the primary control variable for threshold pressure changes, providing fundamental basis for dynamic control of high–water–cut gas reservoirs. Notably, Zhang and Liu identified a critical stress–state transition zone at ~1,500 m depth in coal seams of eastern Hubei Province, central China, located along the margin of the Jianghan Basin. This zone governs abrupt permeability changes and conductivity evolution. Their proposed slow-depressurization, rapid-drainage strategy sustains deep CBM reservoir conductivity, enabling breakthroughs in economic recovery.

2.3 Intelligent decision-making and carbon-constrained development

Unconventional gas development urgently requires overcoming dual bottlenecks: poorly understood microscale seepage mechanisms and high uncertainty in production decision-making. This work focuses on adsorption–seepage–emission reduction coupling mechanisms and intelligent decision algorithms, driving the transition toward intelligently coordinated, carbon-constrained development paradigms (Chiamaka et al., 2024; Di et al., 2021). Notably, Xu et al. employed low-pressure N_2 adsorption combined with SEM imaging to reveal the carbon sequestration mechanisms of methane molecules in anthracite-hosted organic micropores within organic micropores (<2 nm). Their work demonstrates that adsorbed methane desorption requires overcoming critical energy barriers, providing theoretical foundations for efficient CBM development and carbon storage. Furthermore, Li et al. developed an integrated Bayesian network–Gaussian mixture model (BN–GMM) framework to quantify production fluctuation probabilities and carbon footprint sensitivity under multifactorial coupling. By identifying recovery factor and reserve-to-production ratio as the primary controls of production stability, their approach drives the transition from static resource allocation to carbon-constrained intelligent decision-making in natural gas development within the Sichuan Basin.

3 Conclusion

This Research Topic compiles cutting-edge advances in efficient unconventional gas exploration and development, spanning geological modeling, engineering optimization, and intelligent technology integration. Featured studies encompass representative technological pathways including fracture network prediction, gas injection-enhanced recovery, fracturing parameter design and production uncertainty modeling. These contributions demonstrate theoretical innovations and engineering applications across shale gas, CBM, and gas hydrate reservoirs. The methodologies and case studies herein offer valuable references for understanding technological evolution in unconventional gas development while providing actionable insights for future research and practical applications.

Author contributions

ST: Conceptualization, Writing – review and editing. ZZ: Investigation, Writing – review and editing. SC: Investigation, Writing – review and editing. YJ: Supervision, Writing – review and editing. JW: Methodology, Writing – review and editing.

Funding

The author(s) declare that no financial support was received for the research and/or publication of this article.

Acknowledgments

I gratefully acknowledge Frontiers in Earth Science for the opportunity to organize this Research Topic. I sincerely appreciate the professional support and guidance provided by the editorial office throughout the process. I also wish to express my deep gratitude to all contributing authors for their valuable work, and to the reviewers for their rigorous evaluations and constructive feedback, which were instrumental in shaping this collection.

Conflict of interest

Author JW was employed by EMM Consulting Pty Ltd.

The remaining authors declare that the research was conducted in the absence of any commercial or financial relationships that could be construed as a potential conflict of interest.

Generative AI statement

The author(s) declare that no Generative AI was used in the creation of this manuscript.

Any alternative text (alt text) provided alongside figures in this article has been generated by Frontiers with the support of artificial intelligence and reasonable efforts have been made to ensure accuracy, including review by the authors wherever possible. If you identify any issues, please contact us.

Publisher's note

References

Abdulhadi, D., Ali, J. A., and Hama, S. M. (2025). Advanced techniques for improving the production of natural resources from unconventional reservoirs: a state-of-the-art review. *Energy fuels.* 39 (23), 10853–10876. doi:10.1021/acs.energyfuels.5c01259

Akbarabadi, M., Alizadeh, A. H., Piri, M., and Nagarajan, N. (2023). Experimental evaluation of enhanced oil recovery in unconventional reservoirs using cyclic hydrocarbon gas injection. *Fuel* 331, 125676. doi:10.1016/j.fuel.2022.125676

Bocora, J. (2012). Global prospects for the development of unconventional gas. *Procedia Soc. Behav. Sci.* 65, 436–442. doi:10.1016/j.sbspro.2012.11.145

Boswell, R., and Collett, T. S. (2011). Current perspectives on gas hydrate resources. *Energy Environ. Sci.* 4, 1206–1215. doi:10.1039/c0ee00203h

Brown, A. C., Korre, A., and Nie, Z. (2017). A life cycle assessment model development of CO_2 emissions and water usage in shale gas production. *Energy Procedia* 114, 6579–6587. doi:10.1016/j.egypro.2017.03.1796

Carpenter, C. (2023). Machine learning approach empowers well placement in tight gas field. *J. Pet. Technol.* 75 (07), 89–91. doi:10.2118/0723-0089-JPT

Chiamaka, K. H., Ovwenkekpere, H. E., Owunna, I. B., Shorunke, M. O., Jude, I. I., and Lawal, T. D. (2024). Robotics and artificial intelligence in unconventional reservoirs: enhancing efficiency and reducing environmental impact. *World J. Adv. Res. Rev.* 24 (1), 2060–2068. doi:10.30574/wjarr.2024.24.1.3185

Di, S., Cheng, S., Cao, N., Gao, C., and Miao, L. (2021). AI-based geo-engineering integration in unconventional oil and gas. *J. King Saud. Univ. Sci.* 33, 101542. doi:10.1016/j.jksus.2021.101542

Flores, R. M., and Moore, T. (2025). Coalbed gas: a review of research directions from the past to the future as facilitated by bibliometrics. *Int. J. Coal Geol.* 298, 104683. doi:10.1016/j.coal.2024.104683

Gomaa, S., Salem, K. G., and El-hoshoudy, A. N. (2024). Enhanced heavy and extra heavy oil recovery: current status and new trends. *Petroleum* 10 (3), 399–410. doi:10.1016/j.petlm.2023.10.001

Guo, J., Tao, S., Bi, C., Cui, Y., Yu, B., and Wen, Y. (2025). Enrichment geological conditions and resource evaluation methods for the gas in thinly interbedded coal measures: a case study of the chengzihe formation in the Jixi Basin. *Energies* 18, 2584. doi:10.3390/en18102584

Kasala, E. E., Wang, J., Majid, A., Nadege, M. N., and Makembe, C. P. (2025). Advancement perspectives of CH_4 recovery from methane hydrate reservoirs via N_2/CO_2-CH_4 exchange: experiments, simulations, and pilot test applications. *Gas. Sci. Eng.* 142, 205685. doi:10.1016/j.jgsce.2025.205685

Khan, A. M., Anderson, C., Prabhu, R., Beletskaya, A., Kuan, P., Danican, S., et al. (2025). A comprehensive life cycle assessment of hydraulic fracturing. *SPE J.* 30, 2190–2202. doi:10.2118/220480-PA

McLaughlin, H., Littlefield, A. A., Menefee, M., Kinzer, A., Hull, T., Sovacool, B. K., et al. (2023). Carbon capture utilization and storage in review: sociotechnical implications for a carbon reliant world. *Renew. Sustain. Energy Rev.* 177, 113215. doi:10.1016/j.rser.2023.113215

Meng, J., Zhou, Y.-J., Ye, T.-R., Xiao, Y.-T., Lu, Y.-Q., Zheng, A.-W., et al. (2023). Hybrid data-driven framework for shale gas production performance analysis via game theory, machine learning, and optimization approaches. *Pet. Sci.* 20, 277–294. doi:10.1016/j.petsci.2022.09.003

Mirzaee Mahmoodabadi, R., and Zahiri, S. (2023). Formation evaluation and rock type classification of asmari formation based on petrophysical-petrographic data: a case study in one of super fields in Iran southwest. *Petroleum* 9 (2), 143–165. doi:10.1016/j.petlm.2022.01.009

Mubarak, Y., and Koeshidayatullah, A. (2023). Hierarchical automated machine learning (AutoML) for advanced unconventional reservoir characterization. *Sci. Rep.* 13, 13812. doi:10.1038/s41598-023-40904-0

Prochnow, S. J., Raterman, N. S., Swenberg, M., Reddy, L., Smith, I., Romanyuk, M., et al. (2022). A subsurface machine learning approach at hydrocarbon production recovery and resource estimates for unconventional reservoir systems: making subsurface predictions from multimensional data analysis. *J. Petrol. Sci. Eng.* 215, 110598. doi:10.1016/j.petrol.2022.110598

Sambo, C., Liu, N., Shaibu, R., Ahmed, A. A., and Hashish, R. G. (2023). A technical review of CO_2 for enhanced oil recovery in unconventional oil reservoirs. *J. Petrol. Sci. Eng.* 221, 111185. doi:10.1016/j.petrol.2022.111185

Tao, S., Chen, S., and Pan, Z. (2019). Current status, challenges, and policy suggestions for coalbed methane industry development in China: a review. *Energy Sci. Eng.* 7, 1059–1074. doi:10.1002/ese3.358

Wang, H., Fan, N., Deng, C., and Gao, Z. (2025). Numerical study of optimal injected gas mixture proportions for enhancing coalbed methane recovery. *ACS Omega* 10, 6689–6706. doi:10.1021/acsomega.4c08205

Wu, H., Zhang, N., Lou, Y., Zhai, X., Liu, B., and Li, S. (2024). Optimization of fracturing technology for unconventional dense oil reservoirs based on rock brittleness index. *Sci. Rep.* 14, 15214. doi:10.1038/s41598-024-66114-w

Yang, M., Zhang, J., Zhang, L., and Gong, S. (2024). Physicochemical effect on coal pores of hydrocarbon chain length and mixing of viscoelastic surfactants in clean fracturing fluids. *ACS Omega* 9, 19418–19427. doi:10.1021/acsomega.4c00692

Yu, H., Zhu, Y., Jin, X., Liu, H., and Wu, H. (2019). Multiscale simulations of shale gas transport in micro/nano-porous shale matrix considering pore structure influence. *J. Nat. Gas. Sci. Eng.* 64, 28–40. doi:10.1016/j.jngse.2019.01.016

Yuan, Y., Gong, Y., Xu, T., and Zhu, H. (2023). Multiphase flow and geomechanical responses of interbedded hydrate reservoirs during depressurization gas production for deepwater environment. *Energy* 262, 125603. doi:10.1016/j.energy.2022.125603

Yusuf, N., and Al-Ansari, T. (2023). Current and future role of natural gas supply chains in the transition to a low-carbon hydrogen economy: a comprehensive review on integrated natural gas supply chain optimisation models. *Energies* 16 (22), 7672. doi:10.3390/en16227672

Zhao, H., Li, W., Cai, M., Ma, B., Xie, X., Zou, L., et al. (2024). Study on rock fracture mechanism and hydraulic fracturing propagation law of heterogeneous tight sandstone reservoir. *PLOS One* 19, e0303251. doi:10.1371/journal.pone.0303251

Zhou, R., Bai, B., Cai, G., and Chen, X. (2024). Thermo-hydro-mechanic-chemical coupling model for hydrate-bearing sediment within a unified granular thermodynamic theory. *Comput. Geotech.* 167, 106057. doi:10.1016/j.compgeo.2023.106057

frontiers | Frontiers in Earth Science

TYPE Original Research
PUBLISHED 13 June 2024
DOI 10.3389/feart.2024.1419631

OPEN ACCESS

EDITED BY
Qingchao Li,
Henan Polytechnic University, China

REVIEWED BY
Lijun Liu,
Chengdu University of Technology, China
Fankun Meng,
Yangtze University, China

*CORRESPONDENCE
Long Ren,
renlong@xsyu.edu.cn

RECEIVED 18 April 2024
ACCEPTED 28 May 2024
PUBLISHED 13 June 2024

CITATION
Ren L, Dou M, Dong X, Chen B, Zhang L, Sun J, Jing C, Zhang W, Zhou D and Li H (2024), Quantitative characterization of stimulated reservoir volume (SRV) fracturing effects in naturally fractured unconventional hydrocarbon reservoirs.
Front. Earth Sci. 12:1419631.
doi: 10.3389/feart.2024.1419631

Quantitative characterization of stimulated reservoir volume (SRV) fracturing effects in naturally fractured unconventional hydrocarbon reservoirs

Long Ren[1,2]*, Mengyuan Dou[3], Xiaowei Dong[4], Bo Chen[5], Ling Zhang[5], Jian Sun[1,2], Cheng Jing[1,2], Wugang Zhang[1,2], Desheng Zhou[1,2] and Haiyan Li[6]

[1]School of Petroleum Engineering, Xi'an Shiyou University, Xi'an, China, [2]Shaanxi Key Laboratory of Advanced Stimulation Technology for Oil and Gas Reservoirs, Xi'an, China, [3]No.1 Oil Production Plant, PetroChina Changqing Oilfield Company, Yan'an, China, [4]Engineering Technology Research Institute, PetroChina Xinjiang Oilfield Company, Xinjiang, China, [5]No.6 Oil Production Plant, PetroChina Changqing Oilfeld Company, Yulin, China, [6]Party School of Party Committee, Shengli Petroleum Bureau Co., Ltd. Sinopec, Dongying, China

Stimulated reservoir volume (SRV) fracturing has become the most efficient technology in the treatment of unconventional hydrocarbon reservoir formations. This process aims to optimize well productivity by establishing an intricate network of fractures that integrate hydraulic and natural fractures, distal to the wellbore, thereby amplifying the contact area with the subterranean formations and fracture systems. This study introduces a quantitative framework designed to characterize the fracturing effects within naturally fractured unconventional hydrocarbon reservoirs. Leveraging existing fracturing treatment designs and production performance data, the study formulates a mathematical model of the complex fracture network, predicated on the principle of material balance. The model comprehensively accounts for the development degree of natural fractures, the morphological impact of stress differentials on the fracture network, and the imbibition displacement effects of the fracturing fluids. The model's accuracy is verified through an integration with microseismic monitoring data and an enhanced understanding of reservoir development. Building upon this foundation, the study quantitatively dissects the impact of various engineering parameters on the efficacy of SRV fracturing. The proposed quantitative characterization method is adept for widespread application across multiple wells in oil and gas fields, offering a distinct advantage for the swift and precise assessment of SRV fracturing outcomes in naturally fractured unconventional hydrocarbon reservoirs. The research method, which is based on readily accessible fracturing construction data and is more convenient, can to a certain extent improve the efficiency of hydraulic fracturing evaluation work.

KEYWORDS

SRV fracturing, material balance method, imbibition depth, complex fracture network, quantitative evaluation

1 Introduction

The fundamental purpose of evaluating fracturing effects is to enhance the success rate of fracturing operations, optimize fracturing design technology, enhance post-fracturing production, and guide production management post-fracturing (Zhang et al., 2020; Wang et al., 2022; Guo et al., 2023; Luo et al., 2024). The evaluation of the stimulated reservoir volume (SRV) fracturing effect entails a comprehensive assessment of the overall quality of fracturing construction. In a broad sense, it involves a qualitative evaluation of single well or block fracturing construction dynamic monitoring, the alignment of process and design during construction, long-term production performance, and economic viability. In a narrow sense, it focuses on quantitatively characterizing post-fracturing productivity changes, such as SRV, fracture conductivity, and fracture density (geometrical parameters), etc.

Over the recent years, a substantial body of research has been dedicated to the evaluation of hydraulic fracturing within the context of naturally fractured unconventional hydrocarbon reservoirs. These evaluation methodologies are bifurcated into direct and indirect approaches based on the immediacy and objectivity of the resultant data. The direct approach encompasses the acquisition of data through sophisticated monitoring instruments, including microseismic fracture monitoring, isotopic tracers, and inclinometers, to ascertain and interpret a multitude of fracture-related parameters that are indicative of the fracturing process's efficacy (Liu et al., 2019; Eyinla et al., 2023; Wang et al., 2023). In contrast, the indirect approach involves the inversion of fracture geometry and conductivity parameters from production test data, which includes the analysis of production dynamics of fractured wells, well test evaluations, and the application of mathematical models (Niu et al., 2019; Zhang et al., 2020; Wang et al., 2024). Despite these methods, the direct approach often overestimates the SRV in comparison to the effective stimulated reservoir volume (ESRV) that includes a proppant pack (Li et al., 2019; Li et al., 2024). Meanwhile, the indirect approach, with its potential for multiple interpretive solutions, overlooks the imbibition phenomenon, thereby introducing constraints in the precise and quantitative characterization of SRV fracturing effects in horizontal wells within naturally fractured unconventional hydrocarbon reservoirs.

Aiming to address these limitations, this study introduces a novel quantitative characterization model for SRV fracturing effects in naturally fractured unconventional hydrocarbon reservoirs, predicated on the principles of material balance. The model is anchored in empirical fracturing construction and production dynamic data, and it holistically integrates the impact of natural fracture development, stress differentials on fracture network morphology, the imbibition displacement dynamics between the fracture network and matrix pores, and the material balance between the injected and produced fluid systems throughout the fracturing and flowback phases. This model provides a quantitative depiction and assessment of the degree of reserves production within a given well pattern and fracture network distribution, offering a more nuanced evaluation framework for the performance of SRV fracturing in such complex reservoir environments.

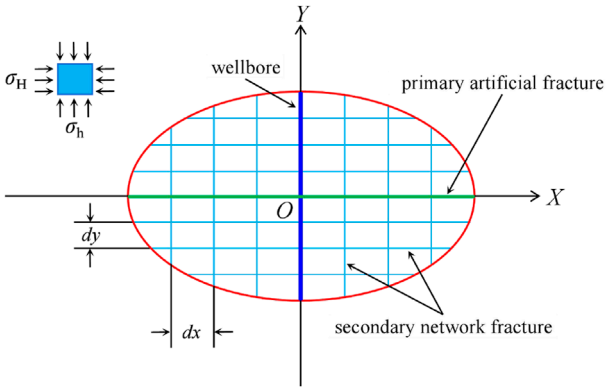

FIGURE 1
Physical model diagram of the fracture network propagation with single-stage SRV fracturing.

2 Mathematical characterization model

2.1 Physical model and assumptions

The formation process of fracture networks in unconventional hydrocarbon reservoirs through volume fracturing is highly complex. In the initial stages of fracture network development, the opening of weak planes on the main fracture walls or the limited extension of natural fractures can be disregarded, leading to the formation of primary fractures. As the geometric dimensions of the primary fractures increase, the pressure loss of the fracturing fluid also rises, necessitating an increase in the construction pressure to propagate the fractures further. At this stage, natural fractures extensively open, resulting in the formation of secondary fractures. Extensive research by numerous scholars has revealed that under constant geostress conditions, the geometric configuration of fracture networks exhibits a degree of regularity and similarity.

Based on the fluid flow and continuity equations for porous media (Li et al., 2015; Liu, 2016; Wang et al., 2018; Fend et al., 2019), while taking into account the interactions between the fluid and the fractures as well as among the fractures themselves, it is posited that the fracture network formed by the single-stage SRV fracturing is constituted by a series of orthogonal primary and secondary fractures that combine in a regular pattern. This network configures into an axisymmetric elliptical cylindrical shape along the wellbore, with the major and minor axes of the ellipse being $2a$ and $2b$, respectively. Building on this conceptual framework, a physical model known as the two-dimensional elliptic orthogonal line network model (Cheng et al., 2013; Shi et al., 2014; Ren et al., 2015; Li et al., 2019; Ren et al., 2019; Zheng et al., 2023) has been developed to encapsulate the propagation dynamics of fracture networks with SRV fracturing in unconventional reservoirs. A visual representation of this model is delineated in Figure 1.

The model is predicated on several key assumptions: 1) both primary and secondary fractures extend through the entire thickness of the reservoir, with their spatial propagation adhering to the characteristics of the elliptic orthogonal line network model; 2) secondary fractures are uniformly distributed in the direction of the

horizontal principal stresses (denoted as σ_H for the maximum and σ_h for the minimum horizontal principal stresses), with uniform spacing of dx and dy, respectively, and consistent fracture width; 3) the effects of viscoelasticity and wall slip on fluid flow are neglected; 4) proppant is uniformly distributed within the fractures; and 5) the impact of fracturing fluid filtration is disregarded.

2.2 Mathematical model description

2.2.1 Wellbore volume

According to the cylinder volume formula, the wellbore volume can be expressed as:

$$V_w = \pi L r_w^2 \tag{1}$$

where V_w is the wellbore volume; r_w is the wellbore radius; L represents the drilling footage.

2.2.2 Pore volume of primary artificial fracture

According to the formula for the volume of a cuboid, the pore volume of the primary artificial fracture is expressed as:

$$V_f = 2x_f w_f H \tag{2}$$

where V_f is the pore volume of the primary artificial fracture; x_f is the main fracture half-length (half of the effective fracture length), that is, half of the long axis of the elliptical physical model; H is the reservoir thickness of the study area; w_f is the fracture width, which satisfies the England-Green equation under plane strain condition. The calculation formula can be given by:

$$w_f = \frac{2(1-v^2)}{E}\left(p_f - \sigma_{\min}\right)h_f \tag{3}$$

where v is the Poisson's ratio; E is the elastic modulus; h_f is the height of the primary fractures; p_f indicates net pressure within the fractures; $\sigma_{\min}$ is the minimum horizontal principal stress.

2.2.3 Pore volume of secondary network fracture

The pore volume of the secondary network fracture is determined by considering the summation of the pore area of the secondary fractures on a given plane. This area can be approximated as an ellipse, where the length of the major axis is equivalent to that of the primary fracture, and the length of the minor axis is proportional to the secondary fractures within the network. According to the volume formula for a cylinder, the pore volume of the secondary network fracture is calculated with the major axis ($2a$) and minor axis ($2b$) derived from the ratio (r) of the longitudinal to transverse lengths of the fracture network detected in microseismic monitoring data from a single fracturing stage in the study area. Specifically, the major axis is given by $2a = 2x_f = r \times 2b$, where r is the aspect ratio. The height of the secondary fracture is considered equal to the thickness of the target reservoir (H). Consequently, the pore volume calculation model for the secondary network fracture can be articulated as:

$$V_s = \frac{\pi \lambda N r}{2M} x_f^2 w_f H \tag{4}$$

where V_s indicates the pore volume of the secondary network fracture; λ is the width ratio of the primary and secondary fracture, which is obtained from typical well coring data; N represents the number of natural fractures within the length M of the target reservoir segment in the study area, which can be obtained from the imaging logging data of typical blocks.

2.2.4 Imbibition displacement volume within matrix pores

The imbibition process, in which the fluid within all matrix blocks is replaced, is analogous to the surface imbibition occurring over the entire elliptical cylinder. The concept of imbibition depth is introduced to quantify and assess the efficacy of imbibition replacement within the matrix pores in proximity to the entire fracture network (Wu et al., 2017a; Wu et al., 2017b; Ju et al., 2019; Dai et al., 2020; Tao et al., 2023). Subsequently, the model for calculating the imbibition displacement volume can be formulated as follows:

$$V_m = \frac{\pi}{r} x_f^2 H - V_f - V_s - \pi \varphi_1 \left(x_f - d\right)\left(\frac{x_f}{r} - d\right)(H - 2d) \tag{5}$$

where V_m is the imbibition displacement volume within matrix pores; d is equivalent imbibition depth; ϕ_1 is the matrix porosity in the end of imbibition replacement.

Therefore, the aforementioned Eqs 1–5 collectively constitute the material balance equation for the fracturing injection fluid system, which can be expressed as:

$$Q = V_w + m\left(V_f + V_s + V_m\right) \tag{6}$$

where Q is the total amount of fracturing fluid; m is the number of fracturing stages.

Given that the quantity of oil recovered through imbibition is equivalent to the decrease in oil saturation within the matrix pore volume, the material balance throughout the imbibition replacement process can be characterized as follows:

$$V_m\left(S_{oi} - S_{or}\right) = \frac{\pi}{r} x_f^2 H \varphi_1 S_{oi} R_o \tag{7}$$

where S_{oi} and S_{or} are the initial oil saturation of cores before imbibition and the residual oil saturation of cores in the end of imbibition replacement, respectively; R_o is the core imbibition recovery factor.

2.2.5 Material balance equation during fracturing fluid flowback period

In accordance with the principle of material balance (Moussa et al., 2020; Ren et al., 2023; Hossain and Dehghanpour, 2024), a correlation is established between the volume of fracturing fluid injected and the subsequent alterations in formation pressure and underground pore volume at the conclusion of the imbibition replacement phase for the injected fracturing fluid. The material balance equation, which accounts for reservoir elasticity during the flowback period post-fracturing, is formulated as follows:

$$Q_i - V_w - m\left(V_f + V_s\right) = V_{c1}(1 - s_{wc})(c_o + c_c)(p_1 - p_i) \tag{8}$$

where Q_i is the injection amount of fracturing fluid in the stage i of horizontal well; c_o is the compression coefficient of crude oil; c_c is the compression factor of reservoir volume; p_1 is the average formation pressure in the end of imbibition replacement; p_i is the

initial formation pressure; V_{c1} is the pressure sweep volume in the end of imbibition replacement and is expressed as $V_{c1} = 4x_f(L+S)H\phi_1$, with S being the spacing of the horizontal well; ϕ_1 is the porosity of the rock in the end of imbibition replacement.

Similarly, a correlation is established between the surface liquid production of the oil well and the variations in formation pressure and subsurface pore volume as follows:

$$N_pB_o + W_pB_w + V_w + m\left(V_f + V_s\right) = V_{c2}(c_o + c_c)(p_1 - p_2 - p_l) \quad (9)$$

where N_p and W_p are the cumulative oil and water production during the flowback period, respectively; B_o and B_w are the volume coefficient of crude oil and formation water, respectively; p_2 is the average formation pressure in the end of fracturing flowback; p_l is the pressure loss of fluid in the wellbore, and the expression is $p_l = 0.0028h$, with h is the wellbore depth; V_{c2} is the reservoir pressure ripple volume with completion of frac flowback expressed as $V_{c2} = 4x_f(L+S)H\phi_2$, with ϕ_2 being the rock porosity in the end of fracturing fluid flowback.

At the culmination of the imbibition replacement process, the rock porosity is described by the following equation of state:

$$\varphi_1 = \varphi_0\left[1 + c_p(p_1 - p_i)\right] \quad (10)$$

where c_p is the compression factor of matrix pores; ϕ_0 is the matrix porosity in the original state of the target reservoir.

At the conclusion of the fracturing fluid flowback, the rock porosity conforms to the following equation of state:

$$\varphi_2 = \varphi_0\left[1 + c_p(p_1 - p_2 - p_l)\right] \quad (11)$$

Building upon the aforementioned equations, the quantitative characterization model for the effects of SRV fracturing in naturally fractured unconventional hydrocarbon reservoirs, grounded in the principle of material balance, is ultimately established. The model requires the determination of four critical parameters: the effective fracture half-length (x_f), the equivalent imbibition depth (d), the average formation pressure (p_1) at the termination of the imbibition replacement phase, and the average formation pressure (p_2) at the conclusion of the fracturing fluid flowback period.

3 Model solving and verification

The material balance Eqs 6–9 and the state Eqs 10, 11 collectively constitute a mathematical model for the quantitative evaluation of SRV fracturing effect. The solution process for this model is meticulously structured and includes several components: a basic data preparation module, a parameter symbol explanation module, an equation set and programming solution module, and an evaluation parameter output module. The program is developed within a Windows 11 environment, utilizing Anaconda3 (64-bit) and the Jupyter Notebook interface for coding and design. The program's final output is formatted as Excel spreadsheets, enabling simultaneous calculations for multiple wells. The computation yields key evaluation parameters such as x_f, d, p_1, and p_2. Furthermore, the volume of each part can be calculated, including V_w, V_f, V_s, and V_m.

The precision of the program's solution for the mathematical characterization model is corroborated through a comprehensive analysis of microseismic monitoring data, pattern spacing, and production performance data from the M56-5 SRV-fractured horizontal well in the tight oil reservoirs within the Tuha oilfield, located in the Santanghu Basin, China. Geological characteristics, high-pressure fluid physical property parameters, and rock mechanics parameters for the target reservoir are detailed in Tables 1, 2, while Table 3 presents the fracturing reconstruction parameters specific to the M56-5 well.

TABLE 1 The geological characteristic and fluid property parameters of the target reservoir.

Parameters (unit)	Data	Parameters (unit)	Data
Formation thickness (m)	38	Crude oil volume factor	1.109
Initial porosity (%)	9.16	Formation water volume factor	1.010
Initial formation pressure (MPa)	21.35	Crude oil compression factor ($\times10^{-4}$ MPa^{-1})	9.56
Initial oil saturation (%)	69	Rock compression coefficient ($\times10^{-4}$ MPa^{-1})	5.83
Residual oil saturation (%)	33	Reservoir volume compression coefficient ($\times10^{-4}$ MPa^{-1})	13.92
Natural fracture spacing (m)	1.5	Average infiltration efficiency (%)	30

TABLE 2 The rock mechanics parameters of the target reservoir.

Parameters (unit)	Data
Young's modulus (GPa)	30.71
Poisson's ratio	0.293
Maximum horizontal principal stress (MPa)	55.87
Minimum horizontal principal stress (MPa)	48.78
Rock fracture pressure (MPa)	60.36
Normal stress (MPa)	49.25

Microseismic monitoring data reveal that the average bandlength and bandwidth of the fracture network formed in each stage of the M56-5 well through SRV fracturing are 346.91 m and 65.64 m, respectively. Nonetheless, in light of the actual production performance, the well spacing has been adjusted to 75 m, and the stage spacing is set at 40 m. The development dynamics indicate that no effective displacement is established between the M56-5 well and the neighboring wells. Consequently, the fracture network system of the M56-5 well remains isolated from adjacent wells, implying that the effective bandlength of fracture network should be less than the well spacing of 75 m.

As per the mathematical model and solution methodology presented in this paper, the average effective bandlength and bandwidth of the fracture network formed during each fracturing stage of the M56-5 well were determined to be 71.36 m and 17.84 m,

TABLE 3 The fracturing reconstruction parameters of M56-5 well.

Parameters (unit)	Data
Well depth (m)	2,939
Number of fracturing stages	10
Total amount of fracturing fluid injection (m^3)	10,260.4
Horizontal section length (m)	754
Cumulative oil production during the flowback period (m^3)	1,174.44
Cumulative water production during the flowback period (m^3)	2,242.44

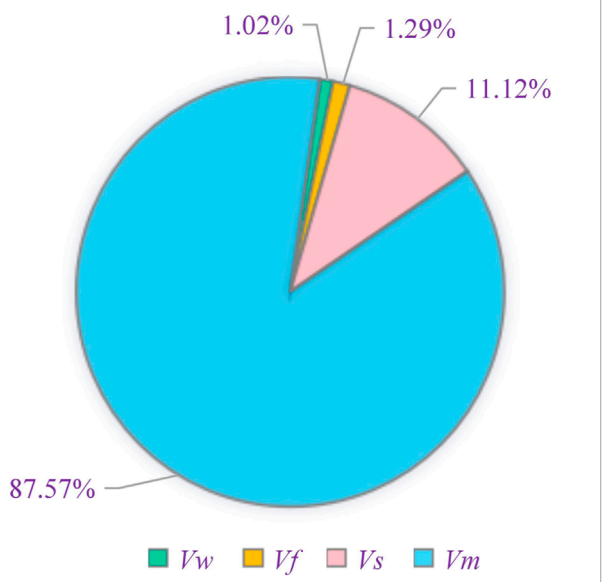

FIGURE 2
The proportion of the injected fluid in the volume of each part.

respectively. Furthermore, this model was applied to calculate the fracture network parameters for 54 other horizontally fractured wells with SRV fracturing within the study area. The outcomes demonstrated a 92.56% concordance rate between the calculated values and actual observations, thereby attesting to the relative reliability of the mathematical characterization model and the solving process established herein.

4 Results and analysis

4.1 Volume proportion of injected fluid

Utilizing the fracture network parameters (x_f, d, p_1, and p_2) derived from all SRV-fractured horizontal wells, the proportion of injected fluid in each part of the volume (V_w, V_f, V_s, and V_m) can be precisely calculated, with the results graphically depicted in Figure 2.

The calculated results indicate that the volume of imbibition displacement within the matrix pores constitutes a substantial 87.57%, underscoring the critical role of imbibition displacement in the development of naturally fractured unconventional hydrocarbon reservoirs. This result also provides a rational explanation for the typically low flowback rates observed in these reservoirs. Tight reservoirs subjected to SRV fracturing have developed a complex network of fractures with multiple pore media, significantly reducing the percolation distance that reservoir fluids must travel. During the early stages of development, there has been a qualitative shift in both the rate and the volume of fluid exchange between the matrix and the fractures. Consequently, imbibition displacement has transitioned from a secondary to a primary mechanism within the reservoir's fluid dynamics. Furthermore, the pore volume of the secondary network fractures represents 11.12% of the total volume, demonstrating that the injection of sand-carrying fracturing fluid to create complex fracture network systems plays a significant role. In contrast, the pore volume of the primary artificial fracture (accounting for only 1.29%) and the wellbore volume (accounting for a mere 1.02%) constitute relatively smaller proportions of the overall volume.

4.2 Statistical rules between SRV fracturing parameters

Based on the fracturing construction parameters and the fracture network parameters calculated by the model in this paper, the relationships between imbibition volume and injection volume of single stage, equivalent imbibition depth and injection volume of single stage, average formation pressure and total injection volume during fracturing processes, and pressure drop and well liquid production during fracturing fluid flowback period were separately explored by mathematical statistical method. The statistical curves and its fitting functions between SRV fracturing parameters can be obtained, as shown in Figure 3.

Analysis of the fitting equations derived from the statistical curves reveals a definite correlation between the parameters of fracturing operations and the resulting fracture network. There is a strong linear correlation between the imbibition volume and the injection volume during a single fracturing stage. Similarly, a pronounced exponential relationship is observed between the equivalent imbibition depth and the injection volume of a single stage. Additionally, the average formation pressure exhibits an exponential relationship with the total injection volume throughout the fracturing process. During the fracturing fluid flowback period, the pressure drop is characterized by a quadratic functional relationship with the liquid production of oil well. These fitting equations offer a convenient and preliminary theoretical foundation for field engineers to design fracturing operations effectively.

4.3 Sensitivity analysis for SRV fracturing effect

To quantitatively analyze the impact of engineering parameters on the SRV fracturing effect, simulations were designed under the condition of a constant horizontal section length. Various total volumes of fracturing fluid injection (3,681 m^3, 7,681 m^3, 11,681 m^3, 15,681 m^3 and 19,681 m^3) and different numbers of

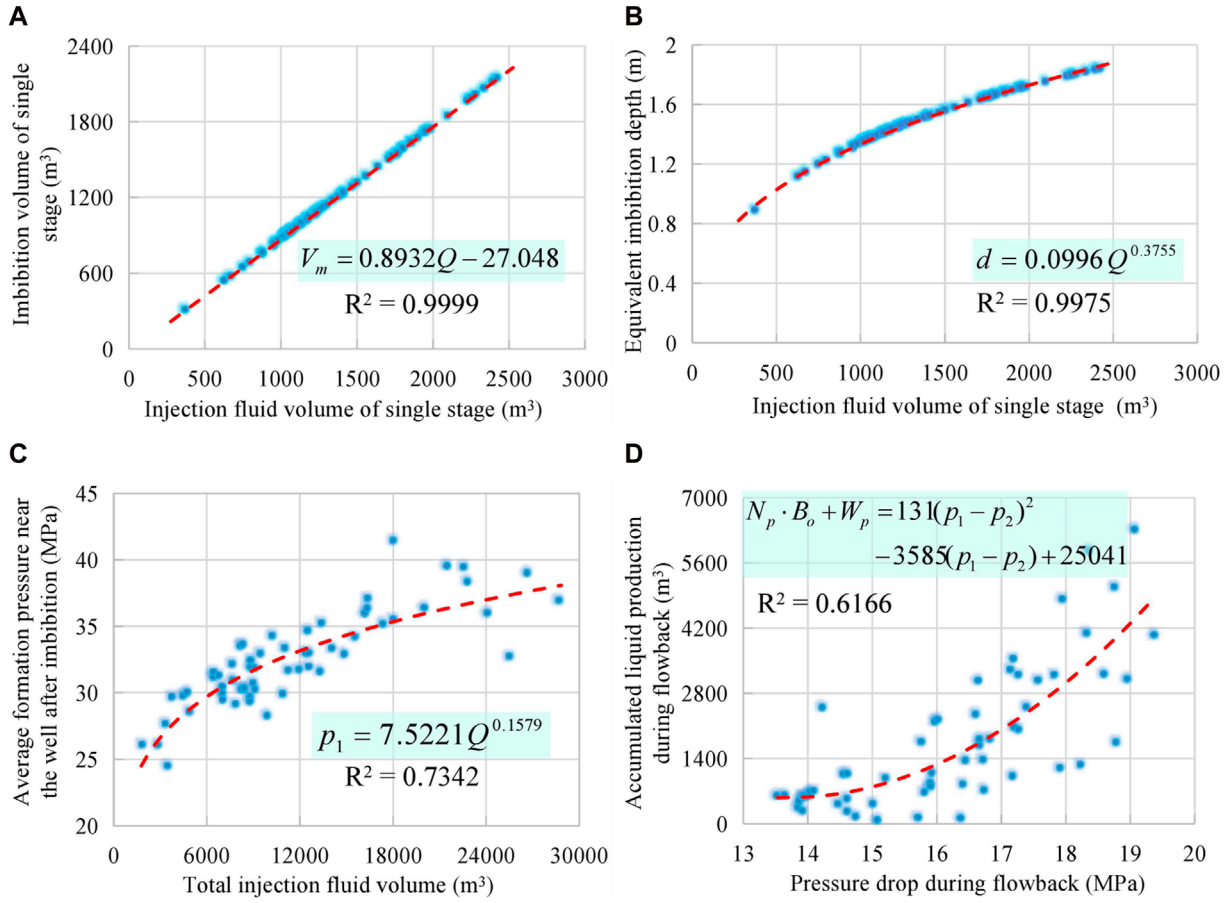

FIGURE 3
Statistical curves and its fitting functions between SRV fracturing parameters. **(A)** Injection and imbibition volume **(B)** Injection volume and imbibition depth **(C)** Injection volume and formation pressure **(D)** Pressure drop and well production.

fracturing stages (6 stages, 7 stages, 8 stages, 9 stages and 10 stages) were considered. Consequently, the effective band length, pore volume and imbibition displacement volume within a single-stage SRV, and equivalent imbibition depth were calculated for each scenario. The influence chart of engineering parameters on SRV fracturing effect is shown in Figure 4.

The influence curve of engineering parameters on the effectiveness of SRV fracturing clearly demonstrates that within the specified range of design parameters, the total volume of injected fracturing fluid exerts a substantial impact on both the pore volume and the imbibition displacement volume of the fracture network. This is attributable to the minimal interference between individual fracturing stages. Nonetheless, as the total volume of injected fracturing fluid increases, its influence on the effective bandlength and equivalent imbibition depth diminishes progressively. This suggests that while a certain amount of fluid is beneficial, an excessive volume may not yield proportional gains in fracture network development. The impact of the total injected fluid volume on the degree of fracture network stimulation is more pronounced when there are fewer fracturing stages. In such cases, the stimulation effect is stronger due to the absence of significant interference. Conversely, when there is a higher number of fracturing stages, the inter-stage interference comes into play, leading to a reduction in the overall stimulation effect of the fracture network. This complex interaction underscores the importance of optimizing the number of fracturing stages and the total volume of injected fluid to achieve the most effective SRV fracturing outcomes.

4.4 Quantitative evaluation of SRV fracturing effect

Based on the SRV fracturing construction parameters for each horizontal well, the bandlength and bandwidth of the fracture network for each fracturing stage are quantitatively computed. Utilizing the well pattern distribution and the three-dimensional spatial distribution of the fracture network parameters, a diagram depicting the well pattern distribution and characterization of the fracture network is established for various development stages of representative blocks within the tight oil reservoirs of the Tuha oilfield, as shown in Figure 5.

The reserves production degree is delineated as the proportion of the stimulated area of all horizontal wells relative to the oil-bearing area of the block. The quantitative evaluation of the SRV fracturing effect is characterized as follows. 1) In the early development phase with an initial well pattern (well spacing

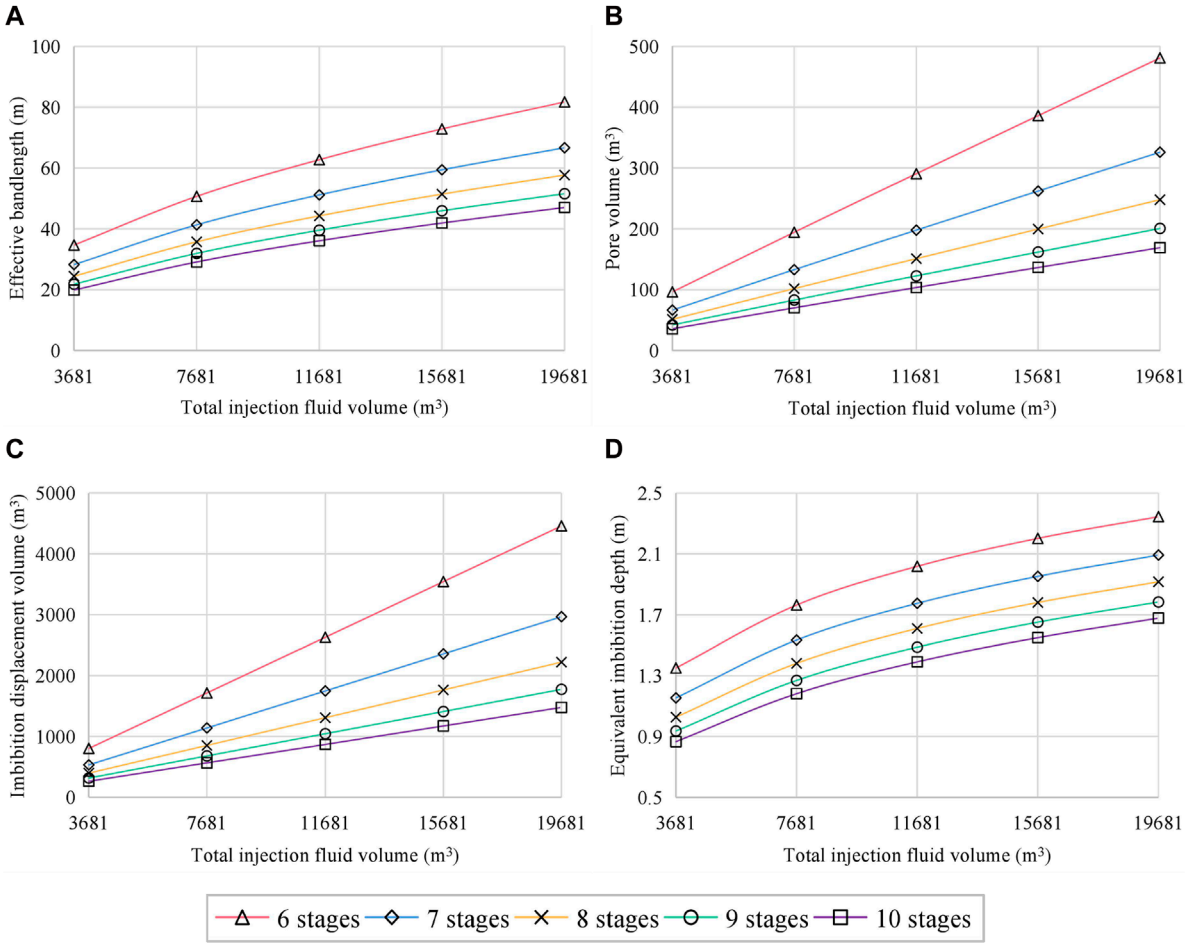

FIGURE 4
Influence chart of engineering parameters on SRV fracturing effect. **(A)** Effective bandlength **(B)** Pore volume within a single-stage SRV **(C)** Imbibition displacement volume within a single-stage SRV **(D)** Equivalent imbibition depth.

of 300–400 m), the SRV for each horizontal well was largely isolated due to the expansive well spacing. This resulted in a inadequate overlapping relationship of fracture networks between the horizontal wells and a low matching degree between the well pattern and the fracture network. Consequently, the reserves production degree under this well pattern condition was a mere 21.31%. 2) Advancing to the primary infill well pattern (well spacing of 150–200 m), the SRV of each well remained relatively isolated, and full match between the well pattern and the fracture network was unattainable. As such, the reserves production degree under this well pattern condition only reached 32.25%. 3) Under the current secondary infill well pattern (well spacing of 75–100 m), the well spacing is sufficiently narrow to preclude any isolated SRV between horizontal wells. This has led to a more effective overlap of fracture networks and a high matching degree of congruence between the well pattern and the fracture network. As a result, the reserves production degree can soar to 83.65%. The actual production performance data from this block indicate that 80% of horizontal wells in the secondary infill well pattern have been positively affected by water flooding from neighboring wells, leading to an increase in production. This has achieved the intended objective of establishing an overlapping relationship between the fracture networks of horizontal wells. In general, the block has experienced a paradigm shift from well-controlled reserves to fracture-controlled reserves following two rounds of well pattern infilling adjustments. With continued reduction in well spacing, alongside the implementation of enhanced oil recovery techniques such as multi-periodic waterflooding huff-n-puff and energized fracturing, it is feasible to transition from single-well imbibition to a synergistic mechanism of well group imbibition and displacement. This transition stands to significantly enhance the overall recovery and productivity of the reservoir.

5 Conclusion

This paper introduces a methodology for the quantitative characterization of the effects of Stimulated Reservoir Volume (SRV) fracturing in naturally fractured unconventional hydrocarbon reservoirs, employing the principle of material balance. The research findings underscore the critical role of imbibition displacement in the development of these reservoirs and provide a credible

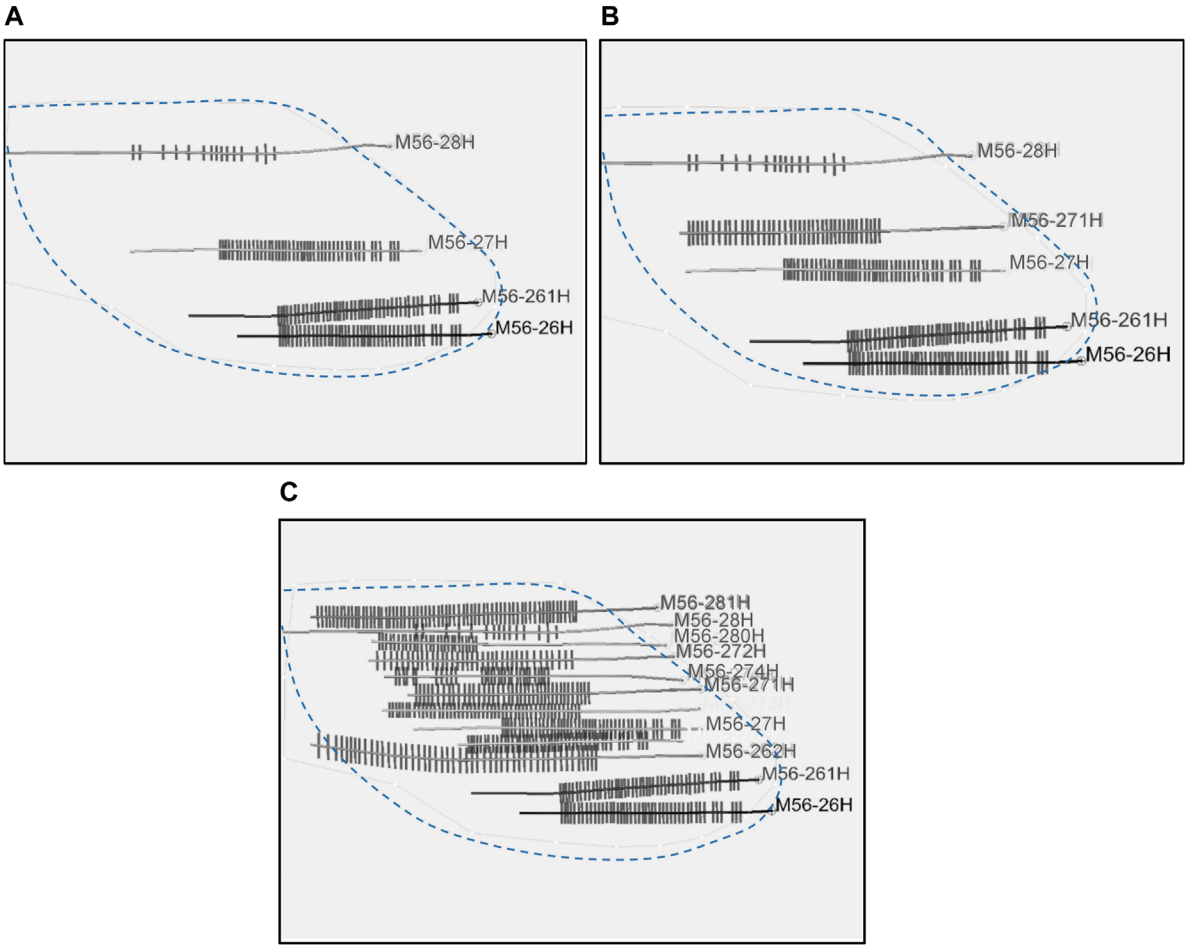

FIGURE 5
Diagram of well pattern distribution and fracture network characterization at different development stages of typical blocks. **(A)** Initial well pattern **(B)** Primary infilling adjustm **(C)** Secondary infilling adjustment.

explanation for the commonly observed low flowback rates in the field. A significant correlation exists between the parameters of the fracturing operation and the resulting fracture network. The total volume of injected fluid is decisive in determining the extent of stimulation of the fracture network induced by SRV fracturing. However, with an increasing number of fracturing stages, the influence of this volume on the degree of stimulation is progressively reduced. The methodology presented herein facilitates a quantitative evaluation of the reserves production degree within the study area, thereby enhancing the efficiency of fracturing operations. Moreover, the results yield a practical reference framework for engineers and technicians to accurately assess the SRV fracturing effects in typical blocks of naturally fractured unconventional hydrocarbon reservoirs. This approach not only refines the understanding of SRV fracturing effects but also informs the design and optimization of future fracturing operations in similar reservoir settings.

Data availability statement

The raw data supporting the conclusion of this article will be made available by the authors, without undue reservation.

Author contributions

LR: Conceptualization, Formal Analysis, Methodology, Writing–original draft. MD: Conceptualization, Methodology, Resources, Writing–review and editing. XD: Formal Analysis, Resources, Writing–review and editing. BC: Data curation, Investigation, Writing–review and editing. LZ: Data curation, Investigation, Writing–review and editing. JS: Methodology, Validation, Writing–review and editing. CJ: Writing–review and editing. WZ: Writing–review and editing. DZ: Supervision, Writing–review and editing. HL: Data curation, Validation, Writing–review and editing.

Funding

The author(s) declare that financial support was received for the research, authorship, and/or publication of this article. This research was supported by the National Natural Science Foundation of China (Nos 52304036; 51934005; U23B2089) and Natural Science Basic Research Plan in Shaanxi Province of China (Nos 2023-JC-YB-344; 2023-JC-YB-433).

Conflict of interest

Authors MD, BC, and LZ was employed by PetroChina Changqing Oilfield Company. Author XD was employed by PetroChina Xinjiang Oilfield Company. Author HL was employed by Shengli Petroleum Bureau Co., Ltd. Sinopec.

The remaining authors declare that the research was conducted in the absence of any commercial or financial relationships that could be construed as a potential conflict of interest.

Publisher's note

All claims expressed in this article are solely those of the authors and do not necessarily represent those of their affiliated organizations, or those of the publisher, the editors and the reviewers. Any product that may be evaluated in this article, or claim that may be made by its manufacturer, is not guaranteed or endorsed by the publisher.

References

Cheng, Y. F., Li, Y. Z., Shi, X., Wu, B. L., Wang, X., and Deng, W. B. (2013). Analysis and application of fracture network models of volume fracturing in shale gas reservoirs. *Nat. Gas. Ind.* 33 (9), 53–59. doi:10.3787/j.issn.1000-0976.2013.09.009

Dai, C. L., Li, Y., Xu, X. P., Zhao, M. W., Yuan, B., Xu, K., et al. (2020). Oil-water two-phase migration in imbibition process of gel breaking fluid of clean fracturing fluid. *Oilfield Chem.* 37 (4), 609–615. doi:10.19346/j.cnki.1000-4092.2020.04.008

Eyinla, D., Henderson, S. K., Emadi, H., Thiyagarajan, S. R., and Arora, A. (2023). Optimization of hydraulic fracture monitoring approach: a perspective on integrated fiber optics and sonic tools. *Geoenergy Sci. Eng.* 231, 212441. doi:10.1016/j.geoen.2023.212441

Fend, F. P., Huang, R., Lei, Y., Guo, B., Hu, C. Y., and Wang, H. Z. (2019). Evaluation of engineering effectiveness of volume fracturing based on energy conservation principles and its application. *J. China Univ. Petroleum Ed. Nat. Sci.* 43 (1), 81–89. doi:10.3969/j.issn.1673-5005.2019.01.010

Guo, T. K., Wang, Y. P., Chen, M., Qu, Z. Q., Tang, S. J., and Wen, D. W. (2023). Multi-stage and multi-well fracturing and induced stress evaluation: an experiment study. *Geoenergy Sci. Eng.* 230, 212271. doi:10.1016/j.geoen.2023.212271

Hossain, S., and Dehghanpour, H. (2024). A theory to model pseudo steady state water production and predict long-term water recovery from fractured reservoirs. *Energy* 288, 129586. doi:10.1016/j.energy.2023.129586

Ju, M. S., Wang, X. Y., Yu, W. S., Yang, S. L., Ye, W. Z., and Zhang, T. Q. (2019). Spontaneous imbibition of tight oil reservoirs based on NMR technology. *Xinjiang Pet. Geol.* 40 (3), 334–339. doi:10.7657/XJPG20190312

Li, Q., Wang, Y. L., and Owusu, A. B. (2019a). A modified Ester-branched thickener for rheology and wettability during CO_2 fracturing for improved fracturing property. *Environ. Sci. Pollut. Res.* 26, 20787–20797. doi:10.1007/s11356-019-05386-6

Li, Q. C., Liu, J., Wang, S. M., Guo, Y., Han, X. Y., Li, Q., et al. (2024). Numerical insights into factors affecting collapse behavior of horizontal wellbore in clayey silt hydrate-bearing sediments and the accompanying control strategy. *Ocean. Eng.* 297, 117029. doi:10.1016/j.oceaneng.2024.117029

Li, X. W., Liu, S., Chen, Q., Su, Y. L., and Sheng, G. L. (2019b). An evaluation of the stimulation effect of horizontal well volumetric fracturing in tight reservoirs with complex fracture networks. *Pet. Drill. Tech.* 47 (6), 73–82. doi:10.11911/syztjs.2019126

Li, X. W., Zhang, K. S., Ma, B., Tian, S. B., and Zhang, J. L. (2015). A new method using material balance equations to interpret the effective stimulation volume of fracture network fracturing in tight reservoirs. *Sci. Technol. Eng.* 15 (36), 56–62.

Liu, J. C., Liu, J. J., Wang, X. Y., and Liu, C. (2019). Micro-seismic technique evaluation of the effect of volumetric fracturing in Zhongmou area. *Contributions Geol. Mineral Resour. Res.* 34 (1), 78–83. doi:10.6053/j.issn.1001-1412.2019.01.012

Liu, X. L. (2016). Well test analysis and evaluation after shale-gas volume fracturing stimulation. *Nat. Gas. Ind.* 36 (8), 66–72.

Luo, Y., Kang, B., Wang, H. H., Guo, J. C., Jiang, L. P., Cheng, Y., et al. (2024). Stacking ensemble learning based inversion for three-dimensional distribution region of hydraulic fractures in shale. *Geoenergy Sci. Eng.* 236, 212712. doi:10.1016/j.geoen.2024.212712

Moussa, T., Dehghanpour, H., Fu, Y. K., and Ezulike, O. (2020). The use of flowback data for estimating dynamic fracture volume and its correlation with completion-design parameters: eagle Ford cases. *J. Petroleum Sci. Eng.* 195, 107584. doi:10.1016/j.petrol.2020.107584

Niu, X. B., Feng, S. B., You, Y., Liang, X. W., Xin, H. G., Dan, W. D., et al. (2019). Fracture extension and distribution pattern of volume fracturing in tight reservoir: an analysis based on actual coring data after fracturing. *Oil Gas Geol.* 40 (3), 669–677. doi:10.11743/ogg20190322

Ren, L., Su, Y. L., Hao, Y. M., Zhang, Q., Meng, F. K., and Sheng, G. L. (2015). Dynamic analysis of SRV-fractured horizontal wells in tight oil reservoirs based on stimulated patterns. *Acta Pet. Sin.* 36 (10), 1272–1279. doi:10.7623/syxb201510010

Ren, L., Su, Y. L., Zhan, S. Y., and Meng, F. K. (2019). Progress of research on productivity prediction methods for stimulated reservoir volume (SRV)-Fractured horizontal wells in unconventional hydrocarbon reservoirs. *Arabian J. Geosciences* 12 (6), 1–15. doi:10.1007/s12517-019-4376-2

Ren, L., Wang, Z. H., Zhao, J. Z., Lin, R., Wu, J. F., Song, Y., et al. (2023). Shale gas effective fracture network volume prediction and analysis based on flow back data: a case study of southern Sichuan Basin shale. *Geoenergy Sci. Eng.* 228, 211963. doi:10.1016/j.geoen.2023.211963

Shi, X., Cheng, Y. F., Jiang, S., Li, Y. Z., Sun, Y. W., and Wang, X. (2014). Simulation of complex fracture network propagation and its application for shale gas reservoir. *Acta Pet. Sin.* 35 (6), 1130–1137. doi:10.7623/syxb201406010

Tao, L. Y., Sheng, J. C., Wang, H. M., Wang, J. G., Zhen, H. F., Huang, T. R., et al. (2023). Synergistic impacts of fracture–matrix system on recovery rate during spontaneous imbibition in tight sandstones. *Geoenergy Sci. Eng.* 234, 212594. doi:10.1016/j.geoen.2023.212594

Wang, F., Liu, W., Deng, J. G., Xu, K. K., Xing, C. W., and Yan, K. (2024). Hydraulic fracture propagation research in layered rocks based on 3D FEM modeling and laboratory experiments. *Geoenergy Sci. Eng.* 234, 212670. doi:10.1016/j.geoen.2024.212670

Wang, J. C., Zhang, H. J., Zhao, L. P., Zha, H. S., Cheng, T. T., Shi, X. H., et al. (2023). Evaluation of the coalbed methane hydraulic fracturing effect based on microseismic event locations and tomography results for surface microseismic monitoring. *Geophys. Prospect. Petroleum* 62 (1), 31–42+55. doi:10.3969/j.issn.1000-1441.2023.01.002

Wang, Y. F., Zhai, G. Y., Hu, Z. F., Li, J., Zhang, Y. X., Kang, H. X., et al. (2022). Reservoir characteristics of the sinian doushantuo formation and the effectevaluation of complex fracturing in yichang, hubei Province. *Acta Geol. Sin.* 96 (4), 1447–1459. doi:10.19762/j.cnki.dizhixuebao.2021214

Wang, Z. Y., Ding, Y. H., Yang, Z. M., He, Y., Wang, X. Y., and Ma, Z. Z. (2018). A material balance zoning productivity prediction model of fractured horizontal well in tight oil reservoirs. *Bull. Sci. Technol.* 34 (12), 44–48. doi:10.13774/j.cnki.kjtb.2018.12.007

Wu, R. T., Yang, S. L., Wang, M. B., Lv, D. P., and Kou, G. (2017a). Experimental study on static imbibition of tight sandstone. *J. Liaoning Univ. Petroleum Chem. Technol.* 37 (3), 24–29. doi:10.3969/j.issn.1672-6952.2017.03.006

Wu, R. T., Yang, S. L., Xie, J. Y., Wang, M. B., and Yan, J. W. (2017b). Experiment and mechanism of spontaneous imbibition of matrix core in tight oil-gas reservoirs. *Petroleum Geol. Recovery Effic.* 24 (3), 98–104. doi:10.13673/j.cnki.cn37-1359/te.2017.03.015

Zhang, A. S., Yang, Z. M., Li, X. S., Xia, D. B., Zhang, Y. P., Luo, Y. T., et al. (2020a). An evaluation method of volume fracturing effects for vertical wells in low permeability reservoirs. *Petroleum Explor. Dev.* 47 (2), 441–448. doi:10.1016/s1876-3804(20)60061-1

Zhang, Z. L., Shen, F., Xu, D. Z., and Li, Q. Y. (2020b). A new inversion method of stimulated reservoir volume fracturing region based on pump-stop data and its application. *Unconv. Oil Gas* 7 (6), 81–89.

Zheng, X. L., Zhang, G. Q., Chen, L., Zhang, M., Qiu, R. Y., Zhou, D. W., et al. (2023). Laboratory investigation on cryogenically induced fractures in shale with beddings. *Geoenergy Sci. Eng.* 222, 211438. doi:10.1016/j.geoen.2023.211438

frontiers | Frontiers in Earth Science

TYPE Methods
PUBLISHED 02 July 2024
DOI 10.3389/feart.2024.1427426

OPEN ACCESS

EDITED BY
Shu Tao,
China University of Geosciences, China

REVIEWED BY
Jun Lu,
China University of Geosciences, China
Shihang Feng,
Los Alamos National Laboratory (DOE), United States
Suzhen Shi,
China University of Mining and Technology, China

*CORRESPONDENCE
Guanyu Zhang,
deitywindsong@163.com

RECEIVED 03 May 2024
ACCEPTED 13 June 2024
PUBLISHED 02 July 2024

CITATION
Zhang G, Huang X, Xu Y, Tang S, Chen K and Peng D (2024), Deep carbonate gas reservoir sweet spot identification with seismic data based on dual-factor control of sedimentary facies and fault system.
Front. Earth Sci. 12:1427426.
doi: 10.3389/feart.2024.1427426

Deep carbonate gas reservoir sweet spot identification with seismic data based on dual-factor control of sedimentary facies and fault system

Guanyu Zhang[1]*, Xuri Huang[1], Yungui Xu[1], Shuhang Tang[1], Kang Chen[2] and Da Peng[2]

[1]School of Geosciences and Technology, Southwest Petroleum University, Chengdu, China, [2]Exploration and Development Research Institute, PetroChina Southwest Oil & Gasfield Company, Chengdu, Sichuan, China

Deep carbonate reservoirs are attractive targets for gas development. These reservoirs are deeply buried, and commonly possess strong heterogeneity and poor seismic data quality, making the identification of favorable production areas ("sweet spots") challenging. Furthermore, sedimentary facies and fault systems markedly impact reservoir quality, and identifying these features in seismic data is also crucial for sweet spot identification. To solve these problems, we propose a dual-factor-controlled sweet spot identification method with two steps. First, sedimentary facies and faults are identified separately at different seismic scales using different attributes by the steerable pyramid (SP) method. The SP method decomposes the original seismic data into high-frequency and low-frequency data. The amplitude attributes from high-frequency data are used to identify sedimentary facies, and coherence attributes based on low-frequency data are used to characterize the fault systems. Second, after separately identifying the sedimentary facies and faults, the two attribute volumes are merged together to identify reservoir sweet spots. The results are verified by using well production data. The results of a field study in the Dengying Formation deep carbonate reservoir in the central Sichuan Basin, China, indicate that reservoir sweet spots are primarily developed in ideal sedimentary facies along strike-slip fault systems. Sedimentary facies generally control the type and distribution of reservoirs, whereas strike-slip fault systems control the migration and accumulation of gas. In addition, the fault systems serve as karst channels that further improve the reservoir properties. The proposed dual-factor method might help to maximize exploration potential in deep carbonate reservoirs with similar settings.

KEYWORDS

Sichuan Basin, Dengying formation, mound-shoal complex, strike-slip fault, reservoir sweet spot, steerable pyramid processing

1 Introduction

Carbonate reservoirs are extremely important for oil and gas development, because they host more than 60% of the world's oil reserves and 40% of gas reserves (Hendry et al., 2021). In recent years, deep carbonate reservoirs (burial depth >3,500 m) have become important targets for hydrocarbon production, such as the pre-salt carbonate reservoir in Brazil, Lower Cretaceous carbonates in Venezuela, and the Sichuan Basin and Tarim Basin carbonates in China (Pppelreiter et al., 2005; Carvalho et al., 2022; Shi et al., 2023). Seismic exploration is commonly applied to identify reservoir distribution and delineate reservoir structure; however, the deep burial depth of reservoirs often results in weak seismic reflections and low seismic resolution, leading to poor seismic data quality (Pan et al., 2020; Chen et al., 2021). Marine carbonate reservoirs generally have strong heterogeneity, making their geophysical response characteristics complex and variable (Azerêdo et al., 2021; Wang et al., 2022). The poor data quality and strong heterogeneity of carbonate reservoirs are important challenges for reservoir sweet spot identification. Additionally, the quality of deep carbonate reservoirs is commonly controlled by various factors, including the depositional environment, lithology, diagenesis, karstification, and tectonic deformation (Massaro et al., 2018; Tian et al., 2020; Wadas et al., 2023). A good understanding of these factors is required for successful reservoir identification (Wang et al., 2024). In general, the main tasks for identifying deep carbonate reservoirs are to improve the seismic data quality and to consider the main reservoir controlling factors.

There are multiple ways to improve seismic data quality, including denoising, deconvolution and frequency decomposition (Naghizadeh, 2012; Liu and Fomel, 2013; Li et al., 2022). Frequency decomposition is a crucial method for post-stack seismic data processing: the method decomposes the original seismic signals into their constituent frequency components (Liu and Fomel, 2013; Chopra and Marfurt, 2016). This technique can enhance the resolution and interpretation of seismic data, allowing geoscientists to better understand subsurface structures and properties. The method has been applied to identify deep carbonate reservoirs (Naseer and Asim, 2018; Xu et al., 2019), but its stability still needs to be improved. Another seismic data processing method is the steerable pyramid method, which is commonly used to detect channels and thin sand bodies in sandstone reservoirs (Mathewson and Hale, 2008; Zhao et al., 2021).

Extensive research has suggested that the sedimentary environment (ideal sedimentary facies) is one of the most important factors controlling the reservoir quality of deep carbonates (Shen et al., 2008; Hairabian et al., 2014; Luo et al., 2015; Azerêdo et al., 2021; Nabawy et al., 2023). Luo et al. (2015) proposed that the deep carbonate reservoirs in the Sichuan Basin are primarily controlled by mound–shoal facies, with effective identification of mound–shoal complexes and accurate restoration of karst paleo-geomorphology being crucial for reservoir characterization. Shen et al. (2008) suggested that carbonate reef complexes are the ideal reservoir facies for platform-margin depositional environments in both Western Australia and South China. Nabawy et al. (2023) concluded that there are three favorable microfacies of Upper Cretaceous carbonates in the Gulf of Suez, and demonstrated that diagenetic modifications, including fracturing, dissolution and dolomitization, have enhanced the reservoir facies properties and quality.

In recent studies, it was found that strike-slip fault systems also control and modify carbonate reservoirs (Jiao et al., 2021; Jia et al., 2022; He et al., 2023; Ma et al., 2023). Jiao et al. (2021) concluded that the large strike-slip fault zone in the central Sichuan Basin can effectively connect hydrocarbon source centers, enhancing hydrocarbon migration and forming favorable fault-controlled natural gas reservoirs. Jia et al. (2022) indicated that strike–slip faults control the development of carbonate reservoirs and the enrichment of oil and gas in the Tarim Basin. He et al. (2023) proposed that strike-slip fault zones develop fractures and karstic cavities, which markedly improve the petrophysical properties of carbonate reservoirs.

Previous studies have achieved considerable progress in analyzing reservoir control factors and have produced innovative reservoir identification methods (Lien Eide et al., 2002; Lucia et al., 2003; Ahr, 2011; Malki et al., 2023; Sarhan, 2024). However, most of these studies applied a single control factor for seismic reservoir identification, and only a few studies comprehensively integrated multiple factors to constrain the identification. For practical application, we found that reservoir identification based on single factors often fails to meet the production requirements for accurately locating reservoir sweet spots; therefore, it is important to consider multiple factors when identifying reservoir sweet spots. In this case, our work begins by considering two aspects: the sedimentary environment and structural background. Taking the example of the Dengying Formation deep carbonate reservoir in the Sichuan Basin, China, we analyze the controlling effects of sedimentary facies and fault systems on the Dengying Formation carbonate reservoirs, and then identify sedimentary facies and faults separately at different seismic scales. Steerable pyramid (SP) processing is deployed to decompose the seismic data into various scales and enhance data quality. Field study suggests that the SP method is more stable and effective than frequency decomposition. Under the dual constraints of sedimentary facies and fault systems, reservoir sweet spots are accurately identified. The aim of this study is to provide technical support for the efficient development of deep carbonate reservoirs, especially those primarily controlled by both sedimentary facies and fault systems.

2 Geological background

2.1 Overview of the study area and stratigraphy

The Anyue Gas Field is located in the eastern wing of the Lesan–Longnvsi Uplift in the Sichuan Basin (Xie et al., 2021), where the widely distributed Sinian Dengying Formation has experienced a long sedimentary period, with deep burial depth (Luo et al., 2015). The main lithology of the Dengying Formation is dolomite (Tian et al., 2020). On the basis of sedimentary and lithological characteristics, the entire Dengying Formation can be divided into four members (Li et al., 2023). This study focuses on the Deng 4 Member. The study area is the Gaoshi-18 well block in the Gaoshiti region of the Anyue Gas Field, for which 3D seismic data for an area of approximately 200 km^2 are available. The Deng 4

Member has burial depths ranging from 5,000 to 5,500 m, and the regional stratigraphic thickness is 260–350 m (Zhang et al., 2021). This member can be further subdivided into upper and lower sub-members, and the upper sub-member contains a widely distributed, continuous siliceous interlayer (Luo et al., 2019). The main storage types of the Deng four member reservoirs are intergranular pores, fractures, and karst caves (Xiao et al., 2018; Zhang et al., 2021). High-quality reservoirs are mainly concentrated within the top 100 m of the Deng 4 Member (Tian et al., 2020).

2.2 Sedimentary environment and favorable sedimentary facies

The sedimentary environment of the Dengying Formation in the Sichuan Basin is a carbonate platform. The main facies are platform margin mound–shoal facies, intra–platform mound–shoal facies, inner–mound marine facies, and evaporite platform facies (Zou et al., 2011; Lan et al., 2019). The platform margin and intra-platform mound–shoal facies are favorable reservoir facies, and were extensively developed in the shallow-water area of the Deyang–Anyue rift margin.

Mound-shoal facies refer to the combined deposition of algal mounds and grain shoals. As algal mounds and grain shoals commonly develop in adjacent areas and both serve as good reservoirs, they are collectively referred to as "mound–shoal complexes" (Lan et al., 2019). Mound–shoal complexes have a mound-like shape. They grow on topographic highs of paleomorphology, with strong hydrodynamic environments and abundant sunlight. This environment is favorable for the development of microbialite mounds and stromatolites, and for the deposition of granular carbonate rocks (Xu et al., 2022).

2.3 Structural background and fault system

The Sichuan Basin has undergone multiple episodes of tectonic movement, such as the Tongwan, Caledonian, Yanshan, and Himalayan Movements (Jiao et al., 2021), which have led to the development of a series of strike-slip fault systems in the Neoproterozoic Dengying Formation (Ma et al., 2023). These strike-slip fault systems initially formed during the late Precambrian as part of the Tongwan II movement. During this period, the Sichuan Basin was characterized by a differential extensional background, with extension that was stronger in the north and weaker in the south. This condition made the region highly prone to the development of obliquely oriented, dextral trans-tensional strike-slip fault systems to accommodate the differential extensional displacement between the northern and southern regions (Ma et al., 2023). In this context, the central Sichuan region developed a series of nearly EW-trending main strike-slip faults, with lengths ranging from 80 to 200 km (Figure 1), which dominated the tectonic evolution of the central Sichuan Basin (He et al., 2023). Controlled by these main faults, secondary strike-slip faults developed in the Gaoshiti–Moxi area: these faults are primarily NW-trending (with a few NE-trending examples) and extend over thousands of meters. These faults exhibit large extension lengths and wide distributions, but relatively small vertical displacements (Wu et al., 2020; Ma et al., 2023). Seismic profiles show that the vertical displacements of the strike-slip faults are generally less than 50 m, and that the faults cut through multiple layers from the Precambrian basement to Permian strata. The strike-slip fault systems were inherited and reactivated at later times, some during the Mesozoic and Cenozoic. The Tongwan II movement also enhanced the reservoir physical properties by exposing the Deng 4 Member strata to extensive karstification.

3 Workflow and methodology

In this study, we create a workflow for reservoir sweet spot identification under dual-factor control (Figure 2). First, considering the sedimentary environment and structural background of the study area, we analyze the reservoir patterns and features of mound–shoal facies and strike-slip faults. By deploying seismic forward modeling, we investigate the seismic response characteristics of the mound–shoal facies and strike-slip faults; Simultaneously, we apply SP processing to the original seismic data. This method effectively decomposes seismic data into sub-band data of different scales. By selecting and recombining these sub-bands, two new seismic datasets are constructed: low-frequency and high-frequency data. After analyzing these datasets, we extract the average absolute amplitude attribute from the high-frequency data to identify mound–shoal facies reservoirs. For the low-frequency data, we extract coherent attribute and apply tensor voting processing to identify the strike-slip fault system. Then, we merge the two identification volumes and achieve 3D spatial characterization of reservoirs under dual-factor control. Finally, we use an attribute fusion method to perform the reservoir sweet spot identification.

4 Results

4.1 Seismic response characteristics of faults and reservoir

4.1.1 Seismic response of mound–shoal facies reservoir

The dominant frequency of seismic data is approximately 30 Hz. Limited by seismic resolution, the morphological characteristics of mound–shoal complexes are difficult to identify directly. Based on the lithological characteristics, we investigate the seismic response of mound–shoal complexes using seismic forward modeling. First, considering the lithological conditions when mound–shoal complexes are not developed, the Deng four upper sub-member can be simplified to the model shown in Figure 3A. The Deng four member consists of tight dolomite with high acoustic impedance, underlain by a 30-m-thick layer of Qiongzhusi Formation shale. The shale has lower P-wave velocity and density than the carbonate rocks. A continuous siliceous interlayer occurs approximately 50 m below the Deng four top boundary, with lower P-wave velocity and density than the surrounding rocks. Seismic forward modeling using a 30 Hz dominant frequency wavelet yields a strong wave peak reflection interface at the Deng four top boundary, with a weaker wave peak reflection occurring at the bottom of the siliceous interlayer (Figure 3B).

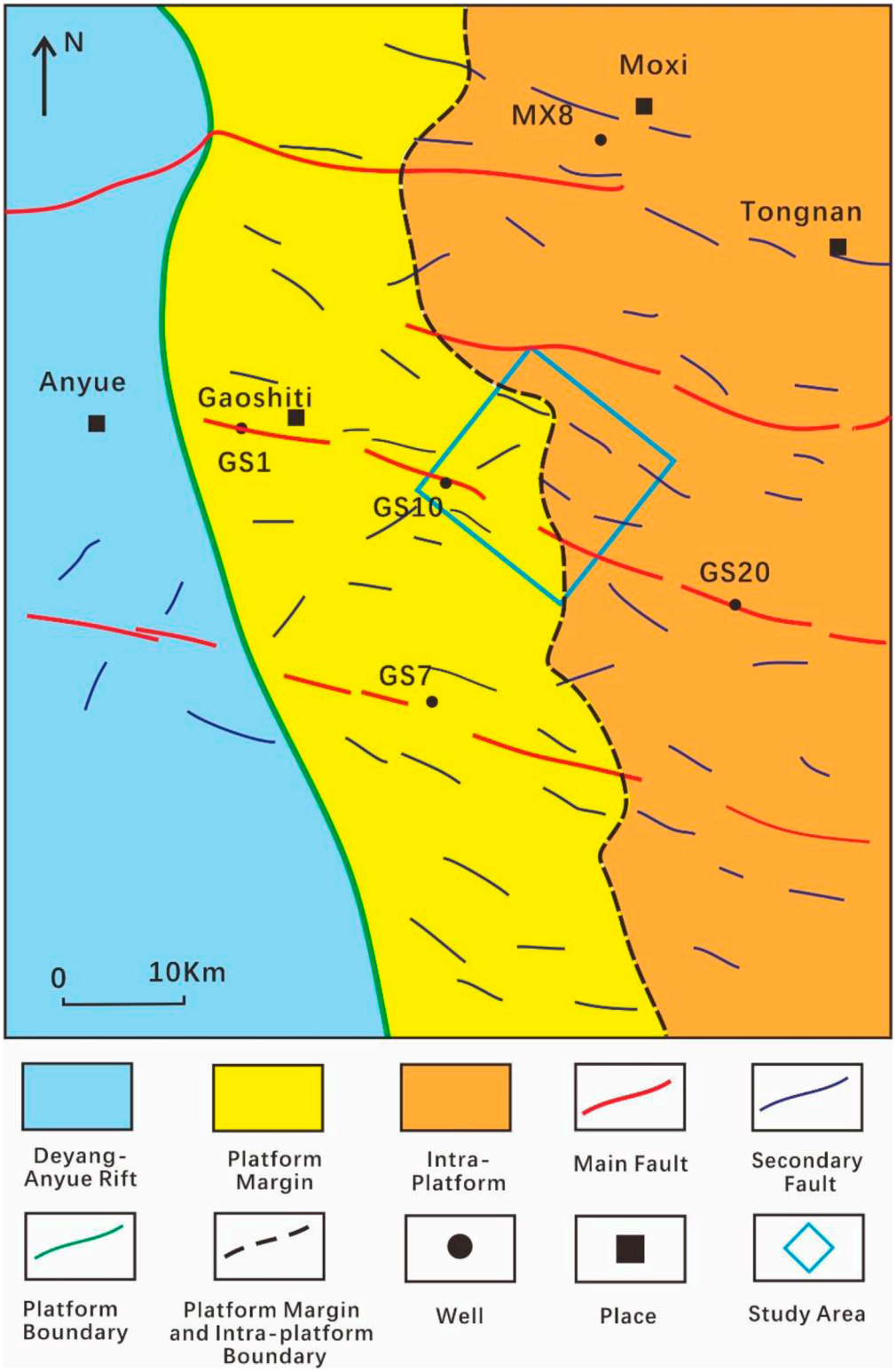

FIGURE 1
Schematic map of the sedimentary environments and strike-slip faults in the Gaoshiti–Moxi region (after Tian et al., 2020; Ma et al., 2023).

Then, we consider the condition when a mound–shoal complex is present near the top of the Deng four member (Figure 3C). The mound–shoal complex has low P-wave velocity and density, resulting in lower acoustic impedance compared than the surrounding tight dolomite. The synthetic seismic record using a 30 Hz wavelet (Figure 3D) shows that the presence of

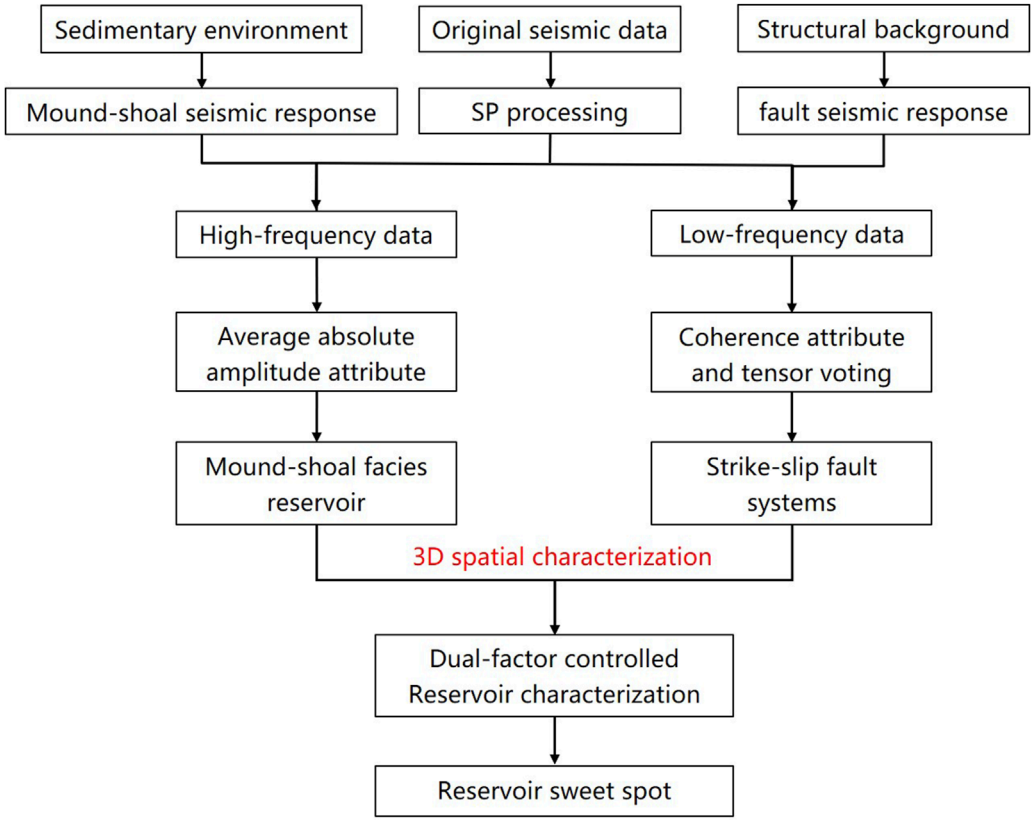

FIGURE 2
Diagram of the research workflow.

a mound–shoal complex leads to a decrease in the acoustic impedance at the Deng four top, causing a pronounced amplitude reduction on the wave peak. A weak amplitude peak response is observed at the mound–shoal complex top, and a decrease in the amplitude of wave trough reflections is observed within the complex reservoir. Additionally, a weaker wave peak response is observed at the base of the mound–shoal complex, suppressing the seismic response of the siliceous interlayer and causing up-shifting of the reflection.

From the forward modeling results, the seismic response of the mound–shoal complex at the Deng four upper member can be summarized as follows: (1) weak amplitude response at the top of the mound–shoal complex, corresponding to a relatively low-amplitude peak at the Deng four top boundary; (2) attenuation of the trough reflection within the mound–shoal complex, possibly with a weak-amplitude peak response at the bottom.

4.1.2 Seismic response of combined strike-slip fault and fault-mound shoal

The main fault type in the Gaoshiti area is strike-slip faults; these faults are characterized by small fault throws and steep dip angles. Rock damage occurs on both sides of the strike-slip fault planes, resulting in the development of fault damage zones and associated fractures. A forward modeling model is established on the basis of the characteristics of strike-slip faults (Figure 4A). Low-impedance fault damage zones (orange areas) are present on both sides of the fault plane, with P-wave velocities ranging from 5,500 to 6,000 m/s and gradually increasing away from the fault plane in both directions. The synthetic seismic record shows time-shift along the seismic event, accompanied by a decrease in amplitude on both sides of the fault damage zone (Figure 4B).

We further consider simultaneous development of strike-slip faults and mound–shoal complexes (Figure 4C). The corresponding seismic response (Figure 4D) shows time-shift along the seismic event and pronounced amplitude reduction on both damage zones. A reflection event up-shift phenomenon is present in the lower trough, faintly indicating the mound-like morphology of the mound–shoal complex.

The seismic characteristics of the strike-slip fault system include high-angle time-shift along the seismic event and amplitude reduction on both sides of the fault damage zone. These characteristics are somewhat similar to the response characteristics of amplitude reduction in the mound–shoal complex. In reality, associated fractures are developed near the fault damage zone of the strike-slip fault, enhancing karstification and further weakening the amplitude along the seismic event. Therefore, in cases where strike-slip faults and mound–shoal complexes are both present, it is difficult to distinguish the two based only on low-amplitude features. Using weak amplitude features as the basis for mound–shoal reservoir identification, while using seismic event time-shift features for identifying strike-slip faults, can effectively reduce interference and improve accuracy.

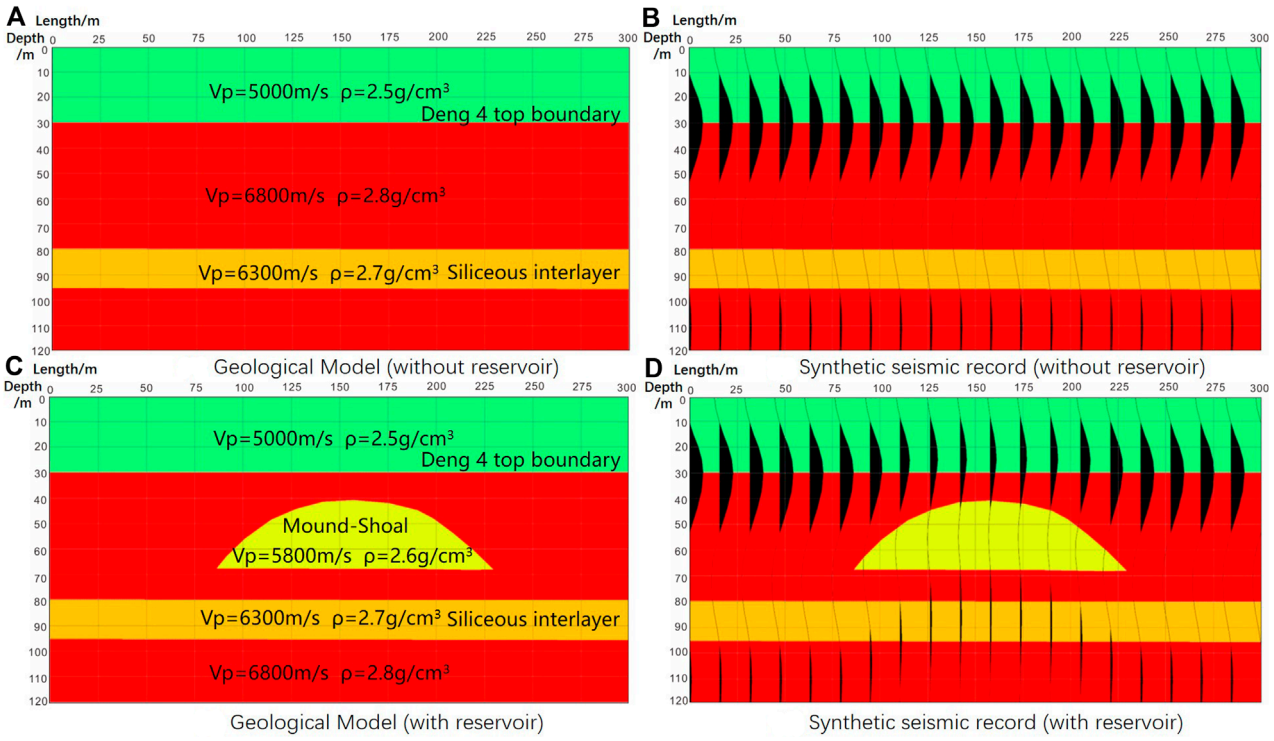

FIGURE 3
Seismic forward modeling of mound–shoal facies reservoirs: **(A)** Geological model (without reservoir) **(B)** Synthetic seismic record (without reservoir) **(C)** Geological model (with reservoir) **(D)** Synthetic seismic record (with reservoir).

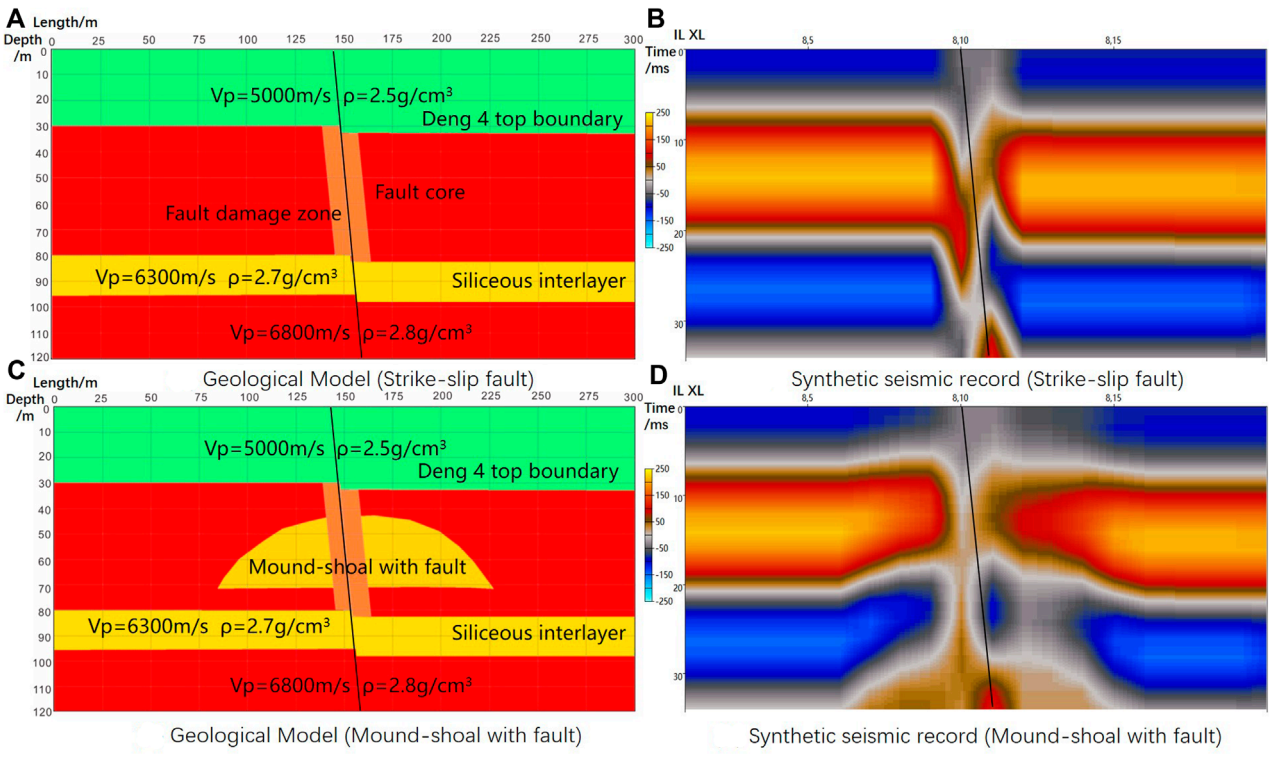

FIGURE 4
Seismic forward modeling of strike-slip fault and faulted-mound shoal: **(A)** Geological model (strike-slip fault) **(B)** Synthetic seismic record (strike-slip fault) **(C)** Geological model (mound–shoal with fault) **(D)** Synthetic seismic record (mound–shoal with fault).

4.2 Reservoir and fault-system identification

This study proposes an approach for multi-scale identification based on the seismic characteristics of reservoirs and fault systems. The thickness of mound–shoal facies reservoirs is generally lower than the vertical resolution of seismic data; thus, further enhancement of seismic resolution and extraction of small-scale features are required to highlight the seismic response characteristics of mound–shoal reservoirs. In contrast, strike-slip faults are characteristically large-scale and extend over long distances, allowing for identification in larger-scale data. Small-scale seismic event folding and discontinuity artifacts may adversely affect identification accuracy. By combining different seismic attributes in seismic data at different scales, we can accurately identify both mound–shoal facies reservoirs and strike-slip fault systems.

4.2.1 Steerable pyramid processing and validation

In this study, the SP method is deployed to perform multi-scale decomposition and reconstruction of seismic data, with the aim of enhancing the quality of seismic data and further highlighting the fault systems. The SP method is a multi-scale data processing method based on image pyramids and directionally steerable filtering. The specific principles of the method can be found in the literature (Freeman and Adelson, 1991; Mathewson and Hale, 2008; Zhao et al., 2021), and will not be further elaborated in this paper. The SP processing decomposes the seismic data of the study area into five different frequency sub-bands (referred to as L1–L5). The seismic profile of the original seismic data and different SP processed sub-band data are shown in Figure 5, and the corresponding spectral analysis of each seismic data is presented in Table 1.

From the seismic profiles and spectral analysis, it can be observed that sub-band L5 has a large scale but very low resolution, and contains only macro-scale seismic information; therefore, its contribution to identifying the fault systems and reservoirs is minimal, and this sub-band is not considered further in this study. L1–L4 are considered to be the key sub-bands for further analysis. L1 has a higher seismic center and dominant frequency compared to the original seismic data, with an overall frequency enhancement of approximately 15 Hz. On the seismic profiles, L1 reveals more details and discontinuities in seismic events, thereby capturing more small-scale geological information and details in the original seismic data. Sub-band L2 is generally similar to the original seismic profile, with a slightly higher center frequency (38.4 Hz) than the original seismic data (32.8 Hz), and exhibits similar geological structures and features while eliminating some noise effects. L3 has a lower center frequency (26.3 Hz) compared to the original seismic data. Although its resolution is slightly lower, it is advantageous for highlighting larger-scale fault features compared to the original seismic data, enhancing the continuity of seismic events and eliminating some fault artifacts. L4 further emphasizes large-scale geological structures compared to L3 but lacks detail, making it suitable for comprehensive analysis in combination with other sub-bands.

For the purpose of reservoir and fault systems identification, the SP processed sub-bands are divided into two groups: the high-frequency group (sub-bands L1 and L2) and the low-frequency group (sub-bands L3 and L4). Then, we stack each group of sub-bands to reconstruct new seismic data, with SP L1+2 representing high-frequency data and SP L3+4 representing low-frequency data. Both new seismic datasets maintain the resolution characteristics of the sub-bands and effectively compensate for the deficiencies in individual sub-band seismic data. In this study, the high-frequency data (SP L1+2) are used for reservoir identification and the low-frequency data (SP L3+4) are used for characterization of fault systems.

To verify the effectiveness and enhancement of the SP processing, we compare the processed datasets with the original seismic data, and also apply the commonly used frequency decomposition (FD) method as a comparison. Corresponding high and low-frequency seismic data were constructed using the FD method. The spectral analysis results for the SP and FD processed data are provided in Table 1. The FD constructed seismic datasets closely match the SP data in terms of dominant frequency and center frequency, achieving maximum control over the frequency aspect. However, as a result of differences in algorithms, the frequency bandwidths of SP processed data are wider than those of frequency decomposition data.

We compare SP low-frequency data with original seismic data and FD low-frequency data (Figure 6). Typical seismic profiles passing through faults are illustrated in Figures 6A–C; the corresponding coherence attribute profiles are shown in Figures 6D–F. Two large strike-slip faults are more clearly visible in both the SP and FD low-frequency data than in the original seismic data (Figures 6A–C). However, there is an obvious amplitude distortion in the lower part of the FD profile, with noticeable changes in the wave peaks and troughs (Figure 6C). This phenomenon is caused by the lack of translation invariance in the FD method, resulting in pronounced amplitude changes on the seismic events. When further considering the attribute profiles, we observe that the coherence attributes of both the SP and FD data clearly show the shape of the strike-slip fault. The difference is that the SP data attribute eliminates some high-frequency noise and attribute artifacts (Figure 6E), whereas the FD data attribute has some noise and artifacts remaining (Figure 6F).

The comparison between the SP high-frequency data, the original data and the FD processed data is illustrated using a cross-well profile (Figure 7). In the original seismic profile, the top boundary of the Deng 4 Formation exhibits strong wave peak reflection characteristics with high continuity. A high-quality mound–shoal reservoir (indicated by red circles in the figure) is present near the top of the Deng four zone in well GS10. However, because of the limited seismic resolution of the original seismic data, wave interference occurs; as a result, the weak amplitude response expected at the reservoir location is not visible in Figure 7A. After SP processing, the seismic resolution is improved, greatly reducing the wave interference phenomenon and revealing the weak amplitude reservoir response at the Deng four top boundary. The SP processing also enhances the seismic response of the siliceous inter-layer throughout the region, corresponding to the continuous wave peak 20 ms below the Deng four top (Figure 7B).

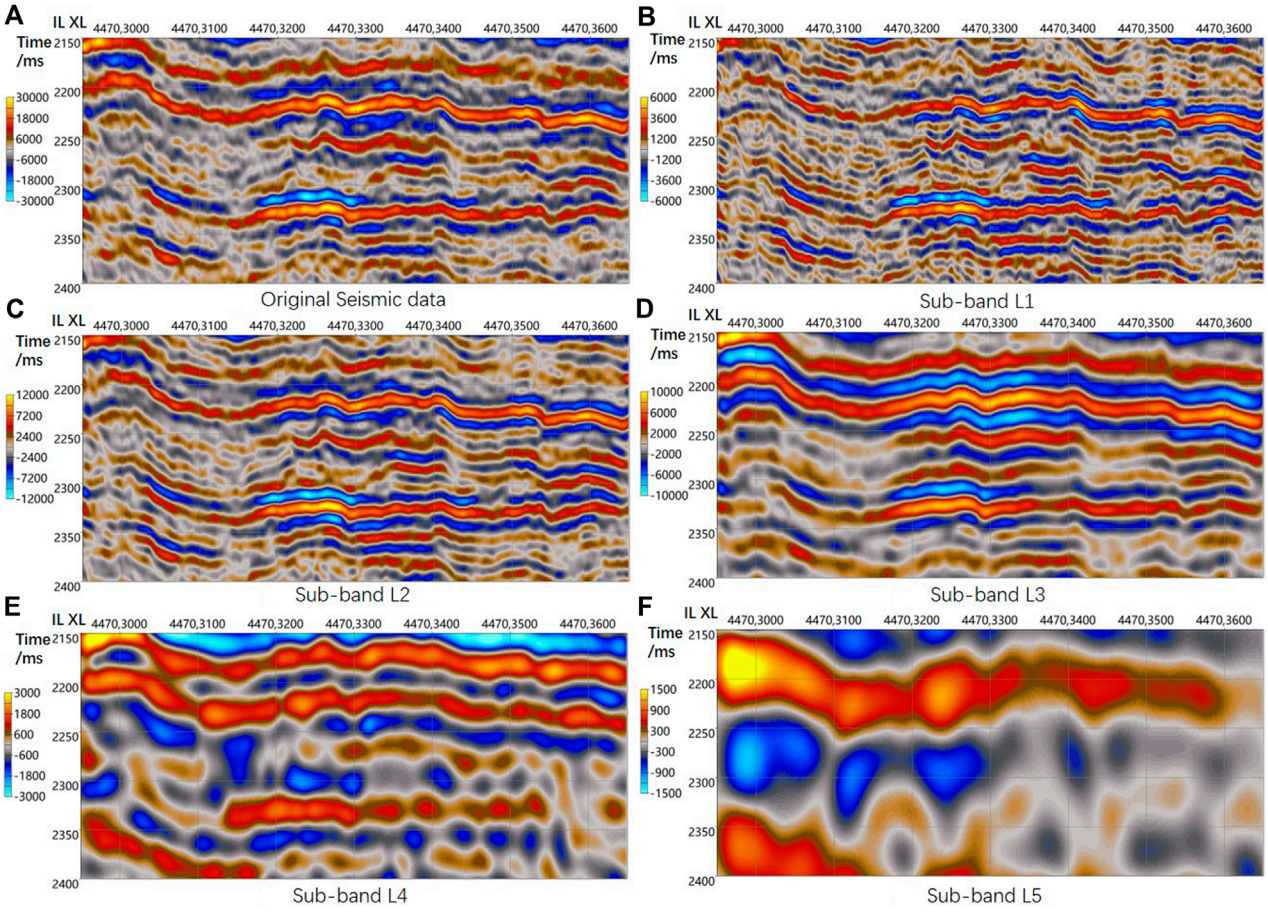

FIGURE 5
Seismic profiles of the original seismic data and SP processed sub-band data: **(A)** Original seismic data **(B)** Sub-band L1 **(C)** Sub-band L2 **(D)** Sub-band L3 **(E)** Sub-band L4 **(F)** Sub-band L5.

TABLE 1 Results of spectral analysis of original seismic data and SP and FD processed data.

Seismic data	Dominant frequency (Hz)	Central Frequency (Hz)	Frequency bandwidth (Hz)
Original seismic	30.4	32.8	16.5–47.7
SP Level 1 (L1)	46.9	44.5	30.7–56.1
SP Level 2 (L2)	39.1	38.4	23.8–50.5
SP Level 3 (L3)	23.6	26.3	17.3–33.3
SP Level 4 (L4)	11.7	15.4	4.4–21.6
SP Level 5 (L5)	7.8	8.2	2.1–12.4
SP Level 1+2	43	40.6	26.2–49.2
FD 1 (high-F)	43	43.1	36.2–50.3
SP Level 3+4	21.4	23.2	13.9–29.8
FD 2 (low-F)	20.1	23.3	16.0–27.2

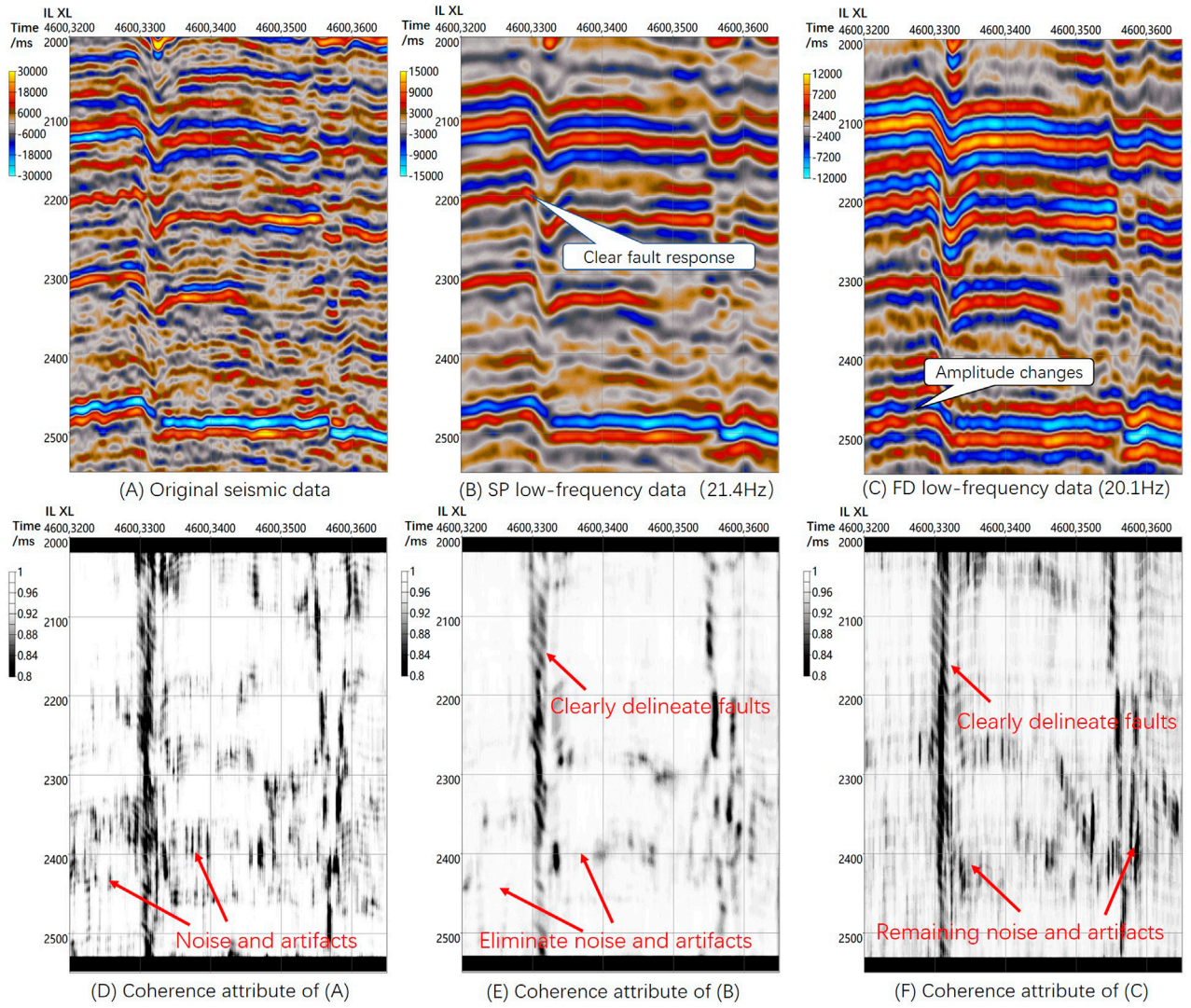

FIGURE 6
Comparison of original seismic data and SP and FD low-frequency data: **(A)** Original seismic data **(B)** SP low-frequency data **(C)** FD low-frequency data **(D)** Coherence attribute of **(A)** **(E)** Coherence attribute of **(B)** **(F)** Coherence attribute of **(C)**.

The FD high-frequency data (Figure 7C) also display weakened amplitude at the Deng four top boundary. Although the weak amplitude feature of the reservoirs in well GS10 are highlighted, the Deng four top boundary shows poor continuity of seismic events with excessively low amplitude. Obvious amplitude distortion on the seismic events can be observed in the middle part of the profile, which differs markedly from the structure of the original seismic data. According to the spectral analysis results, although FD processing enhances the center frequency and dominant frequency of seismic data, the frequency bandwidth of the processed seismic data is narrower. This difference results in the loss of a large amount of low-frequency information, leading to obvious changes in the geological structure and seismic events in the seismic data.

From the above validation and analysis, it can be concluded that SP low-frequency data can clearly characterize the shape of faults by eliminating a large amount of high-frequency noise and artifacts, which aids in interpreting large-scale fault systems. SP high-frequency data markedly improve seismic resolution, highlighting the weak amplitude features of the reservoir at the Deng four top boundary. In the FD data, obvious changes are observed in the stratigraphic structure and seismic events in both high- and low-frequency data. These changes arise because in FD processing the frequency changes lack translational invariance, making it difficult to maintain good consistency between the decomposed frequency components and geological features. In general, the SP method is superior to the FD method in terms of stability and processing effects at different scales.

4.2.2 Mound–shoal facies reservoir identification

We identify the mound–shoal facies reservoirs of the Deng four member using SP high-frequency data. The identification is

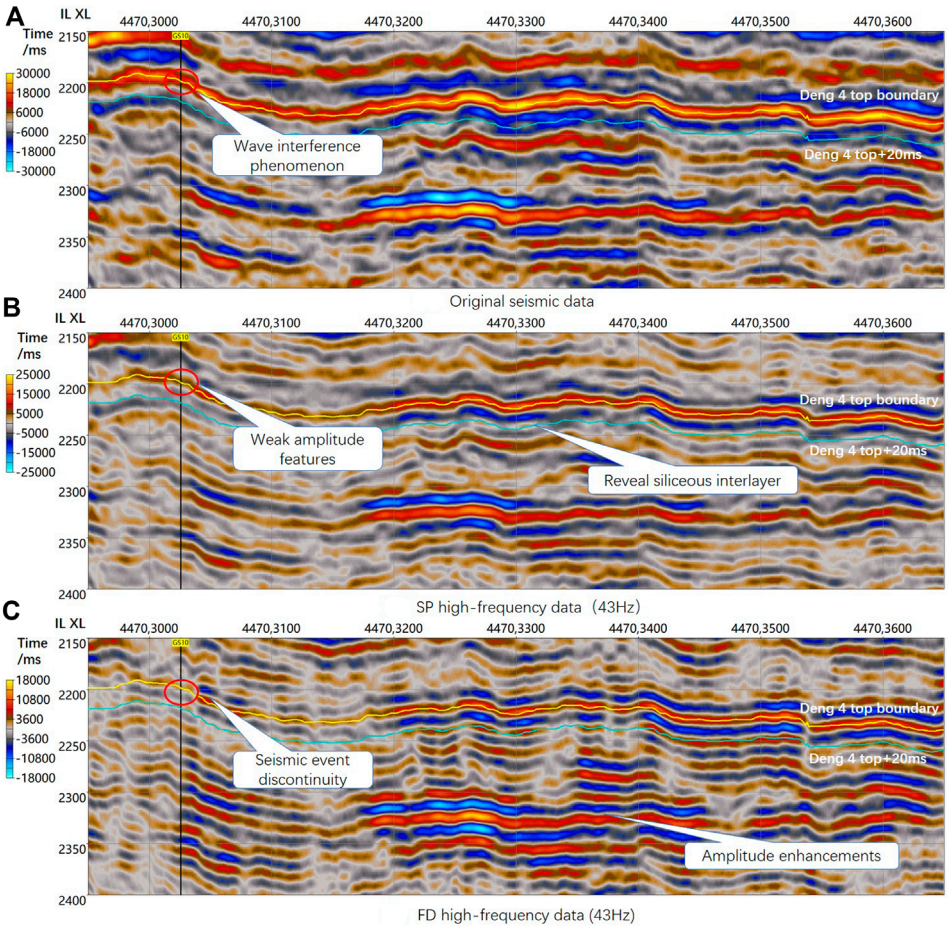

FIGURE 7
Comparison of original seismic data and SP and FD high-frequency data: **(A)** Original seismic data **(B)** SP high-frequency data **(C)** FD high-frequency data. Red circles indicate a high-quality mound–shoal reservoir.

based on the seismic characteristics of the reservoir, which include: (1) weak amplitude response at the Deng four top boundary; and (2) attenuation of the trough reflection within the mound–shoal complex, with decreased amplitude of peaks 20 ms below the Deng four top boundary. These features indicate that the mound–shoal reservoir causes an overall decrease in reflection amplitudes. The average absolute amplitude can effectively be used to visualize the amplitude decrease of the reservoir, with ideal reservoir locations corresponding to low attribute values. We extract the average absolute amplitude using a window from the Deng four top boundary to 20 ms below the boundary to identify mound–shoal reservoirs at the top of the formation.

Wells with higher productivity, such as GS122, GS125, and GS132, have well trajectories passing through large segments of reservoir zones (dark red color in Figure 8), whereas wells with relatively lower productivity, such as GS119 and GS120, are located in the brown-red areas with slightly higher attribute values. When the well productivity is analyzed against the average attribute values (Figure 12A), there is a negative correlation overall, consistent with the understanding described above. However, it is notable that the data points corresponding to wells GS10 and GS118 deviate markedly from the correlation trend line. Well GS10 exhibits good reservoir properties and is located in the low-value area, indicating high-quality reservoirs in this well. The reason for the low well productivity might be because of a shorter reservoir thickness compared to other wells. The trajectory of well GS118 does not fall within the ideal low-amplitude reservoir zone, even though it has very high productivity. It is preliminarily inferred that, because the well trajectory passes through a strike-slip fault, karstification surrounding the fault has resulted in the formation of favorable fracture-porosity reservoirs around the fault zone. As these reservoirs are not mainly controlled by sedimentary facies, their presence is not obvious in the reservoir identification based on detection of mound–shoal facies.

4.2.3 Strike-slip fault system identification

In fault identification, coherence attributes can effectively highlight the features of large-scale fault systems. We extract 3D coherence attributes from SP low-frequency data and identify the fault systems of the Deng four member along the horizon. Strike-slip faults are primarily oriented in the NW direction, with clear shapes for most of the faults (Figure 9A). However, low-continuity areas can be observed in certain faulted locations, and some outlier values result in blurring near the faults. To address these issues,

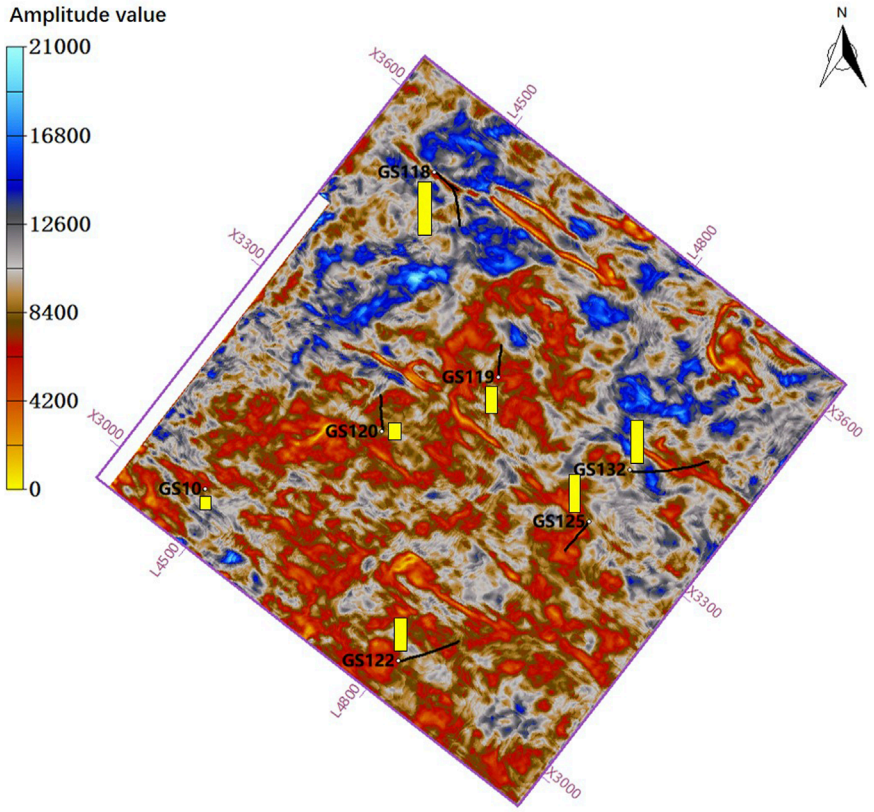

FIGURE 8
Identification of mound–shoal facies reservoirs based on amplitude. Black lines represent well trajectories, yellow bars represent well productivity, and light-colored low-value areas indicate reservoir locations.

we deploy the tensor voting method to enhance the coherence attribute. This method is based on analyzing structural tensor characteristics and using eigenvalues voting to detect and enhance structural features within the seismic data. The process can be summarized in three steps: first, we input a 2D dataset (planar seismic attribute) and use the gradient vectors to construct the structure tensor for each pixel. Next, by analyzing the eigenvalues of the structure tensors, we can extract the pixels with strong anisotropy (referred as seed points, representing potential fault locations). Finally, a specific voting domain is constructed, and voting is performed on each seed point. The seed points of potential faults will receive higher votes. By setting a reasonable threshold, the tensor voting-enhanced attribute result is obtained (Cui et al., 2021).

In this study, tensor voting is applied to coherence attributes to further highlight the morphology of strike-slip fault systems. The tensor voting processing effectively enhances the continuity of large-scale faults and eliminates blurry regions caused by low attribute values and noise interference, achieving an accurate representation of the fault systems (Figure 9B). The major strike-slip faults in the study area are primarily oriented northwest to southeast, with a few faults oriented in northeast to southwest. The faults extend for several kilometers, and some secondary minor faults and fractures are also developed near the fault planes, consistent with the analysis from previous tectonic movement.

To further assess the influence of the strike-slip fault system on reservoir quality, we correlate well productivity with distance from faults. Overall, there is a negative correlation between the two factors (Figure 12B), indicating that wells closer to faults exhibit higher production. The associated fractured zones of the strike-slip faults have a certain impact on the reservoir development within a radius of approximately 2 km, with more pronounced effects observed within a range of 500 m around the fractured zone. This finding suggests that the strike-slip fault system has a controlling effect on reservoirs.

4.3 Reservoir spatial characterization and sweet spot identification

4.3.1 Dual-factor-controlled reservoir spatial characterization

As described above, reservoir identification based solely on sedimentary facies results in a poor match with production data; therefore, considering the control and modification effects of fault systems on reservoirs is necessary. We characterize the distribution of fault systems and mound–shoal sedimentary facies in three-dimensional space, and merge these two volumes to achieve spatial characterization of reservoirs under dual-factor control. First, by setting thresholds to eliminate outlier values in the attribute

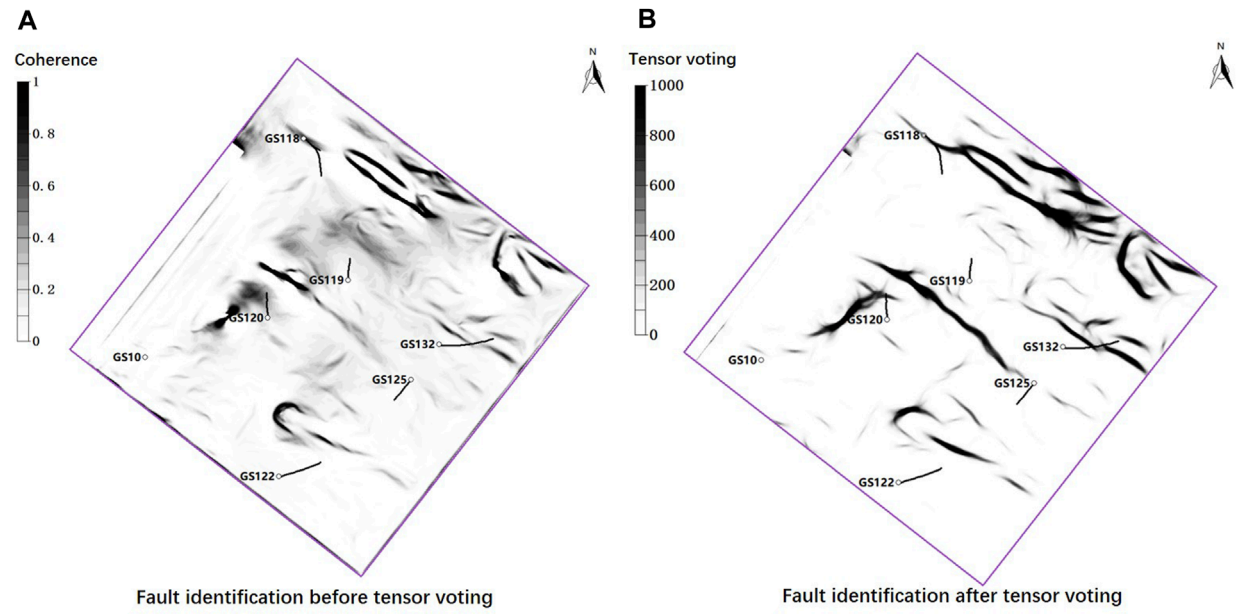

FIGURE 9
Results of fault systems identification: **(A)** Fault identification before tensor voting **(B)** Fault identification after tensor voting.

volumes, 3D characterization volumes of the fault systems and mound–shoal reservoirs are obtained (Figures 10A,B). Then, the two modified attribute volumes are merged with the trajectories of development wells (Figure 10C). The red region in the figure indicates the development of strike-slip fault systems, and the yellow region represents the distribution of mound–shoal facies reservoirs. The mound–shoal facies are more widely distributed than the strike-slip fault systems, and overlap some strike-slip faults. Most of the development wells, such as GS125 and GS132, pass through or are located near mound–shoal reservoirs or strike-slip fault zones.

Thicker reservoir units are developed near the strike-slip fault zones (Figure 10C), further indicating the controlling effect of strike-slip faults on reservoir quality. We conclude that the control of strike-slip fault systems on reservoirs mainly manifests in two aspects: (1) large strike-slip fault zones provide migration channels for oil and gas, making areas near the fault zones more favorable for hydrocarbon accumulation; (2) strike-slip faults and secondary fracture systems enhance karstification of carbonate reservoirs, facilitating the formation of secondary pores and cavities and thus improving reservoir properties. Under karstification, the secondary dissolution porosity of the Deng 4 Member carbonate reservoirs can increase by 5%–20%; additionally, because of the widespread development of fractures associated with faults, the permeability of carbonate matrix rocks can increase by one to two orders of magnitude (Jiao et al., 2021; He et al., 2023).

To summarize, the carbonate reservoirs of the Dengying Formation are controlled by two factors: mound–shoal sedimentary facies and strike-slip fault systems. The mound–shoal facies serve as the main material basis for reservoir development, determining the type and distribution of reservoirs, while the strike-slip fault systems further enhance hydrocarbon accumulation and reservoir properties.

4.3.2 Identification of reservoir sweet spots

To further quantify the influence of sedimentary facies and fault systems on reservoirs and to locate sweet spots, we deploy a method combining normalization attribute fusion with a smoothing filter. First, the planar predictive attributes of fault systems and mound–shoal complexes are normalized separately using the following equation:

$$y = \frac{x - x_{min}}{x_{max} - x_{min}} \tag{1}$$

where x represents the original planar attribute value; x_{max} and $x_{\min}$ correspond to the maximum and minimum values of the original attribute, respectively; and y represents the normalized attribute value.

After normalization, the two attributes are merged to obtain a fusion attribute map that simultaneously reflects faults and sedimentary facies (Figure 11A). In the figure, low values (bright colors) denote the development of sedimentary facies and faults; for example, bright yellow typically corresponds to reservoir areas controlled by both faults and mound–shoal facies.

Finally, we extract favorable reservoir characteristics from the fusion attribute using a 50 × 50 smoothing filter, as shown in Eq. 2:

$$\mathrm{Frac}(m,n) = \sum_{i=-25}^{25}\sum_{j=-25}^{25}\mathrm{Attribute}(m+i, n+j) \tag{2}$$

where m and n respectively correspond to the coordinates of the attribute values; *Attribute* represents the fusion attribute coordinate; and i and j correspond to the size of the smoothing window.

In the filtered fusion attribute map (Figure 11B), the red-colored low-value regions indicate ideal reservoir development areas that are controlled by both strike-slip faults and mound–shoal facies, brown areas represent reservoirs that are likely influenced by single-factor effects, and blue regions indicate reservoirs with low-quality

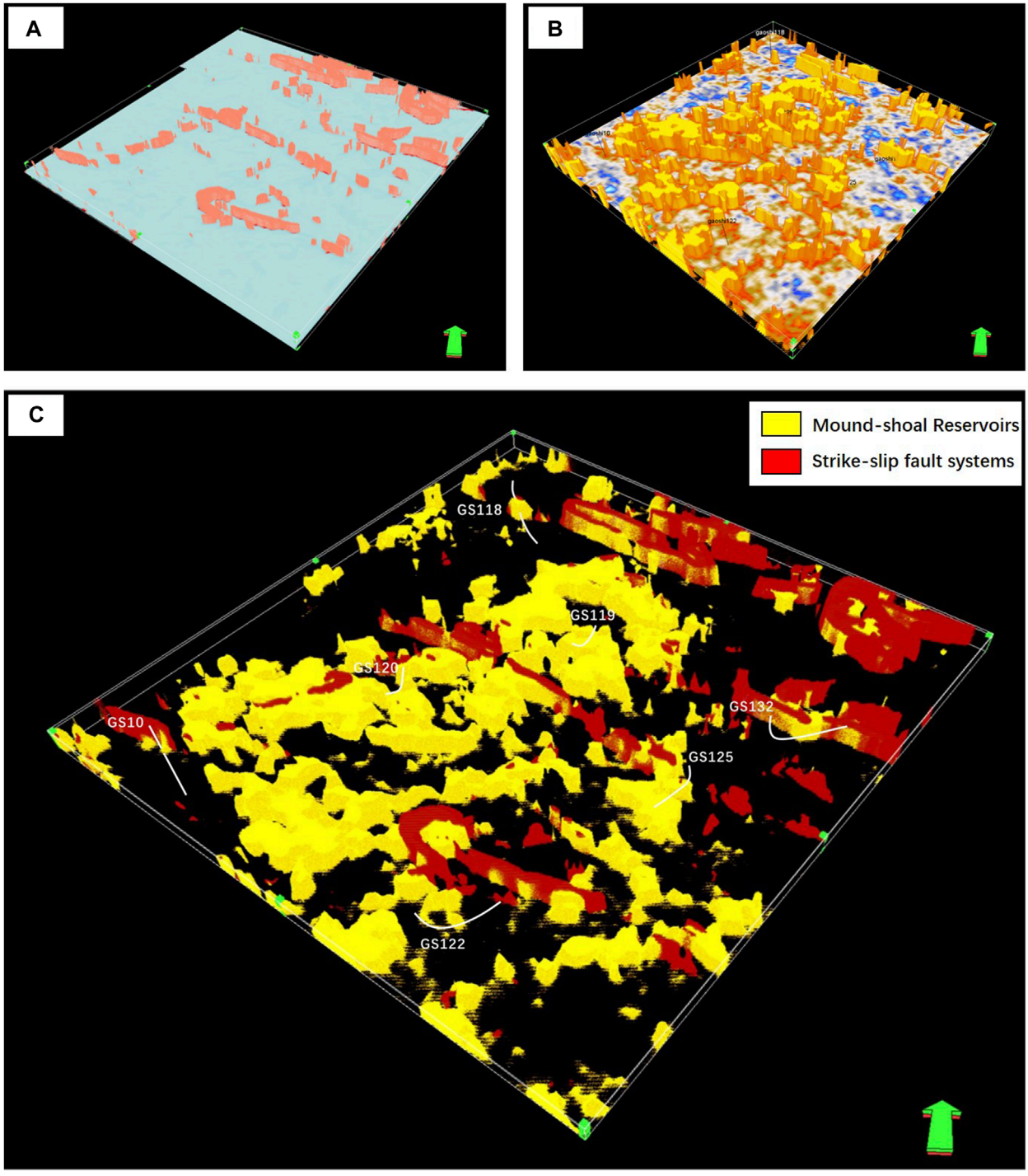

FIGURE 10
Spatial 3D characterization of strike-slip fault systems and mound–shoal reservoirs: **(A)** 3D characterization of the strike-slip fault systems **(B)** 3D characterization of mound–shoal reservoirs **(C)** Dual-factor-controlled 3D characterization.

properties or non-reservoir areas. The overall red "sweet spot" areas are similar to the distribution of mound–shoal facies reservoirs, with a few variations in certain locations. This result further confirms that the sedimentary facies control the reservoir distribution at a larger scale.

There is a clear negative correlation between production data and the filtered fusion attribute values (Figure 12C), indicating a better overall fit and higher reliability compared to single-factor identification results (Figures 12A,B). In summary, wells GS118, GS125, and GS132 are located in the reservoir sweet spot area, which

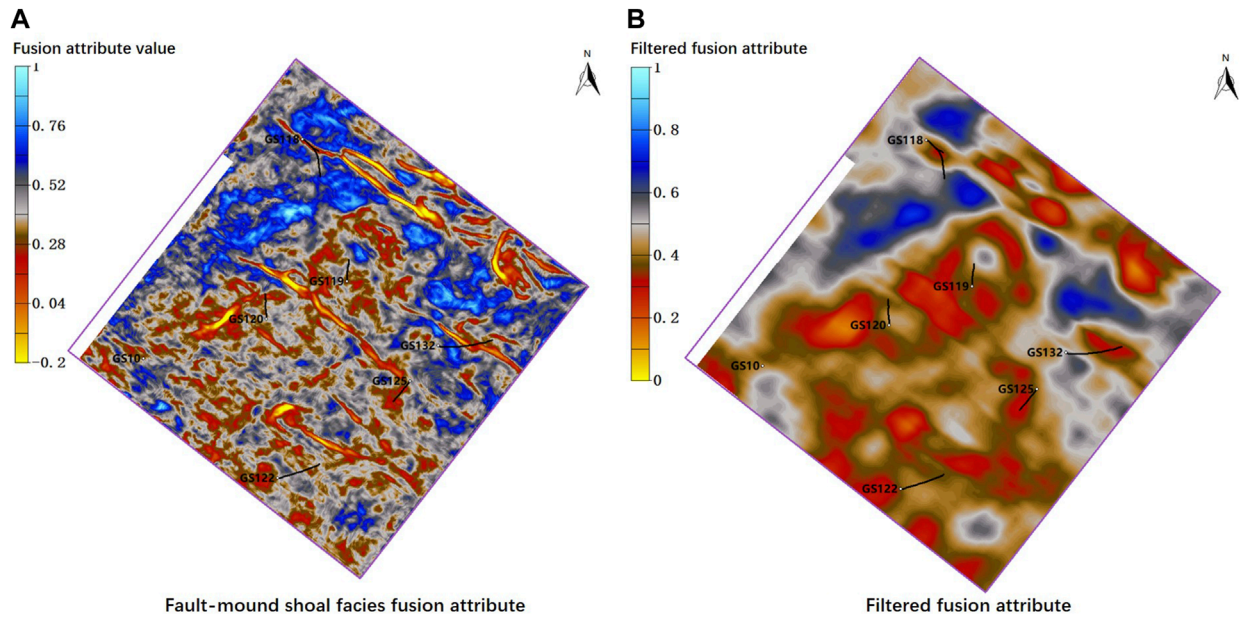

FIGURE 11
Identification of reservoir sweet spots: **(A)** Fusion attribute map of faults and mound–shoal facies **(B)** Fusion attribute map after smooth filtering.

is controlled by both faulting and sedimentary facies, and these wells possess better reservoir properties and higher well productivity compared to other wells. Through this method, the sweet spots (red areas) in the study area can be effectively identified, providing support and assistance for further development in the study area.

5 Discussion

Our study demonstrates that integrating sedimentary facies and fault systems markedly improves the identification of reservoir sweet spots in deep carbonate formations, specifically focusing on the Dengying Formation in the Sichuan Basin.

Considering the complex seismic response characteristics of sedimentary facies and fault systems, it is essential to identify these features separately at different seismic scales. The steerable pyramid (SP) method proved to be very effective at decomposing seismic data into various scales, improving data quality and resolution. This multi-scale method has been shown to be more stable and effective than the traditional frequency decomposition (FD) method, allowing us to better interpret the complex geophysical responses associated with deep carbonate reservoirs.

Selection of appropriate seismic attributes is also important for the identification of sedimentary facies and faults. In this study, we chose average absolute amplitude and coherence attributes based on their seismic response characteristics; in other areas, other types of amplitude-related or phase-related attributes may be useful for identifying sedimentary facies. For fault identification, commonly used attributes such as coherence, variance and curvature are always worth trying, and the results should be verified with well data to decide the proper attribute. Tensor voting has also been proven to be an effective method to enhance the identification results, particularly for improving fault continuity; however, appropriate parameters should be set to prevent over-enhancement.

In deep carbonate reservoirs, favorable sedimentary facies always determine reservoir quality and distribution on a large scale, and precisely locating these facies is the primary task of reservoir identification. Fault systems serve as essential pathways for hydrocarbon migration and accumulation; they also play a crucial role in karstification, which improves reservoir quality. Understanding fault systems helps to locate the ideal reservoir sweet spots. Our identification of sedimentary facies and faults is consistent with previous studies that suggested that both the sedimentary environment and structural influences play critical roles in reservoir quality. However, unlike prior studies that primarily focused on single factors, our workflow provides a more comprehensive analysis.

The implications of our findings are substantial for both theoretical understanding and practical applications of sweet spot identification. By considering multiple control factors, more accurate and reliable reservoir sweet spot identification can be achieved, which is essential for the efficient development of hydrocarbon resources. However, our study has limitations; for example, the specific carbonate reservoir characteristics of the Sichuan Basin may not be directly applicable to other regions. Additionally, in the present work, fault identification mainly focused on large-scale fault systems, and smaller-scale faults and fractures were not fully considered. Future in-depth research will involve several aspects: investigation of the applicability of our methods to deep carbonate reservoirs in other regions; identification of multi-scale faults and their associated fractures by using various seismic attributes with different scales of seismic data, and analysis of the

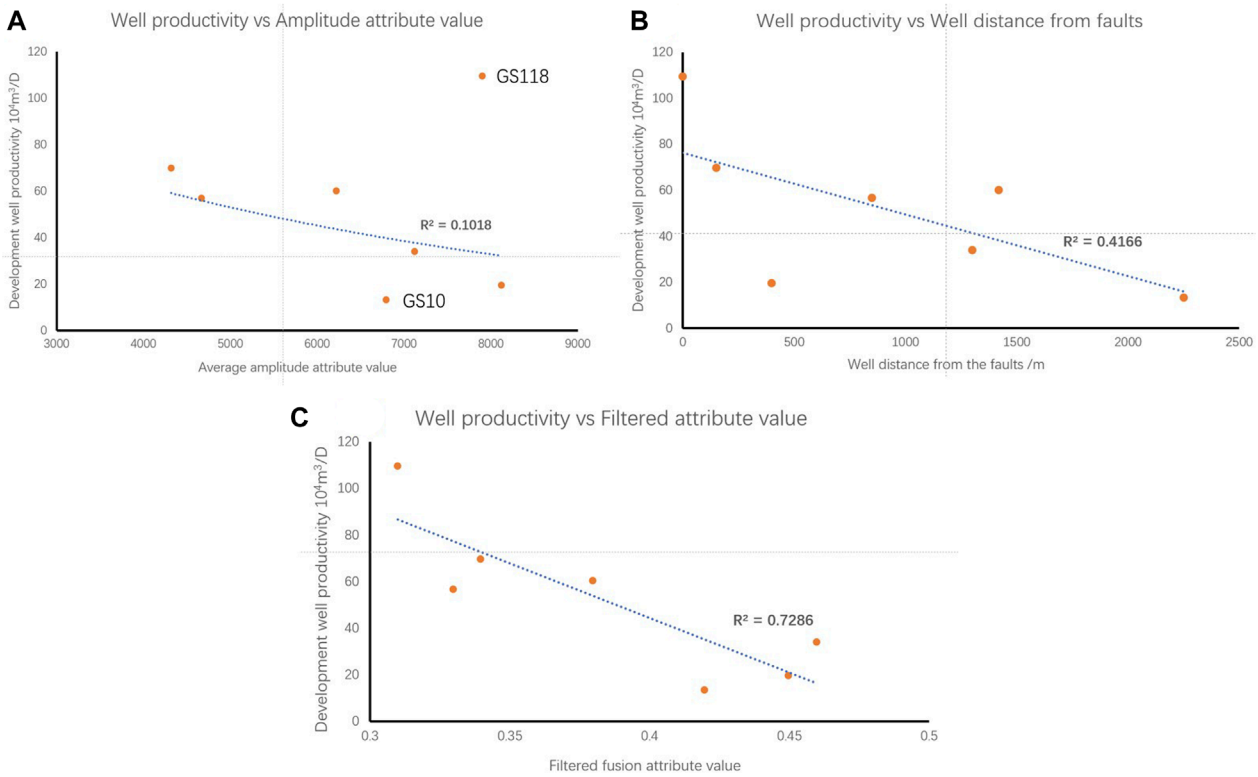

FIGURE 12
Analysis of reservoir controlling factors: **(A)** Well productivity *versus* amplitude attribute values (from Figure 8) **(B)** Well productivity *versus* well distance from faults (from Figure 9B) **(C)** Well productivity *versus* filtered fusion attribute values (from Figure 11B).

contributions of faults and fractures at different scales to carbonate reservoirs.

6 Conclusion

(1) The primary reservoir sedimentary facies in the Dengying Formation is mound–shoal complexes. The study area was influenced by multiple episodes of tectonic movements and has developed fault systems primarily dominated by strike-slip faults. The sedimentary facies were identified at a high-frequency scale using amplitude attributes, and the strike-slip faults were identified with coherence attribute and tensor voting at a lower-frequency scale.

(2) Steerable pyramid processing is an effective way to improve seismic data quality. This method involves decomposition of the original seismic data into high-frequency and low-frequency components. The high-frequency data improve the seismic resolution and highlight the amplitude response characteristics of reservoirs. The low-frequency data effectively eliminate noise interference, facilitating attribute identification. The steerable pyramid method is more stable and effective in practical applications than the traditional frequency decomposition method.

(3) In deep carbonate reservoirs, sedimentary facies and fault systems have marked impacts on reservoir quality. Favorable sedimentary facies generally determine reservoir quality and distribution on a large scale, whereas fault systems serve as essential pathways for hydrocarbon migration and potential channels for carbonate karstification. Identifying sedimentary facies and fault systems separately at different seismic scales is an effective way to detect reservoirs. The proposed dual-factor method can effectively locate reservoir sweet spots as part of deep carbonate reservoir exploration and development.

Data availability statement

The original contributions presented in the study are included in the article/Supplementary material, further inquiries can be directed to the corresponding author.

Ethics statement

Written informed consent was obtained from the individual(s) for the publication of any potentially identifiable images or data included in this article.

Author contributions

GZ: Methodology, Validation, Writing–original draft, Writing–review and editing. XH: Funding acquisition, Project

administration, Supervision, Writing–review and editing. YX: Funding acquisition, Supervision, Writing–review and editing. ST: Funding acquisition, Methodology, Writing–review and editing. KC: Data curation, Project administration, Resources, Writing–review and editing. DP: Data curation, Project administration, Writing–review and editing.

Funding

The author(s) declare that financial support was received for the research, authorship, and/or publication of this article. This research was funded by the National Natural Science Foundation of China (U20B2016) and the Youth Fund of the National Natural Science Foundation of China (42304136).

Acknowledgments

We thank the Exploration and Development Research Institute of CNPC for providing the data and supporting this research. We also thank Lucy Muir, PhD, from Liwen Bianji (Edanz) (www.liwenbianji.cn) for editing the English text of a draft of this manuscript.

Conflict of interest

Authors KC and DP were employed by PetroChina Southwest Oil & Gasfield Company.

The remaining authors declare that the research was conducted in the absence of any commercial or financial relationships that could be construed as a potential conflict of interest.

Publisher's note

References

Ahr, W. M. (2011). *Geology of carbonate reservoirs: the identification, description and characterization of hydrocarbon reservoirs in carbonate rocks*. Hoboken, NJ: John Wiley and Sons.

Azerêdo, A. C., Duarte, L. V., and Silva, A. P. (2021). The challenging carbonates from the Pre-Salt reservoirs offshore Brazil: facies, palaeoenvironment and diagenesis. *J. S. Am. Earth Sci.* 108, 103202. doi:10.1016/j.jsames.2021.103202

Carvalho, A. M. A., Hamon, Y., De Souza, O. G., Carramal, N. G., and Collard, N. (2022). Facies and diagenesis distribution in an Aptian pre-salt carbonate reservoir of the Santos Basin, offshore Brazil: a comprehensive quantitative approach. *Mar. Petroleum Geol.* 141, 105708. doi:10.1016/j.marpetgeo.2022.105708

Chen, Y., Zhao, L., Pan, J., Li, C., Xu, M., Li, K., et al. (2021). Deep carbonate reservoir characterisation using multi-seismic attributes via machine learning with physical constraints. *J. Geophys. Eng.* 18 (5), 761–775. doi:10.1093/jge/gxab049

Chopra, S., and Marfurt, K. J. (2016). Spectral decomposition and spectral balancing of seismic data. *Lead. Edge* 35 (2), 176–179. doi:10.1190/tle35020176.1

Cui, X., Huang, Xi, Yang, J., Zhang, D., Chen, X., and Li, K. (2021). Seismic discontinuity feature enhancement method based on tensor voting. *Pet. Geophys. Explor.* 56 (06), 1351–1358. doi:10.13810/j.cnki.issn.1000-7210.2021.06.018

Freeman, W. T., and Adelson, E. H. (1991). The design and use of steerable filters. *IEEE Trans. Pattern analysis Mach. Intell.* 13 (9), 891–906. doi:10.1109/34.93808

Hairabian, A., Fournier, F., Borgomano, J., and Nardon, S. (2014). Depositional facies, pore types and elastic properties of deep-water gravity flow carbonates. *J. Petroleum Geol.* 37 (3), 231–249. doi:10.1111/jpg.12581

He, X., Tang, Q. S., Wu, G. H., Li, F., Tian, W. Z., Luo, W. J., et al. (2023). Controlling and storage role of sinian strike-slip faults in Anyue gas field, Sichuan Basin. *Petroleum Explor. Dev.* 06, 1116–1127. doi:10.11698/PED.20220611

Hendry, J., Burgess, P., Hunt, D., Janson, X., and Zampetti, V. (2021). Seismic characterization of carbonate platforms and reservoirs: an introduction and review, *Geol. Soc, London, Spec. Pub.* 509, 1–28. doi:10.1144/sp509-2021-51

Jia, C., Ma, D., Yuan, J., Wei, G., Yang, M., Yan, L., et al. (2022). Structural characteristics, formation and evolution and genetic mechanisms of strizke–slip faults in the Tarim Basin. *Nat. Gas. Ind. B* 9 (1), 51–62. doi:10.1016/j.ngib.2021.08.017

Pan, J., Li, J., Wang, H., Li, C., Feng, C., and Zhou, J. (2020). Research progress and trend of seismic prediction technology for deep and ultra-deep carbonate reservoirs. *China Pet. Explor.* 25 (3), 156. doi:10.3969/j.issn.1672-7703.2020.03.014

Jiao, F. Z., Yang, Y., Ran, Q., Wu, G. H., and Liang, H. (2021). Distribution of strike-slip faults and natural gas exploration in the central Sichuan Basin. *Nat. Gas. Ind.* 08, 92–101. doi:10.3787/j.issn.1000-0976.2021.08.009

Lan, C., Xu, Z., Ma, X., Hu, C., Chen, H., and Zou, H. (2019). Development and distribution of mound-shoal complex in the Sinian Dengying Formation, Sichuan Basin and its control on reservoirs. *Acta Pet. Sin.* 40 (9), 1069. doi:10.7623/syxb201909005

Li, C. M., Peng, C., Wei, L. Y., Bie, J., Wang, Z. D., Li, W. Q., et al. (2022). Seismic prediction technology for small-scale cavity-type carbonate reservoirs: a case study of the fourth section of the Dengying Formation reservoir in well GS18, internal belt of the Sichuan Basin. *Fault-Block Oil Gas Field* 02, 189–193. doi:10.6056/dkyqt202202008

Li, J., Yang, C., Xie, W., Rui, Y., Wang, X., Zhang, L., et al. (2023). Differences in natural gas accumulation between the marginal and interior areas of the Sinian platform in Anyue Gas Field, Sichuan Basin, and their exploration implications. *Petroleum Nat. Gas Geol.* 01, 34–45. doi:10.11743/ogg20230103

Lien Eide, A., Omre, H., and Ursin, B. (2002). Prediction of reservoir variables based on seismic data and well observations. *J. Am. Stat. Assoc.* 97 (457), 18–28. doi:10.1198/016214502753479194

Liu, Y., and Fomel, S. (2013). Seismic data analysis using local time-frequency decomposition. *Geophys. Prospect.* 61 (3), 516–525. doi:10.1111/j.1365-2478.2012.01062.x

Lucia, F. J., Kerans, C., and Jennings, J. W. (2003). Carbonate reservoir characterization. *J. petroleum Technol.* 55 (06), 70–72. doi:10.2118/82071-ms

Luo, B., Yang, Y., Luo, W., Wen, L., Wang, W., and Chen, K. (2015). Factors controlling reservoir development and distribution in the ancient uplifts of central Sichuan: a case study of the Dengying Formation. *Acta Pet. Sin.* 04, 416–426. doi:10.7623/syxb201504003

Luo, W., Xu, W., Zhu, Z., Liu, X., Wang, Q., Shen, Y., et al. (2019). Origin and geological significance of siliceous rocks in the fourth member of the Sinian Dengying Formation in the Gaoshiti area of the Sichuan Basin. *Nat. Gas Explor. Dev.* 42 (03), 1–9. doi:10.12055/gaskk.issn.1673-3177.2019.03.001

Ma, B., Liang, H., Wu, G., and Tang, Q. (2023). Formation and evolution of multi-stage strike-slip faults in the central Sichuan Basin. *Petroleum Explor. Dev.* 50 (02), 333–345. doi:10.11698/PED.20220655

Malki, M. L., Saberi, M. R., Kolawole, O., Rasouli, V., Sennaoui, B., and Ozotta, O. (2023). Underlying mechanisms and controlling factors of carbonate reservoir characterization from rock physics perspective: a comprehensive review. *Geoenergy Sci. Eng.* 226, 211793. doi:10.1016/j.geoen.2023.211793

Massaro, L., Corradetti, A., Vinci, F., Tavani, S., Iannace, A., Parente, M., et al. (2018). Multiscale fracture analysis in a reservoir-scale carbonate platform exposure (Sorrento Peninsula, Italy): implications for fluid flow. *Geofluids* 2018, 1–10. doi:10.1155/2018/7526425

Mathewson, J., and Hale, D. (2008). "Detection of channels in seismic images using the steerable pyramid," in SEG International Exposition and Annual Meeting (SEG-2008), Las Vegas, Nevada, November 2008.

Nabawy, B. S., El-Bialy, M., Hamimi, Z., Khamis, H. A., Wahed, S. A. A., Osman, R. A., et al. (2023). Implication of the diagenetic evolution, litho-and microfacies types on the storage capacity of the carbonate rocks in West Esh El Mallaha area, SW onshore Gulf of Suez, Egypt. *J. Afr. Earth Sci.* 204, 104971. doi:10.1016/j.jafrearsci.2023.104971

Naghizadeh, M. (2012). Seismic data interpolation and denoising in the frequency-wavenumber domain. *Geophysics* 77 (2), V71–V80. doi:10.1190/geo2011-0172.1

Naseer, M. T., and Asim, S. (2018). Characterization of shallow-marine reservoirs of Lower Eocene carbonates, Pakistan: continuous wavelet transforms-based spectral decomposition. *J. Nat. Gas Sci. Eng.* 56, 629–649. doi:10.1016/j.jngse.2018.06.010

Pppelreiter, M., Balzarini, M. A., De Sousa, P., Engel, S., Galarraga, M., Hansen, B., et al. (2005). Structural control on sweet-spot distribution in a carbonate reservoir: concepts and 3-D models (Cogollo Group, Lower Cretaceous, Venezuela). *AAPG Bull.* 89 (12), 1651–1676. doi:10.1306/08080504126

Sarhan, M. A. (2024). Editorial: advanced techniques and applications for characterizing the hydrocarbon potential in carbonate reservoirs. *Front. Earth Sci.* 12, 1385645. doi:10.3389/feart.2024.1385645

Shen, J. W., Webb, G. E., and Jell, J. S. (2008). Platform margins, reef facies, and microbial carbonates; a comparison of Devonian reef complexes in the Canning Basin, Western Australia, and the Guilin region, South China. *Earth-Science Rev.* 88 (1-2), 33–59. doi:10.1016/j.earscirev.2008.01.002

Shi, J., Zhao, X., Pan, R., Zeng, L., and Zhu, Z. (2023). Characteristics of natural fractures in the Sinian Dengying Formation carbonate reservoir and their impact on gas well productivity in the central Sichuan area. *Petroleum Nat. Gas Geol.* 02, 393–405. doi:10.11743/ogg20230211

Tian, X., Peng, H., Wang, Y., Yang, D., Sun, Y., Zhang, X., et al. (2020). Reservoir differences and controlling factors of the fourth section of the Sinian Dengying Formation between the platform margin and interior in Anyue Gas Field, central Sichuan. *Nat. Gas. Geosci.* 09, 1225–1238. doi:10.11764/j.issn.1672-1926.2020.04.007

Wadas, S. H., Krumbholz, J. F., Shipilin, V., Krumbholz, M., Tanner, D. C., and Buness, H. (2023). Advanced seismic characterization of a geothermal carbonate reservoir–insight into the structure and diagenesis of a reservoir in the German Molasse Basin. *Solid earth.* 14 (8), 871–908. doi:10.5194/se-14-871-2023

Wang, Q., Zhang, Y., Xie, Z., Zhao, Y., Zhang, C., Sun, C., et al. (2022). The advancement and challenges of seismic techniques for ultra-deep carbonate reservoir exploitation in the Tarim Basin of northwestern China. *Energies* 15 (20), 7653. doi:10.3390/en15207653

Wang, R., Tang, Y., Yang, F., She, J., Li, X., Chen, N., et al. (2024). A fracture modeling method for ultra-deep reservoirs based on geologic information fusion: an application to a low porosity sandstone reservoirs in X gas field of a basin in western China. *Front. Earth Sci.* 11, 1351264. doi:10.3389/feart.2023.1351264

Wu, G. H., Zhang, T., Zhu, Y. F., Wan, X. G., and Xiong, C. (2020). Structure, distribution, and development mechanism of carbonate rock fracture zones. *Geol. Sci.* 55 (01), 68–80. doi:10.12017/dzkx.2020.006

Xiao, F. S., Chen, K., Ran, Q., Zhang, X., Xie, B., Liu, X. G., et al. (2018). New understanding of seismic patterns of high-yield wells in the Sinian Dengying Formation gas reservoirs in Gaoshiti area of Sichuan Basin. *Nat. Gas. Ind.* 02, 8–15. doi:10.3787/j.issn.1000-0976.2018.02.002

Xie, J., Tang, Q., Peng, X., Deng, H., and Xu, W. (2021). Key technologies for the efficient development of ultra-deep ancient dolomite karst gas reservoirs: a case study of the Sinian Dengying Formation gas reservoir in the Anyue gas field of the Sichuan Basin. *Nat. Gas. Ind. B* 8 (6), 588–595. doi:10.1016/j.ngib.2021.11.006

Xu, M., Fu, J., Yang, X., Liu, J., and Wang, Y. (2019). Seismic detection of ultra-deep carbonate pore-fracture zones in the northwest of the Sichuan Basin. *Nat. Gas. Ind.* 39 (11). doi:10.3787/j.issn.1000-0976.2019.11.003

Xu, Z., Lan, C., Zhang, B., Hao, F., Lu, C., Tian, X., et al. (2022). Impact of diagenesis on the microbial reservoirs of the terminal Ediacaran Dengying Formation from the central to northern Sichuan Basin, SW China. *Mar. Petroleum Geol.* 146, 105924. doi:10.1016/j.marpetgeo.2022.105924

Zhang, M., Dai, X. F., Pang, C. X., Jiang, L., Geng, C., and Xu, Y. P. (2021). Recognition and application of high-quality reservoirs in the internal belt of the Dengying Formation in the central Sichuan region. *Nat. Gas. Geosci.* 05, 764–771. doi:10.11764/j.issn.1672-1926.2020.12.007

Zhao, Y., Huang, X., Chen, Y., Song, H., Zhang, D., Cui, X., et al. (2021). Geological body boundary identification method using the steerable pyramid and its application in conglomerate reservoirs. *Geophys. Prospect. Petroleum* (03), 414–420+429. doi:10.3969/j.issn.1000-1441.2021.03.007

Zou, C., Xu, C., Wang, Z., Su, H., Guan, Y., Jun, L., et al. (2011). Geological characteristics and forming conditions of the platform margin large reef-shoal gas province in the Sichuan Basin. *Petroleum Explor. Dev.* 38 (6), 641–651. doi:10.1016/s1876-3804(12)60001-9

frontiers | Frontiers in Earth Science

TYPE Original Research
PUBLISHED 02 July 2024
DOI 10.3389/feart.2024.1418821

OPEN ACCESS

EDITED BY
Yu Jing,
University of New South Wales, Australia

REVIEWED BY
Huazhou Li,
University of Alberta, Canada
Shuaiwei Ding,
Northwest University, China
Junjian Li,
China University of Petroleum, Beijing, China

*CORRESPONDENCE
Shuoliang Wang,
wangshuoliang@cugb.edu.cn

RECEIVED 17 April 2024
ACCEPTED 07 June 2024
PUBLISHED 02 July 2024

CITATION
Zhao L, Zhang L, Su Y, Tan X, Li C and Wang S (2024), *In-situ* CT study on the effect of cyclic gas injection and depletion exploitation on the phase behavior of fractured condensate gas reservoirs.
Front. Earth Sci. 12:1418821.
doi: 10.3389/feart.2024.1418821

In-situ CT study on the effect of cyclic gas injection and depletion exploitation on the phase behavior of fractured condensate gas reservoirs

Lin Zhao[1], Lijun Zhang[1], Yanchun Su[1], Xianhong Tan[1], CongCong Li[2] and Shuoliang Wang[2]*

[1]CNOOC Research Institute Co., Ltd., Beijing, China, [2]China University of Geosciences, Beijing, China

Using subterranean rock cores as samples, the impact of depletion exploitation and cyclic gas injection on the occurrence and dynamic utilization of condensate oil and the damage to reservoirs were studied. Initially, the internal pore structure of the rock core was analysed using computer tomography (CT), followed by depletion and cyclic gas injection experiments, with *in-situ* CT scanning of the samples. The results indicate that under different fracture apertures, condensate oil exhibits wave flow and slug flow states. The production effectiveness of cyclic gas injection is significantly superior to depletion exploitation production, with condensate oil saturation decreasing by over 30%. During cyclic gas injection, fractures serve as the main flow channels, with condensate oil being extracted first. In cyclic gas injection, the most significant effect is seen during the first injection, with a decrease in oil saturation of around 3%. Subsequent injections show decreases of approximately 1% and 0.5% in oil saturation respectively. As the gas injection volume increases, the extent of cumulative production rate improvement also gradually increases; however, once the injection volume reaches the reservoir pressure, the rate of cumulative production rate improvement will gradually decrease. These findings provide technical support for optimizing the development mode of condensate gas reservoirs, clarifying the seepage law of condensate oil and gas, and providing technical support for the efficient development of fractured condensate gas reservoirs.

KEYWORDS

***in-situ* CT, cyclic gas injection, phase behavior, fractured condensate gas reservoirs, depletion exploitation**

1 Introduction

Condensate gas reservoir refers to a special gas reservoir where the formation pressure lies between the critical pressure under original formation conditions and the maximum dew point pressure (Nasriani et al., 2015; Long et al., 2023; Dorhjie et al., 2024). Condensate gas reservoirs exhibit the following characteristics: firstly, they exist in the reservoir in both adsorbed and free states, with various accumulation methods. Secondly, the reservoir contains complex pore structures such as nano-scale intra-granular pores, inter-granular pores, and micro-scale fractures. Lastly, due to the abundant presence of micro-scale

fractures, condensate gas reservoirs involve complex multi-scale phase changes, leading to significant differences in phase behavior compared to conventional phase changes (Hosseinzadegan et al., 2023; Wang, 2023). Before reservoir exploitation, condensate gas reservoirs remain in a gaseous state under the influence of formation temperature and pressure. As the gas reservoir is developed, the formation pressure gradually decreases, and when it reaches and falls below the dew point pressure, a gas-liquid two-phase zone appears (Liu et al., 2024). The precipitation of condensate oil increases the permeability resistance of the surrounding reservoir rock, resulting in a sharp decline in the overall gas reservoir production. Therefore, studying the phase behavior of condensate gas reservoirs in formations with continuously changing pressures is of crucial importance for their development.

Choosing the appropriate method for condensate gas reservoir exploitation is crucial for the recoveries of condensate gas and condensate oil, directly impacting the final economic benefits. During the depletion exploitation phase, when the pressure drops to the maximum anti-condensation pressure, the condensate oil saturation reaches its peak. Despite triggering retrograde condensation after dropping to the secondary dew point pressure, the decrease in condensate oil saturation is relatively small (Jing et al., 2023). The production of condensate oil and the increase in saturation lead to a significant decrease in the relative gas permeability of the reservoir, reducing the gas well productivity. At the same time, condensate oil precipitates and accumulates in the wellbore area, complicating the wellbore conditions, reducing production efficiency, and in severe cases, leading to well shutdown (Salmani et al., 2020; Hosseinzadegan et al., 2023). The principle of cyclic gas injection for exploitation involves periodically injecting high-pressure gas (dry gas, surface-separated gas) to displace condensate oil in wet gas, aiming to increase reservoir pressure and prevent retrograde condensation (Kumar et al., 2015; Zhang et al., 2020; Jiang, 2023). When condensate oil reserves are large and content is high, employing pressure maintenance methods can reduce condensate oil losses. The effectiveness and rationality of maintaining formation pressure depend on factors such as condensate oil content, oil and gas reserves, burial depth, pressure, reservoir homogeneity and connectivity, drilling techniques, high-pressure gas injection processes, and other factors (Faramarzi and Sadeghnejad, 2020; Reis and Carvalho, 2022).

The PVT (Production verification test) experiment is currently a common method for simulating the production conditions of condensate gas (Passoni et al., 2024). Guo et al. (2020) studied the effect of different gas injection methods on the flow pattern of condensate gas through PVT experiments. Wang et al. (2022) used a visual PVT device to study the retrograde condensation phenomenon of condensate gas with temperature/pressure changes, revealing that the dew point pressure of condensate gas in the Wenchang 9-2 low-condensate gas field is close to the reservoir pressure. With the development of artificial intelligence technology, Alarouj et al. (2020) established a large database containing over 700 gas-condensate oil samples and a new model for calculating dew point pressure, which significantly outperforms the simulation results of existing state equations in terms of accuracy. Despite the achievements in AI (Artificial Intelligence) prediction, it is still limited by the quality and size of the dataset. Calculation based on state equations is another method to determine the behavioural characteristics of condensate gas phase. Shi et al. (2015) proposed a new equation for gas condensate well deliverability, considering the phase behaviour of gas condensate fluids in the wellbore. The results indicate that neglecting wellbore phase behaviour can lead to inaccurate predictions of gas and condensate production, and validation cases show good agreement between the new model and actual data. Traditional PVT experiments and AI-based methods both fail to consider the impact of porous media on the behaviour of condensate gas phase. Jing et al. (2023) dynamically characterised the phase transition process of condensate gas in porous media during the depressurisation depletion process using real-time CT scanning and digital rock technology, suggesting that the change in condensate oil content within the porous media occurs synchronously throughout the depletion process. These studies demonstrate the influence of porous media on the phase behaviour of condensate gas, yet the phase transition characteristics of condensate gas in fracture and matrix systems have not been considered.

In summary, the research on the phase transition mechanisms of condensate gas in porous media, especially the dynamic phase evolution of condensate oil in complex fracture systems, under different production processes still requires further refinement. This study focuses on the rock cores in the target area, investigating the dynamic evolution of multi-component condensate gas phases in porous media. The condensate gas components in actual condensate reservoirs were blended and subjected to PVT testing. The CT scan data were processed using PerGeos, and the pore structure of the rock core was analysed. Depletion and cyclic gas injection (CGI) experiments were conducted in the rock core, obtaining the distribution of condensate oil and gas at different pressures using an *in-situ* CT system. Ultimately, the phase characteristics of condensate oil in fractured porous media were described, and the formation process and mechanism were summarised, comparing the effects of different exploitation methods on the development of condensate gas reservoirs.

2 Materials and methods

2.1 Fluid sample mixing

By combining samples of oil and gas collected on-site from the target blocks, corresponding mixing work was carried out. The composition of the oil and gas samples in the on-site separators is shown in Table 1.

2.2 Rock samples

In the research area, the density of rock fractures exhibits diversity, ranging from 1 to 15 fractures per meter. The fractures vary widely in aperture, covering a range from a few micrometers to several hundred micrometers, with a predominance of high-angle fractures followed by vertical ones. Low-angle and horizontal fractures are relatively less abundant (Figure 1). The wettability is water wet, and the contact angle is 67.8°.

Field coring and logging results from the target block and adjacent blocks indicate that the upper weathering zone of the

TABLE 1 Oil and gas components in the separator.

Sample components	Separator gas component mole fraction/%	Separator oil sample component mole fraction/%
CO_2	9.00	—
N_2	0.19	—
C_1	76.99	6.67
C_2	8.27	2.99
C_3	2.95	2.32
iC_4	0.96	1.53
nC_4	0.46	
iC_5	0.35	1.52
nC_5	0.31	
C_6	0.35	2.69
C_{7+}	0.17	82.28

TABLE 2 Pore-fracture statistical results of digital core.

Pore and fracture information of rock samples	Value
Average pore volume (μm^3)	46.108
Average pore diameter (μm)	1.911
Shape factor	1.068
Average maximum fracture opening (μm)	104.057
Average porosity	0.230

target block shows strong dissolution, severe weathering, and mainly irregularly developed weathering mesh fractures, densely interwoven like a spider web. The weathering degree gradually weakens towards the lower part, with strong tectonic stress, mainly developing structurally distributed fractures resembling layers. The reservoir space includes macro fractures, small to medium fractures, micro fractures, as well as intergranular pores, dissolution pores, etc., resulting in a reservoir with multi-scale flow spaces and complex pore-throat structures.

2.3 PVT experimental steps

The experimental fluid samples were prepared under formation pressure of 46.90 MPa and formation temperature of 138°C according to the production gas-oil ratio of 1420.89 m^3/m^3. The sample preparation and PVT analysis method refer to the national standard GB/T26981-2020 "Reservoir Fluid Physical Property Analysis Method."

2.4 Experimental setup and steps

2.4.1 Depletion exploitation

(a) Using the mixed reservoir fluid, the actual fractured core was raised to reservoir temperature and maintained for 3–4 h.
(b) Then a system pressure of 50 MPa was established using methane gas.
(c) Methane in the model was replaced with mixed condensate gas to saturate the actual fractured core under reservoir temperature and pressure conditions. Back pressure was slowly reduced at the set pressure drop rate to initiate simulated depletion exploitation.
(d) The production of oil and gas at the outlet was recorded, and the production dynamics were analyzed.
(e) The CT raw data was processed using PerGeos software to determine the distribution of condensate oil in the rock fractures and pores. Condensate oil saturation is the percentage of the ratio of oil volume in the effective pores in the core to the effective pore volume of the rock (Figure 2).

2.4.2 Cyclic gas injection

(a) Preparation steps were the same as depletion exploitation.
(b) The experimental fluid in the fractured core was saturated under reservoir temperature and pressure conditions with methane from the mixed condensate gas. Back pressure was slowly reduced at the set pressure drop rate to initiate simulated depletion exploitation until 30 MPa.
(c) Associated gas was injected back to reservoir pressure and maintained for half an hour, then production from two production outlets was simultaneously produced, repeating this process three times.

FIGURE 1
Outcrop rock samples and plunger core samples in the study area.

(d) Post-processing steps were the same as depletion exploitation.

3 Results and discussion

3.1 PVT experiment

Traditional methods for studying the behavior of condensate gas phase typically involve experiments to determine the relationship between the pressure, temperature, and volume of the condensate gas. Constant Composition Expansion (CCE) and Constant Volume Depletion (CVD) are the most commonly used experimental methods in PVT units, used to simulate the phase behavior changes of condensate gas reservoirs during development. To simulate the fluid component parameters of the target reservoir block, corresponding separator oil and gas samples were mixed. By conducting CCE and CVD under reservoir temperature and pressure conditions, the laboratory mixed fluid samples closely match the PVT experimental results of the target block oil and gas samples (Figure 3). These results indicate that the mixed fluid samples are representative, therefore, subsequent microscopic experiments will use this oil sample for testing.

Although these experiments can provide essential high-pressure physical properties of condensate gas, they also have limitations. Traditional PVT experiments typically only provide macroscopic properties of the condensate gas and cannot reveal the behavior of condensate gas at a microscopic scale within porous media. Understanding and predicting the productivity and recovery efficiency of condensate gas reservoirs heavily rely on these microscopic behaviors.

3.2 Porosity structure analysis

A representative elementary volume (REV) with voxel dimensions of 400 × 400 × 400 was extracted from the CT scan data of the core. However, due to external disturbances during the scanning process, the resulting images had issues such as uneven brightness, low contrast, and high noise levels. To enhance the image quality, brightness, contrast, and filtering processes were required (Wang et al., 2024).

By sequentially stacking multiple layers of 2D grayscale images, a 3D grayscale image consistent with the actual core was obtained. The watershed algorithm was used for image segmentation (Patmonoaji et al., 2020). The traditional watershed algorithm is a morphological segmentation method based on topological theory. In morphological segmentation methods, images are typically treated as terrain surfaces, with each grayscale level corresponding to a contour line. This approach establishes boundaries known as "watersheds" around each local minimum value in the image, making it straightforward to estimate image gradients and locate gradient peaks for segmentation. Given the significant grayscale variations at the phase edges of the core image, the gradient image effectively describes these variations (Wang et al., 2023).

Following the segmentation process, a 3D digital core model is created, as shown in Figure 4. Lower grayscale values represent fractures within the core, while higher values represent rock matrix particles. In the binary 3D digital core model, the matrix is transparent, and the pore space is displayed in blue. The fracture structures with good connectivity within the rock matrix are clearly visible, presenting a sheet-like distribution. Different colours in the 3D pore-fracture spatial distribution map represent different pore clusters.

3.3 Analysis of condensed gas phase behavior and microscopic mechanism

Based on the characteristics of rock pore structure and the flow behavior of fluids within them, the internal structure is defined as a dual-porosity medium, consisting of fractures and matrix as two major systems. By utilizing CT image threshold segmentation to identify the position of fractures, the blue area represents condensed oil. In the 3D residual oil distribution map, the shape of the condensed oil distribution aligns with the shape of sheet-like fractures, indicating that fractures serve as the main flow channels for condensed oil. Additionally, wave-like flow of condensed oil is observed in large fractures (Figure 5).

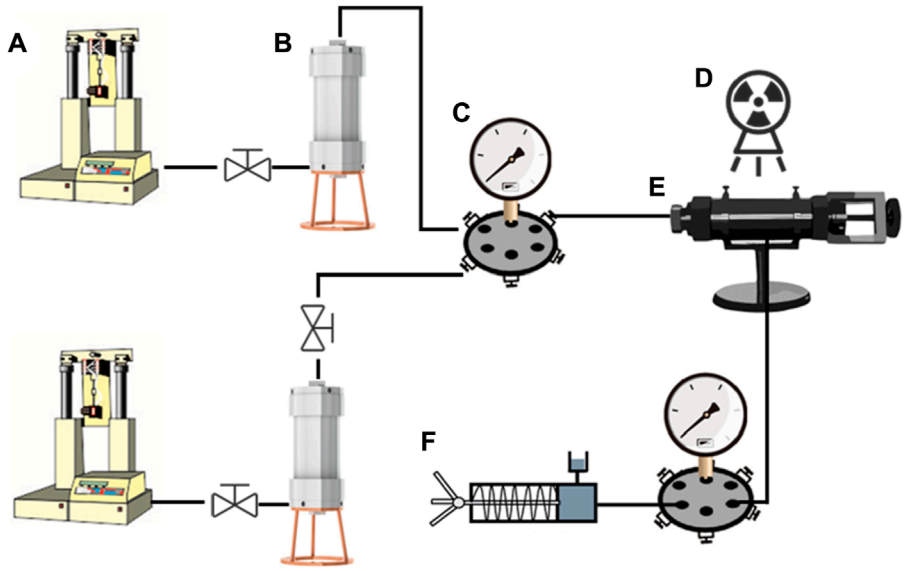

FIGURE 2
Experimental flow, **(A)**: constant speed and constant pressure pump, **(B)**: intermediate vessel, **(C)**: six-way valve, **(D)**: real-time CT device, **(E)**: gripper, **(F)**: hand pump.

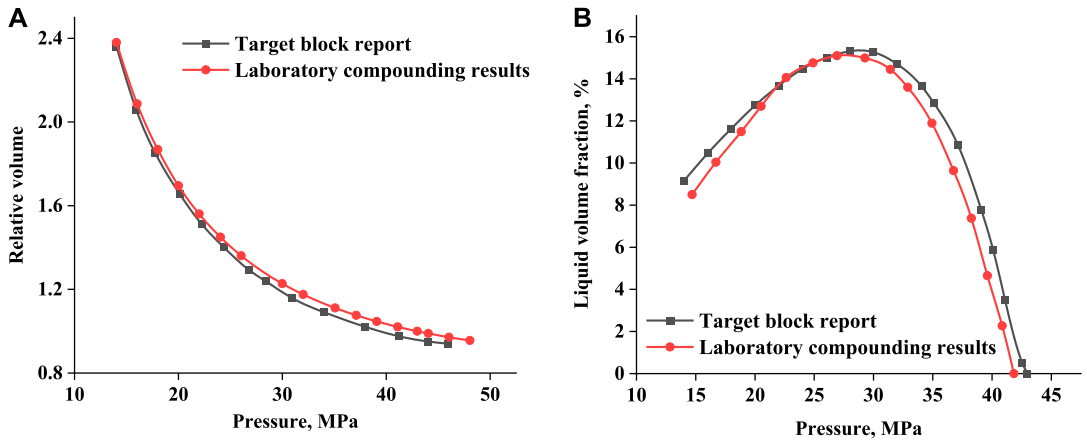

FIGURE 3
Results of PVT experiments **(A)** Comparison of CCE experimental results, **(B)** Comparison of CVD experimental results.

A rock core region containing two intersecting fractures with different apertures was extracted from the rock core data volume (Table 2), with the aperture range of small fractures being 3–8 μm and wide fractures being 20–50 μm. Within the distribution of condensed oil, distinct phenomena of segmented flow and wave-like flow were observed in fractures, with segmented flow predominantly in small fractures and wave-like flow in wide fractures. Segmented flow in small fractures consists of isolated segments without trailing liquid droplets, with a thin oil film covering the fracture wall and surrounding the segments. On the other hand, wave-like flow in wide fractures was influenced by the interaction forces between oil and gas phases and the fracture wall, resulting in a wave-like shape of condensed oil on the fracture wall with significant differences in film thickness between the top and bottom of the fracture.

The existence characteristics of condensed oil in porous media and fractures are based on two fundamental theories: adsorption theory and bound water film theory. Adsorption refers to the continuous accumulation of gas or vapor molecules on the solid surface acting as an "adsorbent" until reaching thermodynamic equilibrium (Dąbrowski, 2001). Bound water refers to a layer of water film adsorbed on the surface of rock particles due to molecular gravity and electrostatic forces, divided into adsorbed water within the water film and thin film water on the outer layer of the water film (Hu et al., 2024).

When the pressure is below the dew point pressure, condensed oil droplets precipitate and adsorb on the surface of rock particles or suspend in the condensed gas. As pressure decreases, the droplets grow and coalesce, transitioning the liquid on the surface into a

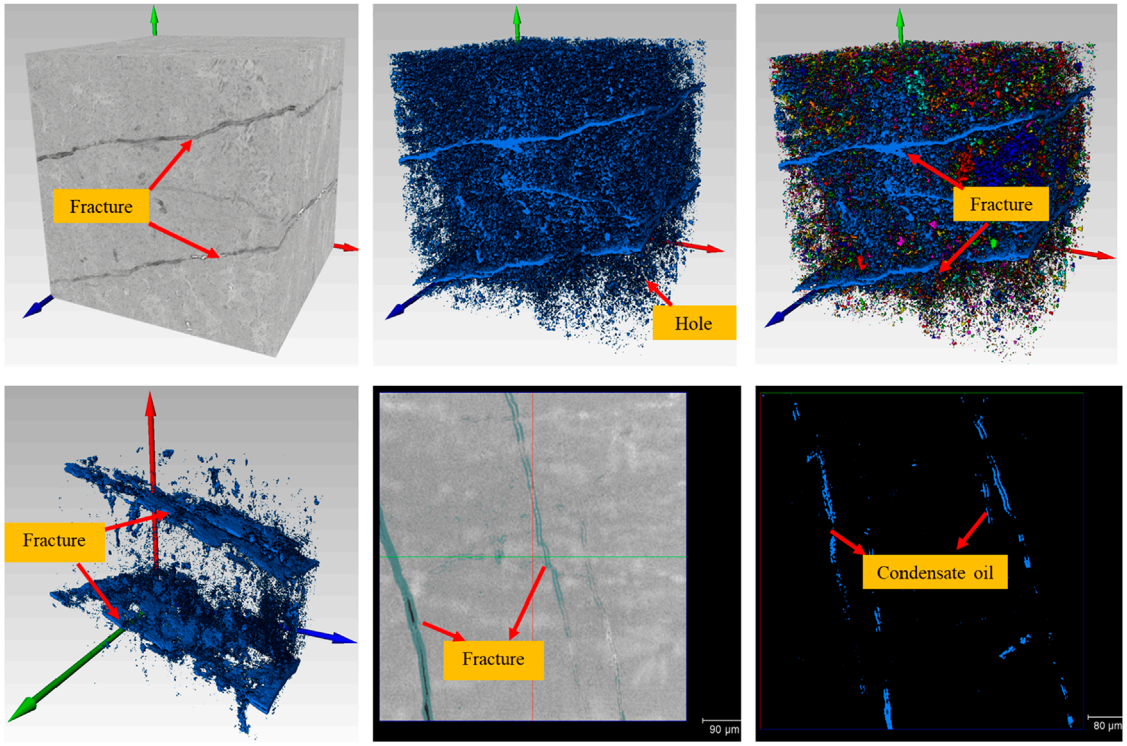

FIGURE 4
Pore structure analysis and residual oil distribution of 3D and 2D digital cores.

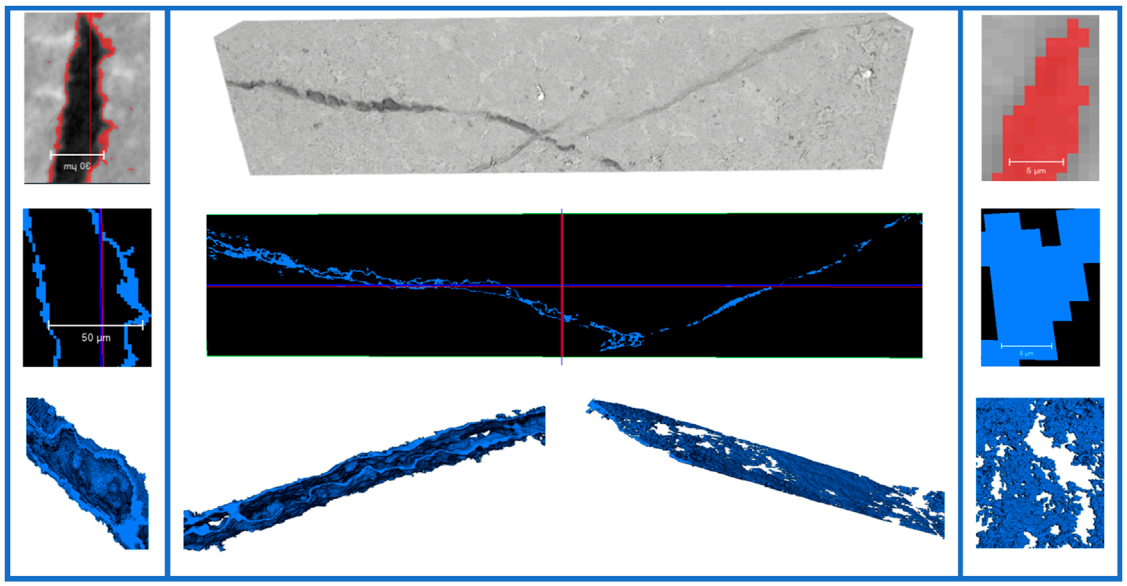

FIGURE 5
Condensate fugacity flow pattern in fractures in 3D core model (wave flow on the left, segment plug flow on the right).

continuous state and initiating gradual flow. The external layer of condensed oil is influenced not only by molecular forces but also by external forces such as gravity, pressure differential, and friction with gas. Pressure differential has the greatest impact on the flow of condensed oil, where the flow of condensed oil along the outer layer of the pore wall is primarily due to pressure differential, directed towards the pressure drop, resulting in the phenomenon of "wave-like flow" of condensed oil (Nabae et al., 2020).

10.3389/feart.2024.1418821

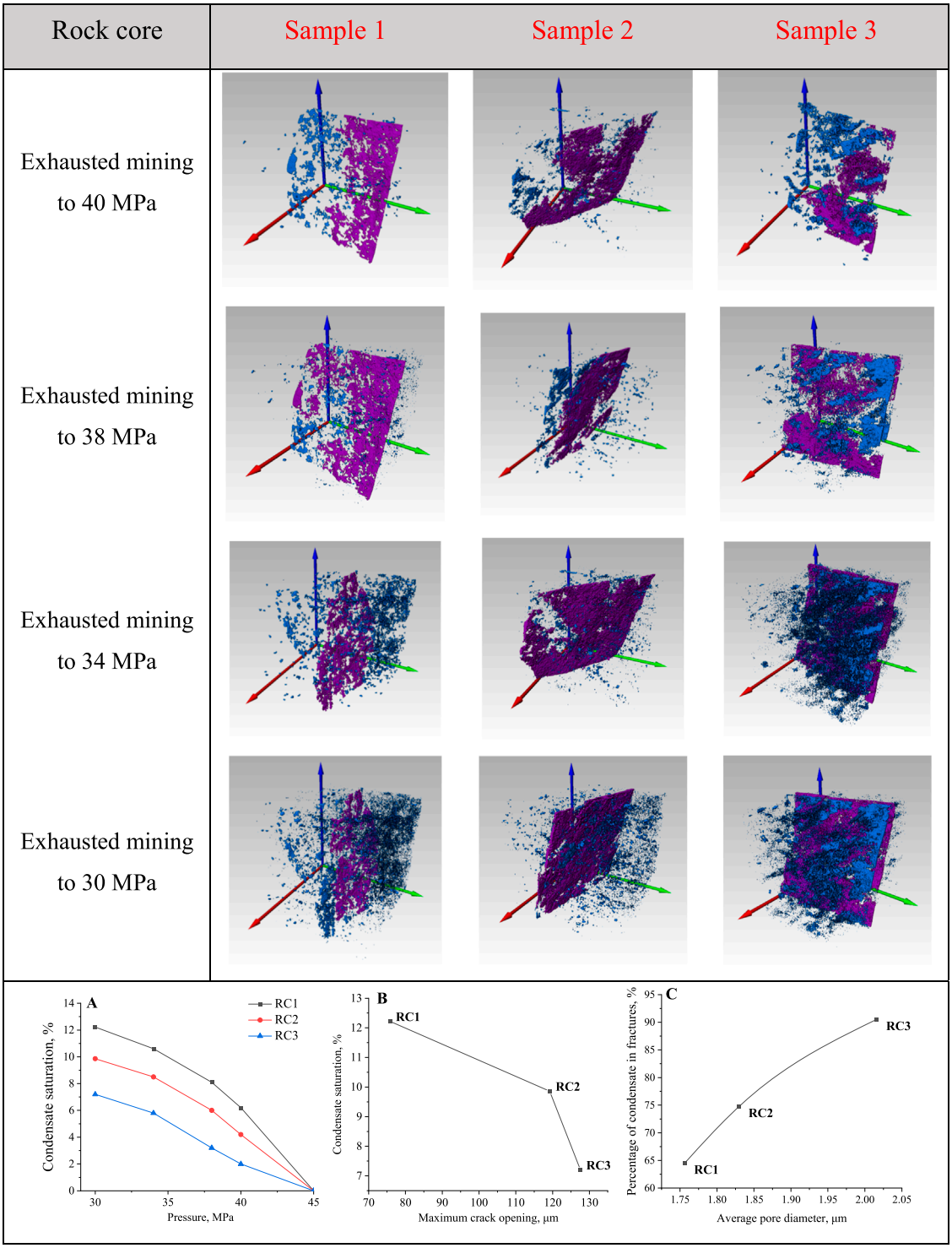

FIGURE 6
Variation of condensate distribution inside the cores under depletion mining mode, **(A)** condensate saturation in the three cores, **(B)** fracture opening versus condensate saturation, **(C)** pore diameter versus fracture condensate percentage.

When an adsorption layer forms on the surface of a wide fracture in a condensed gas system, the thickness of the adsorption layer compared to the pore space can be negligible. However, in nanometer pores or microfractures, the thickness of the adsorption layer cannot be ignored. There is a positive relationship between the aperture of fractures and the ratio of condensed oil volume in fractures to total condensed oil volume, meaning that the smaller the fracture volume, the more difficult it is for the condensed gas

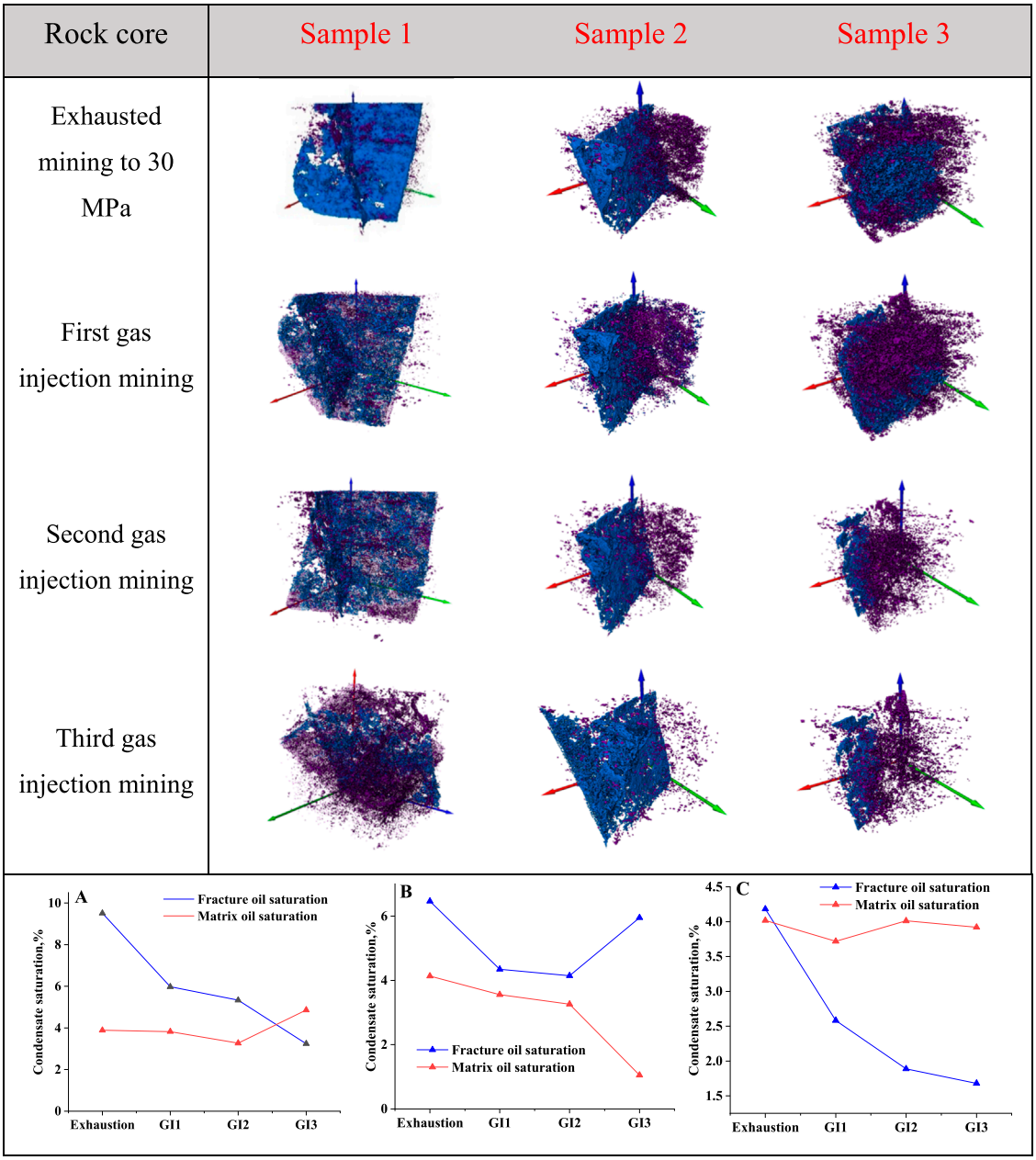

FIGURE 7
Variation of condensate distribution within the core under multiple cycles of gas injection mode, and the proportion of condensate distribution in the fractures and matrix [**(A)** Core I; **(B)** Core II; **(C)** Core III].

to mobilize the condensed oil within the fracture. These condensed oils come into contact, merge, and eventually coalesce under capillary forces, leading to capillary condensation and resulting in the phenomenon of "segmented flow" of condensed oil (Wang et al., 2004).

3.4 Depletion exploitation experiment

Depletion exploitation of condensate gas reservoirs has the advantage of requiring less investment and simpler technology. However, a drawback is the loss of a portion of valuable condensate oil resources in the formation. Therefore, when employing depletion methods for exploitation, the abandoned formation pressure of condensate gas reservoirs is higher than that of dry gas reservoirs, resulting in a lower recovery of condensate gas compared to dry gas reservoirs (Abbasov and Fataliyev, 2016). To align with actual field production, the depletion pressure for this simulation was set at 30 MPa.

In Sample 1, as pressure decreased, the saturation of condensate oil increased from 6.17% at 40 MPa to 12.22% at 30 MPa (Figure 6). Condensate oil primarily migrated through fractures, with

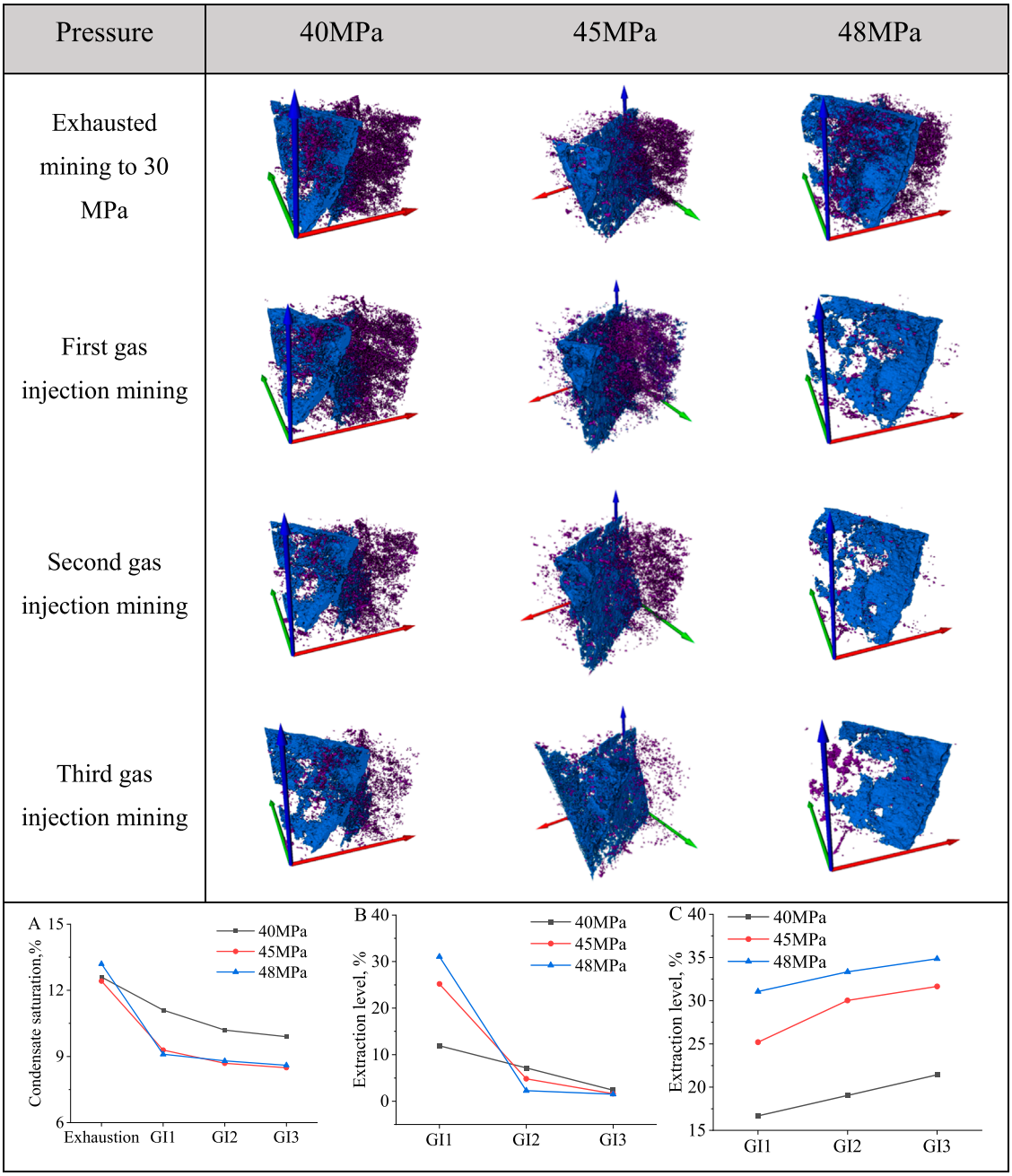

FIGURE 8
Variation of condensate distribution inside the core under multiple cycle gas injection modes with different injection volumes, **(A)** variation of condensate saturation inside the core; **(B)** degree of extraction in a single cycle; **(C)** degree of extraction in a cumulative cycle.

fractures and pores near fractures retaining more condensate oil. Along the *Z*-axis, which was the direction of oil and gas movement, the condensate oil content in the pores near the outlet end of the rock core was greater than that at the inlet end.

In Sample 2, as pressure decreased, the saturation of condensate oil increased from 4.18% at 40 MPa to 9.86% at 30 Mpa. The fracture aperture of Rock Core 2 was nearly twice that of Rock Core 1, allowing condensate oil to almost completely fill the fracture surface at 30 MPa.

In Sample 3, as pressure decreased, the saturation of condensate oil increased from 2.03% at 40 MPa to 7.21% at 30 Mpa. The fracture aperture of Rock Core 3 was slightly larger than that of Rock Core 2, with condensate oil in the fractures forming a complete plane, filling most of the reservoir space with condensate oil. Rock Core 3 had the smallest average pore diameter, and only parts with large pore volumes and connectivity had permeability. Therefore, the condensate oil in the pores of Rock Core 3 was difficult to produce passively, resulting in a relatively high volume fraction of condensate oil in the pores.

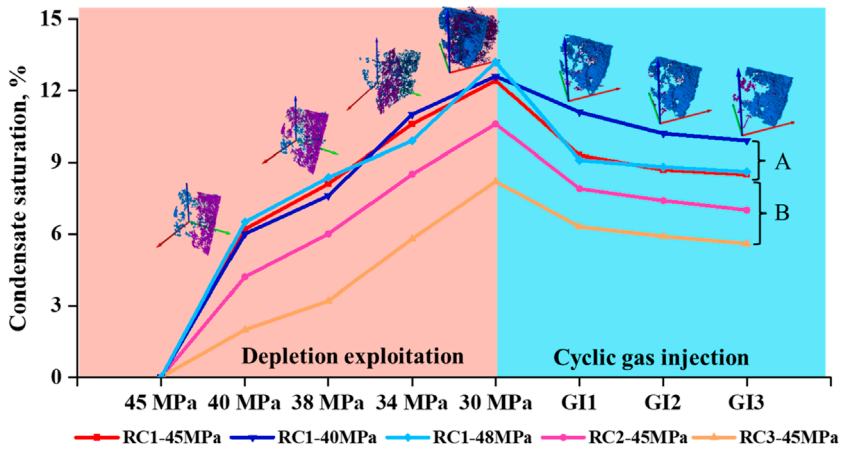

FIGURE 9
Variation of condensate saturation inside the core during depletion exploitation -cycle gas injection, A: variation of condensate saturation during multiple rounds of cycle gas injection with different injection volumes, B: variation of condensate saturation in different cores under the same cycle gas injection condition.

In summary, in the three depletion experiments, when the pressure was reduced to 30 MPa, the average saturation of condensate oil inside the rock cores was around 10%, mainly located in fractures. There is a negative correlation between fracture aperture and condensate oil saturation, meaning that larger fracture apertures make it easier for condensate gas to carry away condensate oil, reducing the impact on exploitation efficiency. Yang et al. (2020) found in full-diameter rock core depletion tests that the gas recovery in rapid depletion tests was lower than in slow depletion tests. Conversely, without considering fluid flow in porous media, the condensate oil recovery in rapid depletion tests was higher than in slow depletion tests. This result is consistent with the conclusion of this study, indicating that a faster gas flow rate leads to a higher condensate oil recovery.

3.5 Cycle gas injection experiment

3.5.1 Influence of cycle gas injection frequency

For low-saturation condensate gas reservoirs with original formation pressure higher than dew point pressure, pressure maintenance development is suitable. This development method first reduces pressure to near the dew point pressure by depressurization and then conducts cyclic gas injection to maintain pressure during production.

In the cycle gas injection experiment, the pressure was depleted from 45 MPa to 30 MPa and then restored to 45 MPa with dry gas for three cycles. In core sample one, after depletion, condensate oil mainly exists in fractures, predominantly distributed in layers. To characterize the distribution of condensate oil in the core, analysis was conducted at the intersection of fractures. The saturation of condensate oil in the core after depletion was 13.4%, and after three cycles of gas injection, it decreased to 9.8%, 8.6%, and 8.1% (Figure 7).

In core sample two, the saturation of condensate oil in the core after depletion was 10.6%, and after three cycles of gas injection, it decreased to 7.9%, 7.4%, and 7.0%. Core sample two has the largest pore diameter, resulting in the most effective utilization of condensate oil in the matrix. After depletion, condensate oil in the matrix accounted for 4.2% of the total porosity, decreasing to 1.1% after the third gas injection.

In core sample three, the saturation of condensate oil in the core after depletion was 8.2%, and after three cycles of gas injection, it decreased to 6.3%, 5.9%, and 5.6%. Core sample three has the largest fracture aperture, resulting in the most effective utilization of condensate oil in the fractures. After depletion, condensate oil in the fractures accounted for 4.2% of the total porosity, decreasing to 1.7% after the third gas injection.

In summary, in the three gas injection experiments, the average condensate oil saturation inside the core was 10% after the initial pressure reduction to 30 MPa, decreasing to 7% after three gas injections. In the condensate gas mixture system, the gas injection process will form a non-equilibrium "gas-gas" coexisting phase characteristic based on the difference in molecular potential energy. When the gas injection pressure approaches the dew point pressure, the injected dry gas will cause the remaining condensate gas system to exhibit a three-phase coexistence phenomenon of dry gas phase, condensate gas phase, and condensate oil phase. However, when the gas injection pressure is higher than the dew point pressure, the system shows a two-phase coexistence state of dry gas and condensate gas (Ganjdanesh et al., 2019; Tang et al., 2021). During the cyclic process, condensate oil in the fractures is first utilized and extracted, with the most significant effect observed during the first gas injection. As the three cycles of gas injection progress, the area of condensate oil in the fractures decreases. The above results are consistent with previous findings, indicating that gas injection can effectively evaporate and push condensate towards production wells, thereby increasing condensate recoveries (Long et al., 2024).

The order of fracture aperture size was Sample 1 < Sample 2 < Sample 3, and the order of pore diameter size was Sample 3 < Sample 1 < Sample 2. After utilizing condensate oil in the fractures, the condensate oil in the matrix was then utilized. Condensate oil

in the fractures was more easily evaporated into associated gas and taken away during the production process compared to condensate oil in the pores. In the three cycles of gas injection in core sample three, the first cycle had the best effect, removing condensate oil from the fractures, while the second and third cycles had less impact on the condensate oil in the pores. The smaller the pore diameter, the more difficult it was for the injected associated gas to utilize the condensate oil within. This study aligned with Tang et al.'s (2021) results in multiple cyclic injection experiments in underground gas storage reservoirs of condensate gas fields, showing that condensate oil in some small-scale pores was challenging to utilize.

3.5.2 Morphology and distribution of condensate oil in different gas injection volume experiments

Two main methods of maintaining pressure during exploitation are full pressure maintenance and partial pressure maintenance. Full pressure maintenance involves keeping the pressure of the entire gas reservoir above the dew point pressure by matching gas production with gas injection until the condensate oil content and production reach their economic limits. Partial pressure maintenance, on the other hand, involves producing more gas than injecting when self-produced gas is insufficient to meet injection requirements. This method helps slow down pressure decline and reduce condensate oil losses.

In the cyclic gas injection experiment with different injection volumes, the pressure was first depleted to 30 MPa, then restored to 40, 45, and 48 MPa in three repetitions, representing fully and partially maintaining reservoir pressure development methods. The results showed that better utilization of condensate oil was achieved when the pressure was restored to higher levels. At pressure restoration to 40, 45, and 48 MPa, the cumulative recovery of condensate oil reached 21.4%, 31.6%, and 34.9% respectively (Figure 8). With increased injection volume, some liquid hydrocarbon components in the remaining condensate oil in the reservoir are extracted and evaporated into the injected gas, resulting in condensate volume contraction. Meng and Sheng (2016) optimized the parameters of gas injection through numerical simulations and found that gas injection was an effective method to increase the condensate oil recovery of shale gas reservoirs, with the optimal injection time being when the pressure in the main condensation area was raised above the dew point pressure.

Under the same injection volume conditions, the effectiveness of condensate oil utilization decreased with each subsequent gas injection. Compared to the other two groups, the effect of the first gas injection was not significant when the gas was restored to 40 MPa. When the gas was restored to 48 MPa, after three gas injections, the best utilization of condensate oil in fractures and matrix was observed, with the saturation of condensate oil in fractures decreasing from 11.04% to 7.4% and in the matrix from 2.62% to 1.1%. As the injection volume increased, the oil production gradually decreased because the injected gas first extracted the light components from the condensate oil. As the injection volume increased, the extraction process became more difficult, leading to a gradual decrease in oil production. Additionally, with increasing injection volume, the cumulative increase in recovery also gradually increased. However, once the injection volume reached a certain value, the rate of cumulative recovery enhancement gradually slowed down.

3.5.3 Comparison of depletion exploitation and cyclic gas injection exploitation effects

In this study, during depletion exploitation when the pressure was reduced to 30 MPa, the average condensate saturation inside the core was 10%. Fractures served as the main flow channels, but there were oil film attachments on the walls. Segment plugs formed in fractures with small apertures, making it difficult to mobilise the condensate oil in the matrix. Upon switching to cyclic gas injection exploitation, the majority of the condensate oil in the fractures was effectively mobilised, while the mobilisation effect in the matrix was weaker. The most significant effect was observed during the first gas injection exploitation, with a decrease of around 3% in condensate saturation. In the second and third gas injection exploitations, the condensate saturation decreased by approximately 1% and 0.5% respectively (Figure 9). Cyclic gas injection extraction with full pressure retention ultimately recovered about 10% more of the internal condensate compared to partial pressure retention. These results indicate that compared to depletion exploitation, cyclic gas injection can significantly increase the condensate oil recovery, avoid the decrease of reservoir permeability caused by condensate oil accumulation, with fracture patterns, volume of injections, and injection recovery pressure being important factors influencing the condensate oil recovery.

4 Conclusion

During the depletion process of condensate gas reservoirs, the decrease in pressure leads to phase change of condensate gas in the porous media, resulting in a reduction of residual condensate oil and thus lowering the recovery. Therefore, studying the dynamic behavior of condensate gas in porous media during different production processes provides an effective way for the seepage mechanism and development optimization of condensate oil and gas, which is of great significance for guiding production.

This study utilised real-time CT scanning technology to dynamically observe and analyse the morphology, occurrence, and characteristics of condensate liquid during depletion and cyclic gas injection processes. The research findings are as follows:

(1) The formation of oil films during the condensation process of condensate gas flowing through rock pores, exhibiting phenomena like "wave flow" and "segmented flow" closely adhering to the inner walls of the pores, is a result of intermolecular gravitational forces.
(2) In the depletion exploitation experiment, when the pressure is reduced to 30 Mpa, the condensate oil saturation in the core is around 10%, mainly present in the fractures. After depletion, with cyclic gas injection, the condensate oil saturation can decrease by over 30%, with the most significant effect seen in the first gas injection, where the passive condensate oil mainly comes from the fractures. After three cycles of gas injection, the saturation of the condensed oil decreased by approximately 3%, 1%, and 0.5% respectively.
(3) In the cyclic gas injection experiment, with pressure restored to 40, 45, and 48 MPa respectively, the cumulative recovery of condensate oil reached 21.4%, 31.6%, and 34.9%, indicating a positive relationship between gas injection volume and

condensate oil recovery. However, once the injection volume exceeds the formation pressure, the increase in condensate oil recovery slows down.

(4) Comparing depletion exploitation and cyclic gas injection, cyclic gas injection significantly improves condensate oil recovery and reduces condensate oil damage to the reservoir. Factors such as fracture pattern, volume of gas injections, and recovery pressure are important factors influencing condensate oil recovery.

In future experimental and numerical simulation studies on condensate gas reservoirs, two key areas may require attention:

(1) Scale transformation: How to apply the condensate oil occurrence and flow laws obtained at the microscale to numerical simulations of gas reservoirs to guide the optimization of production schedule. The scale transformation issue is one of the unresolved challenges in oil and gas reservoir development.

(2) Many indoor experiments and mechanistic studies lag behind field practices. Therefore, it is essential to establish micro-scale numerical simulation methods. However, there are still many challenges in micro-scale numerical simulation work on fractured condensate gas reservoirs, such as how to realize the phase transition while flowing. The mass transfer laws between fractures and matrix under these conditions are not clear. Micro-scale numerical simulation of fractured condensate gas reservoirs is also a significant research direction.

Data availability statement

The original contributions presented in the study are included in the article/supplementary material, further inquiries can be directed to the corresponding author.

Author contributions

LZ: Data curation, Writing–original draft. LJZ: Data curation, Formal Analysis, Writing–original draft. YS: Data curation, Project administration, Writing–review and editing. XT: Conceptualization, Project administration, Writing–original draft. CL: Methodology, Project administration, Writing–review and editing. SW: Resources, Validation, Writing–review and editing.

Funding

The author(s) declare that financial support was received for the research, authorship, and/or publication of this article.

Conflict of interest

Authors LZ, LJZ, YS, and XT were employed by CNOOC Research Institute Co., Ltd.

The remaining authors declare that the research was conducted in the absence of any commercial or financial relationships that could be construed as a potential conflict of interest.

Publisher's note

All claims expressed in this article are solely those of the authors and do not necessarily represent those of their affiliated organizations, or those of the publisher, the editors and the reviewers. Any product that may be evaluated in this article, or claim that may be made by its manufacturer, is not guaranteed or endorsed by the publisher.

References

Abbasov, Z. Y., and Fataliyev, V. M. (2016). The effect of gas-condensate reservoir depletion stages on gas injection and the importance of the aerosol state of fluids in this process. *J. Nat. Gas Sci. Eng.* 31, 779–790. doi:10.1016/j.jngse.2016.03.079

Alarouj, M., Alomair, O., and Elsharkawy, A. (2020). Gas condensate reservoirs: characterization and calculation of dew-point pressure. *Petroleum Explor. Dev.* 47, 1091–1102. doi:10.1016/s1876-3804(20)60120-3

Dąbrowski, A. (2001). Adsorption — from theory to practice. *Adv. Colloid Interface Sci.* 93, 135–224. doi:10.1016/s0001-8686(00)00082-8

Dorhjie, D. B., Aminev, T., Mukhina, E., Gimazov, A., Babin, V., Khamidullin, D., et al. (2024). The underlying mechanisms that influence the flow of gas-condensates in porous medium: a review. *Gas Sci. Eng.* 122, 205204. doi:10.1016/j.jgsce.2023.205204

Faramarzi, N., and Sadeghnejad, S. (2020). Fluid and rock heterogeneity assessment of gas condensate reservoirs by wavelet transform of pressure-transient responses. *J. Nat. Gas Sci. Eng.* 81, 103469. doi:10.1016/j.jngse.2020.103469

Ganjdanesh, R., Yu, W., Fiallos, M. X., Kerr, E., Sepehrnoori, K., and Ambrose, R. (2019). "Gas injection EOR in eagle ford shale gas condensate reservoirs," in SPE/AAPG/SEG Unconventional Resources Technology Conference, Denver, Colorado, 22–24 July 2019, 4744–4759.

Guo, P., Liu, H., Wang, C., DU, J., Fan, B., Jing, M., et al. (2020). The determination of phase behavior properties of high-temperature high-pressure and rich condensate gases. *Fuel* 280, 118568. doi:10.1016/j.fuel.2020.118568

Hosseinzadegan, A., Raoof, A., Mahdiyar, H., Nikooee, E., Ghaedi, M., and Qajar, J. (2023). Review on pore-network modeling studies of gas-condensate flow: pore structure, mechanisms, and implementations. *Geoenergy Sci. Eng.* 226, 211693. doi:10.1016/j.geoen.2023.211693

Hu, X., Pu, L., Ran, A., Xie, J., Li, F., Cheng, Y., et al. (2024). Micro formation mechanism of oil–water inversion in reservoirs based on water film theory—an example from the Dawangzhuang Oilfield in Bohai Bay Basin. *Fuel* 359, 130501. doi:10.1016/j.fuel.2023.130501

Jiang, T. (2023). Study on the supercritical phase behavior of Yaha condensate gas reservoir in Tarim Basin. *Petroleum* 9, 390–394. doi:10.1016/j.petlm.2021.11.007

Jing, W.-L., Zhang, L., Li, A.-F., Zhong, J.-J., Sun, H., Yang, Y.-F., et al. (2023). Phase behavior of gas condensate in porous media using real-time computed tomography scanning. *Petroleum Sci.* 21, 1032–1043. doi:10.1016/j.petsci.2023.11.009

Kumar, A., Gohary, M. E., Pedersen, K. S., and Azeem, J. (2015) "Gas injection as an enhanced recovery technique for gas condensates," in A comparison of three injection gases. Abu dhabi international Petroleum Exhibition and conference.

Liu, X., Chen, H., Chen, Z., Yang, R., Song, L., Bai, M., et al. (2024). Study on characterization and distribution of four regions of tight sandstone condensate gas reservoirs in the depletion development process. *Fuel* 358, 130267. doi:10.1016/j.fuel.2023.130267

Long, K., Tang, Y., He, Y., Luo, Y., Hong, Y., Sun, Y., et al. (2024). Full-cycle enhancing condensate recovery-underground gas storage by integrating cyclic gas flooding and storage from gas condensate reservoirs. *Energy* 293, 130724. doi:10.1016/j.energy.2024.130724

Long, K., Tang, Y., He, Y., Wang, Y., Qin, J., and Tang, L. (2023). Fluid phase behavior during multi-cycle injection and production of underground gas storage based on gas-condensate reservoirs with oil rim. *Geoenergy Sci. Eng.* 226, 211769. doi:10.1016/j.geoen.2023.211769

Meng, X., and Sheng, J. J. (2016). Optimization of huff-n-puff gas injection in a shale gas condensate reservoir. *J. Unconv. Oil Gas Resour.* 16, 34–44. doi:10.1016/j.juogr.2016.09.003

Nabae, Y., Kawai, K., and Fukagata, K. (2020). Prediction of drag reduction effect by streamwise traveling wave-like wall deformation in turbulent channel flow at practically high Reynolds numbers. *Int. J. Heat Fluid Flow* 82, 108550. doi:10.1016/j.ijheatfluidflow.2020.108550

Nasriani, H. R., Borazjani, A. A., Iraji, B., and Moradidowlatabad, M. (2015). Investigation into the effect of capillary number on productivity of a lean gas condensate reservoir. *J. Petroleum Sci. Eng.* 135, 384–390. doi:10.1016/j.petrol.2015.09.030

Passoni, S., Ferrario, A., Ricotti, M. E., and Mereu, R. (2024). Experimental investigation of two-phase flow in Chevron-type compact plate heat exchangers: a Study on pressure drops and flow regimes visualization. *Appl. Therm. Eng.* 242, 122542. doi:10.1016/j.applthermaleng.2024.122542

Patmonoaji, A., Tsuji, K., and Suekane, T. (2020). Pore-throat characterization of unconsolidated porous media using watershed-segmentation algorithm. *Powder Technol.* 362, 635–644. doi:10.1016/j.powtec.2019.12.026

Reis, P. K. P., and Carvalho, M. S. (2022). Pore-scale analysis of gas injection in gas-condensate reservoirs. *J. Petroleum Sci. Eng.* 212, 110189. doi:10.1016/j.petrol.2022.110189

Salmani, N., Fatehi, R., and Azin, R. (2020). On the liquid condensate vertical migration near the production wells of gas-condensate reservoirs. *Eng. Sci. Technol. Int. J.* 23, 715–722. doi:10.1016/j.jestch.2020.03.006

Shi, J., Huang, L., Li, X., and Sepehrnoori, K. (2015). Production forecasting of gas condensate well considering fluid phase behavior in the reservoir and wellbore. *J. Nat. Gas Sci. Eng.* 24, 279–290. doi:10.1016/j.jngse.2015.03.033

Tang, Y., Long, K., Wang, J., Xu, H., Wang, Y., He, Y., et al. (2021). Change of phase state during multi-cycle injection and production process of condensate gas reservoir based underground gas storage. *Petroleum Explor. Dev.* 48, 395–406. doi:10.1016/s1876-3804(21)60031-9

Wang, H. S., Rose, J. W., and Honda, H. (2004). A theoretical model of film condensation in square section horizontal microchannels. *Chem. Eng. Res. Des.* 82, 430–434. doi:10.1205/026387604323050137

Wang, C., Yao, J., Huang, Z., Liu, F., and Yang, Y. (2024). Digital core reconstruction based on discrete element and Markov chain-Monte Carlo methods. *Geoenergy Sci. Eng.* 236, 212422. doi:10.1016/j.geoen.2023.212422

Wang, J., Luo, X., Xu, H., Jiang, H., and Nie, F. (2022). Phase behavior of condensate gas and CO2/CH4 re-injection performance on its retrograde condensation. *Arabian J. Chem.* 15, 104065. doi:10.1016/j.arabjc.2022.104065

Wang, Q. (2023). Origin of gas condensate reservoir in fuman oilfield, tarim basin, NW China. *Petroleum Explor. Dev.* 50, 1295–1307. doi:10.1016/s1876-3804(24)60467-2

Wang, S., Zuo, H., Gao, C.-N., Wang, J.-H., Congcong, L., and Wang, S. (2023). Characterization of differential markers among crude oil samples using UPLC-QE-MS/MS and multivariate statistical analysis. *Energy & Fuels* 37, 11017–11026. doi:10.1021/acs.energyfuels.3c02068

Yang, Y., Lun, Z., Wang, R., and Hu, W. (2020). Non-equilibrium phase behavior in gas condensate depletion experiments. *Fluid Phase Equilibria* 506, 112410. doi:10.1016/j.fluid.2019.112410

Zhang, A., Fan, Z., and Zhao, L. (2020). An investigation on phase behaviors and displacement mechanisms of gas injection in gas condensate reservoir. *Fuel* 268, 117373. doi:10.1016/j.fuel.2020.117373

frontiers | Frontiers in Earth Science

TYPE Original Research
PUBLISHED 04 July 2024
DOI 10.3389/feart.2024.1416308

OPEN ACCESS

EDITED BY
Shida Chen,
China University of Geosciences, China

REVIEWED BY
Yanjun Meng,
Taiyuan University of Technology, China
Jiang Han,
Yanshan University, China
Ang Liu,
The Pennsylvania State University (PSU), United States

*CORRESPONDENCE
Yan Zhang,
geozhangyan@outlook.com

RECEIVED 12 April 2024
ACCEPTED 11 June 2024
PUBLISHED 04 July 2024

CITATION
Zhang Y and Liu J (2024), *In-situ* geological conditions and their controls on permeability of coalbed methane reservoirs in the eastern Ordos Basin.
Front. Earth Sci. 12:1416308.
doi: 10.3389/feart.2024.1416308

In-situ geological conditions and their controls on permeability of coalbed methane reservoirs in the eastern Ordos Basin

Yan Zhang* and Jincheng Liu

[1]Research Institute of Petroleum Exploration and Development, PetroChina, Beijing, China

The eastern Ordos Basin plays an important role in China's coalbed methane (CBM) industry, boasting considerable CBM resources and pronounced reservoir heterogeneity, making it an ideal site for comparative research on deep and shallow CBM geology. In order to dissect the fundamental reasons for significant differences in production capacity between blocks and promote mutual learning from successful development experiences, this paper conducts a systematical study on the distribution characteristics of *in-situ* geological conditions of CBM reservoirs based on extensive well-testing data. Additionally, through coal permeability sensitivity experiments on coal samples with various $R_{o,\ max}$ values, burial depths, and initial permeabilities, this study explores the change law of permeability during the process of CBM extraction. The results indicate that as the burial depth of coal seam increases, so do the temperature, pressure, and stress. Moreover, the distribution of geothermal gradient, reservoir pressure gradient, horizontal stress gradient, and lateral pressure coefficient tends to converge with increasing burial depth, with a turning depth typically between 1,000 and 1,500 m. Coal seams below 1,500 m generally exhibit a normal-fault type stress field with normal-overpressure. *In-situ* permeability decreases with depth, but the permeability in deep stress relief zones can be maintained at a relatively high level. A lower initial permeability corresponds to a smaller stress sensitivity coefficient and reduced temperature sensitivity effects, resulting in slower permeability damage during CBM extraction. However, when the reservoir pressure drops to depletion pressure, the maximum damage rate of permeability increases significantly, underscoring the importance of reservoir reconstruction in deep CBM development. This study provides a theoretical basis for selecting favorable areas for CBM exploration and development, as well as for designing efficient development plans in practice.

KEYWORDS

eastern Ordos Basin, CBM reservoir, *in-situ* geological conditions, depth effect, permeability sensitivity

1 Introduction

Report on China oil and gas resource exploration and development in 2020 (Ministry of Natural Resources, PRC, 2020) shows that, as of the end of 2020, China's proven geological reserves of CBM were 7259.11 × 10^8 m^3, and the cumulative production of CBM reached 288.66×10^8 m^3, mainly from the Qinshui Basin and the eastern Ordos Basin. The development of shallow CBM in the Baode, Sanjiao, Liulin, and Hancheng blocks in the eastern Ordos Basin is relatively mature. In recent years, exploration and development work has gradually expanded to deep blocks such as Yanchuannan, Linxing, Daning-Jixian, Shenfu, and Shilou (Yang et al., 2022). However, the complexity of the geological environment of CBM reservoirs has caused significant differences in the development effects between blocks (Yan et al., 2021).

The *in-situ* geological environment of CBM reservoirs is mainly reflected in three aspects: stress, temperature, and fluid pressure. Based on the measurement data of reservoir stress in different regions, previous researchers have recognized that the lateral pressure coefficient (average horizontal principal stress/vertical stress) of the formation exhibits a clear regularity in the vertical direction (Brown and Hock, 1980; Zhao et al., 2007; Kang et al., 2009; Qin et al., 2012; Chen et al., 2018a; Kang et al., 2019; Fu et al., 2020). The stress field of shallow CBM reservoirs is mainly horizontal stress. Due to its proximity to the surface and high degree of structural development, the measurement results of stress are scattered, and the distribution range of lateral pressure coefficients is large. However, in deep CBM reservoirs, the principal stress gradually transitions to the vertical direction, and the lateral pressure coefficient continuously decreases and converges. As the burial depth increases, the pressure of CBM reservoirs generally shows an increasing trend (Liu et al., 2012; Milkov and Etiope, 2018; Fu et al., 2020). On the one hand, increasing depth and stress can lead to a decrease in pore volume compression, but due to a certain fluid content, it can cause an increase in reservoir fluid pressure (Zhong, 2003). On the other hand, the pressure of the reservoir is also related to the mineralization degree of groundwater. Generally, the higher the mineralization degree, the greater the static water pressure gradient, and the greater the pressure of the CBM reservoir (Wu et al., 2007). The difference in groundwater head height can also cause changes in reservoir pressure and its pressure gradient by controlling the direction of water flow. Generally, the lower the head height, the smaller the pressure gradient, and the lower the reservoir pressure (Zhang and Tang, 2001; Jing, 2012). Qin et al. (2012) analyzed the fluid dynamics characteristics of the Shanxi and Taiyuan formations in the eastern part of the Ordos Basin and found that due to differences in rock permeability, the pressure system of deep CBM reservoirs is significantly controlled by sedimentary frameworks, often having relatively independent gas and pressure systems. At the same time, coal seam temperature is widely believed to have a linear positive correlation with burial depth (Liu, 2006; Wu et al., 2013; Zhao et al., 2019; Fu et al., 2020). However, some scholars have pointed out that the relationship between ground temperature and burial depth is much more complex than a linear relationship (Chapman et al., 1984). In addition to burial depth, multiple factors can affect reservoir temperature (Xiao et al., 2009), and ground temperature cannot be calculated solely by depth (Gan et al., 2019).

As a reservoir mainly composed of organic matter, coal seams are more sensitive to stress, pressure, and temperature than conventional "inorganic" reservoirs. Under the influence of high stress and formation temperature, the geological conditions of deep CBM reservoirs are more complex (Chen et al., 2018b; Salmachi et al., 2021). The permeability of coal seams is an important indicator for the optimization of CBM exploration and development areas, and the extremely low permeability of deep coal seams is currently the key obstacle to the exploitation and utilization of deep CBM resources (Ranathunga et al., 2014). The permeability of CBM reservoirs is influenced by multiple factors such as stress, reservoir pressure, and temperature (Li et al., 2012; Song et al., 2013). Among them, the tectonic stress field is the dominant factor in the permeability of coal seams. The ancient tectonic stress field determines the formation and development of fractures, while the current tectonic stress field determines the closure degree of fractures (Bell, 2006; Chatterjee et al., 2019). Some scholars have found that with the increase of effective stress, the permeability of coal seams decreases exponentially (Dabbous et al., 1974; Karacan and Okandan, 2001). However, some scholars hold different views and explain the overall law of dynamic changes in permeability. They believe that during the elastic-plastic strain stage, as stress increases, fresh microcracks will continue to develop in coal, and permeability will continue to improve; The closer to the peak stress, the greater the generation of microcracks, which are interconnected and have a sharp increase in permeability; After reaching the peak strength, the coal rock loses its maximum bearing capacity, and the permeability continues to increase, but the growth rate slows down; When the elastic deformation reaches a certain level, the permeability reaches its minimum value, and the maximum permeability occurs during the softening or plastic flow stage (Harpalani and Chen, 1992; Li et al., 2001; Wang et al., 2018). It can be seen that the *in-situ* stress control effect of CBM reservoir permeability characteristics still needs further research, but it can be affirmed that as the burial depth increases, the anisotropy of stress state will gradually increase its impact on coal seam permeability, which needs to be paid attention to (Paul and Chatterjee, 2011; Reisabadi et al., 2021).

The effect of temperature on coal seam permeability is also a focus of attention for scholars. The control effect of coal seam temperature on permeability is mainly reflected in two aspects: on the one hand, as the temperature increases, the coal body continuously expands, the methane migration channels decrease, and the gas phase permeability also continuously decreases; On the other hand, methane viscosity decreases with increasing temperature, flow resistance decreases, and gas-phase permeability increases accordingly (Cheng et al., 1998; Yang et al., 2005a; Pan and Connell, 2011; Liu et al., 2021). Some scholars believe that temperature has a certain negative effect on permeability as a whole, but this negative effect is only more obvious when the stress level is low, and gradually weakens with increasing stress (Yang and Zhang, 2008; Gao, 2019). Moreover, the temperature sensitivity of permeability in CBM reservoirs of different coal ranks is different and generally weakens with increasing coal ranks (Wu et al., 2017).

The eastern Ordos Basin is a hot area for CBM exploration and development, with diverse geological conditions, providing an excellent platform for comparative research. At present, due

to the lack of core sampling and testing data of deep wells, the study of differences between blocks is still chaotic, and the permeability controlling mechanism of CBM reservoirs is not yet clear, making it difficult to learn from successful development experiences. Based on the analysis of drilling and well testing data during the exploration and development of CBM, this study determines the distribution characteristics of *in-situ* temperature, pressure, stress, and permeability, as well as explores the stress/temperature sensitivity and depth effect of permeability through coal permeability sensitivity experiments.

2 Geological setting

The Ordos Basin is located in the western part of the North China Plate in China and is a typical large-scale superimposed basin with stable craton margins. The overall shape is rectangular with a north-south distribution, and the terrain and structural complexity continuously decrease from the basin edge to the inside of the basin. The entire basin is composed of six primary tectonic units (Figure 1A). The eastern Ordos Basin is mainly located in the Jinxi Flexural Belt (Wang et al., 2010), transitioning to the Yishan Slope on the west side, and bordered by the Lishi Fault on the east, adjacent to the Shanxi Platform. Spanning 500 km from north to south and with a width of 40–60 km from east to west, the basin covers an area of 2.7×10^4 km^2. It exhibits a monocline structure with a high eastern side and a low western side, with a dip angle of 2°–3°. The CBM work area in eastern Ordos Basin is divided into ten major blocks from north to south based on the structural pattern, namely,: Baode, Shenfu, Linxing (East/Central/West), North Sanjiao, Sanjiao, Liulin, Shilou (North/West/South), Daning-Jixian, Yanchuannan, and Hancheng blocks (Figure 1B).

The Carboniferous-Permian coal-bearing strata in the eastern Ordos Basin have undergone four tectonic changes since sedimentation, including the Hercynian, Indosinian, Yanshanian, and Himalayan periods (Li and Zhang, 2020) (Figure 1C). In the Hercynian period, the North China ancient plate entered a slow subsidence stage and began to receive sedimentation. The coal-bearing strata of the Carboniferous-Permian marine-continental transition phase was formed as a result (310–280 Ma). By the end of the Late Permian, the burial depth of the top surface of the Taiyuan Formation increased from north to south, ranging from 200 to 1,200 m. From the early Triassic to the end of the late Triassic, the subsidence rate of the strata increased sharply, and the subsidence depth of the strata showed a nearly linear increase. The subsidence rate was relatively stable, and the ancient temperature also rapidly increased, leading to differences in the degree of coal metamorphism. In the Indosinian movement, the strata experienced slight uplift and subsidence fluctuations. By the end of the Middle Jurassic, the top surface of the Taiyuan Formation reached its maximum burial depth, distributed from north to south within the range of 1,600–3,600 m. Due to differences in burial depth, the temperature difference between the north and south regions reached 80°C (Li and Zhang, 2020). The Yanshan Movement has significant implications for the evolution of tectonic morphology in the eastern margin. At the end of the Early Cretaceous, the crust rapidly uplifted, ending the sedimentation of the depression basin. The overlying strata suffered from strong weathering and erosion, continuous thinning, and greater uplift at the edge of the basin. During the Himalayan period, the subsidence and uplift amplitude of the coal seam are relatively small. According to the lithological combination, the Carboniferous Permian strata in the eastern Ordos Basin were divided from bottom to top into the Benxi Formation, Taiyuan Formation, Shanxi Formation, Lower Shihezi Formation, and Upper Shihezi Formation with multiple sets of coal seams developed in Taiyuan and Shanxi formations (Chen, 1989) (Figure 2). The coalification process in the eastern Ordos Basin is mainly characterized by deep metamorphism, except for the Zijinshan area, and the degree of coal metamorphism is increasing from north to south as a whole (Li and Zhang, 2020).

3 Materials and methods

3.1 *In-situ* parameters acquisition

In-situ parameters including temperature, pressure, stress and permeability are mainly derived from injection/pressure drop well testing reports. The data obtained from hydraulic fracturing in Central Linxing Block is limited, which is not enough to characterize the difference in regional stress fields. Therefore, log data are used to inversion the *in-situ* stress in the Central Linxing Block. For detailed steps of the two methods, please refer to Pu et al. (2022).

3.2 Coal permeability sensitivity experiment

Eleven coal samples with various $R_{o,\,max}$ values, burial depths, and initial permeabilities were selected from different blocks of the eastern Ordos Basin, including Central Linxing, Liulin, Yanchuannan, and Hancheng, for comparative analysis of the stress and temperature sensitivity of coal permeability. The basic information of the coal samples is shown in Table 1. The instrument used in this experiment is the AP-608 automated permeameter-porosimeter produced by CoreTest in the United States. Permeability measurement is based on the unsteady-state pressure decay method. The confining pressure is loaded through Hassler type/hydrostatic pressure, with a variation range of 500–9,500 psi, which is 3.45–65.5 MPa. To measure permeability, a pressure pulse within the range of 100–250 psi (0.67–1.72 MPa) is sent through the sample. The instrument has a pressure sensor accuracy of ±0.1%, and the measurement range for permeability is 0.001–10000 mD. The testing gas source uses high-purity helium gas.

In order to investigate the impact of stress on coal permeability, we employed changes in net confining pressure to simulate variations in effective stress within the coal seam. Subsequently, the coal permeability was measured in relation to changes in net confining pressure, and the relationship between permeability and effective stress was analyzed. The pressure of the CBM reservoirs in the Liulin and Hancheng districts is within the range of 2.2–9.9 MPa and 4.1–11.9 MPa, respectively, with a maximum value not exceeding 12 MPa. In order to better reflect the dynamic change process of coal seam permeability with the increase of effective

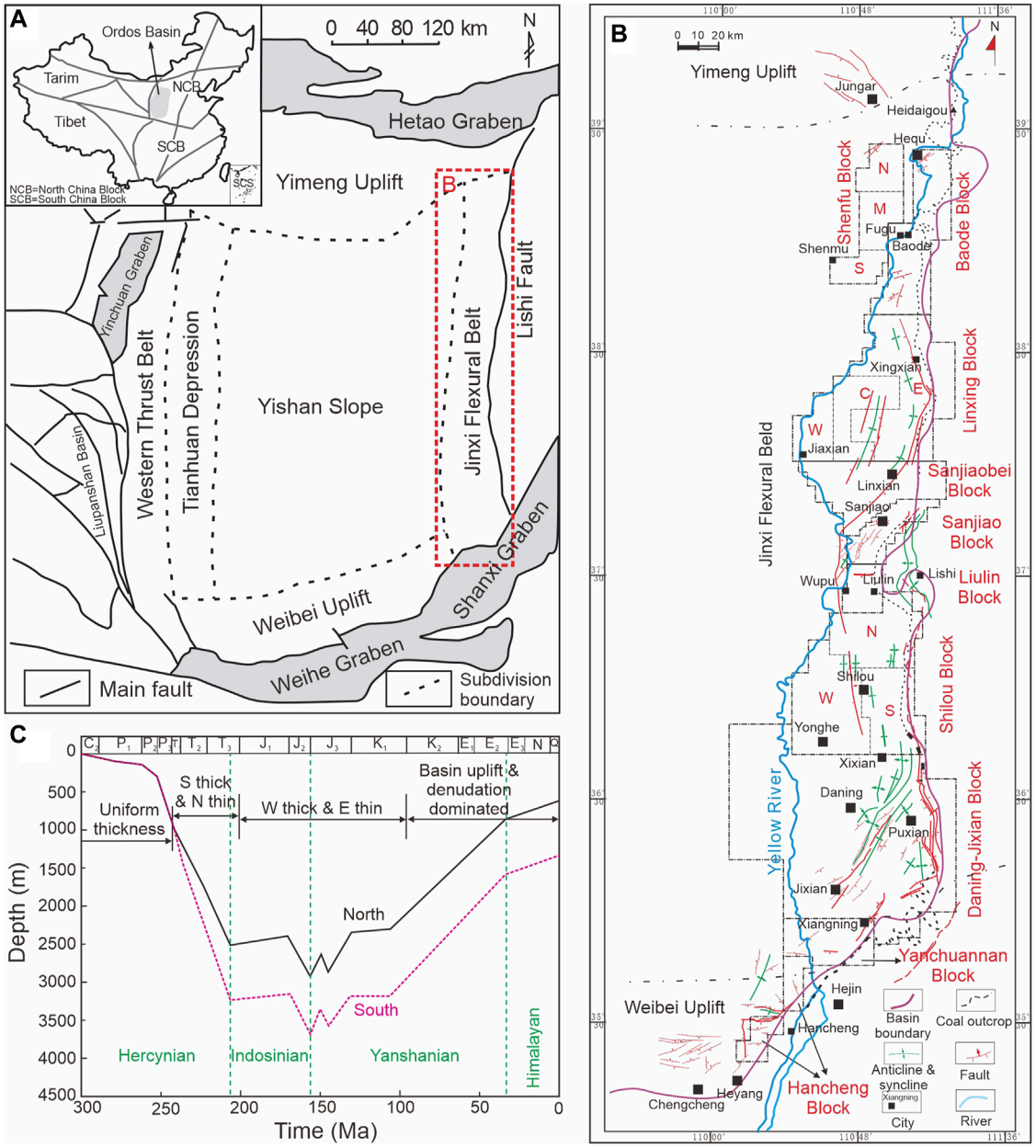

FIGURE 1
Geological map of the eastern Ordos Basin **(A)** Tectonic location; **(B)** Schematic map of CBM block zoning; **(C)** Schematic diagram of differential tectonic evolution (modified from Li and Zhang (2020)).

stress in the process of CBM drainage in the Liulin and Hancheng blocks, the experimental confining pressure range is 3.45–12 MPa, and a total of 4 pressure points of 3.45, 6, 9, and 12 MPa are set. For the Linxing and Yanchuannan samples with deeper burial depth, due to their reservoir pressure reaching up to 21.22 MPa, the testing pressure range is set to 3.45–25 MPa, and a total of 6 pressure points of 3.45, 5, 10, 15, 20, and 25 MPa are set. In addition, due to the temperature of deep CBM reservoirs reaching 60°C, exploring the effect of temperature on the permeability of CBM reservoirs is also of great significance. Therefore, in addition to the above tests conducted at room temperature (20°C), temperature sensitivity tests were conducted on the Lin 1 and Yan 1 samples, with two additional experimental control groups of 40°C and 60°C added.

4 Results and discussion

4.1 *In-situ* geological conditions

4.1.1 Geotemperature field

The temperature conditions of coal seams directly affect the adsorption, desorption, and production processes of CBM. Therefore, revealing the *in-situ* temperature conditions of the coal

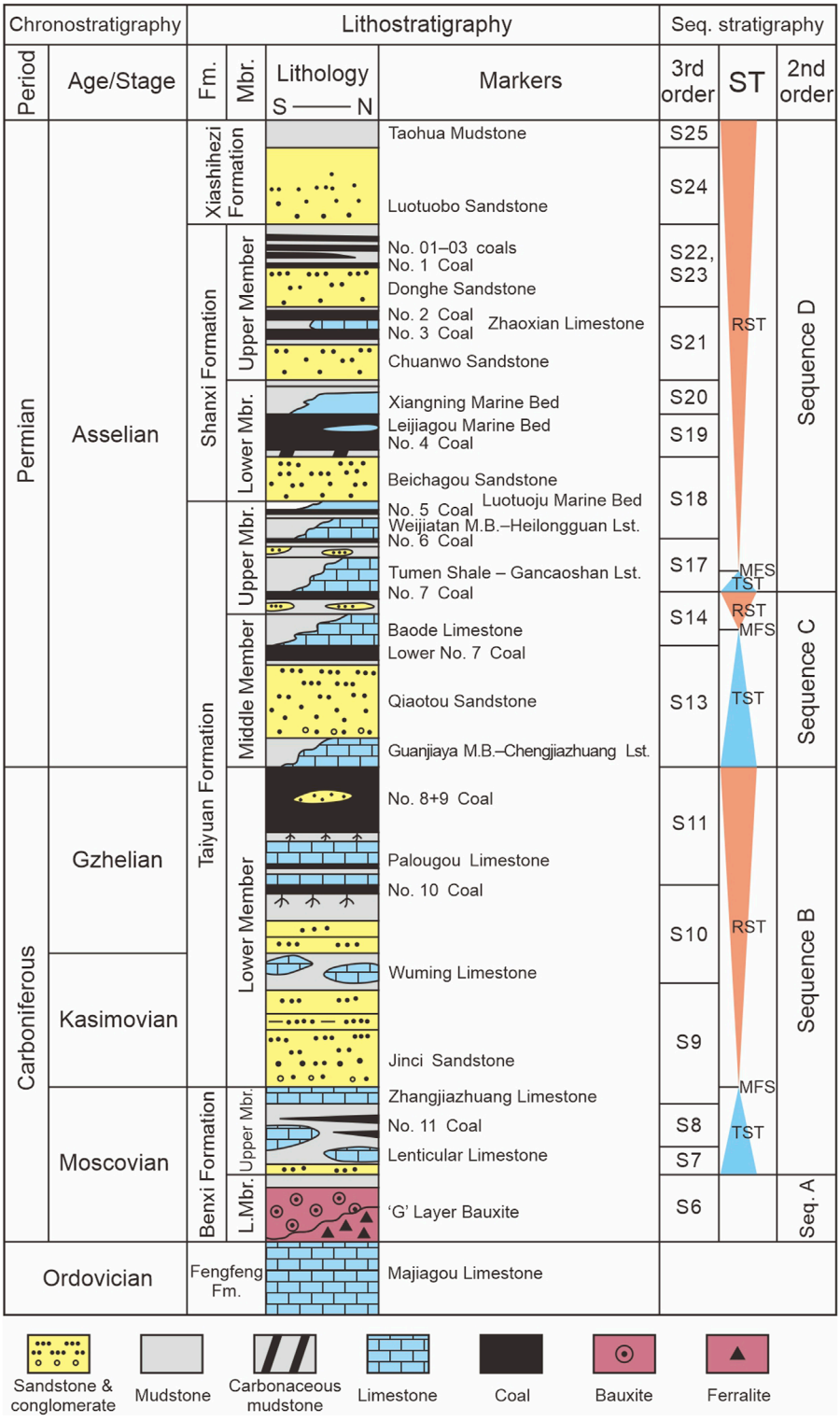

FIGURE 2
Composite stratigraphic column of the Permo-Carboniferous coal-bearing strata in the eastern Ordos Basin (chronostratigraphy from Shen et al. (2022), petrostratigraphy from Chen (1989), sequence stratigraphy from Liu, (2020)). Abbreviations: ST—systems tracts; TST—transgressive systems tract; RST—regressive systems tract; MFS—maximum flooding surface.

seams in the eastern Ordos Basin is a prerequisite for conducting in-depth theoretical research on deep/shallow CBM. The temperature of strata may be influenced by multiple factors such as burial depth, lithology, structural conditions, magmatic activity, groundwater dynamic conditions, and the thickness of Cenozoic loose layers (Tan et al., 2009; Liu et al., 2012; Zhang, 2012; Wu et al., 2013;

TABLE 1 Basic information of the coal samples in coal permeability sensitivity experiment.

Block	No.	Depth (m)	$R_{o,max}$ (%)	Initial permeability (mD)	Stress sensitivity coefficient ($^{-1}$MPa)	Maximum damage rate of permeability (%)
Cental Linxing	Lin 1	1873	1.38	0.0432	0.102	87.55
	Lin 2	1,631	1.23	0.2358	0.135	94.21
	Lin 3	1,588	1.16	0.3903	0.127	92.23
Liulin	Liu 1	546	1.29	1.8214	0.226	84.95
	Liu 2	661	1.32	1.9702	0.193	80.37
	Liu 3	982	1.25	0.1236	0.240	86.66
Yachuannan	Yan 1	1,395	2.32	0.0659	0.160	96.59
	Yan 2	1,072	2.01	0.5093	0.128	93.58
	Yan 3	1,233	2.18	0.1501	0.172	97.55
Hancheng	Han 1	709	1.9	0.4891	0.206	82.48
	Han 2	634	1.85	2.2453	0.285	91.31

Békési et al., 2020; Jiang et al., 2020). Among them, burial depth is considered the most important influencing factor. Most scholars have found through data statistics that coal seam temperature shows a linear increasing trend with increasing burial depth (Peng et al., 2017; Li et al., 2018; Békési et al., 2020), while geothermal gradient is dispersed in the shallow part of the formation and concentrated in the deep part (Yuan et al., 2009; Peng et al., 2017; Li et al., 2018). By statistically analyzing the temperature and geothermal gradient of CBM reservoirs in different areas of the eastern Ordos Basin, and plotting their relationship with the burial depth of coal seams (Figure 3), a similar pattern was found: the shallower of the coal seam, the lower the temperature of the CBM reservoir, and the wider the range of geothermal gradient changes. For example, coal seams shallower than 648 m have a maximum temperature of no more than 40°C, but their geothermal gradient changes in the range of 0.62°C–4.93°C/100 m. This indicates that the shallower the burial depth of the coal seam, the more complex the geological factors that affect the temperature of its reservoir (Lu et al., 2013); The deeper the coal seam is buried, the more stable the geological conditions are, the more significant the dominance of depth on reservoir temperature, and the stronger the linear correlation between the two. On the plane, the West Linxing Block with the deepest coal seam has the highest reservoir temperature, followed by the Central Linxing Block, with the highest reservoir temperatures reaching over 60°C. The average geothermal gradient shows a gradually increasing trend from north to south (Table 2).

4.1.2 Reservoir pressure field

The definition of CBM reservoir pressure is the pressure acting on the fluid inside the pores and fractures. It not only controls the adsorption-desorption ability of coal seams to methane and other gases but also serves as the driving force for the transportation and production of CBM (Fu et al., 2001; Yang, 2015). Li et al. (2004) found through analysis of well-testing data from 151 coal seams in China that due to a series of factors such as complex geological structure evolution, strong stratigraphic uplift and erosion, poor coal seam permeability, complex stress conditions, and variable hydrogeological conditions, CBM reservoirs are mainly under-pressure reservoirs. Regarding the relationship between CBM reservoir pressure and its gradient with burial depth, it is generally believed that there is a linear positive correlation between reservoir pressure and burial depth (Xu et al., 2010; Zhao et al., 2016; Guo et al., 2020), while the pressure gradient of CBM reservoirs has a characteristic of gradually converging from discretization as burial depth increases from shallow to deep (Qin and Shen, 2016; Chen et al., 2018a). This study collected 192 well-testing reservoir pressure data points from 13 different blocks in the eastern Ordos Basin and found similar patterns with a certain uniqueness. As shown in Figure 4, there is a good linear correlation between the CBM reservoir pressure from 427 to 2,195 m and the burial depth (R^2=0.7847), which is mainly because the pore volume compression degree and groundwater mineralization degree are higher and the water head height is lower as the depth increases (Zhong, 2003; Wu et al., 2007; Jing, 2012). However, it should be noted that within the depth range of 1,300–1,500 m, the pressure of the CBM reservoir is relatively low. As for the relationship between reservoir pressure gradient and depth, it is more complex. At depths below 1,300 m, it exhibits the characteristic of "large interval span", ranging from 0.314 to 1.25 MPa/100 m. Within the range of 1,300–1,500 m, it exhibits obvious "under-pressure" characteristics, ranging from 0.321 to 0.8

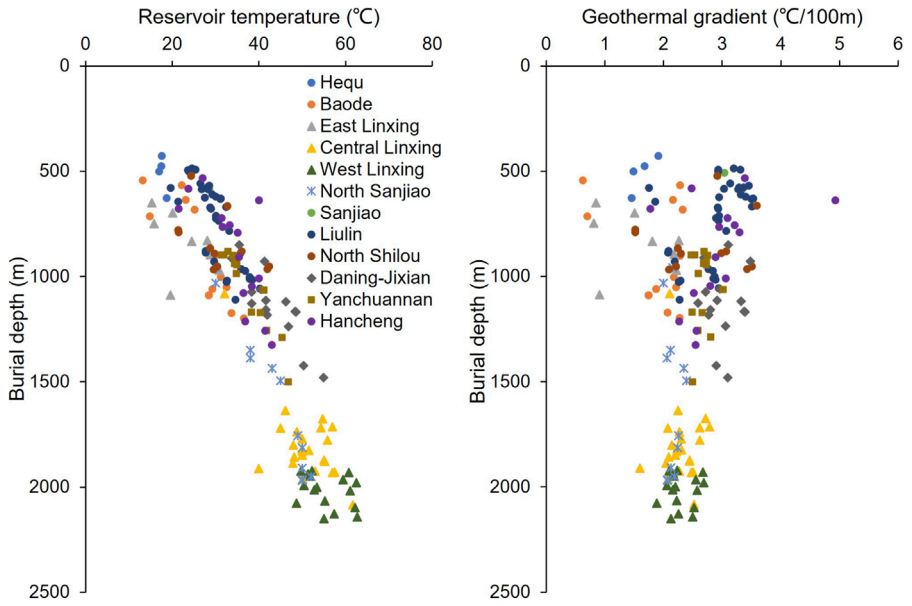

FIGURE 3
The variation law of reservoir temperature and geothermal gradient of CBM reservoirs in different areas of the eastern Ordos Basin with burial depth.

MPa/100 m. Within the range of 1,500–2,200 m, it exhibits obvious "normal to overpressure" characteristics, ranging from 0.706 to 1.169 MPa/100 m.

4.1.3 Stress field

Stress not only determines the degree of development and closure of coal seam fractures but also controls the shape and direction of fracturing fractures, thus playing an important role in controlling the permeability of CBM reservoirs (Kang et al., 2010; Meng et al., 2010; Kang et al., 2017). The gravity effect and tectonic movement are the main reasons for the formation of the stress field, with horizontal tectonic changes having the greatest impact on the distribution characteristics of the stress field (Zoback et al., 2003; Zhao et al., 2007; Ju et al., 2018). In addition, the changes in the *in-situ* stress field of different types of rocks are generally determined by the differences in the internal characteristics (composition, structure, mechanical properties, etc.) (Ward, 2016; Weniger et al., 2016; Mukherjee et al., 2021) and external environment (burial depth, temperature, pressure, etc.) of the rocks (Bell, 2006; Burra et al., 2014). Generally speaking, the *in-situ* stress increases with the increase of the Young's modulus of the rocks. In terms of horizontal stress, magmatic rocks are higher, followed by metamorphic rocks, and sedimentary rocks are generally lower (Zhu and Tao, 1994). As an organic matter aggregate with lower mechanical strength, CBM reservoirs have a lower minimum horizontal principal stress than other sedimentary rocks (Meng et al., 2011). In addition, various geological structures such as faults, folds, and collapse columns are widely developed in coal-bearing strata, and their stress heterogeneity is significant. According to the different directions of stress, stress can be divided into maximum horizontal principal stress (σ_h), minimum horizontal principal stress (σ_H), and vertical principal stress (σ_v).

Through a large amount of statistical analysis of the stress data obtained from well testing parameters and the stress data obtained from logging inversion, it was found that in addition to vertical stress, the maximum and minimum horizontal principal stresses also increase with increasing burial depth (Figure 5), which is similar to previous research results (Xu et al., 2016; Zhao et al., 2016; Chen et al., 2017; Chen et al., 2018b; Ju et al., 2021). Among them, the linear relationship between the minimum horizontal principal stress and the burial depth of the coal seam is more significant than that of the maximum horizontal principal stress. The correlation coefficient R^2 of the former is 0.8336, and the correlation coefficient R^2 of the latter is 0.6356. In the vertical direction, there is a transition surface around 1,500 m. That is, at depths smaller than 1,500 m, the relation between the maximum horizontal principal stress and the vertical stress is uncertain, while at depths more than 1,500 m, the maximum horizontal principal stress is smaller than the vertical stress. According to the magnitude of the minimum horizontal principal stress, the stress levels of CBM reservoirs at different depths can be divided into four categories, including low-stress areas ($0 < \sigma_h < 10$ MPa), medium-stress zone ($10 < \sigma_h < 18$ MPa), high-stress zone ($18 < \sigma_h < 30$ MPa), and ultra-high stress zone ($\sigma_h > 30$ MPa). Therefore, coal seams buried at depths of 500–1,000 m are mostly low to medium stress, coal seams buried at depths of 1,000–1,500 m are mostly medium to high stress, and coal seams buried below 1,500 m are mostly high to ultra-high stress. As shown in Figure 6, both the maximum and minimum horizontal principal stress gradient changes exhibit the characteristics of "strong dispersion in the shallow and strong convergence in the deep". This indicates that the shallower the coal seam is buried, the greater the influence of geological tectonic conditions on the stress field, and the more severe the differentiation of the minimum and maximum horizontal principal stress gradients. At depths of over 1000m, the minimum and maximum horizontal

TABLE 2 *In-situ* geological parameters of CBM reservoirs in different blocks in the eastern Ordos Basin.

Parameters	Hequ	Baode	East Linxing	Central Linxing	Liulin	North Shilou	Daning-Jixian	Yanchuanan	Hancheng
Depth (m)	4,27–627 508	542–1,173 791	699–1,087 839	1,069–2,161 1879	486–1,110 730	521–967 843	849–1,481 1,137	881–1,501 1,095	532–1,325 887
Reservoir Pressure (Ma)	2.7–4.6 3.3	2.6–11.8 6.2	5.1–9.3 6.9	9.43–21.22 16.5	2.2–9.9 6.0	3.8–9.9 7.3	4.6–12.1 8.3	2.8–10.6 6.3	4.1–11.9 7.3
Pressure Gradient (MPa/100 m)	0.60–0.78 0.68	0.47–0.98 0.76	0.73–0.91 0.84	0.83–1.02 0.96	0.41–1.12 0.82	0.74–1.13 0.87	0.32–0.98 0.75	0.31–0.86 0.55	0.48–1.14 0.79
σ_h (MPa)	4.0–8.8 6.9	8.2–22.1 11.7	9.8–20.8 13.4	14.32–41.39 29.08	5.8–20.9 13.75	11.2–20.8 16.5	14.7–24.1 19.7	9.0–23.2 15.3	10.0–31.9 17.6
Gradient of σ_h (MPa/100 m)	0.94–1.97 1.44	1.18–2.06 1.53	1.27–2.19 1.62	1.17–1.98 1.55	1.19–2.98 1.95	1.42–2.37 1.99	1.33–1.89 1.65	0.98–1.90 1.40	1.03–2.45 1.89
σ_H (MPa)	4.1–14.5 9.7	8.8–31.4 15.9	11.4–31.9 18.3	18.72–58.16 36.82	3.63–32.8 20.46	13.0–32.3 24.5	22.1–40.5 30.0	9.5–37.2 21.6	9.3–53.3 26.2
Gradient of σ_H (MPa/100 m)	0.97–3.24 2.04	1.24–3.02 2.11	1.41–3.35 2.23	1.39–2.81 1.96	0.74–4.78 2.90	1.52–3.68 2.95	1.90–2.92 2.49	1.07–3.00 1.97	1.23–4.99 2.96
Reservoir temperature (°C)	17.0–18.7 17.7	13.2–36.5 24.3	15.3–30.9 22.9	32.1–62.5 52.2	19.6–40.2 30.0	21.4–42.35 31.2	33.7–54.9 43.5	31.5–46.8 37.4	21.5–43.0 34.3
Gradient of temperature (°C/100 m)	1.46–1.91 1.64	0.62–2.33 1.88	0.81–2.26 1.57	1.59–2.79 2.31	1.75–3.53 2.88	1.52–3.51 2.62	2.58–3.48 3.01	2.48–3.02 2.66	1.78–4.93 2.92

10.3389/feart.2024.1416308

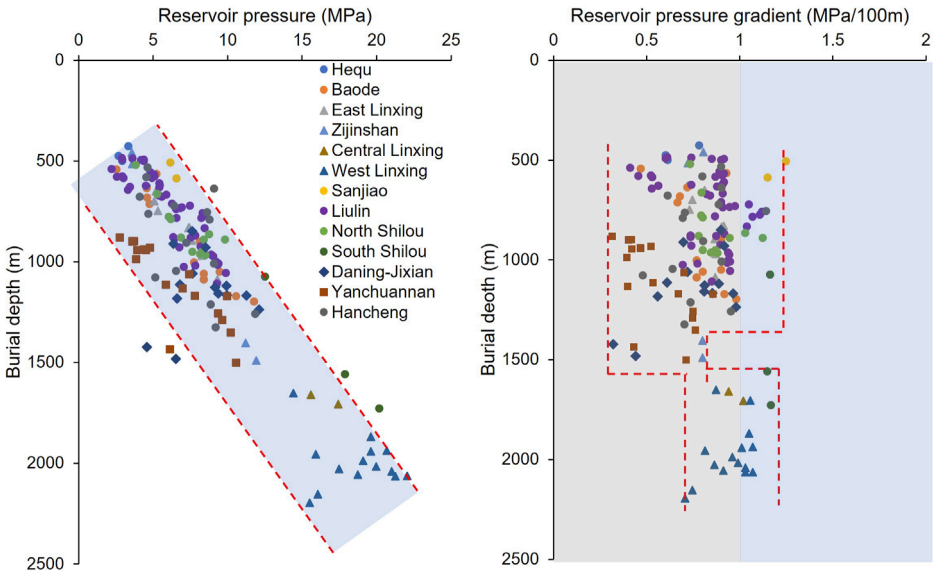

FIGURE 4
The variation law of CBM reservoir pressure and reservoir pressure gradient with burial depth in the eastern Ordos Basin.

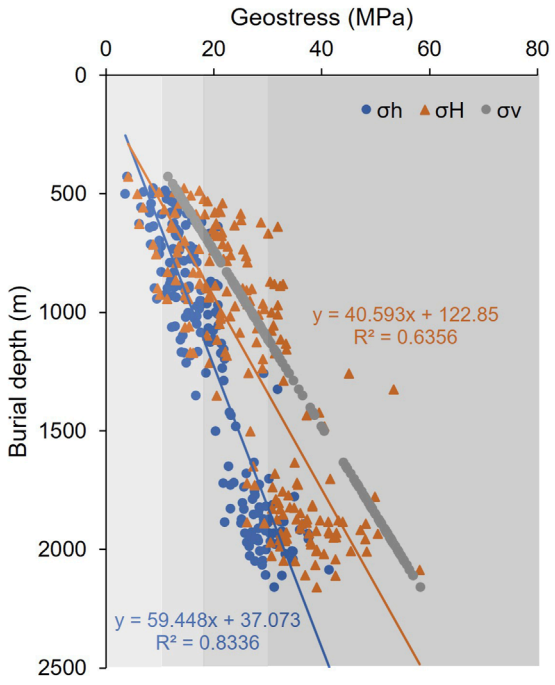

FIGURE 5
The variation law of coal seam stress with burial depth in the eastern Ordos Basin.

principal stress gradients decrease to below 2 MPa/100m and 3 MPa/100m, respectively.

Regarding the variation of lateral pressure coefficient (the ratio of average horizontal principal stress to vertical stress), Brown and Hock (1980) summarized the relationship between lateral pressure coefficient and coal seam burial depth through a large amount of stress data from different regions around the world. That is, the lateral pressure coefficient of shallow coal seams is higher, and the variation range is larger, and as the burial depth increases, both the lateral pressure coefficient and the variation range continuously decrease. The above characteristics indicate that the shallow CBM reservoir is mainly dominated by horizontal stress, while the direction of the main stress in the deep CBM reservoir gradually changes to vertical. Zhao et al. (2007) drew inspiration from Hoek and Brown's stress research method and fitted a regression curve between China's lateral pressure coefficient and burial depth. They compared it with Hoek and Brown's global stress statistical regression curve, showing that China's stress has a similar vertical evolution law to the world's, and pointed out that the critical depth is around 1,000 m. This study found that the lateral pressure coefficient of CBM reservoirs in the eastern Ordos Basin shows a characteristic of "dispersion at shallow and convergence at deep" in the vertical direction and is overall above the Chinese average line and the Hoek and Brown's average line, that is, the lateral pressure coefficient of coal seams is smaller under the same burial depth conditions, which is largely related to the lower mechanical strength of coal rock compared to other rock layers (Figure 7). In addition, there is a transition interface between the lateral pressure coefficient and the depth of the coal seam, with a wide distribution range of lateral pressure coefficients ranging from 0.31 to 1.53 below 1,000 m; At depths of 1,000 m or more, the lateral pressure coefficient is generally less than 1.

The relative magnitude of σ_v, σ_h, and σ_H can reflect different *in-situ* stress mechanisms. Where $\sigma_v > \sigma_H > \sigma_h$ represents the normal fault stress mechanism, that is, overlying gravity load dominates; $\sigma_H > \sigma_v > \sigma_h$ represents the mechanism of reverse fault stress and $\sigma_H > \sigma_h > \sigma_v$ represents the mechanism of strike-slip fault stress, representing two forms of structural compression in different directions. Figure 8 shows the stress field types of different blocks in the eastern Ordos Basin. The Hequ, Baode, East Linxing, and

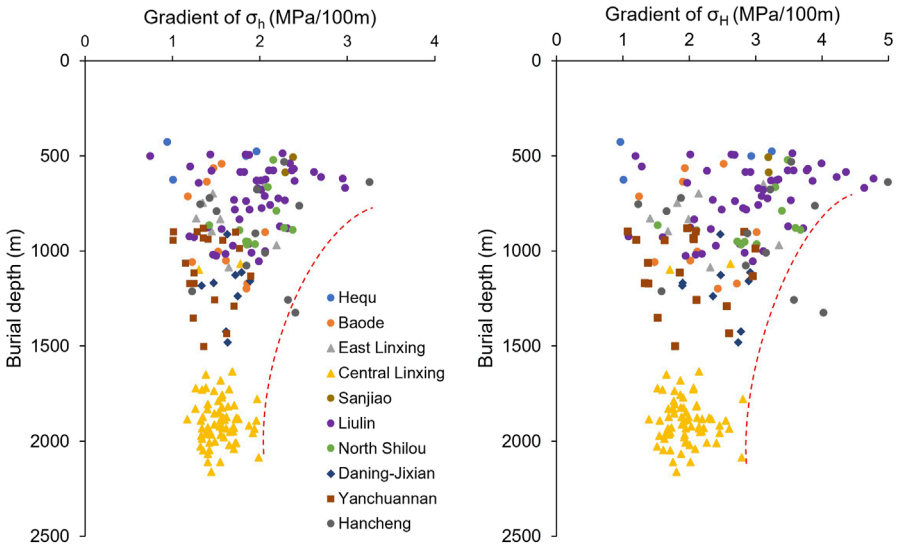

FIGURE 6
Variation law of minimum/maximum horizontal principal stress gradient with burial depth in the eastern Ordos Basin.

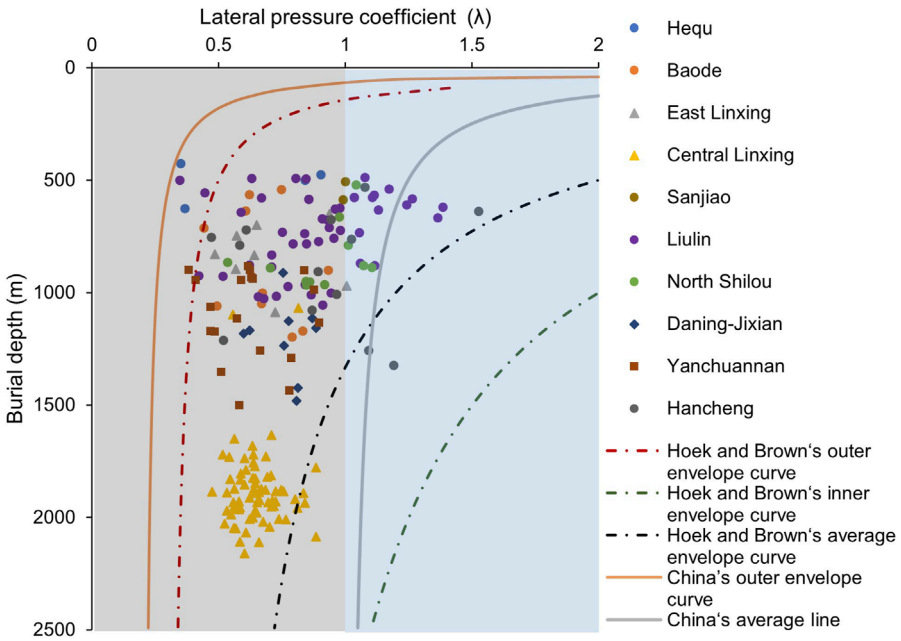

FIGURE 7
Vertical evolution of lateral pressure coefficient of CBM reservoir in the eastern Ordos Basin.

Central Linxing blocks show $\sigma_v > \sigma_H > \sigma_h$ type stress field as a whole. The reason is that Hequ, Baode, and Linxing Dong were affected by the NW-SE stretching and developed a series of northeastward normal faults (Chen et al., 2014) during the Himalayan period, while the coal seam in central Linxing Block was buried too deep and the structure was relatively stable. In Sanjiao, Liulin, and North Shilou blocks in central China, 62.90% of the CBM reservoirs exhibit $\sigma_H > \sigma_v > \sigma_h$ type stress field, 33.87% exhibit $\sigma_v > \sigma_H > \sigma_h$ type, and 3.23% exhibit $\sigma_H > \sigma_h > \sigma_v$ type, indicating that the stress mechanism of inverse fault is dominant and that of normal fault is supplemented. To the Daning-Jixian, and Yanchuannan blocks, the stress state transitioned to the normal fault stress mechanism ($\sigma_v > \sigma_H > \sigma_h$), with local reverse fault stress mechanism ($\sigma_H > \sigma_v > \sigma_h$). To the southernmost Hancheng Block, the stress state of CBM reservoir is again transformed into the reverse fault type compressive stress field, that is, $\sigma_H > \sigma_v > \sigma_h$, which is

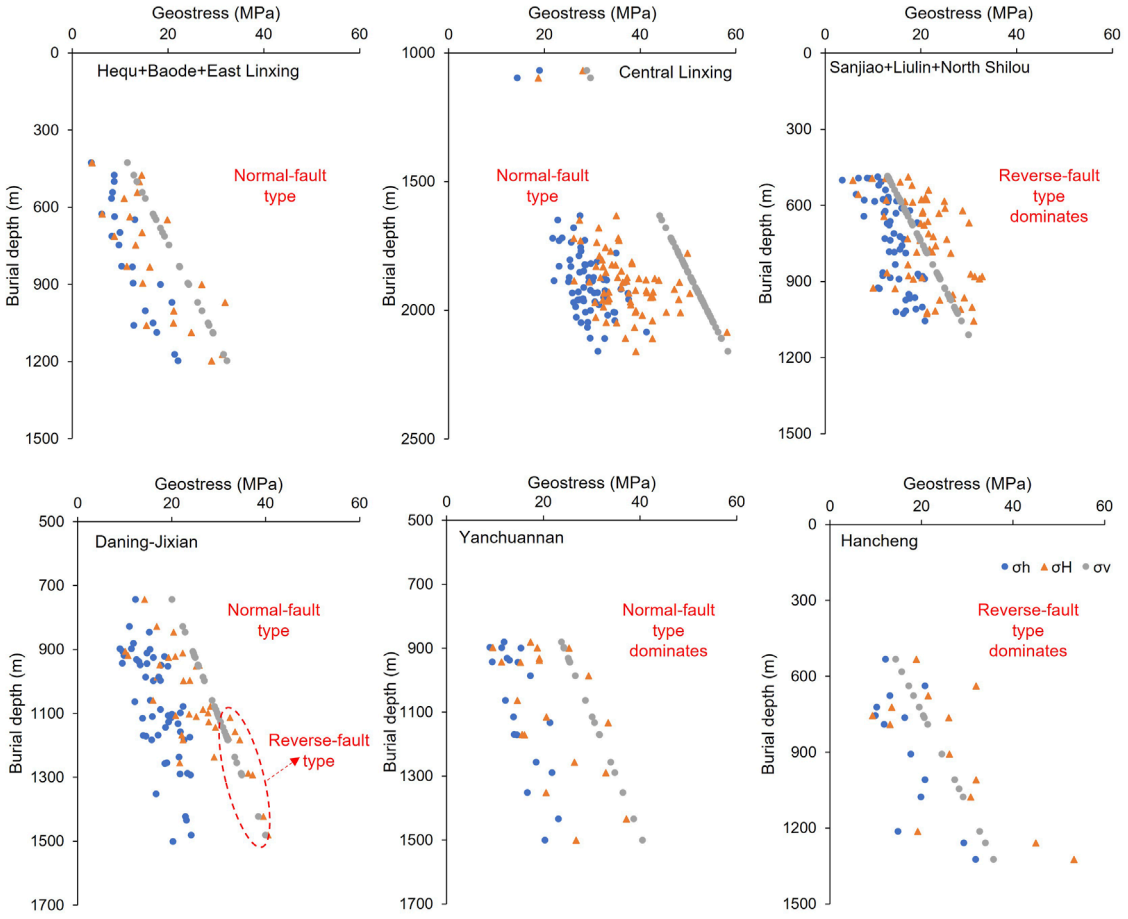

FIGURE 8
Stress field types of different blocks in the eastern Ordos Basin.

consistent with the structural density. On the whole, the stress fields of three deep blocks, including central Linxing, Daning-Jixian and Yanchuannan, are normal fault-type stress mechanisms dominated by vertical stress. Among them, the Yanchuannan has the most significant normal fault-type stress mechanism, and it has the lowest average maximum/minimum horizontal principal stress gradient and reservoir pressure gradient in the eastern Ordos basin (Table 2).

4.2 *In-situ* permeability

The permeability characteristics of CBM reservoirs directly determine the effectiveness of CBM development and are important parameters for evaluating the potential of CBM extraction and selecting favorable areas. At present, there are various methods for measuring permeability, including core laboratory testing, well-testing, reservoir simulation, and well logging inversion. Among them, injection/pressure drop well-testing permeability is the most widely used and can better reflect the characteristics of *in-situ* permeability. This study statistically analyzed 140 well-testing permeability data from 9 different blocks (Figure 9). Among them, the permeability of Hequ, Baode, and East Linxing in the northern part is the highest, mainly distributed in 0.1–10 mD. The permeability of Sanjiao, Liulin, and North Shilou in the middle is lower than that in the north, mainly distributed in 0.01–1 mD, and there are locally high permeability areas greater than 1 mD. The permeability variation range of the 5# coal seam in the Daning-Jixian Block is 0.004–6.74 mD, and the permeability of the 8# coal seam is between 0.008 and 4.36 mD, with a large variation amplitude and a decreasing trend with the increase of coal seam burial depth. The permeability distribution of the 2# coal reservoir in the Yanchuannan Block is between 0.013 and 0.99 mD, with an average of 0.224 mD. The southernmost Hancheng Block has a permeability distribution of 0.003–4.52 mD, with an average of 0.41 mD. The permeability of CBM reservoir generally decreases with the increase of burial depth, but the deep stress release zone can also have high permeability, showing a large regional difference (Mukherjee et al., 2020; 2021). In the Daning-Jixian Block, the Taoyuan anticline axis and vicinity of faults are high-permeability zones (Li et al., 2019). In the Yanchuannan Block, high-permeability zones are distributed in areas with higher structural elevation and relatively well-developed small fault zones (Chen et al., 2019; Zhang et al., 2020). In the central Linxing Block, the intrusion of Zijinshan rock mass has a strong reforming effect on the permeability of coal reservoir (Pu et al., 2022).

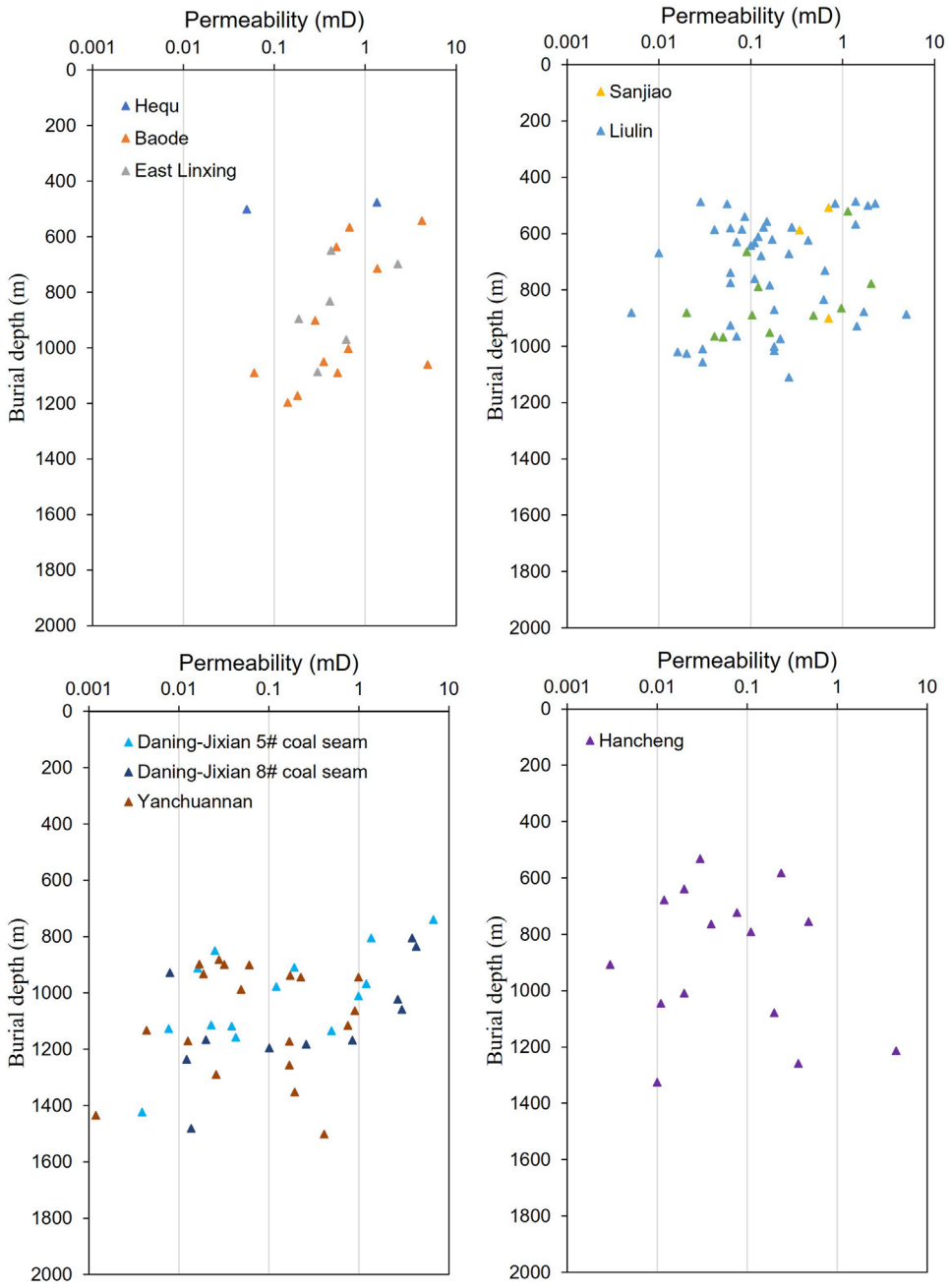

FIGURE 9
Distribution of well test permeability with burial depth in different blocks in the eastern Ordos Basin.

4.3 Permeability sensitivity analysis

4.3.1 Stress sensitivity analysis

As shown in Figure 10, the permeability of coal decreases in a negative exponential form with the increase of effective stress. The fitting curve formula can be uniformly expressed as follows:

$$K = \alpha e^{-bP} \quad (1)$$

In Eq. 1, K is the gas permeability of coal under given effective stress conditions, mD; P is the equivalent effective stress, MPa; α is the gas permeability of coal at an effective stress of 0 MPa, i.e., the initial permeability of coal; b is the permeability modulus, also known as the stress sensitivity coefficient of permeability, MPa^{-1}. The larger the value of b, the more sensitive the coal permeability as effective stress changes, that is, within the same stress variation range, the greater the decrease in gas permeability (Wu et al., 2017).

The fitting results of 11 samples all have a high correlation, with correlation coefficients between 0.9735 and 0.9998. The fitting results show that the initial permeability of the samples is between 0.0432 and 2.2453 mD. Overall, the original permeability of coal in the central Linxing and Yanchuannan blocks is significantly lower than that in the Liulin and Hancheng, which is consistent with

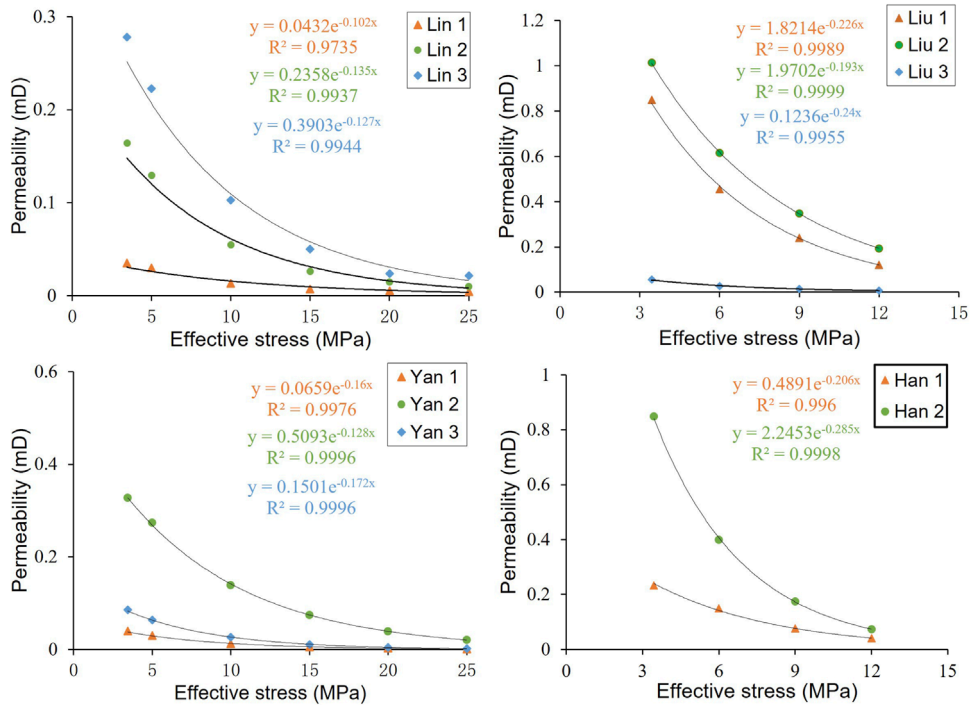

FIGURE 10
The variation law of coal permeability with effective stress increase.

the low permeability characteristics of deep CBM reservoirs. At the same time, the fitting curve shows that under experimental conditions, the stress sensitivity coefficient of coal rock samples is between 0.102 and 0.285, and there is a significant difference in stress sensitivity between blocks. The relative sizes are Central Linxing < Yanchuannan < Liulin < Hancheng, with corresponding mean values of 0.121, 0.153, 0.220, and 0.246 $^{-1}$MPa, respectively (Figure 10; Table 1). This is characterized by the lower the initial permeability value, the smaller the stress sensitivity coefficient. On the contrary, the greater the initial permeability, the larger the stress sensitivity coefficient, and the faster the stress damage.

It can also be seen from Figure 10 that the 11 coal samples tested overall reflect the following rules: when the effective stress is below 10 MPa, the CBM reservoir has strong stress sensitivity, and the permeability decreases exponentially as the effective stress increases; After the effective stress is greater than 10 MPa, the permeability of the CBM reservoir slowly decreases with the increase of effective stress, and the stress sensitivity weakens. To further quantitatively characterize the change of coal permeability with effective stress, the concepts of permeability stage damage rate (D_{ki}) and permeability maximum damage rate (D_{km}) are introduced.

D_{ki} refers to the proportion of permeability reduction before and after pressurization, and its calculation formula can be expressed as:

$$D_{ki} = \frac{K_i - K_{i+1}}{K_i} \times 100\% \quad (2)$$

Where K_i is the permeability of coal at the i th pressure point, mD; K_{i+1} is the permeability of coal at the $i+1$ th pressure point.

The maximum damage rate of permeability (D_{km}) refers to the damage rate after the confining stress increases to the highest stress point, which can be expressed as:

$$D_{km} = \frac{K_1 - K_{min}}{K_1} \times 100\% \quad (3)$$

Where K_1 is the coal permeability at the first pressure point, mD; K_{min} is the minimum permeability of coal achieved after applying the maximum effective stress.

Figure 11 shows the trend of permeability damage rate of 11 coal rock samples with increasing effective stress. It can be seen that as the effective stress increases, the trend of the curve slows down, that is, the permeability stage damage rate (Eq. 2) decreases with the increase of effective stress, and the cumulative damage rate continuously increases until it reaches the maximum damage rate. The maximum permeability damage rate (Eq. 3) of 11 samples ranges from 80.37% to 97.55%. Among them, the maximum permeability damage rate of coal in Liulin and Hancheng areas is mostly less than 90%, with an average of 83.99% and 86.90%, respectively. In contrast, the maximum permeability damage rate of coal samples in central Linxing and Yanchuannan during the entire pressurization process is basically above 90%, with an average of 91.33% and 95.91%, respectively.

4.3.2 Temperature sensitivity analysis

With the increasing depth of CBM extraction, the influence of temperature on the permeability of CBM reservoirs is also receiving more and more attention. As shown in Figure 12, when the same coal sample is subjected to the same effective stress, the higher the temperature, the lower the permeability of coal, and the overall negative effect of temperature is exhibited. This negative effect is mainly concentrated under conditions where the effective stress is less than 10 MPa, and gradually weakens as the effective stress increases.

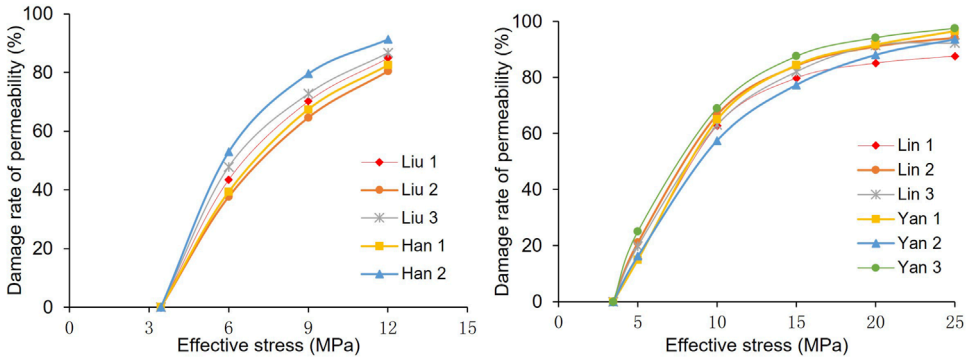

FIGURE 11
Variation law of permeability damage rate of coal rock with the increase of effective stress.

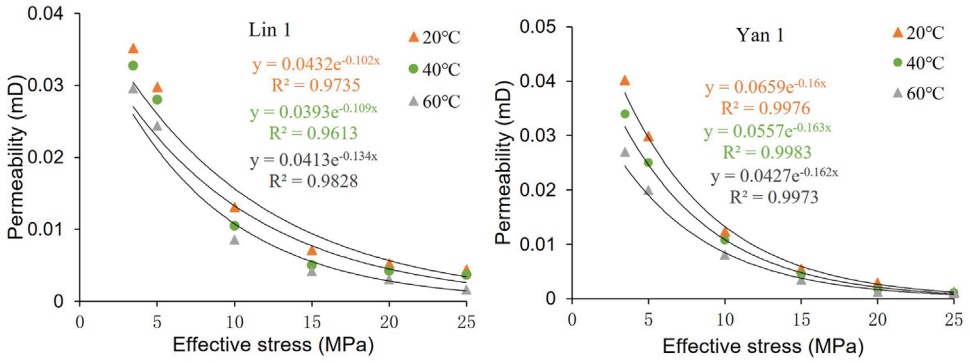

FIGURE 12
Superimposed effect of stress and temperature sensitivity on coal permeability.

This is because the coal skeleton undergoes thermal expansion with increasing temperature, causing a reduction in methane migration channels and a decrease in coal permeability (Yang et al., 2005b). However, when the effective stress is high, the pore and fracture space in the coal has been greatly compressed, and the expansion space of the coal matrix is extremely limited, so the negative effect of temperature is no longer significant. In addition, it can be observed that the higher the temperature, the greater the stress sensitivity coefficient of coal rock permeability, and the faster the permeability damage (Figure 12). Overall, both high temperature and high-stress conditions can damage the permeability of coal, but the impact of temperature on the permeability of CBM reservoirs is much smaller than stress, especially under high-stress conditions.

4.3.3 Depth effect of coal permeability sensitivity

The depth effect of reservoir permeability sensitivity is complex. The influence of depth on coal permeability is reflected in many aspects, such as stress conditions, temperature, pore pressure, initial permeability difference, and material composition, etc., but the basic reason is the compression difference of coal pores and fractures under different depths and stress conditions (Burra et al., 2014; Zhang et al., 2019). Therefore, the geological conditions and *in-situ* conditions of different depths and regions are various, and the evolution of permeability related parameters with depth is also different, but there are basic rules to follow in the same region. As shown in Figure 13, the initial permeability and stress sensitivity coefficient of coal in the four blocks are strongly negatively correlated with the depth of coal seam, and positively correlated with the maximum damage rate of permeability. That is, the deeper the coal seam is, the lower the permeability and stress sensitivity coefficient are, and the slower the permeability damage will be in the process of CBM drainage and production. However, when the reservoir pressure drops to the depletion pressure, the maximum damage rate of permeability increases. During the development process of shallow CBM, the permeability can be maintained at a relatively high level, which is beneficial for mining and is in good agreement with the actual mining situation. As far as deep CBM is concerned, its initial permeability is very low and is getting worse during the development process. Taking several deep CBM Wells in Central Linxing Block as an example, although most of them have obtained industrial gas flow in the gas testing stage and their resource conditions have been proved to be excellent, most of them in the drainage stage show the characteristics of short initial gas discovery time, low water production and short stable production time (Chen et al. 2024a). Therefore, for deep CBM, a completely different approach should be adopted from shallow CBM.

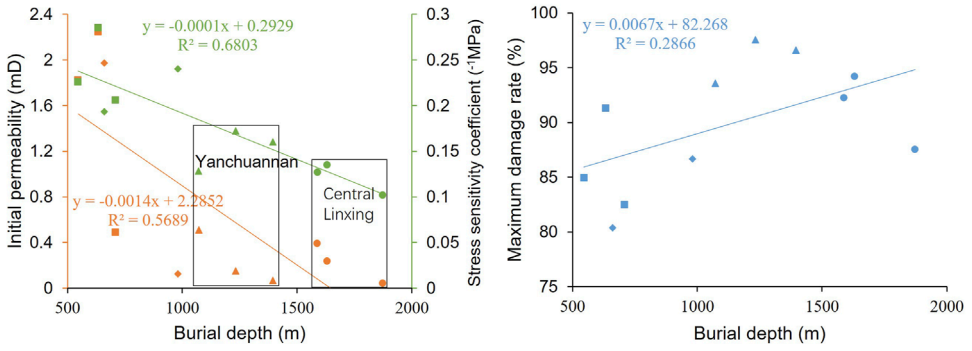

FIGURE 13
Depth effect of stress sensitivity.

4.4 Implications for deep CBM development

The exploration paradigm for deep CBM has shifted from targeting resource sweet spots to high-production sweet spots (Xu et al., 2022). High-production zones must not only possess a certain level of resource abundance but also exhibit relatively high permeability and low stress, enabling extensive reservoir reconstruction measures (Song et al., 2016). Drawing from the practical development outcomes of deep CBM blocks, two primary types of favorable zones can be discerned. One type is the structural high section with a broad and gentle configuration (positive micro-amplitude structure zone), denoting the coal reservoir that underwent deep burial initially, followed by a certain degree of structural uplift, leading to shallower burial depth of the local coal seam and development of secondary cleats. This results in increased permeability; however, without significant structural damage to the roof and floor, the original gas reservoir remains relatively well-preserved. The release of *in-situ* stress forms a relatively low-stress area, with the two wings of the high section serving as conduits for gas migration to the top. This facilitates the formation of CBM-enriched and high-yield regions with high gas content, saturation, and permeability. For instance, wells W7-5 and W6-10X1 in the Hukou slope of the Daning-Jixian Block exhibit stable gas production ranging from 4,000 to 5,000 m^3/d (Yan et al., 2021). The Yan 16 well group in the southern segment of the Wanbaoshan structural belt in the Yanchuannan Block has maintained stable production exceeding 2,000 m^3/d for 8 years, with a peak daily production of 8,000 m^3/d (Chen et al., 2024b). The other type is the upper slope of the enrichment area, formed at the top of the slope belt due to the combined effects of compressive stress and uneven crustal uplift. Taking the Daning-Jixian Block as an example, the western part of the Taoyuan anticline represents a west-dipping monoclinic structure. The upper slope zone in this region showcases the best superimposition effect of gas content, permeability, and *in-situ* stress characteristics. For example, Daning-Jixian's TU1 and TL1 wells achieved average production of 1,266.82 m^3/d and 2,827.21 m^3/d respectively, and cumulative gas production of 3,409,006 m^3 and 5,962,587 m^3 (Zhang et al., 2022).

Due to the low permeability of deep CBM reservoirs that characterized by primary and fragmented structures, vertical stress predominating, a lateral pressure coefficient less than 1, making the formation of horizontal and long fractures challenging during the vertical well fracturing process. The CBM development practices in the Yanchuannan Block, Daning-Jixian Block, and Qinshui Basin have demonstrated that the vertical well + horizontal well combination mode not only reduces well spacing but also interconnects a large number of fracture systems, facilitating regional pressure reduction and enhancing the utilization of CBM reserves (Zhu et al., 2019; Jiang and Yang, 2021; Zhang et al., 2022). Deep CBM reservoirs exhibit large horizontal principal stress differences, and artificially expanded fractures often intersect natural fractures directly, posing challenges in forming a three-dimensional fracture network (Dunlop et al., 2017). This issue has been addressed in the Yanchuannan and Daning-Jixian blocks through the implementation of high liquid volume (1,016–6,874 m^3) and large-scale fracturing measures (Yan et al., 2021; Chen et al., 2024b). The effective fracturing approach of "creating long fractures and remote support" in deep high-stress environments has led to a breakthrough in the productivity of deep CBM wells (Yan et al., 2021).

In contrast to shallow CBM reservoirs which are predominantly undersaturated, deep CBM reservoirs, under the coupled control of high temperature and pressure conditions, contain a significant amount of saturated to supersaturated gas reservoirs (Kang et al., 2019). Given the permeability sensitivity of deep coal reservoir, the conventional "continuous, stable, long-term, slow" drainage method suitable for shallow CBM is no longer viable. Production practices in the Yanchuannan Block have shown that rapid depressurization, coupled with effective fracturing and support, is more conducive to achieving efficient and stable high yield in deep CBM wells (Zhao et al., 2021). This is primarily attributed to the fact that effective fracturing and support can to some extent mitigate reservoir stress sensitivity effects; rapid depressurization can prompt rapid desorption and accumulation of CBM in the near-well region during the rapid or sensitive desorption stage, while enhancing coal-rock matrix shrinkage effects to drive subsequent gas production; rapid depressurization can also increase reservoir pressure differentials near and far from the wellbore, enhancing gas mass transfer efficiency in low-permeability CBM reservoirs (Su et al., 2019; Zhao et al., 2021). Building on the successful experience of the Yanchuannan Block, the application of rapid

depressurization in deeper-buried coal reservoirs with higher gas saturation in the Daning-Jixian and Central Linxing blocks warrants further theoretical exploration and practical validation.

5 Conclusion

This study integrates extensive *in-situ* geological data from the eastern Ordos Basin and conducts coal permeability sensitivity experiments to dissect the fundamental reasons for significant production capacity differences between deep and shallow blocks and promote mutual learning from successful development experiences. The main conclusions drawn are as follows:

(1) Shallower coal seams usually have lower temperatures and a wider variation range of geothermal gradients. Reservoir temperature is more heavily influenced by depth in deeper coal seams.

(2) CBM reservoir pressure increases linearly with burial depth within the range of 427–2,195 m, with localized pressure low anomalies observed at depths of 1,300–1,500 m. The pressure gradient spans from 0.314 to 1.25 MPa/100 m at depths below 1,300 m, while 1,300–1,500 m is the "under-pressure zone" and 1,500–2,200 m is the "normal to overpressure zone.

(3) The vertical conversion interface of stress is located at 1,500 m, below which the vertical stress is dominant. The horizontal stress gradient and lateral stress coefficient both exhibit the characteristic of "strong dispersion in shallow areas and strong convergence in deep areas" with a critical depth of 1,000 m. The stress field of CBM reservoirs is the result of the coupling effect of tectonic condition and burial depth.

(4) *In-situ* permeability of CBM reservoirs decreases with increasing burial depth, primarily influenced by tectonic stress fields. Stress release zones in deep CBM reservoirs often exhibit high permeability, emphasizing the importance of reservoir optimization and reconstruction for efficient CBM development.

(5) Deep CBM high-yield areas are typically found in structurally elevated regions with wide, gentle morphology and in the upper slope in gas-rich zones. It is advised to utilize a combination of vertical + horizontal wells and employ a fracturing technique featuring "large-scale, high-volume, multi rounds, continuous proppant injection". Additionally, implementing a "rapid depressurization" drainage system is recommended to optimize production and efficiency.

Data availability statement

The original contributions presented in the study are included in the article/Supplementary Material, further inquiries can be directed to the corresponding author.

Author contributions

YZ: Conceptualization, Data curation, Formal Analysis, Investigation, Methodology, Software, Validation, Visualization, Writing–original draft, Writing–review and editing. JL: Formal Analysis, Software, Validation, Writing–review and editing.

Funding

The author(s) declare that financial support was received for the research, authorship, and/or publication of this article. This research was funded by National Natural Science Foundation of China (grant number 42230812) and the Postdoctoral Fellowship Program of CPSF (grant number GZC20233110).

Acknowledgments

We acknowledge the editors and reviewers for critical review and constructive comments.

Conflict of interest

Authors YZ and JL were employed by PetroChina.

Publisher's note

References

Békési, E., Struijk, M., Bonté, D., Veldkamp, H., Limberger, J., Fokker, P. A., et al. (2020). An updated geothermal model of the Dutch subsurface based on inversion of temperature data. *Geothermics* 88, 101880. doi:10.1016/j.geothermics.2020.101880

Bell, J. S. (2006). *In-situ* stress and coal bed methane potential in Western Canada. *Bull. Can. Petroleum Geol.* 54 (3), 197–220. doi:10.2113/gscpgbull.54.3.197

Brown, E. T., and Hock, E. B. (1980). *Underground excavations in rock*. London: The institute of minng and metallurgy.

Burra, A., Esterle, J. S., and Golding, S. D. (2014). Horizontal stress anisotropy and effective stress as regulator of coal seam gas zonation in the Sydney Basin, Australia. *Int. J. coal Geol.* 132, 103–116. doi:10.1016/j.coal.2014.08.008

Chapman, D. S., Keho, T., Bauer, M. S., and Picard, M. D. (1984). Heat flow in the Uinta Basin determined from bottom hole temperature (BHT) data. *Geophysics* 49 (4), 453–466. doi:10.1190/1.1441680

Chatterjee, R., Paul, S., and Pal, P. K. (2019). Relation between coalbed permeability and *in-situ* stress magnitude for coalbed methane exploration in Jharia and Raniganj coalfields, India. *Lead. Edge* 38 (10), 800–807. doi:10.1190/tle38100800.1

Chen, B., Li, S., Tang, D., Pu, Y., and Zhong, G. (2024a). Evaluation of recoverable potential of deep coalbed methane in the linxing block, eastern margin of the Ordos Basin. *Sci. Rep.* 14 (1), 9192. doi:10.1038/s41598-024-59128-x

Chen, H., Jiang, B., Qu, Z., Wang, J., and Wang, L. (2014). Diversity structural characteristics and control action on coal bed gas content in Linfen and Baode area. *J. China Coal Soc.* 39 (3), 510–517. doi:10.13225/j.cnki.jccs.2013.1574

Chen, S., Tang, D., Tao, S., Xu, H., Li, S., and Zhao, J. (2018a). Statistic analysis on macro distribution law of geostress field in coalbed methane reservoir. *Coal Sci. Technol.* 46 (6), 57–63. doi:10.13199/j.cnki.cst.2018.06.010

Chen, S., Tang, D., Tao, S., Xu, H., Li, S., Zhao, J., et al. (2017). *In-situ* stress measurements and stress distribution characteristics of coal reservoirs in major coalfields in China: implication for coalbed methane (CBM) development. *Int. J. Coal Geol.* 182, 66–84. doi:10.1016/j.coal.2017.09.009

Chen, S., Tang, D., Tao, S., Xu, H., Zhao, J., Fu, H., et al. (2018b). *In-situ* stress, stress-dependent permeability, pore pressure and gas-bearing system in multiple coal seams in the Panguan area, western Guizhou, China. *J. Nat. Gas Sci. Eng.* 49, 110–122. doi:10.1016/j.jngse.2017.10.009

Chen, S., Tao, S., and Tang, D. (2024b). *In situ* coal permeability and favorable development methods for coalbed methane (CBM) extraction in China: from real data. *Int. J. Coal Geol.* 284, 104472. doi:10.1016/j.coal.2024.104472

Chen, Z. (1989). *Sedimentary environment and coal accumulation law of late Paleozoic coal-bearing rock series in the eastern margin of Ordos Basin*. Wuhan: China University of Geosciences Press.

Chen, Z., Guo, T., Li, X., Xiao, C., and Jin, X. (2019). Enrichment law and development technology of deep coalbed methane in South Yanchuan Coalbed Methane Field. *Coal Sci. Technol.* 47 (9), 112–118. doi:10.13199/j.cnki.cst.2019.09.011

Cheng, R., Chen, H., Xian, X., and Wang, G. (1998). Experimental study on the influence of temperature on permeability coefficient of coal sample. *Coal Eng.* (1), 13–16.

Dabbous, M., Reznik, A., Taber, J., and Fulton, P. (1974). The permeability of coal to gas and water. *Soc. Petroleum Eng. J.* 14 (06), 563–572. doi:10.2118/4711-a

Dunlop, E., Warner, D., Warner, P. E., and Coleshill, L. (2017). Ultra-deep Permian coal gas reservoirs of the Cooper Basin: insights from new studies. *APPEA J.* 57 (1), 218–262. doi:10.1071/aj16015

Fu, H., Yan, D., Yang, S., Wang, X., Zhang, Z., and Sun, M. (2020). Characteristics of *in situ* stress and its influence on coalbed methane development: a case study in the eastern part of the southern Junggar Basin, NW China. *Energy Sci. Eng.* 8 (2), 515–529. doi:10.1002/ese3.533

Fu, X., Qin, Y., Xue, X., Li, G., and Wang, W. (2001). Research on fractals of pore and fracture-structure of coal reservoirs. *J. China Univ. Min. Technol.* 30 (3), 225–228. doi:10.3321/j.issn:1000-1964.2001.03.003

Gan, J., Wu, D., Zhang, Y., Liu, S., Guo, M., Li, X., et al. (2019). Distribution pattern of present-day formation temperature in the qiongdongnan basin: implications for hydrocarbon generation and preservation. *Geol. J. China Univ.* 25 (6), 952–960. doi:10.16108/j.issn1006-7493.2019053

Gao, X. (2019). *Study on porosity and permeability evolution mechanism and fracturing reconstruction feasibility of deep coal reser-voirs in linxing area*. Beijing: China University of Mining and Technology.

Guo, M., Song, P., Zhang, B., Chen, M., and Wu, W. (2020). Origin and evolution of paleo- overpressure in the Upper Paleozoic in Linxing area, the eastern margin of Ordos Basin. *J. Xi'an Shiyou Univ. Nat. Sci. Ed.* 35 (4), 19–25. doi:10.3969/j.issn.1673-064X.2020.04.003

Harpalani, S., and Chen, G. (1992). "Effect of gas production on porosity and permeability of coal," in Proceedings of the Symposium of Coalbed Methane R and D in Australia, Townsville, Australia, 19 - 21 November 1992, 67–73.

Jiang, X., Wu, C., Zhang, E., and Zhang, S. (2020). Geotemperature-geopressure system and its distribution characteristics of Yuwang block in Laochang mining area. *J. Henan Polytech. Univ. Nat. Sci.* 39 (2), 32–37. doi:10.16186/j.cnki.1673-9787.2020.2.5

Jiang, Y., and Yang, S. (2021). New technology of dewatering gas recovery for CBM wells in southern Yanchuan Block, eastern margin of Ordos Basin. *Petroleum Reserv. Eval. Dev.* 11 (3), 384–389. doi:10.13809/j.cnki.cn32-1825/te.2021.03.013

Jing, X. (2012). Study on pressure distribution law and control factors of coal bed methane reservoir in south part of Qinshui Basin. *Coal Sci. Technol.* 40 (2), 116–120. doi:10.13199/j.cst.2012.02.121.jingxp.004

Ju, W., Yang, Z., Qin, Y., Yi, T., and Zhang, Z. (2018). Characteristics of *in-situ* stress state and prediction of the permeability in the Upper Permian coalbed methane reservoir, western Guizhou region, SW China. *J. Petroleum Sci. Eng.* 165, 199–211. doi:10.1016/j.petrol.2018.02.037

Ju, W., Yang, Z., Shen, Y., Yang, H., Wang, G., Zhang, X., et al. (2021). Mechanism of pore pressure variation in multiple coal reservoirs, western Guizhou region, South China. *Front. Earth Sci.* 15, 770–789. doi:10.1007/s11707-021-0888-7

Kang, H., Jiang, T., Zhang, X., and Yan, L. (2009). Research on *in-situ* stress field in Jincheng mining area and its application. *Chin. J. Rock Mech. Eng.* 28 (1), 1–8. doi:10.3321/j.issn:1000-6915.2009.01.001

Kang, H., Yi, B., Gao, F., and Lv, H. (2019). Database and characteristics of underground in–situ stress distribution in Chinese coal mines. *J. China Coal Soc.* 44 (1), 23–33. doi:10.13225/j.cnki.jccs.2018.5032

Kang, H. P., Zhang, X., Si, L. P., Wu, Y., and Gao, F. (2010). *In-situ* stress measurements and stress distribution characteristics in underground coal mines in China. *Eng. Geol.* 116 (3-4), 333–345. doi:10.1016/j.enggeo.2010.09.015

Kang, Y., Sun, L., Zhang, B., Gu, J., Ye, J., Jiang, S., et al. (2017). The controlling factors of coalbed reservoir permeability and CBM development strategy in China. *Geol. Rev.* 63 (5), 1401–1418. doi:10.16509/j.georeview.2017.05.019

Karacan, C., and Okandan, E. (2001). Adsorption and gas transport in coal microstructure: investigation and evaluation by quantitative X-ray CT imaging. *Fuel* 80 (4), 509–520. doi:10.1016/s0016-2361(00)00112-5

Li, C., Jiang, B., Ju, W., Cheng, G., and Song, Y. (2019). Characteristics of tectonic deformation in the Daning-Jixian region, eastern Ordos Basin: implications for the exploration and development of coalbed methane. *Energy Explor. Exploitation* 37 (3), 907–921. doi:10.1177/0144598718816607

Li, G., and Zhang, H. (2020). Evolution history of coalbed methane reservoir and its difference in eastern Ordos Basin. *China Coalbed Methane* 17 (3), 3–8.

Li, S., Qian, M., and Shi, P. (2001). Permeability-strain equation relation to complete stress-strain path of coal sample. *Coal Geol. Explor.* 29 (1), 22–24. doi:10.3969/j.issn.1001-1986.2001.01.007

Li, S., Tang, D., Pan, Z., Xu, H., Tao, S., Liu, Y., et al. (2018). Geological conditions of deep coalbed methane in the eastern margin of the Ordos Basin, China: implications for coalbed methane development. *J. Nat. Gas Sci. Eng.* 53, 394–402. doi:10.1016/j.jngse.2018.03.016

Li, S., Tang, D. Z., Xu, H., and Yang, Z. (2012). Characteristics of coal reservoirs in Zhijin and Nayong regions, Guizhou province, China. *J. China Univ. Min. Technol.* 41 (6), 951–958.

Li, Z., Zhou, W., and Wu, Y. (2004). Generic analysis on the abnormal pressure of the gas reservoirs in the coal layers in China. *Mineralogy Petrology* 24 (4), 87–92. doi:10.19719/j.cnki.1001-6872.2004.04.016

Liu, C. (2006). Research on the earth temperature of surveying coal resources. *Coal Hebei* (3), 12–13. doi:10.3969/j.issn.1007-1083.2006.03.006

Liu, J. (2020). "*Sequence Stratigraphy and mineral resource Distribution in the late paleozoic cratonic Interior of western north China*,". Doctor (Beijing: China University of Mining and Technology).

Liu, J., Kang, Y., Chen, M., You, L., Zhang, T., Gao, X., et al. (2021). Investigation of enhancing coal permeability with high-temperature treatment. *Fuel* 290, 120082. doi:10.1016/j.fuel.2020.120082

Liu, Z., Zhu, W., Sun, Q., Jin, B., Xu, X., and Zhang, H. (2012). Characteristics of geotemperature-geopressure systems in petroliferous basins of China. *Acta Pet. Sin.* 33 (1), 1–17. doi:10.7623/syxb201201001

Lu, L., Qin, Y., and Guo, C. (2013). Modern geothermal field and coal seam heating temperature in Buzuo exploration area, Western Guizhou. *Coal Geol. China* 25 (10), 12–17. doi:10.3969/j.issn.1674-1803.2013.10.03

Meng, Z., Tian, Y., and Li, G. (2010). Characteristics of *in-situ* stress field in Southern Qinshui Basin and its research significance. *J. China Coal Soc.* 35 (6), 975–981. doi:10.13225/j.cnki.jccs.2010.06.014

Meng, Z., Zhang, J., and Wang, R. (2011). *In-situ* stress, pore pressure and stress-dependent permeability in the Southern Qinshui Basin. *Int. J. Rock Mech. Min. Sci.* 48 (1), 122–131. doi:10.1016/j.ijrmms.2010.10.003

Milkov, A. V., and Etiope, G. (2018). Revised genetic diagrams for natural gases based on a global dataset of> 20,000 samples. *Org. Geochem.* 125, 109–120. doi:10.1016/j.orggeochem.2018.09.002

Mukherjee, S., Rajabi, M., and Esterle, J. (2021). Relationship between coal composition, fracture abundance and initial reservoir permeability: a case study in the Walloon Coal Measures, Surat Basin, Australia. *Int. J. Coal Geol.* 240, 103726. doi:10.1016/j.coal.2021.103726

Mukherjee, S., Rajabi, M., Esterle, J., and Copley, J. (2020). Subsurface fractures, *in-situ* stress and permeability variations in the Walloon coal measures, eastern surat basin, queensland, Australia. *Int. J. Coal Geol.* 222, 103449. doi:10.1016/j.coal.2020.103449

Ministry of Natural Resources, PRC (2020). *Report on China oil and gas resource exploration and development in 2020*. http://gi.m.mnr.gov.cn/202109/t20210918_2681270.html. Beijing: Ministry of Natural Resources of the People's Republic of China.

Pan, Z., and Connell, L. D. (2011). Modelling of anisotropic coal swelling and its impact on permeability behaviour for primary and enhanced coalbed methane recovery. *Int. J. Coal Geol.* 85 (3-4), 257–267. doi:10.1016/j.coal.2010.12.003

Paul, S., and Chatterjee, R. (2011). Determination of *in-situ* stress direction from cleat orientation mapping for coal bed methane exploration in south-eastern part of Jharia coalfield, India. *Int. J. Coal Geol.* 87 (2), 87–96. doi:10.1016/j.coal.2011.05.003

Peng, T., Ren, Z., Wu, J., and Zhang, H. (2017). Distribution characteristics of the present-day geothermal field and its structural controls in deep part of panji mining area. *Geol. J. China Univ.* 23 (1), 157–164. doi:10.16108/j.issn1006-7493.2016161

Pu, Y., Li, S., Tang, D., and Chen, S. (2022). Effect of magmatic intrusion on *in situ* stress distribution in deep coal measure strata: a case study in linxing block, eastern margin of Ordos Basin, China. *Nat. Resour. Res.* 31 (5), 2919–2942. doi:10.1007/s11053-022-10099-8

Qin, Y., and Shen, J. (2016). Disccussion on the fundamental issues of deep coalbed methane geology. *Acta Pet. Sin.* 37 (1), 125–136. doi:10.7623/syxb201601013

Qin, Y., Shen, J., Wang, L., Yang, S., and Zhao, L. (2012). Accumulation effects and coupling relationship of deep coalbed methane. *Acta Pet. Sin.* 33 (1), 48–54. doi:10.7623/syxb201201006

Ranathunga, A. S., Perera, M. S. A., and Ranjith, P. (2014). Deep coal seams as a greener energy source: a review. *J. Geophys. Eng.* 11 (6), 063001. doi:10.1088/1742-2132/11/6/063001

Reisabadi, M. Z., Haghighi, M., Sayyafzadeh, M., and Khaksar, A. (2021). Stress distribution and permeability modelling in coalbed methane reservoirs by considering desorption radius expansion. *Fuel* 289, 119951. doi:10.1016/j.fuel.2020.119951

Salmachi, A., Rajabi, M., Wainman, C., Mackie, S., McCabe, P., Camac, B., et al. (2021). History, geology, *in situ* stress pattern, gas content and permeability of coal seam gas basins in Australia: a review. *Energies* 14 (9), 2651. doi:10.3390/en14092651

Shen, B., Shen, S., Wu, Q., Zhang, S., Zhang, B., Wang, X., et al. (2022). Carboniferous and permian integrative stratigraphy and timescale of north China block. *Sci. China Earth Sci.* 65 (6), 983–1011. doi:10.1007/s11430-021-9909-9

Song, Y., Liu, S., Ju, Y., Hong, F., Jiang, L., Ma, X., et al. (2013). Coupling between gas content and permeability controlling enrichment zones of high abundance coal bed methane. *Acta Pet. Sin.* 34 (3), 417–426. doi:10.7623/syxb201303001

Song, Y., Liu, S., Ma, H., Li, J., Ju, Y., Li, G., et al. (2016). Research on formation model and geological evaluation method of the middle to high coal rank coalbed methane enrichment and high production area. *Earth Sci. Front.* 23 (3), 1–9. doi:10.13745/j.esf.2016.03.001

Su, X., Liu, Y., Cui, Z., Zhang, J., Li, Y., and Wang, K. (2019). Influence of depressurization rate on gas production capacity of high-rank coal in the south of Qinshui Basin, China. *Petroleum Explor. Dev.* 46 (3), 642–650. doi:10.1016/s1876-3804(19)60044-3

Tan, J., Ju, Y., Hou, Q., Zhang, W., and Tan, Y. (2009). Distribution characteristics and influence factors of present geo-temperature field in Su-Lin mine area. *Huaibei Coalf.* 52 (3), 732–739.

Wang, G., Qin, Y., Shen, J., Chen, S., Han, B., and Zhou, X. (2018). Dynamic-change laws of the porosity and permeability of low-to medium-rank coals under heating and pressurization treatments in the eastern junggar basin, China. *J. Earth Sci.* 29, 607–615. doi:10.1007/s12583-017-0908-4

Wang, X., Zhang, Q., Wang, L., Ge, R., and Chen, J. (2010). Structural features and tectonic stress fields of the Mesozoic and Cenozoic in the eastern margin of the Ordos basin, China. *Geol. Bull.* 29 (8), 1168–1176. doi:10.3969/j.issn.1671-2552.2010.08.009

Ward, C. R. (2016). Analysis, origin and significance of mineral matter in coal: an updated review. *Int. J. Coal Geol.* 165, 1–27. doi:10.1016/j.coal.2016.07.014

Weniger, S., Weniger, P., and Littke, R. (2016). Characterizing coal cleats from optical measurements for CBM evaluation. *Int. J. Coal Geol.* 154, 176–192. doi:10.1016/j.coal.2015.12.005

Wu, C., Qin, Y., and Fu, X. (2007). Elastic energy of coal reservoir and its controlling effect on coalbed methane accumulation. *Sci. China (D)* 37 (9), 1163–1168. doi:10.3969/j.issn.1674-7240.2007.09.003

Wu, S., Peng, T., and Guo, Y. (2013). Ground temperature distribution pattern and its abnormal factor analysis in qianyingzi coalmine, northern anhui. *Coal Geol. China* 25 (6), 30–35. doi:10.3969/j.issn.1674-1803.2013.06.007

Wu, S., Tang, D., Li, S., Wu, H., Hu, X., and Zhu, X. (2017). Effects of geological pressure and temperature on permeability behaviors of middle-low volatile bituminous coals in eastern Ordos Basin, China. *J. Petroleum Sci. Eng.* 153, 372–384. doi:10.1016/j.petrol.2017.03.034

Xiao, Y., Liu, D., Kong, X., and Lian, D. (2009). Analysis of No.9 coal geotemperature characteristics and impacting factors in longfeng minefield. *Coal Geol. China* 21 (1), 45–47. doi:10.3969/j.issn.1674-1803.2009.01.013

Xu, F., Yan, X., Lin, Z., Li, S., Xiong, X., Yan, D., et al. (2022). Research progress and development direction of key technologies for efficient coalbed methane development in China. *Coal Geol. Explor.* 50 (3), 1–14. doi:10.3969/j.issn.1001-1986.2022.03.001

Xu, H., Sang, S., Yang, J., Jin, J., Hu, Y., Liu, H., et al. (2016). *In-situ* stress measurements by hydraulic fracturing and its implication on coalbed methane development in Western Guizhou, SW China. *J. Unconv. Oil Gas Resour.* 15, 1–10. doi:10.1016/j.juogr.2016.04.001

Xu, H., Tang, D., Tang, S., Zhang, W., Zhang, S., Tao, S., et al. (2010). Coal reservoir characteristics and prospective areas for Jurissic CBM exploitation in western Ordos basin. *Coal Geol. Explor.* 38 (1), 26–28+ 32. doi:10.3969/j.issn.1001-1986.2010.01.006

Yan, X., Xu, F., Nie, Z., and Kang, Y. (2021). Microstructure characteristics of Daji area in east Ordos Basin and its control over the high yield dessert of CBM. *J. China Coal Soc.* 46 (8), 2426–2439. doi:10.13225/j.cnki.jccs.CB21.0751

Yang, S., Cui, F., Yang, S., and Zhang, S. (2005a). Experimental study on mechanism of gas flow in coal bed. *China Coalbed Methane* 2 (1), 36–39. doi:10.3969/j.issn.1672-3074.2005.01.009

Yang, S., Xiao, C., Wang, X., and Yang, Q. (2005b). Stress sensitivity of rock and its influence on productivity for gas reservoirs with abnormal high pressure. *Nat. Gas. Ind.* 25 (5), 94–95. doi:10.3321/j.issn:1000-0976.2005.05.030

Yang, X. (2015). Characteristics of CBM reservoir in Huangling-Longxian coalfield. *Coal Geol. Explor.* 43 (4), 41–45. doi:10.3969/j.issn.1001-1986.2015.04.009

Yang, X., Xu, F., Wang, H., Li, S., Lin, W., Wang, W., et al. (2022). Exploration and development process of coalbed methane in eastern margin of Ordos Basin and its enlightenment. *Coal Geol. Explor.* 50 (3), 5. doi:10.3969/j.issn.1001-1986.2022.03.004

Yang, X., and Zhang, Y. (2008). Experimental study of effect of temperature on coal gas permeability under gas-solid coupling. *J. Geomechanics* 14 (4), 374–380. doi:10.3969/j.issn.1006-6616.2008.04.007

Yuan, Y., Zhu, W., Mi, L., Zhang, G., Hu, S., and He, L. (2009). "Uniform geothermal gradient" and heat flow in the qiongdongnan and pearl river mouth basins of the south China sea. *Mar. Petroleum Geol.* 26 (7), 1152–1162. doi:10.1016/j.marpetgeo.2008.08.008

Zhang, L. (2012). Geotemperature characteristics and impacts from geological factors in Shunhexi Mine Area. *Coal Geol. China* 24 (7), 29–33. doi:10.3969/j.issn.1674-1803.2012.07.07

Zhang, Y., Li, S., Tang, D., Liu, J., Lin, W., Feng, X., et al. (2022). Geological and engineering controls on the differential productivity of CBM wells in the Linfen block, southeastern Ordos Basin, China: insights from geochemical analysis. *J. Petroleum Sci. Eng.* 211, 110159. doi:10.1016/j.petrol.2022.110159

Zhang, Y., Li, S., Tang, D., Zhao, X., Zhu, S., and Ye, J. (2020). Structure-and hydrology-controlled isotopic coupling and heterogeneity of coalbed gases and co-produced water in the Yanchuannan block, southeastern Ordos Basin. *Int. J. Coal Geol.* 232, 103626. doi:10.1016/j.coal.2020.103626

Zhang, Y., and Tang, S. (2001). Research on coal reservoir pressure of some mine areas in north China. *Acta Geosci. Sin.* 22 (2), 165–168. doi:10.3321/j.issn:1006-3021.2001.02.014

Zhang, Z., Zhang, R., Wu, S., Deng, J., Zhang, Z., and Xie, J. (2019). The stress sensitivity and porosity sensitivity of coal permeability at different depths: a case study in the Pingdingshan mining area. *Rock Mech. Rock Eng.* 52 (5), 1539–1563. doi:10.1007/s00603-018-1633-8

Zhao, D., Chen, Z., Cai, X., and Li, S. (2007). Analysis of distribution rule of geostress in China. *Chin. J. Rock Mech. Eng.* 26 (6), 1265–1271. doi:10.3321/j.issn:1000-6915.2007.06.024

Zhao, J., Tang, D., Lin, W., Qin, Y., and Xu, H. (2019). *In-situ* stress distribution and its influence on the coal reservoir permeability in the Hancheng area, eastern margin of the Ordos Basin, China. *J. Nat. Gas Sci. Eng.* 61, 119–132. doi:10.1016/j.jngse.2018.09.002

Zhao, J., Tang, D., Xu, H., Li, Y., Li, S., Tao, S., et al. (2016). Characteristic of *in situ* stress and its control on the coalbed methane reservoir permeability in the eastern margin of the Ordos Basin, China. *Rock Mech. Rock Eng.* 49 (8), 3307–3322. doi:10.1007/s00603-016-0969-1

Zhao, X., Tang, D., and Zhang, Y. (2021). Establishment and optimization of drainage system for deep coalbed methane in south Yanchuan CBM field. *Coal Sci. Technol.* 49 (6), 251–257. doi:10.13199/j.cnki.cst.2021.06.030

Zhong, L. (2003). Pressure characteristics of coal reservoirs in China. *Nat. Gas. Ind.* 23 (5), 132–134. doi:10.3321/j.issn:1000-0976.2003.05.043

Zhu, H., and Tao, Z. (1994). Distribution of geostress in different rocks. *Acta Seismol. Sin.* 16 (1), 49–63.

Zhu, Q., Lu, X., and Yang, Y. (2019). Coupled activation technology for low-efficiency productivity zones of high-rank coalbed methane in Zhengzhuang block, Shanxi. *China* 44 (8), 2547–2555. doi:10.13225/j.cnki.jccs.KJ19.0428

Zoback, M., Barton, C., Brudy, M., Castillo, D., Finkbeiner, T., Grollimund, B., et al. (2003). Determination of stress orientation and magnitude in deep wells. *Int. J. Rock Mech. Min. Sci.* 40 (7-8), 1049–1076. doi:10.1016/j.ijrmms.2003.07.001

frontiers | Frontiers in Earth Science

TYPE Original Research
PUBLISHED 13 August 2024
DOI 10.3389/feart.2024.1413069

OPEN ACCESS

EDITED BY
Ebrahim Fathi,
West Virginia University, United States

REVIEWED BY
Qian Zhang,
Peking University, China
Fengli Li,
Suzhou University, China
Haoze Li,
China University of Mining and Technology, China

*CORRESPONDENCE
Ruyue Wang,
wry1990@vip.qq.com
Zhengguang Zhang,
zhengguang0411@163.com

RECEIVED 06 April 2024
ACCEPTED 29 July 2024
PUBLISHED 13 August 2024

CITATION
Xu Q, Wang R, Wang Z, Zhao Y, Miao Q, Zhang Z, Bai X and Xinxin F (2024) Nanoscale pore structure in anthracite coals and its effect on methane adsorption capacity. *Front. Earth Sci.* 12:1413069. doi: 10.3389/feart.2024.1413069

Nanoscale pore structure in anthracite coals and its effect on methane adsorption capacity

Qiang Xu[1,2], Ruyue Wang[3]*, Zebin Wang[4], Yue Zhao[1,2], Quanyun Miao[1,2], Zhengguang Zhang[1,2]*, Xiujia Bai[1,2] and Feng Xinxin[5]

[1]General Prospecting and Research Institute of China National Administration of Coal Geology, Beijing, China, [2]Key Laboratory of Transparent Mine Geology and Digital Twin Technology, National Mine Safety Administration, Beijing, China, [3]Sinopec Petroleum Exploration and Production Research Institute, Beijing, China, [4]PetroChina Coalbed Methane Company Limited, Beijing, China, [5]Shaanxi Tiancheng Petroleum Technology Company Limited, Xi'an, China

Although significant amounts of methane are present in anthracite coal seams, coalbed methane resources cannot be extracted effectively and quickly. This study mainly focused on investigating the pore system and methane adsorption capacity to clarify the storage of coalbed methane. Anthracite coal samples from the Anzenan coalbed methane block in China were collected, and pore characterization methods (low-pressure N_2 adsorption, mercury injection experiments, and scanning electron microscopy (SEM) observations) and methane isothermal adsorption experiments were conducted. The results showed that few mesopores and nanoscale macropores were present in the anthracite coal samples. The volume of the 2–300 nm pores in these coal samples obtained from the N_2 adsorption experiment was lower than 0.01 cm^3/g. SEM observations also revealed that only a small number of mesopores and nanoscale macropores could be seen, and most of these pores were isolated. In terms of the methane isothermal adsorption data, it was found these anthracite coals have a large methane adsorption capacity, and the Langmuir volume ranges from 19.5 to 28.4 cm^3/g, with an average of 22.2 cm^3/g. With increasing ash yield, the Langmuir volume decreased linearly, indicating that methane molecules were mainly adsorbed in the organic matter of coal. As methane is mainly adsorbed in the micropores of coal organic matter and there are few mesopores and nanoscale macropores in the organic pores in coal, there are not enough tunnels to transport the adsorbed methane molecules to the outside. Thus, it is difficult to extract coalbed methane from anthracite. This study reveals the impact of pore system limitations on the storage and extraction of coalbed methane in anthracite coal. The findings can be applied to the extraction of coalbed methane from anthracite coal seams worldwide.

KEYWORDS

anthracite coal, coalbed methane, pore system, methane adsorption capacity, ash yield

1 Introduction

There are huge amounts of coalbed methane resources in the underground coal seams (Moore, 2012; Qin et al., 2018; Hou et al., 2020; Joshi et al., 2023). However, most of these natural gas resources have not been effectively exploited. In addition, coalbed methane is a key factor threatening the safety of coal mining (Cheng and Pan, 2020; Tu et al., 2022; Wang

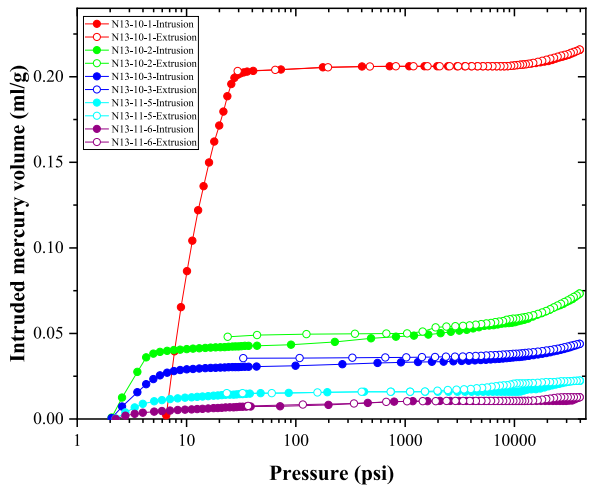

FIGURE 1
Mercury injection and mercury extraction curves of the coal samples.

and Cheng, 2023). Although many studies have been conducted on coalbed methane over the past 40 years, researchers have not found many ways to exploit it (Bustin et al., 2016; Akhondzadeh et al., 2021). Global coalbed methane production has decreased in recent years. The exploration and exploitation of coalbed methane help reduce the use of coal and mitigate greenhouse effects and climate warming (Cho et al., 2019; Fan et al., 2019). Thus, more efforts are needed to study coalbed methane.

Unlike conventional gas, coalbed methane is primarily stored in coal as an absorbed gas (Chattaraj et al., 2016; Hou et al., 2020; Mohamed and Mehana, 2020; Liu et al., 2021). Thus, the evaluation of the methane adsorption capacity of coal is very important for understanding the reservoir mechanism of coalbed methane (Song et al., 2012; Liu et al., 2021). Isothermal adsorption experiments (volumetric and gravimetric methods) are often used to test the methane adsorption capacity of coal samples (Bustin and Clarkson, 1998; Lorenz and Wessling, 2013). Previous studies found that most methane adsorption data for coal conform to the Langmuir equation (Moore, 2012; Perera et al., 2012). With increasing pressure, the amount of methane adsorption first increases significantly and then approaches a constant value (Langmuir volume) (Moore, 2012). When the experimental temperature increased, the amount of methane adsorbed decreased, indicating that temperature had a negative effect on methane adsorption in coal (Zhang et al., 2011; Li et al., 2022). In addition, the methane adsorption capacity of coal is affected by many factors, such as maturity, ash yield, and moisture (Crosdale et al., 1998; Chalmers and Marc Bustin, 2007). During the coalification process, the coalification of coal changes in stages: it first increases (Ro < 1.4%), then decreases (Ro = 1.4–3.7%), and finally decreases again (Ro > 3.7%) (Zhong and Zhang, 1990; Zhong, 2004; Liu et al., 2021). In addition, large amounts of methane have been generated from these anthracite coals during past geological times, and the gas content in anthracite coal seams is usually very high (Su et al., 2005; Cai et al., 2011; Meng et al., 2017).

Previous studies have shown that the pore systems of coal samples are complex, with most pores in coal being nanoscale (Mastalerz et al., 2012; Wang et al., 2014; Nie et al., 2015; Yan et al., 2020; Yu et al., 2020). Coalbed methane researchers usually use CO_2 adsorption experiments to study micropores (<2 nm) (Nie et al., 2015; Zhao et al., 2016; Hu et al., 2020), and they use mercury injection experiments and N_2 adsorption experiments to characterize the mesopores (2–50 nm) and macropores (>50 nm) in coal (Cai et al., 2013). In addition, scanning electron microscopy (SEM) has been used to observe pores in coal. However, the SEM technique can only observe pores larger than 30 nm (Li et al., 2020; Zou et al., 2020). Although many techniques have been applied in studies of coal pores, some key issues regarding coal pores remain unclear. For example, we do not know how differently sized pores connect or the generation mechanism of different types of pores. Pores are not only storage spaces but also transport channels of coalbed methane. Thus, the lack of clarity in the pore system limits the effective exploration and exploitation of coalbed methane.

Laboratory studies and exploration data have shown that the coalbed methane content of anthracite coal reservoirs is very high (Qin et al., 2018; Wang et al., 2020). However, the reason for the difficulty in extracting these coalbed methane molecules remains unclear (Wang Ruyue et al., 2018a; 2021). Therefore, this study aims to determine the key factors affecting methane storage and transport tunnels. Eight anthracite coal samples were collected from Anzenan coalbed methane blocks in the Qinshui Basin, China. Low-pressure N_2 adsorption experiments, mercury injection experiments, and SEM were performed to study the pore systems in anthracite coal. In addition, methane isothermal adsorption experiments were conducted to investigate the methane storage in coal.

2 Samples and methods

2.1 Samples

Samples were collected from coalbed methane drilling cores in the Anzenan coalbed methane block. The Anzenan coalbed methane block is located in the Qinshui Basin, the most successful coalbed methane basin in China (Qin et al., 2018). Four of the eight coal samples belong to the 10# coal seam, and the other four belong to the 11# coal seam. Sampling was conducted from top to bottom without channel sampling. All the samples were anthracite coal, and the vitrinite reflectance (VRo) was approximately 2.1%. The ash yield of the coal samples ranged from 9.49% to 30.45%, with an average of 22.57%. The ash yields of the samples from the 10# coal seam were usually higher than those of the 11# coal sample. In terms of the maceral composition, vitrinite comprised more than 80% of the total organic matter in coal samples. Inertinite content ranged from 5.89% to 19.21%, with an average of 14.23%.

2.2 Experiments

2.2.1 High-pressure mercury injection experiments

High-pressure mercury injection experiments have proven to be one of the most effective methods for testing pores >10 nm in size (Okolo et al., 2015; Guan et al., 2020). This method has

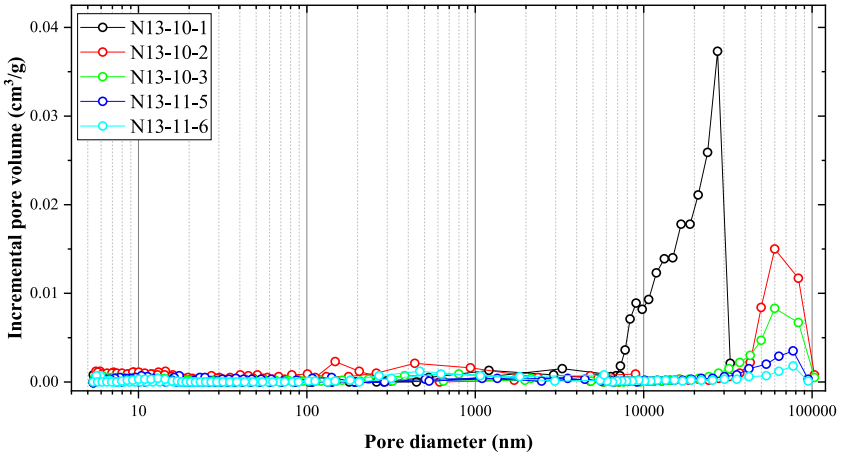

FIGURE 2
Pore size distribution of the coal sample obtained from the high-pressure mercury injection experiment.

advantages, including a wide pore-testing range (Okolo et al., 2015). Before testing, the coal samples were crushed into small pieces (approximately 1 cm^3). During the experiment, the test pressure was set to approximately 1–40,000 psi, and the corresponding pore diameters ranged from approximately 200,000 to 5 nm.

2.2.2 N_2 adsorption experiment

Low-temperature N_2 adsorption experiments are commonly used to test the nanopores in porous materials (Zhao et al., 2016; Wang et al., 2017; Wang et al., 2018b). The size of the pores tested by N_2 adsorption experiments usually ranges from 2 to 300 nm (Clarkson et al., 2013). The testing instrument used in this study was ASAP 2420 (Micromeritics). The experimental temperature was 77 K. Approximately 2–3 g of the powder sample was used in the experiment. As some air molecules can be adsorbed in the pores of coal and occupy pore space, automatic degassing was performed before the experiment. The degassing process would reduce the effect of adsorbed air in the pores of the coal samples. Considering that high degassing temperatures may cause changes in the pore structure of the coal, as coal will undergo further coalification at elevated temperatures, the degassing temperature should not be set too high. In addition, based on the previous study by Adesida et al. (2011), when the degassing temperature does not exceed 100°C, it does not significantly affect the experimental results. During the experiment, the equilibration interval was set to 10 s.

2.2.3 Methane isothermal experiment

Methane isothermal experiments were performed according to the Chinese standard GB/T 19560-2008. Before the experiment, the samples were crushed to 60–80 mesh. During the experiment, the temperature was set to 30°C. Approximately 30 g of the coal powder sample was used during the experiment. Moisture was added to the coal samples before they were placed in the sample cell. Helium was used to measure the sample volume and vacuum space.

2.2.4 SEM

SEM was performed using the ZEISS Scanning Electron Microscope. The coal samples used in the SEM experiment were blocks rather than power samples. Pores in the coal samples were examined during the experiment. Some typical minerals were also observed.

3 Results

3.1 Experimental data of high-pressure mercury injection

The mercury injection and extraction curves of the five coal samples are shown in Figure 1. It can be seen that the hysteresis loops of the mercury injection and extraction curves are narrow. This indicated that most of the mercury injected into the coal sample was extracted when the pressure decreased, and the pores in the coal samples were mainly open. Based on Figure 1, it can be seen that the amount of intruded mercury in sample N13-10-1 was much larger than that of the other coal samples. The main growth in the intruded mercury volume is mainly located at 5–20 psi. In addition, a slight increase can also be observed in the high-pressure stage (pressure is greater than 10,000 psi). It should also be noted that at high-pressure stages, small nanopores generally tend to be overestimated due to the compression effect of the coal matrix (Peng et al., 2017; Li et al., 2021). However, in the samples discussed in this study, these compression effects are not apparent. For example, the experimental data of N13-11-6 showed that with the mercury injection pressure increasing from 2,081.311 psi to 27,866.113 psi, the cumulative intruded mercury volume remained unchanged at 0.0105 mL/g.

Figure 2 illustrates the pore size distribution data of the coal sample obtained from the high-pressure mercury experiment. The pores in the coal were mainly macropores (larger than 50 nm). The peaks of the incremental pore volume curve were mainly located at 10,000 nm to 100,000 nm. The incremental pore volume with a pore size smaller than 1,000 nm was low, indicating that a few nanopores were formed in the coal samples. In addition, the peak

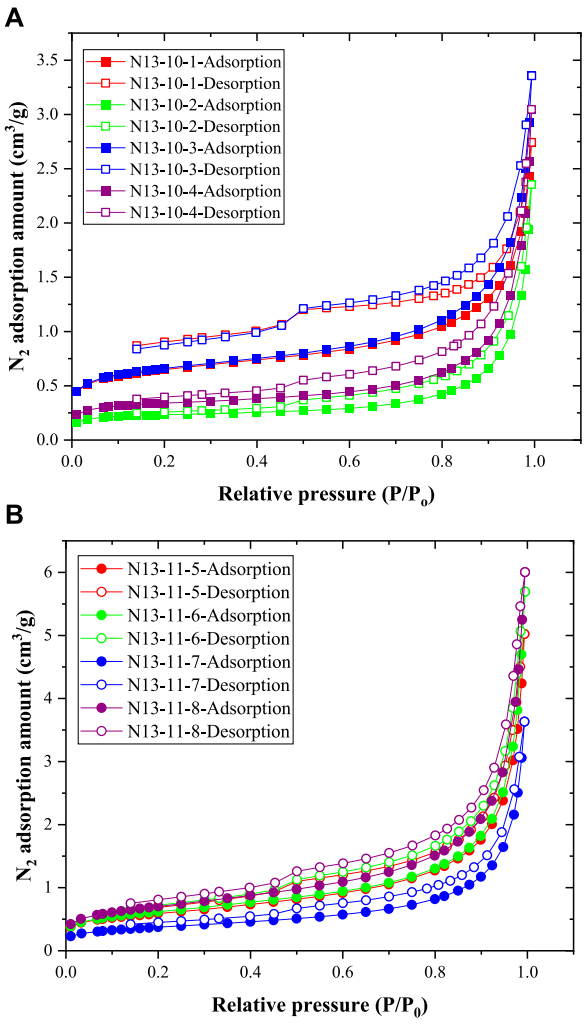

FIGURE 3
N_2 adsorption and desorption curves of coal samples: **(A)** data of four coal samples from the 10# coal seam; **(B)** data of the other four coal samples from the 11# coal seam.

of the incremental volume in the N13-10-1 sample was mainly located at 10,000–30,000 nm, and comparably, the peaks of the incremental volume of the other four coal samples were mainly located between 40,000 nm and 100,000 nm. These large pores are mainly cracks and cleats in the coal sample, which can form during both the coalification and sample preparation processes. In summary, the most important result of the mercury injection experiment (Figures 1, 2) is that a few nanopores (<1,000 nm) were found.

3.2 Experimental data of the low-pressure N_2 adsorption experiment

The N_2 adsorption and desorption curves of the eight coal samples obtained in the N_2 adsorption experiments are shown in Figures 3A, B. The N_2 adsorption and desorption curves of the coal samples from the 10# coal seam differed slightly from those of the 11# coal seam. First, the N_2 adsorption amounts of the coal samples from the 10# coal seam were smaller than those from the 11# coal seam. Second, the hysteresis loops of the coal samples from the 10# coal seam were larger than those from the 11# coal seam. In addition, for all eight coal samples, the N_2 adsorption amount increased significantly when the relative pressure exceeded 0.8. In addition, the desorption curves decreased at a P/P_0 ratio of approximately 0.5.

Based on the N_2 adsorption data and BJH model, the pore size distribution data were calculated, as shown in Figure 4. Generally, the incremental pore volume increased with increasing pore size. This indicates that larger nanopores contribute significantly more pore volume than smaller nanopores. Among the eight coal samples, the incremental pore volumes of the four coal samples (N13-10-1, N13-10-2, N13-10-3, and N13-10-4) from the 10# coal seam were smaller than those from the 11# coal seam (N13-11-5, N13-11-6, N13-11-7, and N13-11-8).

The pore surface area distribution is illustrated in Figure 5. These data were calculated using the BJH model and N_2 adsorption data. Comparing Figures 4, 5, the pore surface area distribution curves significantly differed from the pore volume size distribution. Because the pore surface area of smaller nanopores is much larger than that of larger nanopores of the same volume, pores smaller than 10 nm contributed to a large proportion of the total pore surface area. In addition, there were peaks in the pore surface area curves located at 30–50 nm, indicating that the large nanopores contributed significantly to the pore surface area. Similar to the pore volume size distribution, the pore surface area at each pore size of the coal samples from the 11# coal seam was larger than that of the 10# coal seam.

3.3 Experimental data of high-pressure methane adsorption

Methane adsorption data are shown in Figure 6. The lines in Figure 6 show the fitting lines for the Langmuir adsorption equation. The fitting coefficient (R^2) values were all approximately 0.99, indicating that the methane adsorption behavior of these coal samples agreed with the Langmuir adsorption model. Generally, the incremental amount in methane adsorption capacity increased with increasing pressure. In the low-pressure stage (<3 MPa), methane adsorption increased quickly. However, in the high-pressure stage, the amount of methane adsorbed increases slightly with increasing pressure. The coal sample N13-10-1 exhibited the largest amount of methane adsorption at each pressure. The methane adsorption capacity of sample N13-11-6 was the lowest.

4 Discussion

4.1 Nanopore and micro-scale pores in coal

Previous studies identified different types of pores in coal (Laubach et al., 1998; Mastalerz et al., 2012; Okolo et al., 2015; Liu et al., 2017). In terms of pore size, coal pores can be divided into

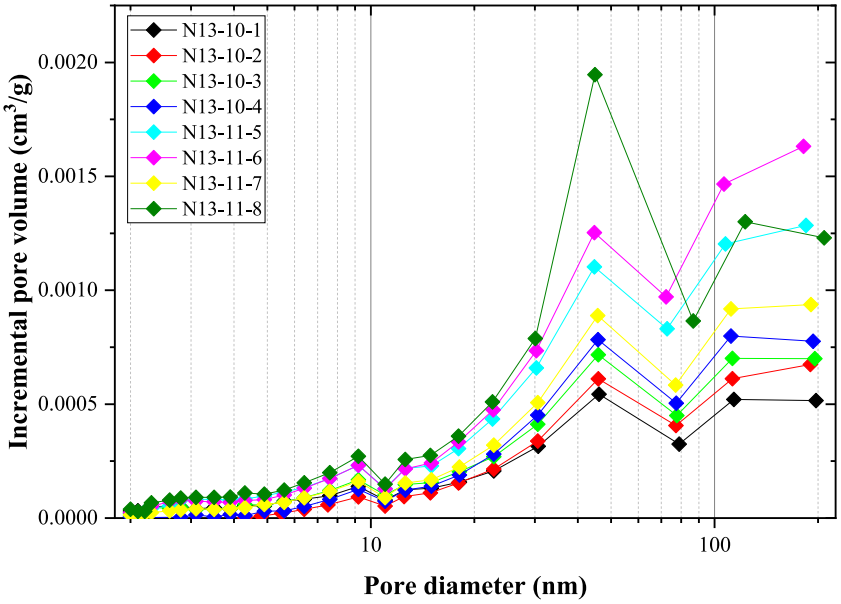

FIGURE 4
Pore size distribution of the eight coal samples obtained from the N_2 adsorption experiment.

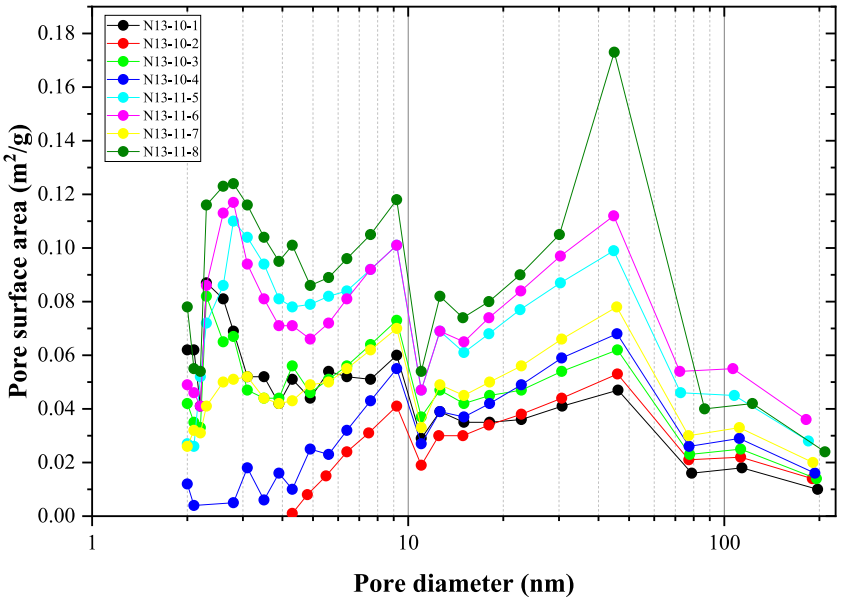

FIGURE 5
Pore surface area distribution of the coal samples.

micropores (<2 nm), mesopores (2–50 nm), macropores (>50 nm), fractures, and cleats (Okolo et al., 2015; Zou et al., 2016). Pores in coal can be divided into organic and inorganic pores (clay pores, pyrite pores, etc.) (Liu et al., 2017). Mesopores and nanopores were rare, as illustrated in Figure 4. The pore volume of the 2–300 nm pores in the coal samples, as obtained from the N_2 adsorption experiment, was less than 0.01 cm^3/g, which is relatively low (Wang et al., 2022). A previous study found that organic matter can provide many micropores, which are the primary sites for methane adsorption (Liu et al., 2021). Thus, the methane adsorption capacity increased with increasing organic matter content in coal.

Figure 7 shows the correlation between the pore volume obtained from the N_2 adsorption experiment and ash yield. With increasing ash yield, the pore volume (2–300 nm pores) of the coal samples increased linearly. This means that minerals

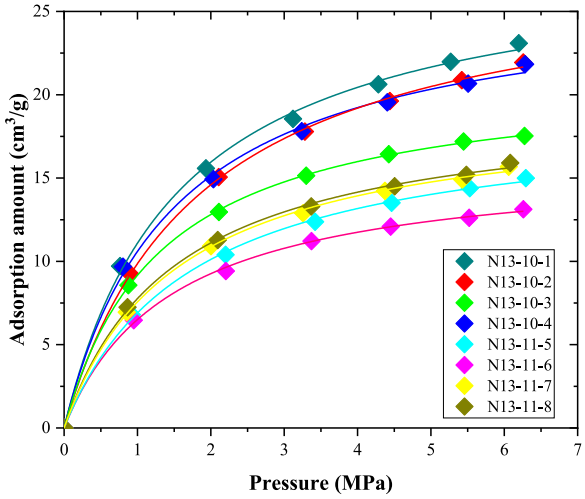

FIGURE 6
Methane isothermal data of the coal samples (30°C).

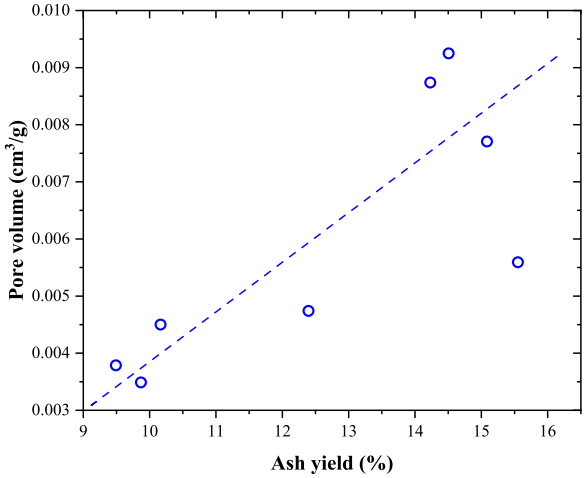

FIGURE 7
Correlation between pore volume obtained by the N_2 adsorption experiment and ash yield.

have a positive effect on the generation of 2–300 nm pores. SEM observations revealed small amounts of organic pores in the coal samples. Although some organic pores were observed, they appeared to be isolated. In the N_2 adsorption experiments, the tested pores were connected to the outside environment. In addition, although some methane molecules may be present in the isolated pores, they are not transported to the coalbed methane wells because there are no transport tunnels for these molecules. Some inorganic pores were observed in the SEM images. As shown in Figure 8, some organic pores were formed by pyrites, and some inorganic pores were formed between the inorganic particles.

4.2 Key factors controlling the methane adsorption capacity of coal

The methane adsorption capacity of coal is controlled by different factors, as suggested in previous studies (Bustin and Clarkson, 1998; Laxminarayana and Crosdale, 1999; Laxminarayana and Crosdale, 2002). During coalification, the methane adsorption capacities of coal samples first increase and then decrease (moisture-equipped coal samples) (Zhong, 2004). In addition, the ash yield, maceral composition, and pore structure are important factors affecting the methane adsorption capacity (Bustin and Clarkson, 1998; Laxminarayana and Crosdale, 1999; Laxminarayana and Crosdale, 2002). In this study, because the coal samples were collected from the drilling core, the maturity of all the samples was similar (Table 1). Thus, it is necessary to investigate other factors that control the methane adsorption capacity. Figure 9 shows the correlation between the Langmuir volume and ash yield. With increasing ash yield, the Langmuir volume decreased linearly. This indicates that the methane adsorption capacity of the minerals in the coal was very low. These minerals contributed little to the total methane adsorption. Previous studies found that clay minerals in coal have methane adsorption capacities. In most previous studies, the minerals in coal decreased the methane adsorption amount (Laxminarayana and Crosdale, 1999).

As illustrated in Figure 10, the relationship between the Langmuir volume and BET surface area (obtained from the N_2 adsorption experiment) of these coal samples was not very obvious. Overall, the Langmuir volume decreases with increasing BET surface area. A similar correlation was also found in Figure 11, where the correlation between the Langmuir volume and pore volume was obtained from the N_2 adsorption amount. With an increase in the volume of the 2–300 nm pores, the methane adsorption capacity decreased. The BET surface area and pore volume obtained from the low-pressure N_2 adsorption experiment were contributed by 2–300 nm pores. However, the number of 2–300 nm pores (obtained from the N_2 adsorption experiment) in the coal samples was very low. In addition, micropores (<2 nm) mainly contributed to the total pore surface area of the coal samples. Methane molecules were mainly adsorbed in the micropores because adsorption was caused by the interaction forces between the methane molecules and the coal surface. These mesopores have a weak effect on the methane adsorption capacity. The 2–300 nm pores in coal were mainly contributed by minerals, and as the mineral content increased, the pore volume increased. Comparably, the methane adsorption capacity was mainly contributed by organic matter and decreased with increasing mineral content.

Considering that minerals have a significant effect on the methane adsorption capacity, the methane adsorption capacity on an ash-free basis was calculated (Equation 1). With increasing volatile matter content, both the Langmuir volume and ash-free Langmuir volume decreased. When the influence of minerals was removed, volatile matter had a negative effect on the methane adsorption capacity. There may be several reasons why the methane adsorption capacity decreased with increasing volatile matter content. During this stage (anthracite coal), micropores were formed between the aromatic rings, and a lower volatile matter content indicated more aromatic rings (Liu et al., 2021). During the volatile

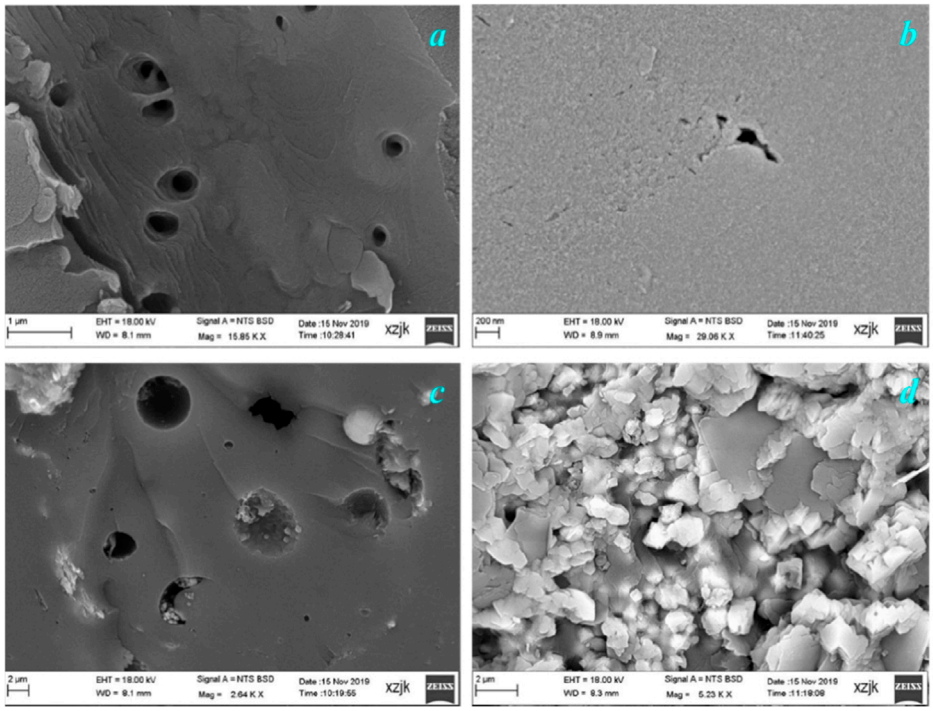

FIGURE 8
Pores in coal sample imaged by the SEM experiment. **(A)** Organic pores (N13-10-1 coal sample), **(B)** organic pores (N13-10-4 coal sample), **(C)** organic and inorganic pores formed by pyrite minerals (N13-10-1 coal sample), and **(D)** inorganic pores (N13-10-3 coal sample).

TABLE 1 Properties of the coal samples.

Sample no.	Coal seam	Vitrinite reflectance	Proximate analysis				Maceral composition	
			M_{ad} (%)	Ad (%)	V_{daf} (%)	FC_d (%)	Vitrinite (%)	Inertinite (%)
N13-10-1	10#	2.13	1.24	12.95	9.49	78.79	94.11	5.89
N13-10-2	10#	2.42	1.16	16.35	9.87	75.39	80.79	19.21
N13-10-3	10#	2.06	0.64	22.87	12.40	67.57	80.87	19.13
N13-10-4	10#	2.10	1.12	14.84	10.17	76.51	81.33	18.67
N13-11-5	11#	2.30	0.88	30.45	15.09	59.06	85.6	14.4
N13-11-6	11#	2.17	0.81	29.09	14.23	60.82	87.2	12.8
N13-11-7	11#	2.10	0.68	29.43	15.55	59.60	89.55	10.45
N13-11-8	11#	2.02	0.74	24.58	14.51	64.48	86.72	13.28

matter test, some minerals generated gas. In addition, volatile matter was produced during mineral catalysis. Thus, more minerals resulted in more volatile matter. Considering that minerals have a negative effect on methane adsorption capacity, the Langmuir volume decreased with increasing volatile matter (Figure 12). We also compared the methane adsorption capacities of different maceral compositions and found that the maceral composition had a weak effect on the methane adsorption capacity of the coal samples. This is mainly because the maturities of the coal samples are relatively high (Ro>2.0%), and the structure of vitrinite is similar to that of inertinite.

$$V_{af} = \frac{V}{(1\text{-}Ad)}. \quad (1)$$

Here, V_{af} represents the methane adsorption capacity (Langmuir volume) on an ash-free basis; V represents the Langmuir volume obtained from isothermal methane experiment; and Ad represents the ash yield.

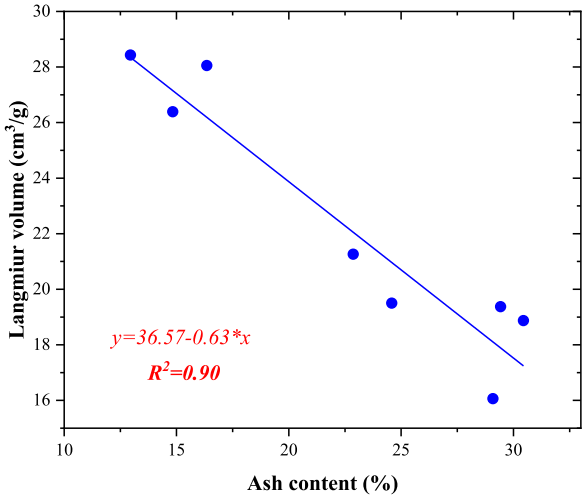

FIGURE 9
Correlation between the methane adsorption capacity (Langmuir volume) and ash yield.

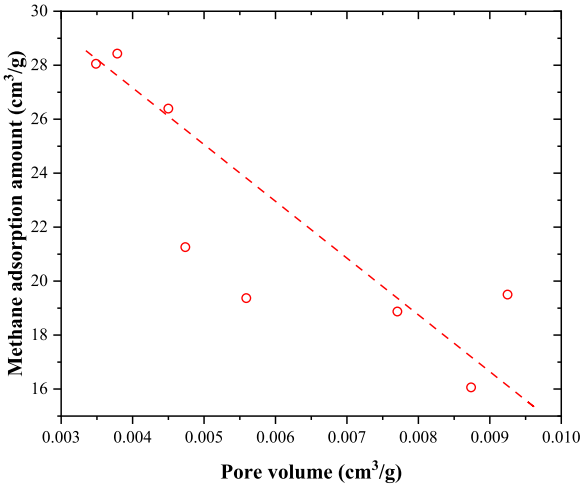

FIGURE 11
Correlation between Langmuir volume and pore volume obtained from the N_2 adsorption amount.

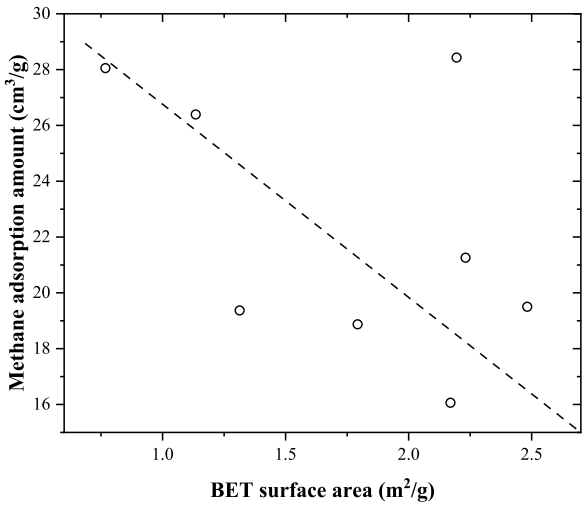

FIGURE 10
Relationship between the methane adsorption capacity (Langmuir volume) and BET surface area obtained from the N_2 adsorption experiment.

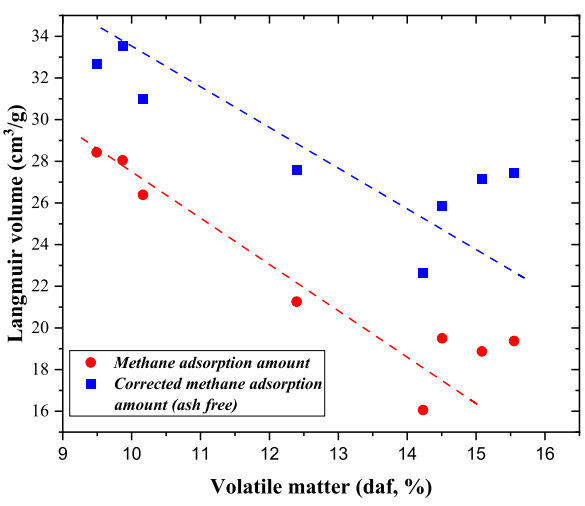

FIGURE 12
Correlation between the volatile matter and methane adsorption capacity.

4.3 Effects of the pore system and adsorption capacity on coalbed methane extraction

The coal samples in this study were all anthracite coal, and as shown in Figure 6, these samples had a strong methane adsorption capacity. Based on previous studies and the experimental data obtained in this study, anthracite has a strong methane adsorption capacity. This is one of the key reasons for the abundance of coalbed methane resources in anthracite coal samples. However, the mercury injection and the low-pressure N_2 adsorption experiments showed that the volume and surface area of the mesopores and nanoscale macropores were quite low, indicating that there were few mesopores and nanoscale macropores in the anthracite coals. Based on the SEM observations, a similar conclusion was drawn; mesopores and macropores were found on the surface of the coal matrix. In addition, as the volume of mesopores and nanoscale macropores increased with the mineral content, inorganic pores occupied a significant proportion of the total mesopores and nanoscale macropores. This means that the organic matter in coal rarely forms mesopores or nanoscale macropores. In addition, the mesopores and nanopores contributed little to the total amount of methane adsorbed because they could not provide many adsorption sites. Comparably, methane molecules in anthracite are mainly stored in micropores (Cheng et al., 2017; Liu et al., 2021). These micropores are primarily formed by coal molecules (Liu et al., 2018).

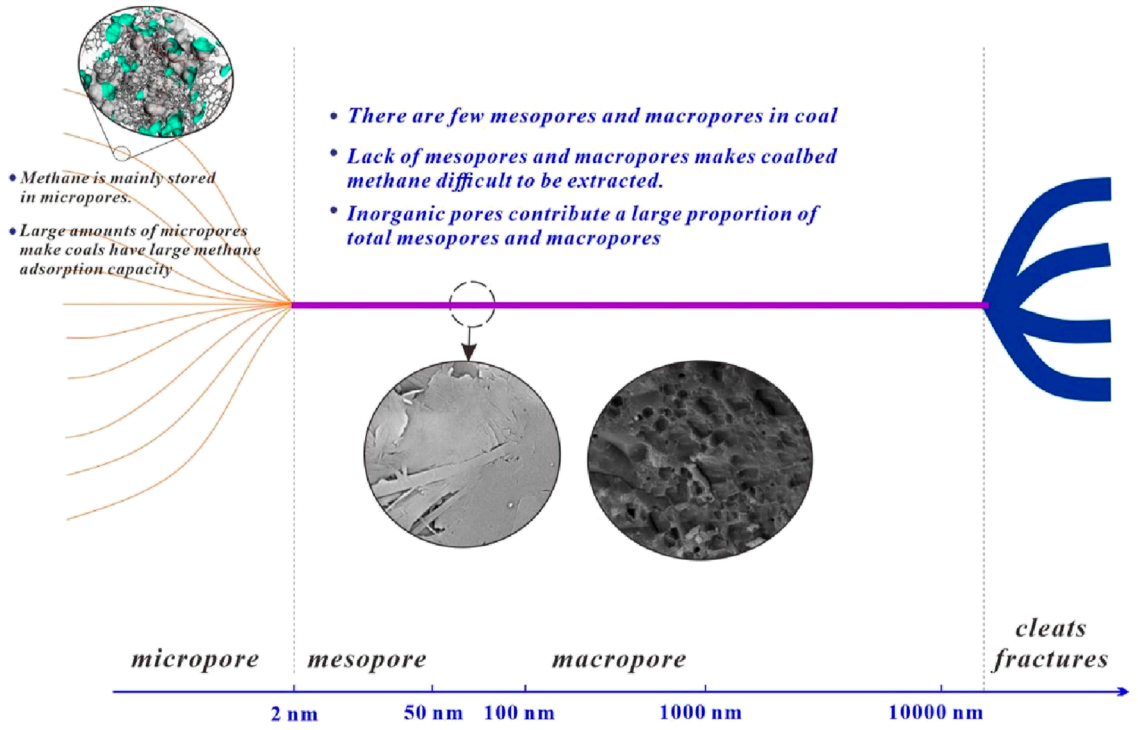

FIGURE 13
Pore system and the effect on coalbed methane extraction in anthracite coals.

Based on mercury injection, low-pressure N_2 adsorption, SEM observations, and methane isothermal adsorption experimental data, the pore system of anthracite coals was clarified (Figure 13). The pore system of anthracite can be divided into three parts. The size and formation mechanisms of the different parts are different. The first part consisted of micropores. Because these pores are formed by coal molecules, micropores are universally developed in the coal matrix (Cheng et al., 2017; Liu et al., 2021). Thus, numerous micropores are present in anthracite coal (Liu et al., 2018). These pores provide a large space and surface area for methane adsorption, and anthracite coals have a large methane adsorption capacity, as illustrated by the methane isothermal adsorption data (Figure 6). The second part comprised mesopores and nanoscale macropores. The volumes and surface areas of these pores were quite low. Additionally, a large proportion of these pores were inorganic. The third part comprised cleats and fractures. The sizes of these parts were on the micro-meter scale. These pores can form during coalification and tectonic movements (Laubach et al., 1998; Cheng and Pan, 2020). There were a certain number of cleats and fractures in the coal samples used in this study, as indicated by the mercury injection data.

It should be noted that most of the methane molecules are stored in micropores, and when these methane molecules are transported outside the coal, they usually need to be transported through mesopores and macropores and then to fractures and cleats. Only a small number of micropores are directly connected to the fractures and cleats in the coal. However, there were a few mesopores and nanoscale macropores. This means that there are insufficient tunnels to transport methane molecules from the micropores to the cleats and fractures. This makes the extraction of coalbed methane difficult. In the exploitation of coalbed methane, it is important to create tunnels to facilitate the transport of methane molecules from micropores to cleats and fractures. The pore structure and methane adsorption characteristics of anthracite coal observed in this study are common features of anthracite (Markowski, 1998; Adsul et al., 2023). Anthracite from other regions of the world also exhibits similar characteristics, such as well-developed micropores, a lack of nanoscale pores, and strong adsorption capacity, but a shortage of nanoscale migration pathways (Mohanty and Pal, 2017). Therefore, these findings can be universally applied to research on coalbed methane extraction from anthracite.

5 Conclusion

(1) Different types of pore characterization methods (low-pressure N_2 adsorption, mercury injection experiment, and SEM observation) showed that there were few mesopores and nanoscale macropores in the eight anthracite coal samples from the Anzenan coalbed methane block in the Qinshui Basin, China.
(2) The volume of 2–300 nm pores in the eight anthracite coal samples increased with increasing ash yield, indicating that the organic matter of anthracite coal rarely formed pores on this scale.
(3) The anthracite coal had a large methane adsorption capacity, and the Langmuir volume increased with decreasing ash yield, indicating that the methane molecules were mainly

adsorbed in the micropores of the organic matter in the coal. Considering that the coal samples are typical anthracite, these findings are also applicable to other anthracite coals worldwide. Therefore, creating pore connectivity pathways is crucial for the extraction of coalbed methane from anthracite coal globally.

Data availability statement

The original contributions presented in the study are included in the article/supplementary material; further inquiries can be directed to the corresponding authors.

Author contributions

QX: conceptualization, data curation, formal analysis, funding acquisition, investigation, methodology, project administration, resources, software, supervision, validation, visualization, writing–original draft, and writing–review and editing. RW: methodology, investigation, supervision, and writing–review and editing. ZW: methodology, conceptualization, data curation, formal analysis, project administration, resources, and writing–original draft. YZ: conceptualization, data curation, formal analysis, funding acquisition, investigation, methodology, project administration, resources, software, supervision, validation, visualization, and writing–original draft. QM: conceptualization, data curation, formal analysis, investigation, validation, visualization, and writing–original draft. ZZ: data curation, investigation, methodology, supervision, and writing–review and editing. XB: data curation, formal analysis, investigation, methodology, and writing–original draft. FX: data curation, investigation, methodology, validation, visualization, and writing–original draft.

Funding

The author(s) declare that financial support was received for the research, authorship, and/or publication of this article. This work was supported by the corporate Scientific Research Project [LGP FH-02 (ZJ) 2206007] and Research and Application of Key Technologies for the Integration of Exploration and Development of Deep Coalbed Methane in the Yushe–Wuxiang Block, Shanxi Province.

Conflict of interest

Author ZW was employed by PetroChina Coalbed Methane Company Limited. Author FX was employed by Shaanxi Tiancheng Petroleum Technology Company Limited.

The remaining authors declare that the research was conducted in the absence of any commercial or financial relationships that could be construed as a potential conflict of interest.

Publisher's note

References

Adesida, A. G., Akkutlu, I. Y., Resasco, D. E., and Rai, C. S. (2011). "Kerogen pore size distribution of Barnett shale using DFT analysis and Monte Carlo simulations[C]," in *SPE annual technical conference and exhibition. SPE: spe-147397-MS.*

Adsul, T., Ghosh, S., Kumar, S., Tiwari, B., Dutta, S., and Varma, A. K. (2023). Biogeochemical controls on methane generation: a review on Indian coal resources. *Minerals* 13 (5), 695. doi:10.3390/min13050695

Akhondzadeh, H., Keshavarz, A., Awan, F. U. R., Ali, M., Al-Yaseri, A., Liu, C., et al. (2021). Liquid nitrogen fracturing efficiency as a function of coal rank: a multi-scale tomographic study. *J. Nat. gas Sci. Eng.* 95, 104177. doi:10.1016/j.jngse.2021.104177

Bustin, A. M. M., Bustin, R. M., Chikatamarla, L., Downey, R., and Mansoori, J. (2016). Learnings from a failed nitrogen enhanced coalbed methane pilot: piceance Basin, Colorado. *Int. J. Coal Geol.* 165, 64–75. doi:10.1016/j.coal.2016.07.010

Bustin, R. M., and Clarkson, C. R. (1998). Geological controls on coalbed methane reservoir capacity and gas content. *Int. J. Coal Geol.* 38 (1), 3–26. doi:10.1016/s0166-5162(98)00030-5

Cai, Y., Liu, D., Pan, Z., Yao, Y., Li, J., and Qiu, Y. (2013). Pore structure and its impact on CH4 adsorption capacity and flow capability of bituminous and subbituminous coals from Northeast China. *Fuel* 103, 258–268. doi:10.1016/j.fuel.2012.06.055

Cai, Y., Liu, D., Yao, Y., Li, J., and Qiu, Y. (2011). Geological controls on prediction of coalbed methane of No. 3 coal seam in Southern Qinshui Basin, North China. *Int. J. Coal Geol.* 88 (2-3), 101–112. doi:10.1016/j.coal.2011.08.009

Chalmers, G. R. L., and Marc Bustin, R. (2007). On the effects of petrographic composition on coalbed methane sorption. *Int. J. Coal Geol.* 69 (4), 288–304. doi:10.1016/j.coal.2006.06.002

Chattaraj, S., Mohanty, D., Kumar, T., and Halder, G. (2016). Thermodynamics, kinetics and modeling of sorption behaviour of coalbed methane – a review. *J. Unconv. Oil Gas Resour.* 16, 14–33. doi:10.1016/j.juogr.2016.09.001

Cheng, Y., Jiang, H., Zhang, X., Cui, J., Song, C., and Li, X. (2017). Effects of coal rank on physicochemical properties of coal and on methane adsorption. *Int. J. Coal Sci. & Technol.* 4 (2), 129–146. doi:10.1007/s40789-017-0161-6

Cheng, Y., and Pan, Z. (2020). Reservoir properties of Chinese tectonic coal: a review. *Fuel* 260, 116350. doi:10.1016/j.fuel.2019.116350

Cho, S., Kim, S., and Kim, J. (2019). Life-cycle energy, cost, and CO2 emission of CO2-enhanced coalbed methane (ECBM) recovery framework. *J. Nat. Gas Sci. Eng.* 70, 102953. doi:10.1016/j.jngse.2019.102953

Clarkson, C. R., Solano, N., Bustin, R., Bustin, A., Chalmers, G., He, L., et al. (2013). Pore structure characterization of North American shale gas reservoirs using USANS/SANS, gas adsorption, and mercury intrusion. *Fuel* 103, 606–616. doi:10.1016/j.fuel.2012.06.119

Crosdale, P. J., Beamish, B. B., and Valix, M. (1998). Coalbed methane sorption related to coal composition. *Int. J. COAL Geol.* 35 (1-4), 147–158. doi:10.1016/s0166-5162(97)00015-3

Fan, C., Elsworth, D., Li, S., Chen, Z., Luo, M., Song, Y., et al. (2019). Modelling and optimization of enhanced coalbed methane recovery using CO2/N2 mixtures. *Fuel* 253, 1114–1129. doi:10.1016/j.fuel.2019.04.158

Guan, M., Liu, X., Jin, Z., and Lai, J. (2020). The heterogeneity of pore structure in lacustrine shales: insights from multifractal analysis using N2 adsorption and mercury intrusion. *Mar. Petroleum Geol.* 114, 104150. doi:10.1016/j.marpetgeo.2019.104150

Hou, X., Liu, S., Zhu, Y., and Yang, Y. (2020). Evaluation of gas contents for a multi-seam deep coalbed methane reservoir and their geological controls: *in situ* direct method versus indirect method. *Fuel* 265, 116917. doi:10.1016/j.fuel.2019.116917

Hu, B., Cheng, Y., He, X., Wang, Z., Jiang, Z., Wang, C., et al. (2020). New insights into the CH4 adsorption capacity of coal based on microscopic pore properties. *FUEL* 262 (UNSP 116675), 116675. doi:10.1016/j.fuel.2019.116675

Joshi, D., Prajapati, P., Sharma, P., and Sharma, A. (2023). Past, present and future of Coal Bed Methane (CBM): a review with special focus on the Indian scenario. *Int. J. Coal Prep. Util.* 43 (2), 377–402. doi:10.1080/19392699.2022.2051014

Laubach, S. E., Marrett, R. A., Olson, J. E., and Scott, A. R. (1998). Characteristics and origins of coal cleat: a review. *Int. J. Coal Geol.* 35 (1–4), 175–207. doi:10.1016/s0166-5162(97)00012-8

Laxminarayana, C., and Crosdale, P. J. (1999). Role of coal type and rank on methane sorption characteristics of Bowen Basin, Australia coals. *Int. J. Coal Geol.* 40 (4), 309–325. doi:10.1016/s0166-5162(99)00005-1

Laxminarayana, C., and Crosdale, P. J. (2002). Controls on methane sorption capacity of Indian coals. *AAPG Bull.* 86 (2), 201. doi:10.1306/61eeda8a-173e-11d7-8645000102c1865d

Li, F., Jiang, B., Cheng, G., and Song, Y. (2022). Methane adsorption behavior and energy variations of brittle tectonically deformed coal under high temperature and high pressure. *ACS Omega* 7 (3), 2737–2751. doi:10.1021/acsomega.1c05383

Li, Y., Song, D., Liu, S., Ji, X., and Hao, H. (2021). Evaluation of pore properties in coal through compressibility correction based on mercury intrusion porosimetry: a practical approach. *Fuel* 291, 120130. doi:10.1016/j.fuel.2021.120130

Li, Y., Yang, J., Pan, Z., and Tong, W. (2020). Nanoscale pore structure and mechanical property analysis of coal: an insight combining AFM and SEM images. *Fuel Guildf.* 260, 116352. doi:10.1016/j.fuel.2019.116352

Liu, S., Sang, S., Wang, G., Ma, J., Wang, X., Wang, W., et al. (2017). FIB-SEM and X-ray CT characterization of interconnected pores in high-rank coal formed from regional metamorphism. *J. Petroleum Sci. Eng.* 148, 21–31. doi:10.1016/j.petrol.2016.10.006

Liu, Y., Zhang, C., and Zhang, Y. (2021). Evolution mechanism of methane adsorption capacity in vitrinite-rich coal during coalification. *J. Nat. Gas Sci. Eng.* 96, 104307. doi:10.1016/j.jngse.2021.104307

Liu, Y., Zhu, Y., Liu, S., Chen, S., Li, W., and Wang, Y. (2018). Molecular structure controls on micropore evolution in coal vitrinite during coalification. *Int. J. Coal Geol.* 199, 19–30. doi:10.1016/j.coal.2018.09.012

Lorenz, K., and Wessling, M. (2013). How to determine the correct sample volume by gravimetric sorption measurements. *Adsorption* 19 (6), 1117–1125. doi:10.1007/s10450-013-9537-0

Markowski, A. K. (1998). Coalbed methane resource potential and current prospects in Pennsylvania. *Int. J. Coal Geol.* 38 (1-2), 137–159. doi:10.1016/s0166-5162(98)00036-6

Mastalerz, M., He, L., Melnichenko, Y. B., and Rupp, J. A. (2012). Porosity of coal and shale: insights from gas adsorption and SANS/USANS techniques. *Energy & Fuels* 26 (8), 5109–5120. doi:10.1021/ef300735t

Meng, Z., Yan, J., and Li, G. (2017). Controls on gas content and carbon isotopic abundance of methane in qinnan-east coal bed methane block, Qinshui Basin, China. *Energy & Fuels* 31 (2), 1502–1511. doi:10.1021/acs.energyfuels.6b03172

Mohamed, T., and Mehana, M. (2020). Coalbed methane characterization and modeling: review and outlook. *Energy Sources, Part A Recovery, Util. Environ. Eff.*, 1–23. doi:10.1080/15567036.2020.1845877

Mohanty, M. M., and Pal, B. K. (2017). Sorption behavior of coal for implication in coal bed methane an overview. *Int. J. Min. Sci. Technol.* 27 (2), 307–314. doi:10.1016/j.ijmst.2017.01.014

Moore, T. A. (2012). Coalbed methane: a review. *Int. J. Coal Geol.* 101, 36–81. doi:10.1016/j.coal.2012.05.011

Nie, B., Liu, X., Yang, L., Meng, J., and Li, X. (2015). Pore structure characterization of different rank coals using gas adsorption and scanning electron microscopy. *Fuel* 158, 908–917. doi:10.1016/j.fuel.2015.06.050

Okolo, G. N., Everson, R. C., Neomagus, H. W. J. P., Roberts, M. J., and Sakurovs, R. (2015). Comparing the porosity and surface areas of coal as measured by gas adsorption, mercury intrusion and SAXS techniques. *Fuel* 141, 293–304. doi:10.1016/j.fuel.2014.10.046

Peng, S., Zhang, T., Loucks, R. G., and Shultz, J. (2017). Application of mercury injection capillary pressure to mudrocks: conformance and compression corrections. *Mar. Petroleum Geol.* 88, 30–40. doi:10.1016/j.marpetgeo.2017.08.006

Perera, M. S. A., Ranjith, P. G., Choi, S. K., Airey, D., and Weniger, P., 2012. Estimation of gas adsorption capacity in coal: a review and an analytical study. *Int. Journal of Coal Preparation and Utilization*. 32(1): 25–55. doi:10.1080/19392699.2011.614298

Qin, Y., Moore, T. A., Shen, J., Yang, Z., Shen, Y., and Wang, G. (2018). Resources and geology of coalbed methane in China: a review. *Int. Geol. Rev.* 60 (5-6), 777–812. doi:10.1080/00206814.2017.1408034

Song, Y., Liu, S., Zhang, Q., Tao, M., Zhao, M., and Hong, F. (2012). Coalbed methane genesis, occurrence and accumulation in China. *Petroleum Sci.* 9 (3), 269–280. doi:10.1007/s12182-012-0209-6

Su, X., Lin, X., Liu, S., Zhao, M., and Song, Y. (2005). Geology of coalbed methane reservoirs in the southeast Qinshui Basin of China. *Int. J. Coal Geol.* 62 (4), 197–210. doi:10.1016/j.coal.2005.01.002

Tu, Q., Xue, S., Cheng, Y., Zhang, W., Shi, G., and Zhang, G. (2022). Experimental study on the guiding effect of tectonic coal for coal and gas outburst. *Fuel* 309, 122087. doi:10.1016/j.fuel.2021.122087

Wang, C., and Cheng, Y. (2023). Role of coal deformation energy in coal and gas outburst: a review. *Fuel Guildf.* 332, 126019. doi:10.1016/j.fuel.2022.126019

Wang, F., Cheng, Y., Lu, S., Jin, K., and Zhao, W. (2014). Influence of coalification on the pore characteristics of middle–high rank coal. *Energy & Fuels* 28 (9), 5729–5736. doi:10.1021/ef5014055

Wang, F., Yao, Y., Wen, Z., Sun, Q., and Yuan, X. (2020). Effect of water occurrences on methane adsorption capacity of coal: a comparison between bituminous coal and anthracite coal. *Fuel* 266, 117102. doi:10.1016/j.fuel.2020.117102

Wang, R., Gong, D., Leng, J., Wang, X., Cong, S., Ding, W., et al. (2017). Developmental characteristics of the Lower Cambrian Niutitang shale reservoir in Northern Guizhou area: a case study in the Cengong block. *Earth Sci. Front.* 24 (6), 286–299. doi:10.13745/j.esf.yx.2017-10-4

Wang, R., Hu, Z., Dong, L., Gao, B., Sun, C., Yang, T., et al. (2021). Advancement and trends of shale gas reservoir characterization and evaluation. *Oil & Gas Geol.* 42 (1), 54–65. doi:10.11743/ogg20210105

Wang, R., Hu, Z., and Long, S. (2022). Reservoir characteristics and evolution mechanisms of the upper ordovician wufeng-lower silurian longmaxi shale, Sichuan basin. *Oil & Gas Geol.* 43 (2), 353–364. doi:10.11743/ogg20220209

Wang, R., Hu, Z., and Nie, H., Comparative analysis and discussion of shale reservoir characteristics in the Wufeng–Longmaxi and Niutitang formations: a case study of the well JY1 in SE Sichuan Basin and well TX1 in SE Guizhou area. 2018b, 40 (5) 639–649.

Wang, R., Hu, Z., Sun, C., Liu, Z., Zhang, C., Gao, B., et al. (2018a). Comparative analysis of shale reservoir characteristics in the Wufeng-Longmaxi (O_3w-S_1l) and Niutitang ($\epsilon_1 n$) Formations: a case study of wells JY1 and TX1 in the southeastern Sichuan Basin and its neighboring areas, southwestern China. *Interpretation* 6 (4), SN31–SN45. doi:10.1190/int-2018-0024.1

Yan, J., Meng, Z., Zhang, K., Yao, H., and Hao, H. (2020). Pore distribution characteristics of various rank coals matrix and their influences on gas adsorption. *J. Petroleum Sci. Eng.* 189, 107041. doi:10.1016/j.petrol.2020.107041

Yu, S., Bo, J., Ming, L., Chenliang, H., and Shaochun, X. (2020). A review on pore-fractures in tectonically deformed coals. *Fuel* 278, 118248. doi:10.1016/j.fuel.2020.118248

Zhang, L., Aziz, N., Ren, T. X., and Wang, Z. (2011). Influence of temperature on coal sorption characteristics and the theory of coal surface free energy. *Procedia Eng.* 26, 1430–1439. doi:10.1016/j.proeng.2011.11.2320

Zhao, J., Xu, H., Tang, D., Mathews, J. P., Li, S., and Tao, S. (2016). A comparative evaluation of coal specific surface area by CO2 and N2 adsorption and its influence on CH4 adsorption capacity at different pore sizes. *Fuel* 183, 420–431. doi:10.1016/j.fuel.2016.06.076

Zhong, L. (2004). Adsorptive capacity of coals and its af fecting factors. *Earth Sci.* 29 (03), 327–332+368.

Zhong, L., and Zhang, X. (1990). The relationship between methane adsorption capacity and the rank and composition of coal. *Coal Geol. & Explor.* (04), 29–36+71-74.

Zou, G., She, J., Peng, S., Yin, Q., Liu, H., and Che, Y. (2020). Two-dimensional SEM image-based analysis of coal porosity and its pore structure. *Int. J. Coal Sci. & Technol.* 7, 350–361. doi:10.1007/s40789-020-00301-8

Zou, M., Wei, C., Huang, Z., Zhang, M., and Lv, X. (2016). Experimental study on identification diffusion pores, permeation pores and cleats of coal samples. *J. ENERGY Resour. TECHNOLOGY-TRANSACTIONS ASME* 138, 0212012. doi:10.1115/1.4031610

frontiers | Frontiers in Earth Science

TYPE Original Research
PUBLISHED 15 August 2024
DOI 10.3389/feart.2024.1443458

OPEN ACCESS

EDITED BY
Zhengguang Zhang,
China National Administration of Coal Geology (CNACG), China

REVIEWED BY
Xiaowei Hou,
Hefei University of Technology, China
Junjian Zhang,
Shandong University of Science and Technology, China
Ang Liu,
The Pennsylvania State University (PSU), United States

*CORRESPONDENCE
Yanming Zhu,
ym63z@cumt.edu.cn

RECEIVED 04 June 2024
ACCEPTED 05 August 2024
PUBLISHED 15 August 2024

CITATION
Mu X, Zhu Y, Dou K, Shi Y and Huang M (2024) Logging response prediction of high-lithium coal seam based on K-means clustering algorithm.
Front. Earth Sci. 12:1443458.
doi: 10.3389/feart.2024.1443458

Logging response prediction of high-lithium coal seam based on K-means clustering algorithm

Xiwei Mu[1,2,3,4], Yanming Zhu[1,2]*, Kailong Dou[1,2], Ying Shi[1,2] and Manli Huang[1,2]

[1]Key Laboratory of Coalbed Methane Resources and Reservoir Formation Process, Ministry of Education, China University of Mining and Technology, Xuzhou, China, [2]School of Resources and Geoscience, China University of Mining and Technology, Xuzhou, China, [3]Geological Exploration Research Institute, Guizhou Bureau of Coal Geological Exploration, Guiyang, China, [4]Guizhou Provincial Key Laboratory of Fluidized Mining of Coals, Guiyang, China

Lithium in coal, as a new type of associated mineral resource, has considerable potential for exploration. Exploration of high-lithium coal seams is essential for developing and using the associated lithium resources. To explore the distribution of lithium resources in the early stages of development in coal seams, the relationship between coal seam logging data and lithium content was analyzed by taking Guojiadi Coal Mine (China) as example. By analyzing the correlation between the different logging curves and the lithium content in coal and combining the K-means algorithm to identify the logging characteristics of different lithium-containing coal seams, we finally obtained the logging identification characteristics of high-lithium coal seams. The results reveal differences in the logging curves of coal seams with different lithium contents. The natural gamma and lateral resistivity of high-lithium coal seams are approximately 80 API and 100 Ω.M, respectively. Our study shows that the early identification of high-lithium coal seams can be evaluated from a logging perspective. We propose a preliminary identification method of high-lithium coal seam based on logging curve parameters by clustering analysis of borehole logging data to achieve accurate prediction.

KEYWORDS

lithium, high-lithium coal seam, logging curve, logging response, cluster analysis, Kmeans algorithm

1 Introduction

Lithium is a vital strategic metal that plays an important role in modern industry and new energy technology (Dai and Finkelman, 2018; Li et al., 2024). When the lithium content in coal exceeds a certain grade, lithium deposits associated with the coal can be formed as sedimentary lithium deposits (Zhao et al., 2022). Global lithium resources are plentiful, mainly distributed in North and South America. At the national level, lithium is distributed in the US, Australia, and China (Kesler et al., 2012; Ambrose and Kendall, 2020; Jiu et al., 2022). In recent years, European countries, Russia, South Africa, China, and other coal-producing countries have researched key metals such as lithium in coal and have successively discovered key metal deposits in the coal system (Dai et al., 2020). The development and use of associated lithium minerals in coal can be an important supplementary source of lithium resources, which is of great importance to the research

and development of metal element mineral resources in coal. China is rich in coal resources. The enrichment of associated lithium has been found in coal in many regions of China, and the quantity of resources is considerable (Zhang et al., 2024). Western Guizhou is a crucial coal-producing area in southwest China. The main coal-bearing strata are in the Upper Permian Longtan Formation. Coal from multiple Late Permian coal-bearing basins in western Guizhou is highly enriched in critical metals (Liu et al., 2019; Liu et al., 2021), particularly lithium. Most research on associated lithium resources in coal has focused on the geochemical characteristics, occurrence status, enrichment sources, and mineralization rules of key metals in coal based on numerous samples (Hu et al., 2018; Tang et al., 2022). Nevertheless, few studies have focused on predicting lithium enrichment areas in coal.

In exploration and drilling, a series of logging activities are often carried out on the borehole. Conventional logging mainly includes natural gamma logging and resistivity logging. Logging data record stratigraphic information, geophysical parameters, and other related information, which is widely used in lithofacies identification, stratigraphic division, and other fields (Yan et al., 2018; Day-Stirrat et al., 2021; Lai et al., 2023). In addition, trace element-abnormal strata can be realized through a deeper interpretation of the logging data. Many scholars use different data processing methods, such as machine learning, neural networks, support vector machines, and other methods, to interpret logging data from multiple angles and successfully achieve different purposes, such as coal rock detection and coal facies discrimination (Puskarczyk et al., 2019; Hayat et al., 2020; Baudzis et al., 2021). With the rapid development of modern logging technology, a substantial amount of data are produced in the process of logging. Nevertheless, choosing the appropriate means to deal with huge amounts of data is particularly important. As a big data analysis method, clustering analysis is suitable for processing of massive data and can extract effective key information (Amjad and Chen, 2020). The K-means algorithm is important in clustering analysis. The algorithm is simple and efficient and can be applied to different analysis purposes by flexibly selecting the K value (Ikotun et al., 2023). Zhang et al. (2024) utilized K-means clustering for data preprocessing and accurately predicted reservoir porosity and permeability using conventional logging curves as input. Jing et al. (2021) selected different mechanical parameters of rock samples, analyzed geophysical logging data based on the K-means dynamic clustering method, and realized a lithology classification. Lai et al. (2024) also used the K-means algorithm to realize the automatic identification of lithology and evaluated the water saturation of shale reservoirs in combination with logging curves. However, few studies have focused on the identification of abnormally high-lithium concentrations in coal seams using logging data.

Therefore, the J1301 well of Guojiadi Coal Mine in Liupanshui Coalfield of Western Guizhou was taken as the research object, and the systematic logging was carried out to determine the lithium content. Using the K-means clustering algorithm, we combined the logging data with the lithium content in the coal seam to obtain the logging response characteristics of the high-lithium coal seam. The whole well-logging data are identified. It is hoped that high-lithium coal seams can be identified during coal seam exploration and drilling to provide theoretical guidance for the exploration and development of associated lithium mineral resources in coal.

2 Samples and methods

2.1 Sample collection

The Guojiadi Coal Mine is a part of the Liupanshui Coalfield (Figure 1A), which is located in the southeast wing of the Qingshan Syncline in Panxian County and Pu'an County, southwest of the Liupanshui Coalfield, Guizhou Province (China). The main axis of the Qingshan syncline is distributed in the NE-SW direction, with an inclination angle of 3°–25°. The southeast limb is locally steep, and secondary folds and faults in the NE–SW direction have developed on both limbs (Huang and Qu, 2021). The Liupanshui Coalfield is located in western Guizhou Province and is a set of marine-terrigenous coal-bearing deposits (Figure 1B). The paleogeography of coal accumulation is the long delta plain type, and the sedimentary environment is the upper and lower delta plains. The main sedimentary system is the delta sedimentary system. The sedimentary type is based on distributary channel deposition, including natural levees, crevasse fans, and interdistributary bays on both sides of the river channel. The transition zone between the upper and lower delta plains is the ideal location for coal accumulation, with the best coal-bearing properties (Bilal et al., 2023; Jamaluddin et al., 2023). Generally, there are many coal seams, with mainly medium–thick coal seams. The coal seams are widely distributed. The stability is good, and the ash and sulfur contents are low (Jiang et al., 2020).

Well J1301 is located in the Guojiadi Coal Mine. The coal-bearing strata include coal seams No. 12, 17, 18, 20, 26, and 28, as well as a few thin coal seams. The coal seam has a thickness of 0.45–2.11 m and a depth of 196–383 m. The lithology of the whole borehole is mainly sandstone, including siltstone, argillaceous siltstone, fine sandstone, and limestone. All coal seam samples were collected during the drilling process and immediately stored bags to prevent contamination. The coal seams encountered during drilling were numbered 1M–11M from top to bottom (Figure 1C). Long-source distance gamma (GGFR), natural gamma (NG01), lateral resistivity (GR01), and apparent resistivity (RS01) logging were performed simultaneously.

2.2 Test methods

Lithium content was determined by inductively coupled plasma–mass spectrometry (ICP–MS, NEXION 2000-B, PerkinElmer, Inc.). The determination was conducted according to GB/T 14506.30–2010. Firstly, the sample is ground to a particle size of 200 mesh. The ICP-MS sample digestion method is as follows: precisely weigh 50 mg of coal sample ground to a particle size of 0.075 mm and transfer it into a PTEF digestion vessel. Subsequently, add HF and HNO_3, seal the vessel, and heat it at a constant temperature of 190°C for 36 h. Once complete digestion is achieved, remove the sample and dry it thoroughly. Then, introduce 1 mL of HNO_3 (1:1) at a temperature of 24°C followed by another drying step. Dissolve the salts using HNO_3 (1:1) solution and subsequently add Rh internal standard solution (500 mg). Further addition includes 2 mL of HNO_3 and 3 mL of deionized water before placing it back in the steel container for heating at 140°C for 5 hours. After cooling down, remove the digestion vessel, shake well, and transfer an aliquot volume of 0.4 mL into a centrifuge tube with subsequent adjustment to reach a final volume of 10 mL prior to instrument analysis.

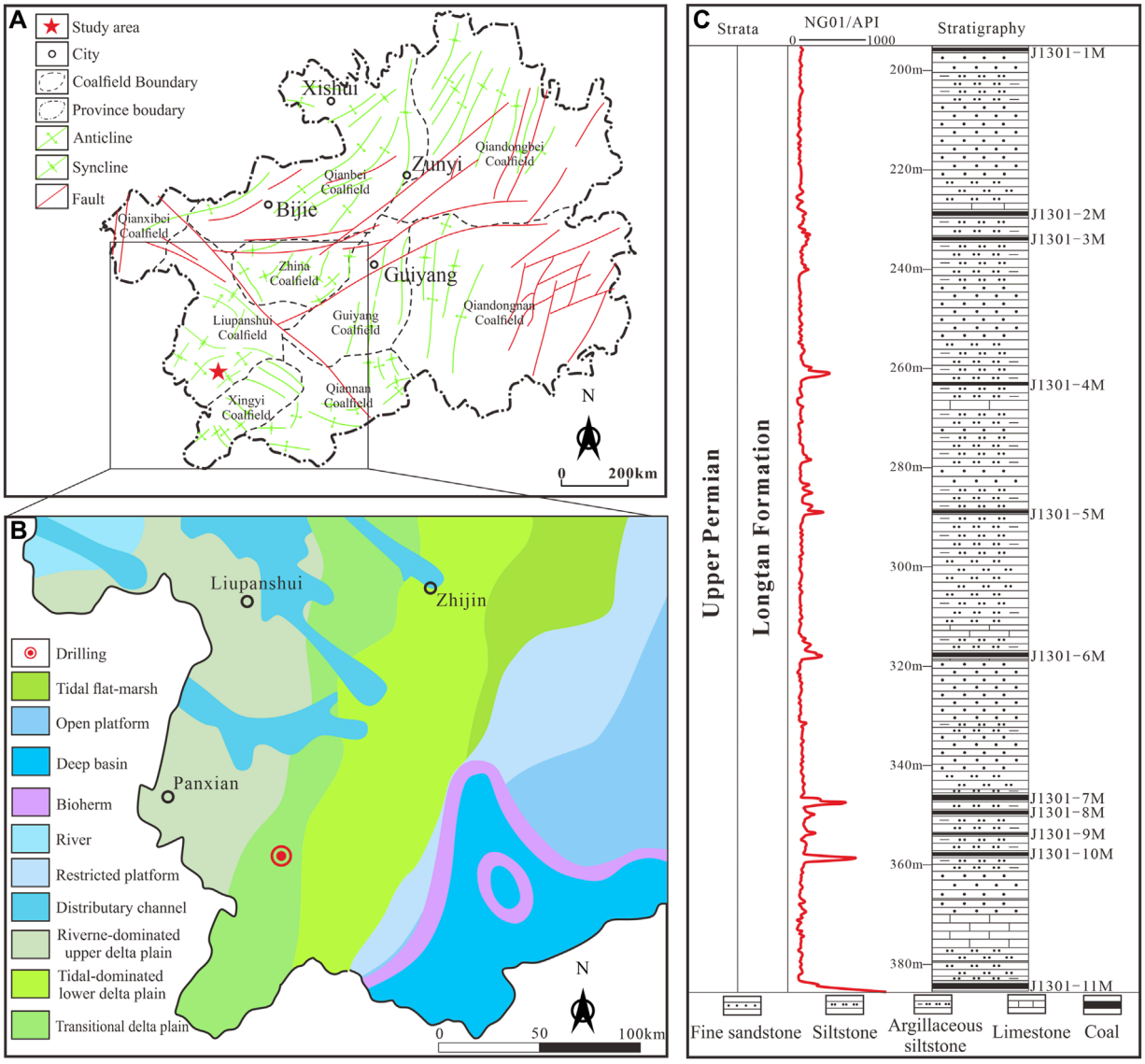

FIGURE 1
Location of well J1301 **(A)** Location of the study area; **(B)** Sedimentary environment of the study area; **(C)** Lithologic map of well J1301.

The cluster analysis method is used to identify the logging characteristics of coal seams with different lithium contents. The core concept of cluster analysis is "birds of a feather flock together." The algorithm classifies data objects separately based on the degree of similarity between them, which is an unsupervised learning method (Ahmed et al., 2020; Chen et al., 2020). The K-means clustering algorithm is often used in practice. K-means clustering is a fast, iterative process (Shahrivari and Jalili, 2016; Capó et al., 2017). Figure 2 illustrates the workflow of the K-means algorithm.

3 Results

3.1 Sample Li content and logging results

By conducting GGFR, NG01, GR01, RS01 logging in the J1301 well, and measuring the lithium content in the coal seam, we obtained the lithium content in Well J1301 and the average value of the corresponding log curves (Figure 3).

GGFR is a logging method used to obtain the formation density using the gamma photon counting rate received by the instrument. For different lithology strata, the scattering and absorption capacities of the gamma photons are different, and the count rates of gamma photons received by the detector are also different (Chen and Zhang, 2022). The GGFR value of coal seams ranges from 300 to 2700 CPS, with a mean of 900 CPS. The GGFR value of the lithium-rich coal seam is between 300 and 1350 CPS. NG01 is closely related to the ash content of coal but is generally to the organic matter composition or the humic acid content of coal (Gao et al., 2015). The NG01 values of coal seams range from 35 to 200 API, with an average of 133 API. The NG01 values of a lithium-rich coal seam are between 35 and 120 API. The GR01 curve is mainly affected by the sedimentary environment, original rock mineral composition, porosity, and cement. The electrical

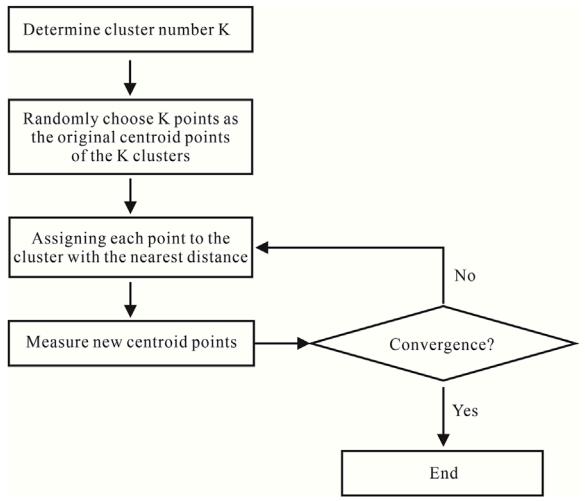

FIGURE 2
K-means flow chart.

parameters of each lithology vary greatly (Duan et al., 2023). The GR01 value of coal seams ranges from 45 to 1300 Ω.M., averaging of 214 Ω.M. The GR01 value of a lithium-rich coal seam is between 50 and 200 Ω.M. Generally, the measured resistivity is called the apparent resistivity, RS01. The RS01 of coal seams ranges from 50 to 500 Ω.M, averaging 218 Ω.M. The RS01 of a lithium-rich coal seam is between 60 and 260 Ω.M. The lithium content in the coal seam of Well J1301 varies greatly, as shown in Figure 3.

The lithium content ranged from 4.46 μg/g to 171.93 μg/g, with a mean of 82.44 μg/g. It shows a certain regularity in the vertical direction, and the lithium content decreases from the upper coal seam to the lower coal seam. The coal seams from J1301-5 coal and above show different logging response characteristics from the coal seams below. The lithium content of the J1301-5 coal and above coal seams is above 90 μg/g. GGFR is between 300 and 600 CPS; NG01 is less than 100 API; GR01 is between 75 and 135 Ω.M, and RS01 is less than 200 Ω.M. The lithium content in the coal seam below the J1301-5 coal is below 90 μg/g. The GGFR range is 938–2183 CPS, and the fluctuation is large. The NG01 range is greater than 100 API. GR01 is greater than 250 Ω.M, and RS01 is greater than 250 Ω.M.

3.2 Well-logging characteristics

Radar maps of the logging characteristics of different lithologies are obtained by counting the logging characteristics of different types of lithology (Figure 4). The logging characteristics of coal are quite different from those of other lithologies. The GGFR and NG01 values of coal are much higher than those of fine sandstone and siltstone. They are also quite different from argillaceous siltstone and limestone. The RS01 of coal is similar to that of argillaceous siltstone and lower than that of limestone, siltstone, and fine sandstone. The GR01 of coal is larger than that of argillaceous siltstone and smaller than that of fine sandstone, siltstone, and limestone. The RS01 of coal is similar to that of argillaceous siltstone and lower than that of limestone, siltstone, and fine sandstone. The GR01 of coal is larger than that of argillaceous siltstone and smaller than that of fine sandstone, siltstone, and limestone. Compared with the logging characteristics of other lithologies, the logging characteristics of coal have specific identification characteristics. The well-logging data can be further identified by cluster analysis.

A scatter plot of the lithium content and different logging responses at the corresponding depths is drawn for correlation analysis (Figure 5). The lithium content strongly correlated with RS01, with R^2 reaching 0.60. The lithium content shows the next highest correlation with NG01 and GR01 (R^2 of 0.40). The correlation between the lithium content and GGFR is the lowest, with R^2 of 0.14.

3.3 Cluster identification of high-lithium coal seams

K-means clustering analysis was performed on the J1301 well logging data using SPSS (Statistical Package for the Social Sciences) data analysis software to obtain the logging clustering center. Based on the lithium content in coal seams, coal seams are divided into high-lithium coal seams (lithium content >50 μg/g) and low-lithium coal seams (lithium content <50 μg/g) (Sun et al., 2014). Lithium-containing coal seams are the sum of high- and low-lithium coal seams. The overall logging characteristics of the lithium-bearing coal seam in Well J1301 in Guojiadi are as follows: GGFR = 901 CPS, NG01 = 133 API, GR01 = 214 Ω.M, RS01 = 218 Ω.M. K-means clustering was performed on the lithium-containing, high-lithium, and low-lithium coal seams, and the number of clusters was divided into 2, 3, and 4. Tables 1–3 list the clustering results.

The GGFR cluster center has a large fluctuation range, from 535 to 2503 CPS, but there is no apparent distinction in RS01. No similarity is observed in the different center point gaps for the different cluster numbers. A plot of the NG01 and GR01 (Figure 6) reveals some differences between the and low-lithium coal seams. The NG01 and GR01 of the high-lithium coal seam are approximately 80 API and 100 Ω.M, respectively. NG01 and GR01 of the low-lithium coal seam approximately 100 API and 150 Ω.M, respectively. Hence, high-lithium coal seams can be identified using the above indicators. K-means clustering is performed on the logging data of the J1301 well using the above values as the logging response characteristics of the well. A clustering center consistent with the target horizon appears when the clustering number is set to a higher value. The clustering results can be found in Tables 4, 5.

It can be found by clustering the whole-well data (Figure 7): NG01 of the cluster center of cluster 15 is 83 API, and the GR01 is 102 Ω.M, which is consistent with the aforementioned high-lithium target layer. The corresponding strata of cluster 15 are mapped individually, and a cluster prediction map is prepared. The high-lithium coal seams are comprehensively identified, and more lithium-containing layers are identified in the non-coal parts, as shown in Figure 8.

4 Discussion

Herein, lithium-bearing coal seams, high-lithium coal seams, and low-lithium coal seams were divided according to their lithium

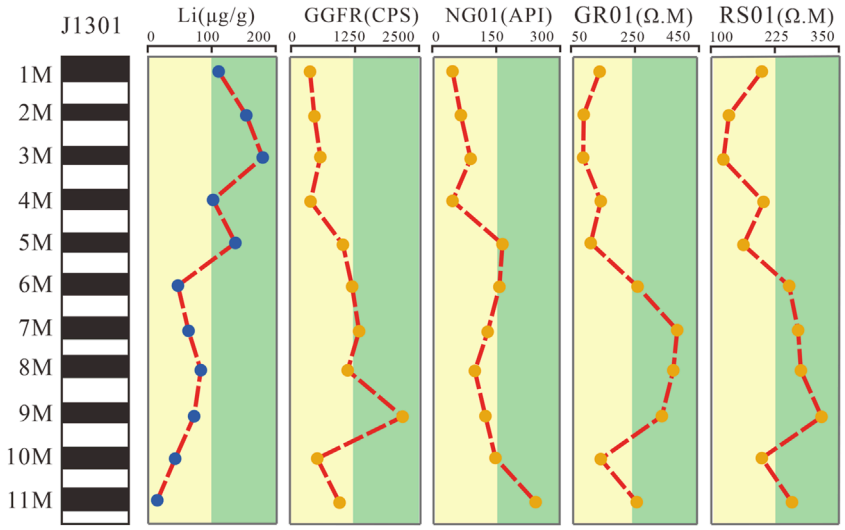

FIGURE 3
Lithium content and corresponding logging curves for Well J1301.

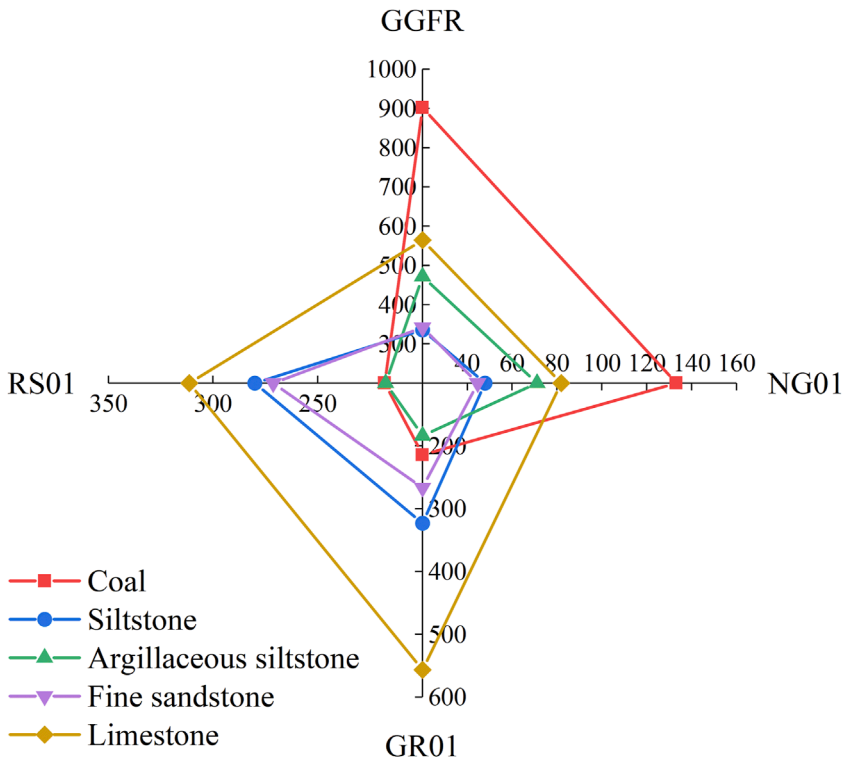

FIGURE 4
Lithology logging identification template.

contents. Using statistical logging response characteristics, coal seams with different lithium contents were compared, and the logging response characteristics of the different lithologies were analyzed. NG01 and GR01 of the low-lithium coal seams were higher than those of the high-lithium coal seams. Some scholars have studied the logging response of coal seams in different regions and found that the gamma ray of coal is 20–50 cps, and the resistivity is 500–1200 Ω.M, which is different from the high-lithium coal seam in Guojiadi (Bhaskar, 2006; Chatterjee and Paul, 2013; Ghosh et al., 2016). The analysis of the high-lithium coal seam in Guojiadi shows that the high-lithium coal seam has a high gamma ray value and a low resistivity value.

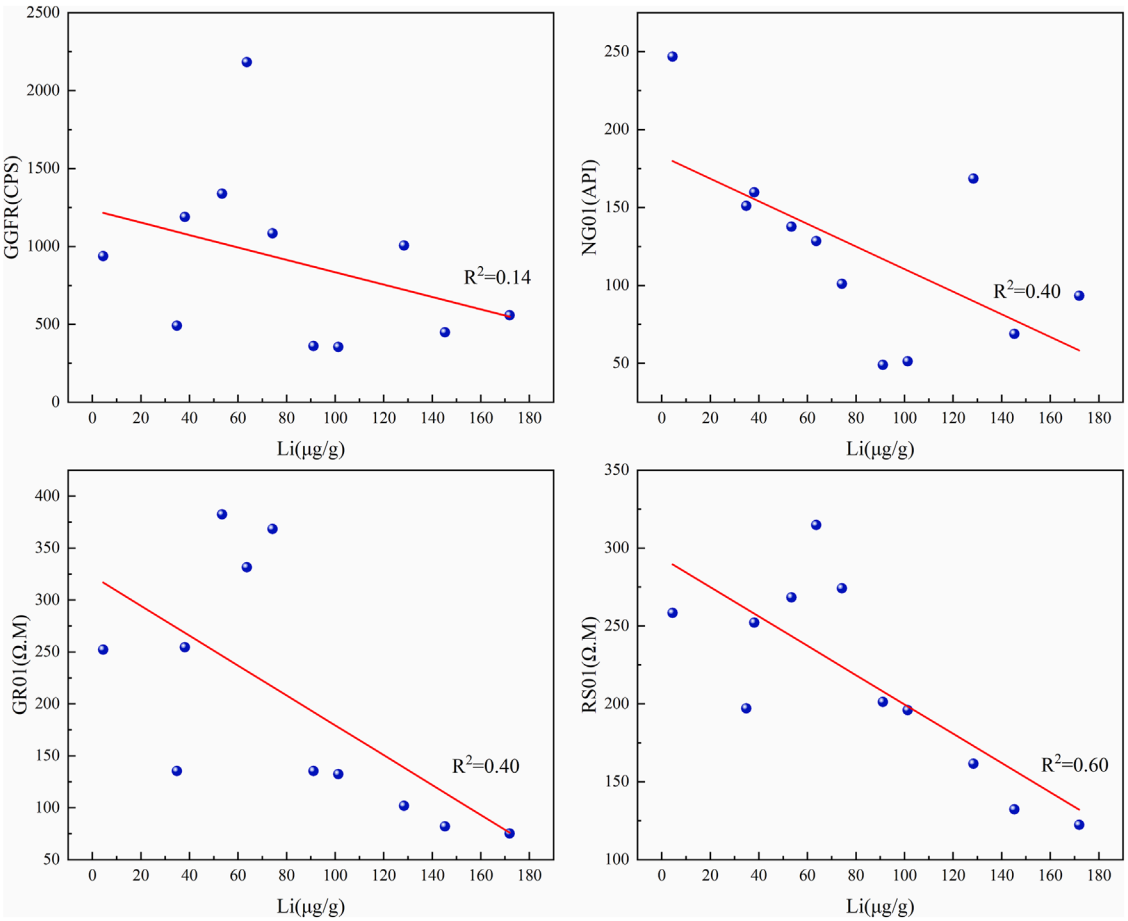

FIGURE 5
Correlation diagram between lithium content and well logging.

TABLE 1 Clustering center of lithium-bearing coal seam in Well J1301 in Guojiadi.

logging curve	Cluster 1		Cluster 2			Cluster 3			
	Center 1	Center 2	Center 1	Center 2	Center 3	Center 1	Center 2	Center 3	Center 4
GGFR(CPS)	1706.85	534.32	1399.15	2386.40	495.36	432.19	1074.11	2426.96	1603.11
NG01(API)	212.44	96.97	221.21	172.60	89.97	76.53	208.13	172.43	207.08
GR01(Ω.M)	425.20	118.01	337.33	551.36	117.63	116.08	150.53	552.87	509.48
RS01(Ω.M)	325.08	169.12	289.36	365.33	168.15	166.21	203.41	364.91	359.95

TABLE 2 Clustering center of high-lithium coal seam in Well J1301 in Guojiadi.

logging curve	Cluster 1		Cluster 2			Cluster 3			
	Center 1	Center 2	Center 1	Center 2	Center 3	Center 1	Center 2	Center 3	Center 4
GGFR(CPS)	1957.55	549.37	2512.82	1424.00	491.04	433.95	972.20	1634.24	2512.82
NG01(API)	126.81	85.68	122.45	137.47	79.30	69.52	141.42	131.62	122.45
GR01(Ω.M)	483.34	102.17	334.55	400.90	98.30	97.74	118.63	599.82	334.55
RS01(Ω.M)	351.75	157.04	316.07	303.09	153.01	152.28	175.02	383.42	316.07

TABLE 3 Clustering center of low-lithium coal seam in Well J1301 in Guojiadi.

logging curve	Cluster 1		Cluster 2			Cluster 3			
	Center 1	Center 2	Center 1	Center 2	Center 3	Center 1	Center 2	Center 3	Center 4
GGFR(CPS)	535.94	1613.71	502.36	2272.36	1389.17	408.07	1706.03	2503.33	1118.09
NG01(API)	116.22	256.87	107.27	210.36	268.16	88.47	253.73	194.83	241.22
GR01(Ω.M)	147.90	408.78	148.97	755.71	293.20	150.14	456.13	1051.17	170.58
RS01(Ω.M)	192.15	316.67	192.70	412.31	279.59	192.39	347.49	464.92	219.33

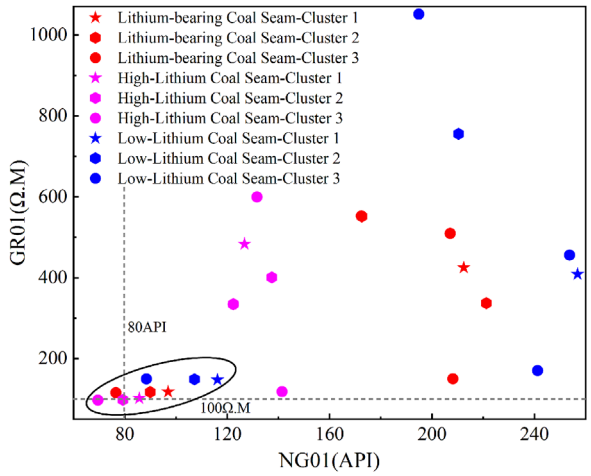

FIGURE 6
Clustering results of different lithium-bearing coal seams.

The variation in lithium content can be essentially explained by the difference in physical characteristics between high-lithium and low-lithium coal seams. Lithium is generally hosted in clay minerals, and high-lithium coal seams tend to have higher clay mineral contents, which cause physical differences between seams, thus affecting the logging characteristics. This result may be due to the following reasons. 1) Lithium is generally found in clay minerals in coal, and we can obtain lithium information indirectly by analyzing the logging reflections of clay minerals in coal. When the clay content is high, the lithium content in coal tends to be higher than that in coal seams with lower clay content (Li et al., 2023). Clay minerals tend to show lower gamma responses in the gamma logs because their content is usually low, and as fine granular materials, they exist in tiny particles in reservoirs such as coal seams. Therefore, the peak value of clay minerals in NG01 logging curves is usually low, and the NG01 signal may be weak compared to other common minerals (such as quartz and feldspar) (Ehsan and Gu, 2020; Jiang, 2021). 2) Common minerals such as quartz and feldspar usually have high electrical conductivity, so they will show higher values in the resistivity logs. However, clay minerals contain relatively more water and salt plasmas, resulting in lower lateral resistivity (Han and Misra, 2018; Zhao et al., 2019). Many scholars have also pointed out that coal has a wide range of gamma ray response, especially when some thin coal seams are mixed with surrounding rocks, which will make some coal seams have a higher gamma ray response. This may lead to incorrect predictions of high-lithium coal seams when using cluster analysis methods (Keskinsezer, 2019; Yusefi and Ramazi, 2019).

A cluster center consistent with the target layer appears when the whole-well logging data are clustered and the number of clusters is set to a higher value. This result may be due to the following reasons. 1) From the perspective of the K-means clustering algorithm principle, setting different cluster numbers will have different effects on the clustering results. An increase in the number of clusters leads to an increase in the number of cluster centers, and the distance between each cluster center will increases. A larger number of clusters can better separate different clusters. 2) From a practical perspective, rocks with different lithologies will be encountered as the drilling depth increases. These rocks have experienced different sedimentary and diagenetic processes, and the corresponding logging characteristics will differ. A higher clustering number can classify rocks of different lithologies more accurately. At the same time, we also need to consider other factors, such as the depth of the coal seam and its thickness, which will affect the identification of high-lithium coal seams. This increases the uncertainty of identification (Antariksa et al., 2022).

The relationship between well-logging curves and lithium content was obtained by analyzing and summarizing the responses of well-logging curves of different types of coal seams in high-lithium areas. The response characteristics of the logging curves of coal seams with different lithium contents differed. For NG01 and GR01, there are still similar cluster centers when different cluster numbers are set. This shows that coal seams with different lithium contents are also significantly different, and this center can be used as a basis for identifying high-lithium coal seams. The well-logging curves were clustered and compared with the aforementioned high-lithium coal seam clustering centers. High-lithium coal seam clustering data were distributed throughout the well. Hence, the data of the whole well can be identified using this method, not just limited to a specific range, and some high-lithium coal seams can be identified with high accuracy.

In connection with reality, lithium exists in coal seams, and may also be enriched in other rocks, such as roof and floor plates (Dai and Finkelman, 2018). In the clustering, a high-lithium coal seam clustering center exists in the coal seam, and is distributed widely in other lithologies, which is consistent with the above. The

TABLE 4 Well logging clustering center of Guojiadi J1301 well (1–10).

logging curve	Cluster									
	Center 1	Center 2	Center 3	Center 4	Center 5	Center 6	Center 7	Center 8	Center 9	Center 10
GGFR(CPS)	277.65	2026.73	237.20	1920.41	1219.41	1666.68	250.19	299.95	2501.00	331.26
NG01(API)	31.05	722.95	17.20	192.91	175.94	469.38	22.69	34.59	189.60	51.61
GR01(Ω.M)	810.41	218.00	2489.60	543.68	183.00	179.76	1928.50	443.77	1135.80	143.54
RS01(Ω.M)	433.04	259.22	580.58	380.20	224.31	230.58	547.11	354.38	477.63	204.84

TABLE 5 Well logging clustering center of Guojiadi J1301 well (11–20).

logging curve	Cluster									
	Center 11	Center 12	Center 13	Center 14	Center 15	Center 16	Center 17	Center 18	Center 19	Center 20
GGFR (CPS)	1635.50	2014.02	2534.33	272.89	469.54	1662.48	2087.29	311.65	795.51	1510.88
NG01 (API)	130.75	46.55	150.21	21.55	83.69	69.76	800.00	42.96	122.56	131.00
GR01 (Ω.M)	994.75	298.17	367.58	1356.50	102.44	258.78	475.14	252.20	109.96	533.23
RS01 (Ω.M)	460.12	301.64	326.95	500.96	157.56	279.18	362.72	280.77	161.58	376.95

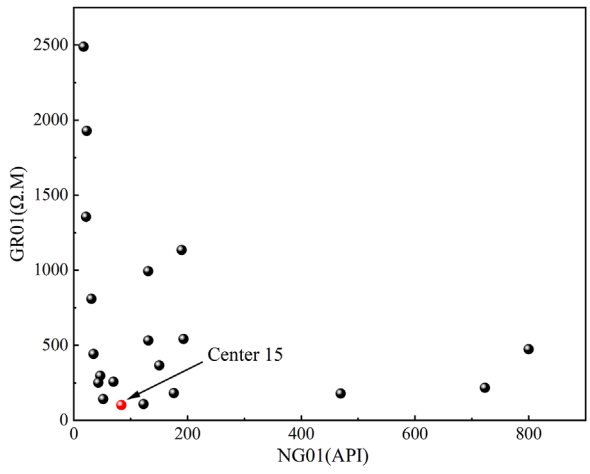

FIGURE 7
Clustering center.

trace element content cannot be determined directly from the logging curves because they only reflect the physical, chemical, and petrological characteristics of the formation. However, by analyzing the logging response characteristics of coal seams, coal seams with different lithium contents can be distinguished and used as criterion. This means that the early identification of high-lithium coal seams can be evaluated from the perspective of logging. The possibility of trace elements and their content range can be inferred from a comprehensive analysis of the whole logging data and other geological data. Further experimental analysis is required to confirm the existence and content of trace elements.

5 Conclusion

The lithium content in the Guojiadi Coal Mine is high, averaging 82.44 μg/g, which is much higher than the international lithium content in coal and is highly representative. The lithium content in the coal seam is strongly correlated with the RS01, GR01, and NG01 logging curves. Coal seams with different lithium contents have different logging characteristics. The NG01 and GR01 values of high-lithium coal seams are approximately 80 API and 100 Ω.M, respectively. The NG01 and GR01 values of low-lithium coal seams are approximately 100 API and 150 Ω.M, respectively. Hence, high-lithium coal seams can be identified by performing K-means clustering on the natural gamma and lateral resistivity logs of the entire drilling well and comparing the log characteristics of regional high-lithium coal seams. The k-means clustering method is used to identify high-lithium coal seams in Guojiadi Coal Mine. Although there are some wrong classifications of high-lithium coal seams, the differential analysis of different lithium-bearing coal seams and the rapid identification of high-lithium coal seams are the main contributions of this work. Most importantly, this study shows that

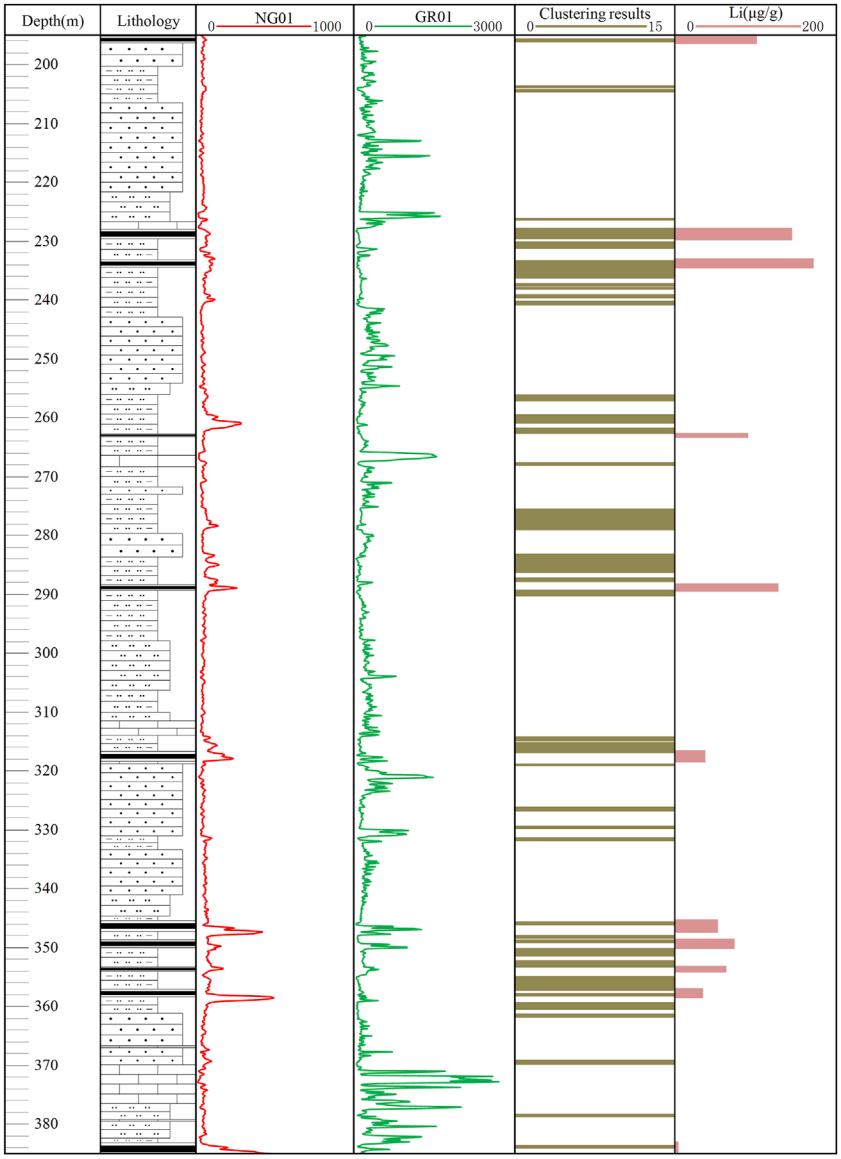

FIGURE 8
Clustering result diagram.

the early identification of high-lithium coal seams can be evaluated from a logging perspective.

Data availability statement

The original contributions presented in the study are included in the article/supplementary material, further inquiries can be directed to the corresponding author.

Author contributions

XM: Conceptualization, Data curation, Funding acquisition, Supervision, Writing–original draft. YZ: Conceptualization, Methodology, Supervision, Writing–review and editing. KD: Funding acquisition, Supervision, Writing–review and editing. YS: Data curation, Software, Writing–original draft. MH: Data curation, Software, Writing–original draft.

Funding

The author(s) declare that financial support was received for the research, authorship, and/or publication of this article. This work was financially supported by the National Natural Science Foundation of China (42172156), the Fundamental Research Funds for the Central Universities (2022YCPY0201), and the National Key R&D Program of China (No. 2020YFA 0711800).

Acknowledgments

Thanks to the Key Laboratory of Coalbed Methane Resources and Reservoir Formation Process and the Guizhou Provincial Key Laboratory of Fluidized Mining of Coals for all the support provided to this study.

Conflict of interest

The authors declare that the research was conducted in the absence of any commercial or financial relationships that could be construed as a potential conflict of interest.

Publisher's note

All claims expressed in this article are solely those of the authors and do not necessarily represent those of their affiliated organizations, or those of the publisher, the editors and the reviewers. Any product that may be evaluated in this article, or claim that may be made by its manufacturer, is not guaranteed or endorsed by the publisher.

References

Ahmed, M., Seraj, R., and Islam, S. (2020). The k-means algorithm: a comprehensive survey and performance evaluation. *Electronics-Switz* 9 (8), 1295. doi:10.3390/electronics9081295

Ambrose, H., and Kendall, A. (2020). Understanding the future of lithium: Part 1, resource model. *J. Ind. Ecol.* 24 (1), 80–89. doi:10.1111/jiec.12949

Amjad, A., and Chen, S. (2020). Characterization of well logs using K-mean cluster analysis. *J. Pet. Explor. Prod. Te.* 10 (6), 2245–2256. doi:10.1007/s13202-020-00895-4

Antariksa, G., Muammar, R., and Lee, J. (2022). Performance evaluation of machine learning-based classification with rock-physics analysis of geological lithofacies in Tarakan Basin, Indonesia. *J. Petrol Sci. Eng.* 208, 109250. doi:10.1016/j.petrol.2021.109250

Baudzis, S., Karłowska-Pik, J., and Puskarczyk, E. (2021). Electrofacies as a tool for the prediction of true resistivity using advanced statistical methods—case study. *Energies* 14 (19), 6228. doi:10.3390/en14196228

Bhaskar, G. (2006). Electro lithofacies analysis for depositional history and stratigraphy of Manuguru coalfield using geophysical well logs. *J. Ind. Geophys. Union* 10 (3), 241–254.

Bilal, A., Yang, R., Lenhardt, N., Han, Z., and Luan, X. (2023). The Paleocene Hangu formation: a key to unlocking the mysteries of Paleo-Tethys tectonism. *Mar. Petrol. Geol.* 157, 106508. doi:10.1016/j.marpetgeo.2023.106508

Capó, M., Pérez, A., and Lozano, J. A. (2017). An efficient approximation to the K-means clustering for massive data. *Knowl-Based Syst.* 117, 56–69. doi:10.1016/j.knosys.2016.06.031

Chatterjee, R., and Paul, S. (2013). Classification of coal seams for coal bed methane exploitation in central part of Jharia coalfield, India – a statistical approach. *Fuel* 111, 20–29. doi:10.1016/j.fuel.2013.04.007

Chen, J., Zhang, J., Wu, J., Wu, Y., Si, H., and Lin, K. (2020). Review on the research of K-means clustering algorithm in big data. *ICECE*, 107–111. doi:10.1109/icece51594.2020.9353036

Chen, S., and Zhang, Y. (2022). Cluster analysis logging curve method for lithology classification of coal-bearing strata. *Inn. Mong. Coal Econ.* 07, 22–24. doi:10.3969/j.issn.1008-0155.2022.07.009

Dai, S., and Finkelman, R. B. (2018). Coal as a promising source of critical elements: progress and future prospects. *Int. J. Coal Geol.* 186, 155–164. doi:10.1016/j.coal.2017.06.005

Dai, S., Zhao, L., Wei, Q., Song, X., Wang, W., Liu, J., et al. (2020). Resources of critical metals in coal-bearing sequences in China: enrichment types and distribution. *Chin. Sci. Bull.* 65, 3715–3729. doi:10.1360/tb-2020-0112

Day-Stirrat, R. J., Hillier, S., Nikitin, A., Hofmann, R., Mahood, R., and Mertens, G. (2021). Natural gamma-ray spectroscopy (NGS) as a proxy for the distribution of clay minerals and bitumen in the Cretaceous McMurray Formation, Alberta, Canada. *Fuel* 288, 119513. doi:10.1016/j.fuel.2020.119513

Duan, Z., Xiao, K., Yang, Y., Huang, X., Wang, D., Xu, Y., et al. (2023). Logging identification of borehole lithology of sandstone-type uranium deposit in Songliao Basin. *Prog. Geophys.* 38 (6), 2490–2501. doi:10.6038/pg2023hh0120

Ehsan, M., and Gu, H. (2020). An integrated approach for the identification of lithofacies and clay mineralogy through Neuro-Fuzzy, cross plot, and statistical analyses, from well log data. *J. Earth Syst. Sci.* 129 (1), 101. doi:10.1007/s12040-020-1365-5

Gao, J., Fu, X., Liu, A., and Luo, P. (2015). Logging response prediction of 15# coalbed coal quality parameters in Heshun area Qingshui Basin. *J. Xi'an Univ. Sci. Technol.* 35 (01), 50–55. doi:10.13800/j.cnki.xakjdxxb.2015.0109

Ghosh, S., Chatterjee, R., and Shanker, P. (2016). Estimation of ash, moisture content and detection of coal lithofacies from well logs using regression and artificial neural network modelling. *Fuel* 177, 279–287. doi:10.1016/j.fuel.2016.03.001

Han, Y., and Misra, S. (2018). Joint petrophysical inversion of multifrequency conductivity and permittivity logs derived from subsurface galvanic, induction, propagation, and dielectric dispersion measurements. *Geophysics* 83 (3), D97–D112. doi:10.1190/geo2017-0285.1

Hayat, U., Ali, A., Murtaza, G., Ullah, M., Ullah, I., Celis, A., et al. (2020). Classification of well log data using vanishing component analysis. *Pure Appl. Geophys.* 177 (6), 2719–2737. doi:10.1007/s00024-019-02374-2

Hu, P., Hou, X., Zhang, J., Li, S., Wu, H., Damø, A. J., et al. (2018). Distribution and occurrence of lithium in high-alumina-coal fly ash. *Int. J. Coal Geol.* 189, 27–34. doi:10.1016/j.coal.2018.02.011

Huang, W., and Qu, Z. (2021). CBM occurrence characteristics and suggestions for exploration and development in digua exploration area of baotian qingshan block in Guizhou. *China Coalbed Methane* 18 (02), 30–35. doi:10.3969/j.issn.1672-3074.2021.02.008

Ikotun, A. M., Ezugwu, A. E., Abualigah, L., Abuhaija, B., and Heming, J. (2023). K-means clustering algorithms: a comprehensive review, variants analysis, and advances in the era of big data. *Inf. Sci.* 622, 178–210. doi:10.1016/j.ins.2022.11.139

Jamaluddin, Wagreich, M., Gier, S., Schöpfer, K., and Battu, D. P. (2023). Sedimentary environments and paleoclimate control of the middle miocene balikpapan group, lower kutai basin (Indonesia): implications for evaluation of the hydrocarbon potential. *Minerals-Basel* 13 (10), 1259. doi:10.3390/min13101259

Jiang, F., Bi, W., and Wang, S. (2020). Study on natural gamma border detection technology for horizontal wells geosteering. *Contemp. Chem. Ind.* 49 (1), 121–124. doi:10.3969/j.issn.1671-0460.2020.01.030

Jiang, Y. (2021). Analysis of sedimentary environment and coal accumulation regularity of late permian coalfields in Guizhou. *Shandong Coal Sci. Technol.* 39 (10), 158–161. doi:10.3969/j.issn.1005-2801.2021.10.055

Jing, J., Ke, S., Li, T., and Wang, T. (2021). Energy method of geophysical logging lithology based on K-means dynamic clustering analysis. *Environ. Technol. Inno.* 23, 101534. doi:10.1016/j.eti.2021.101534

Jiu, B., Huang, W., and Mu, N. (2022). Mineralogy and elemental geochemistry of Permo-Carboniferous Li-enriched coal in the southern Ordos Basin, China: implications for modes of occurrence, controlling factors and sources of Li in coal. *Ore Geol. Rev.* 141, 104686. doi:10.1016/j.oregeorev.2021.104686

Keskinsezer, A. (2019). Determination of coal layers using geophysical well-logging methods for correlation of the Gelik-Zonguldak and Kazpınar-Amasra (Bartin) coalfields, Turkey. *Geomech. Geophys. Geo-energ. Geo-resour.* 5, 223–235. doi:10.1007/s40948-019-00105-4

Kesler, S. E., Gruber, P. W., Medina, P. A., Keoleian, G. A., Everson, M. P., and Wallington, T. J. (2012). Global lithium resources: relative importance of pegmatite, brine and other deposits. *Ore Geol. Rev.* 48, 55–69. doi:10.1016/j.oregeorev.2012.05.006

Lai, F., Liu, Y., Tan, X., Wang, R., Peng, S., and Gao, X. (2024). A composite water saturation model of continental mixed shale oil reservoirs based on complex lithology identification. *Geol. J.* 59 (4), 1401–1415. doi:10.1002/gj.4934

Lai, J., Wang, G., Fan, Q., Zhao, F., Zhao, X., Li, Y., et al. (2023). Toward the scientific interpretation of geo-physical well logs: typical misunderstandings and countermeasures. *Surv. Geophys.* 44 (2), 463–494. doi:10.1007/s10712-022-09746-9

Li, J., Liu, L., Kang, X., Li, K., Zhang, S., and Liu, Q. (2023). Enrichment of lithium in the claystone coal gangue from the malan mine, xishan coalfield, shanxi Province, northern China. *Geochemistry-germany* 83 (2), 125972. doi:10.1016/j.chemer.2023.125972

Li, X., Wei, Y., Cao, D., Wei, J., Liu, X., Zhang, Y., et al. (2024). Cooperative exploration model of coal–lithium deposit: a case study of the haerwusu coal–lithium deposit in the jungar coalfield, inner Mongolia, northern China. *Minerals-Basel* 14 (2), 179. doi:10.3390/min14020179

Liu, J., Dai, S., Song, H., Nechaev, V. P., French, D., Spiro, B. F., et al. (2021). Geological factors controlling variations in the mineralogical and elemental compositions of Late Permian coals from the Zhijin-Nayong Coalfield, western Guizhou, China. *Int. J. Coal Geol.* 247, 103855. doi:10.1016/j.coal.2021.103855

Liu, J., Song, H., Dai, S., Nechaev, V. P., Graham, I. T., French, D., et al. (2019). Mineralization of REE-Y-Nb-Ta-Zr-Hf in wuchiapingian coals from the Liupanshui coalfield, Guizhou, southwestern China: geochemical evidence for terrigenous input. *Ore Geol. Rev.* 115, 103190. doi:10.1016/j.oregeorev.2019.103190

Puskarczyk, E., Jarzyna, J. A., Wawrzyniak-Guz, K., Krakowska, P. I., and Zych, M. (2019). Improved recognition of rock formation on the basis of well logging and laboratory experiments results using factor analysis. *Acta geophys.* 67 (6), 1809–1822. doi:10.1007/s11600-019-00337-8

Shahrivari, S., and Jalili, S. (2016). Single-pass and linear-time k-means clustering based on MapReduce. *Inf. Syst.* 60, 1–12. doi:10.1016/j.is.2016.02.007

Sun, Y., Zhao, C., Li, Y., and Wang, J. (2014). Minimum mining grade of the selected trace elements in Chinese coal. *J. China Coal Soc.* 39 (4), 744–748. doi:10.13225/j.cnki.jccs.2013.1718

Tang, B., Fu, Y., Yan, S., Chen, P., Cao, C., Guo, C., et al. (2022). The source, host minerals, and enrichment mechanism of lithium in the Xinmin bauxite deposit, northern Guizhou, China: constraints from lithium isotopes. *Ore Geol. Rev.* 141, 104653. doi:10.1016/j.oregeorev.2021.104653

Yan, J., He, X., Hu, Q., Liang, Q., Tang, H., Feng, C., et al. (2018). Lower Es3 in Zhanhua Sag, Jiyang Depression: a case study for lithofacies classification in lacustrine mud shale. *Appl. Geophys.* 15 (2), 151–164. doi:10.1007/s11770-018-0678-5

Yusefi, A., and Ramazi, H. (2019). ProxInLAS, a software program for detecting coal layers and estimating parameters of layers, using geophysical well-logs. *Earth Sci. Inf.* 12, 415–427. doi:10.1007/s12145-019-00382-3

Zhang, J., Wang, R., Jia, A., and Feng, N. (2024). Optimization and application of XGBoost logging prediction model for porosity and permeability based on K-means method. *Appl. Sci.* 14 (10), 3956. doi:10.3390/app14103956

Zhang, W., Zhao, L., Wang, W., Nechaev, V. P., French, D., Graham, I., et al. (2024). Enrichment of critical metals (Li, Ga, and rare earth elements) in the early Permian coal seam from the Jincheng Coalfield, southeastern Qinshui Basin, northern China: with an emphasis on cookeite as the Li host. *Ore Geol. Rev.* 167, 105939. doi:10.1016/j.oregeorev.2024.105939

Zhao, J., Zhang, L., Li, S., Li, Z., Niu, Z., and Guo, X. (2019). Research on the prediction method of shale clay mineral and quartz content in the Z area of Taihang. *Prog. Geophys.* 34 (2), 0681–0686. doi:10.6038/pg2019cc0075

Zhao, L., Wang, X., and Dai, S. (2022). Lithium resources in coal-bearing strata: occurrence, mineralization, and resource potential. *J. China Coal Soc.* 47 (5), 1750–1760. doi:10.13225/j.cnki.jccs.mj22.0418

frontiers | Frontiers in Earth Science

TYPE Original Research
PUBLISHED 20 August 2024
DOI 10.3389/feart.2024.1444690

OPEN ACCESS

EDITED BY
Jyoti Phirani,
Indian Institute of Technology Delhi, India

REVIEWED BY
Yanghui Li,
Dalian University of Technology, China
Xiangchao Shi,
Southwest Petroleum University, China

*CORRESPONDENCE
Na Wei,
weina8081@163.com
Cong Li,
202114000002@stu.swpu.edu.cn

RECEIVED 06 June 2024
ACCEPTED 06 August 2024
PUBLISHED 20 August 2024

CITATION
Wei N, Li C, Zhao X, Li H, Zhang L, Zhao J, Kvamme B and Coffin RB (2024) Numerical simulation of depressurization exploitation in class 1 hydrate reservoirs under different development factors in Shenhu area, South China sea.
Front. Earth Sci. 12:1444690.
doi: 10.3389/feart.2024.1444690

Numerical simulation of depressurization exploitation in class 1 hydrate reservoirs under different development factors in Shenhu area, South China sea

Na Wei[1,2]*, Cong Li[1,2]*, Xingxin Zhao[1,2], Haitao Li[1,2], Liehui Zhang[1,2], Jinzhou Zhao[1,2], Bjørn Kvamme[1,2] and Richard B. Coffin[1,2]

[1]State Key Laboratory of Oil and Gas Reservoir Geology and Exploitation, Southwest Petroleum University, Chengdu, China, [2]State Key Laboratory of Natural Gas Hydrate, Beijing, China

Most of the implemented marine gas hydrate test exploitation in the world adopt the depressurization method to break down the hydrate in the reservoir into natural gas and then extract it, but because the gas production results are still a certain distance away from the commercial exploitation, and it mainly stays in the stage of theoretical research and trial exploitation. Based on two trial productions in the Shenhu area of the South China Sea, this study established a model for hydrate exploitation and investigated the impact of different well types on the recovery rates of hydrates and free gas in different development layers during depressurization. For the Class 1 hydrate reservoirs, horizontal wells are the optimal solution to extract hydrate and free gas simultaneously when exploiting the hydrate three-phase layer. Meanwhile, the effect of different well spacing in vertical wells on the recovery rate of hydrate and free gas was studied. It is found that the best recovery efficiency is achieved when the spacing between two wells is 80 m. The lower the bottom flow pressure of the well, the higher the production capacity, but its influence is limited.

KEYWORDS

class 1 hydrate reservoirs, depressurization exploitation, numerical simulation, recovery rate, horizontal well

1 Introduction

Natural gas hydrate (NGH), commonly known as combustible ice, is a clathrate crystalline compound formed by hydrocarbon gases such as methane and water under high pressure and low temperature (McMullan and Jeffrey, 1965; Sloan and Koh, 2007). NGH has the characteristics of high energy density, wide distribution, large scale, high combustion value, clean and no pollution, etc. It is an energy source that has not yet been effectively developed on a large scale on earth and is also known as the new alternative energy source with the most development potential in the 21st century (Xu and Li, 2015; Chibura et al., 2022; Wei et al., 2022). The efficient development of hydrate resources from marine sediments is crucial in addressing the world's energy shortage (Zhao et al., 2017; Xu et al., 2019; Wei et al., 2021).

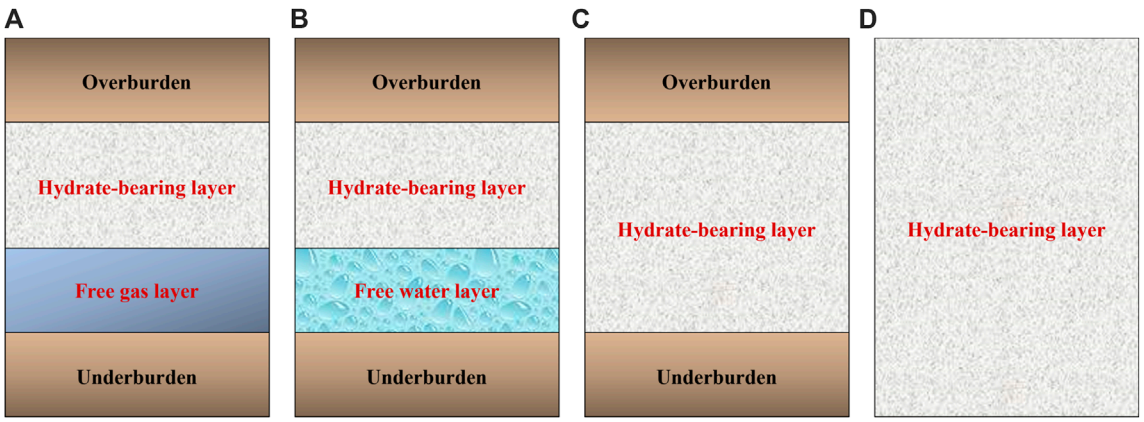

FIGURE 1
Classification of natural gas hydrate reservoirs. **(A)** Class 1, **(B)** Class 2 **(C)** Class 3 **(D)** Class 4.

Moridis et al. divided the natural hydrate accumulations into four main classes that are defined by their geologic features and their initial conditions (Moridis and Collett, 2003; Moridis and Reagan, 2007a; Moridis and Reagan, 2007b; Moridis et al., 2007; Moridis and Sloan, 2007), and most of the current studies have been conducted based on this classification. As shown in Figure 1, the Class 1 accumulations are composed of two layers: the Hydrate-Bearing Layer (hereafter referred to as HBL) and an underlying two-phase fluid layer containing gas and liquid water. In Class 1 deposits, the bottom of the HBL occurs under equilibrium conditions and defines the bottom of the stability zone. In addition, depending on the composition of the HBL, it is divided into two types: water-saturated (Class 1W) and gas-saturated (Class 1G) (Moridis and Reagan, 2011a). In Class 2 deposits, an HBL overlies a layer of mobile water. Class 3 accumulations are composed of a single zone, the hydrate interval (HBL), and are characterized by the absence of an underlying zone of mobile fluids. A fourth class (Class 4) involves exclusively oceanic systems, and involves dispersed, low-saturation hydrate deposits that lack confining geologic strata. Among them, the Class 1 accumulations are currently the preferred target for hydrate exploitation because the temperature and pressure conditions in this class of hydrate reservoir are close to the phase equilibrium line, meaning that only a small amount of decomposition driving force is required for hydrate decomposition. Additionally, the Class 1 hydrate reservoirs have the advantage that even if the hydrate decomposition is minimal, a certain amount of gas can still be recovered during exploitation due to the underlying free gas.

Natural gas hydrates are extracted by decomposing solid hydrates into water and methane gas in the reservoir environment, and then collecting the methane gas through extraction wells. Currently, the exploitation methods of natural gas hydrate mainly include depressurization (Wang et al., 2013; Zhao et al., 2015), thermal stimulation (Cranganu, 2009; Nair et al., 2016), inhibitor injection (Li et al., 2007; Villano et al., 2009), N_2/CO_2 replacement (Ohgaki et al., 1996; Goel, 2006), and solid fluidization exploitation methods proposed for the development of marine non-diagenetic natural gas hydrate (Zhou et al., 2014; Zhou et al., 2017; Wei et al., 2018; Zhou et al., 2018). Of these methods, depressurization and heating methods are relatively simple to implement. However, compared to the heating method, depressurization is more cost-effective and has higher gas production efficiency. It is the main method used in recent test exploitation and will be the primary method for gas hydrate exploitation in the future. During production in the Messoyakha hydrate reservoirs, depressurization was the dominant mechanism (Makogon and Omelchenko, 2013). The first oceanic hydrate production trial in the Eastern Nankai Trough achieved a gas production rate of 20,000 m^3/d via depressurization (Yamamoto, 2015). China conducted two trial productions in the Shenhu Area of the South China Sea in 2017 and 2020, respectively. The first trial production used straight wells for depressurization development, and the average daily gas production was only 5,151 m^3/d (Li et al., 2018), while the second trial production used horizontal wells for depressurization development, and the average daily gas production increased significantly to 2.87×10^4 m^3/d (Ye et al., 2020).

Due to the complexity, high investment, and unpredictability of hydrate test exploitation projects, it is beneficial to use powerful, flexible, and cost-effective numerical simulation research methods to pre-evaluate hydrate reservoirs before their extraction (Moridis, 2003; Konno et al., 2017). Various widely used hydrate simulators, including TOUGH + HYDRATE (T + H) (Moridis et al., 2011; Sun et al., 2019), HydrateResSim (Gamwo and Liu, 2010), MH21-HYDRES (Masuda et al., 2008; Kurihara et al., 2009), STOMP-HYD (Anderson et al., 2011), and CMG-STARS (Myshakin et al., 2012; Lin et al., 2020), can be utilized to analyze the hydrate production performance and determine exploitation strategy preferences. At present, many numerical simulation studies have been carried out on the depressurization production of natural gas hydrate reservoirs.

Hong and Pooladi-Darvish (2003) simulated the depressurization u7production of a two-dimensional cylindrical natural gas hydrate reservoir, studied the influence of various parameters on gas production behavior, and analyzed the natural gas production potential of gas hydrate bearing formation. Moridis and Reagan analyzed the production performance of hydrate reservoir under different heat injection and depressurization conditions. Li et al. (2011) established a single hydrate reservoir production model and discussed the gas production efficiency of

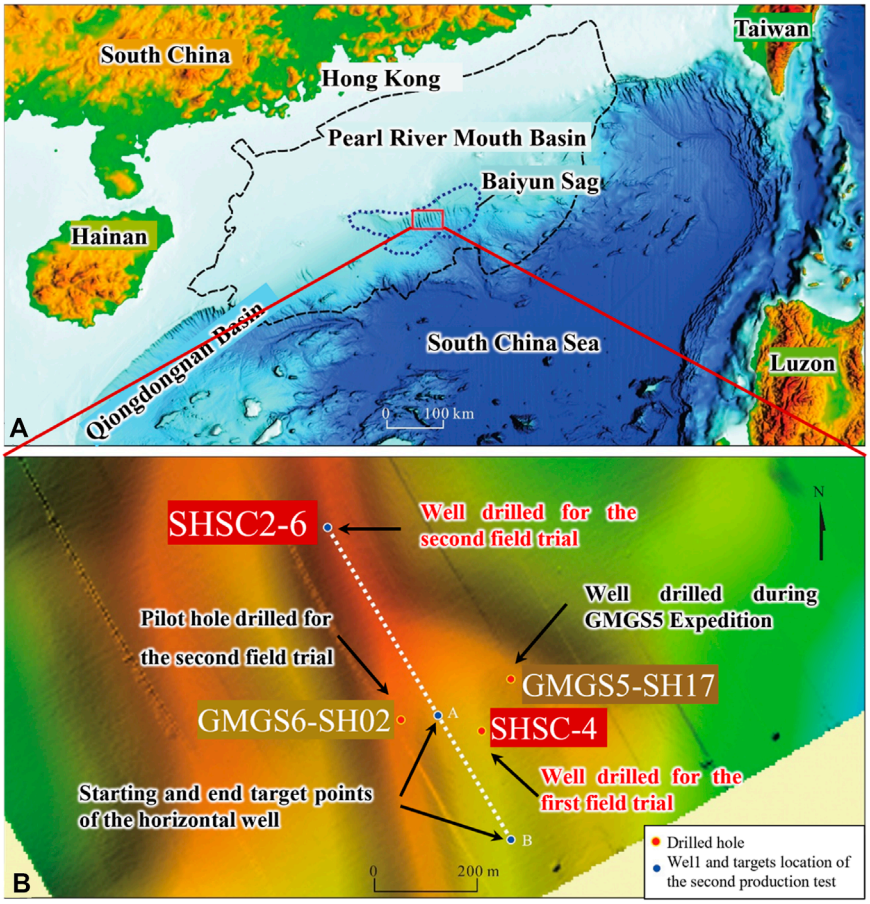

FIGURE 2
The regional geological setting and location of the two offshore NGH production test sites. The red rectangle in **(A)** indicates the production test area. **(B)** illustrates the topography surrounding the production well and the trajectory of the well (Yu et al., 2021).

depressurization production in horizontal wells. In 2011, Moridis and Reagan et al. (2011b) used the T + H to perform depressurizing dissociation simulations of actual geological gas hydrate reservoirs. The calculation results show that the gas production phase can be divided into two phases. The first is the phase where the gas production gradually increases, and the water production gradually decreases, and the second is the phase where the fluid production rate is very low. Moridis also compared the performance of a vertical well and a horizontal well and found that production using horizontal wells is approximately two orders of magnitude larger than that from vertical wells accessing the same section of the HBL. In 2012, Su et al. (2012) established a vertical shaft depressurization mining model using T+H study based on the real geological parameters in the Shenhu Sea, South China Sea. The simulation results showed that the proportion of hydrate decomposition produced water was too large when the vertical wells were mined by depressurization, and the area could not be mined economically and efficiently by using the depressurization method alone. In 2015, Feng et al. (2015) compared the hydrate production efficiency of single horizontal and double horizontal wells. In 2018, Chen et al. (2018) tablished a geological model for the hydrate trial production area in the Shenhu Sea area of the South China Sea and predicted the potential production behavior of the area. In 2022, Guo et al. (2022) demonstrated that the recovery rates of hydrate and free gas are significantly influenced by well placement and stimulation in different development configurations.

In 2021, Yu et al. (2019) further investigated the free gas accumulation behavior in a methane hydrate reservoir by using a multiple-well system with an assumed WS. They found that the free gas accumulation zone was dramatically enlarged with the increase in well spacing, which means a proper WS should be carefully determined. Similarly, Terzariol and Santamarina. (2021) also studied reasonable well spacing under the condition of multi-well depressurization production of hydrate to explore the synergistic interactions among wells. Their investigation also indicated the optimal WS is mainly dependent on the characteristic lengths, burdens permeability, well pressure, and formation thickness. In 2023, Sun et al. (2023) compared the production performance of vertical and horizontal wells with different well spacing. The results show that the relatively longer WS in homogeneous sediments with the same ultra-low permeability means lower cumulative gas recovery, but the full opposite phenomenon will be observed after increasing the formation permeability, and subsequently, a method to determine the

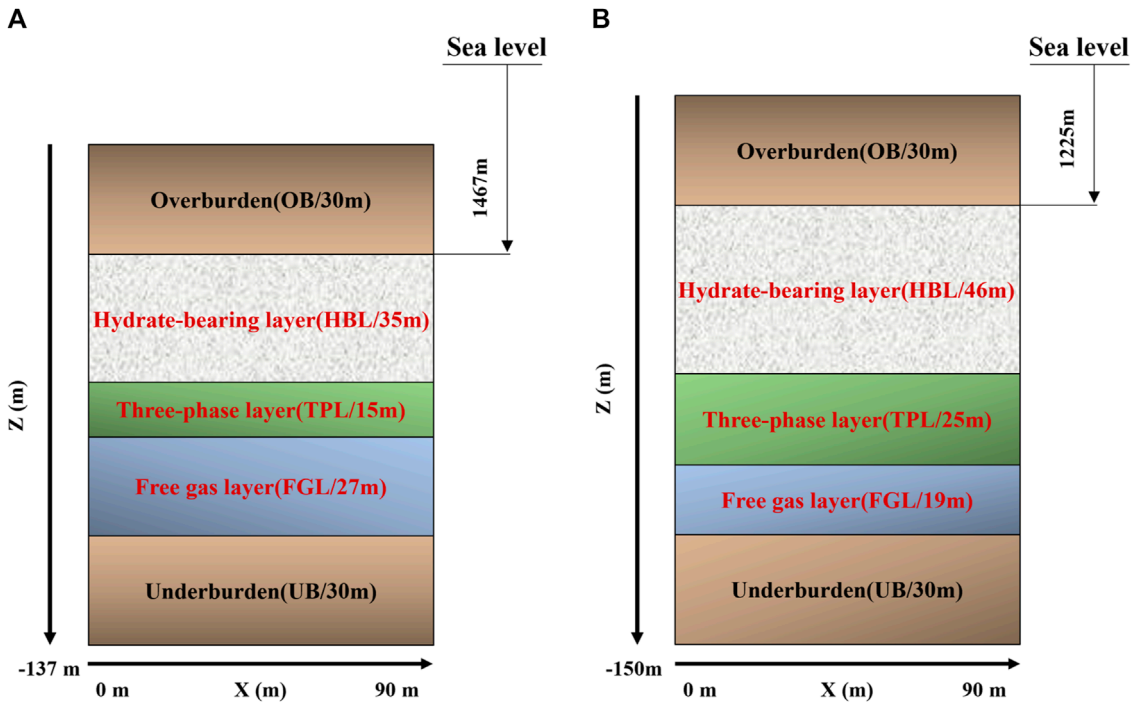

FIGURE 3
Construction of the class 1 hydrate reservoirs model for depressurization exploitation in the Shenhu Sea, South China Sea. **(A)** Hydrate reservoir model, 2017. **(B)** Hydrate reservoir model, 2020.

optimal well spacing by the minimum radius of curvature method was proposed.

In 2013, Zhao et al. (2013) used T + H to numerically simulate the gas production potential of a single vertical well gas hydrate reservoir in the Qilian Mountain permafrost zone of the Qinghai-Tibet Plateau with bottomhole pressures of 1, 1.5, and 2.5 MPa, respectively. The results suggest that lower production pressures may not be conducive to exploiting the gas production potential of hydrate reservoirs. Fan et al. (2013) utilized the HydrateResSim simulator to model a horizontal well for hydrate extraction under constant temperature and pressure reduction, defining three pressure scenarios to analyze heat injection efficiency and gas production rates. Results indicated that the hydrate gas production rate increased over time before stabilizing, with higher pressure reductions leading to increased production capacity. In 2017, Merey and Sinayuc et al. (2017) performed pressure reduction mining analyses on hydrate reservoirs of varying thicknesses using the HydrateResSim simulator for pressure reductions ranging from 2.0 to 6.0 MPa. Xia et al. (2019) introduced a novel depressurization mode with decreasing bottom-hole pressure in 2020, investigating its production characteristics numerically. They discovered that as the depressurization exponent decreased, gas production, dissociation, and the gas-to-water ratio all increased. Compared to the proposed depressurization model, the index for hydrate production at constant bottom-hole pressure was better; however, it resulted in higher energy consumption within the hydrate reservoir and more severe hydrate alteration. Therefore, a suitable depressurization exponent should be selected to achieve a balance between production and reservoir energy consumption during depressurization production.

In summary, despite numerous preliminary evaluations conducted on various well types, well spacings, and bottomhole pressures, systematic discussions on the impact of different production intervals on hydrate recovery rates, particularly for Type 1 hydrate reservoirs, remain scarce. This study not only updates the simulation benchmarks based on the latest trial production data but also systematically investigates the effects of distinct development intervals on the recovery rates of Type 1 hydrate reservoirs. Through a comparative analysis of two hydrate trial production campaigns conducted in the Shenhu area of the South China Sea in 2017 and 2020, this research, for the first time, elaborates on the specific impacts of well types and development intervals on the recovery rates of hydrates and free gas, which have often been overlooked in previous studies. Furthermore, we assess the influence of varying well spacings for vertical wells on production performance, offering fresh insights into optimizing well spacing designs. Unlike previous studies that primarily focused on geological factors, our research underscores the significance of development factors, such as well type selection and production strategies, in enhancing recovery rates, and it presents, for the first time, an Inflow Performance Relationship (IPR) curve for hydrate production. These novel findings provide vital engineering references for the development of hydrate reservoirs in the South China Sea and other maritime regions worldwide, particularly in implementing depressurization-based extraction projects.

TABLE 1 Parameters and models used in the simulations (Li et al., 2018; Ye et al., 2020).

Parameter	Value and model	
Year	1st test (2017)	2nd test (2020)
Water depth (m)	1,266	1,225
Reservoir depth (mbsf)	200–278	207–297
Reservoir thickness (m)	78	90
The hydrate-bearing layer thickness (m)	35	46
The hydrate three-phase layer thickness (m)	15	25
The free gas layer thickness (m)	27	19
Initial temperature at the bottom of the three-phase layer (°C)	15.12	16.15
Initial pressure at the bottom of the three-phase layer (MPa)	15.05	15.95
Geothermal gradient (°C/100 m)	5.4	5.4
Average hydrate saturation in hydrate-bearing layer (%)	34	31
Average hydrate saturation in hydrate three-phase layer (%)	31	11.7
Average gas saturation in hydrate three-phase layer (%)	16.4	13.2
Average gas saturation in free gas layer (%)	7.8	7.3
Average permeability of hydrate-bearing layer (mD)	2.9	2.38
Average permeability of hydrate three-phase layer (mD)	1.5	6.63
Average permeability of free gas layer (mD)	7.4	6.8
Average porosity of hydrate-bearing layer (%)	35	37.3
Average porosity of hydrate three-phase layer (%)	33	34.6
Average porosity of free gas layer (%)	32	34.7
Relative permeability model	$K_{rA} = (S_A\text{-}S_{irA})/(1\text{-}S_{irA})^n$	
	$K_{rG} = (S_G\text{-}S_{irG})/(1\text{-}S_{irA})^{nG}$	
Composite thermal conductivity model	$K_\theta = K_{\theta RD} + \left(S_A^{1/2} + S_H^{1/2}\right) \times (K_{\theta RW}\text{-}K_{\theta RD}) + \varphi S_I K_{\theta I}$	
λ, P_0, n, n_G, S_{irA}, S_{irG}	0.30, 10^5 Pa, 3.5, 2.5, 0.3, 0.05	

2 Mathematical model

2.1 T + H code introduction

The TOUGH+HYDRATE code (T+H) was developed by the Lawrence Berkeley National Laboratory (LBNL) in the United States and has been extensively used internationally in the field of hydrates. T + H is a fully implicit compositional simulator that accounts for four phases (gas, water, ice, hydrate) as well as three components (CH_4, H_2O, NaCl), to simulate the decomposition and formation processes of hydrates under different exploitation modes, equilibrium conditions, and kinetic conditions. By solving the coupled mass-energy balance equations and satisfying Darcy's law, T+H can simulate the coupled processes of phase transition, heat transfer, and multiphase flow during hydrate extraction in natural gas hydrate deposits (Moridis and Reagan, 2007b).

2.2 Model assumptions

The assumptions in this model are listed as follows (Moridis and Reagan, 2007b). 1) Hydrate is a single methane hydrate with a methane content of 100%. 2) Darcy's law is valid in the simulated domain under the conditions of the study. 3) Neglecting the mechanical dispersion of dissolved gases and inhibitors in the aqueous phase during transport, disregarding molecular diffusion and hydrodynamic diffusion. 4) Dissolved salts do not precipitate as their concentration increases during water freezing. 5) The concentration of the dissolved inhibitors is such that it does not affect the thermophysical properties of the aqueous phase. 6) Inhibitors do not react with reservoir minerals. 7) The pressure $P < 100$ MPa (14,504 psi).

2.3 Mathematical model in T+H code

In the T + H code, mass and heat balance considerations in every subdomain (gridblock) into which the simulation domain is been subdivided by the integral finite difference method dictate that:

$$\frac{d}{dt}\int_{V_n} M^k dV = \int_{\Gamma_n} \mathbf{F}^k \cdot \mathbf{n} d\Gamma + \int_{V_n} q^\kappa dV \tag{1}$$

where V_n is volume of subdomain n, m^3; M^k is mass accumulation term of component κ, $kg{\cdot}m^{-3}$; κ is hydrate(h) or methane (m) or water (w) or water-soluble inhibitor (i) or heat (θ); $\mathbf{F}^k$ is Darcy flux vector of component κ, $kg{\cdot}m^{-2}{\cdot}s^{-1}$; Γ_n is surface area of subdomain n, m^2; $\mathbf{n}$ is inward unit normal vector; q^κ is source/sink term of component κ, $kg{\cdot}m^{-3}{\cdot}s^{-1}$; t is time, s.

Under equilibrium conditions, the mass accumulation terms M^k in Equation 1 is given by Equation 2 below.

$$M^\kappa = \sum_{\beta \equiv A,G,I,H} \phi S_\beta \rho_\beta X_\beta^\kappa, \kappa \equiv w, m, i \tag{2}$$

where ϕ is porosity, dimensionless; β is solid-hydrate (H) or aqueous (A) or gaseous (G) or solid-ice (I); S_β is saturation of phase β, dimensionless; ρ_β is density of phase β, $kg{\cdot}m^{-3}$; X_β^κ is mass fraction of component $\kappa \equiv w, m, i$ in phase β, kg/kg.

The mass fluxes of water, CH_4, and inhibitor include contributions from the aqueous and gaseous phases, are shown in Equation 3.

$$\mathbf{F}^\kappa = \sum_{\beta \equiv A,G} \mathbf{F}_\beta^\kappa, \kappa \equiv w, m, i \tag{3}$$

because they are immobile, the contributions of the two solid phases ($\beta \equiv I, H$) to the fluid fluxes are zero. The heat flux accounts for conduction, advection, and radiative heat transfer, and is given by Equation 4.

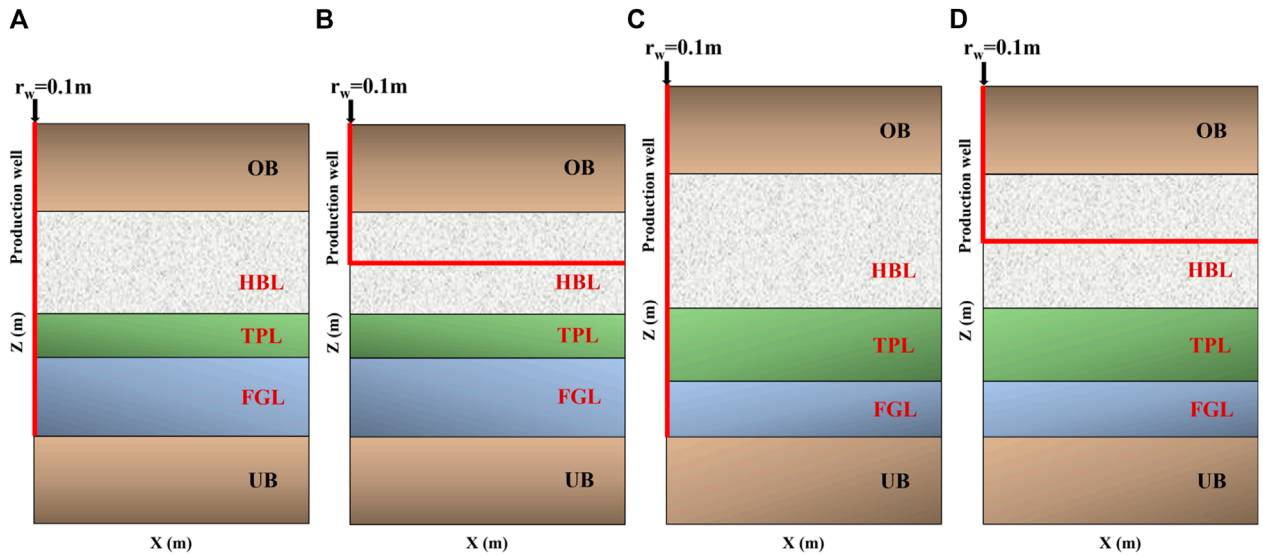

FIGURE 4
Schematic diagram of production well design for two offshore NGH production test in the Shenhu Sea, South China Sea. **(A)** Vertical well model 2017. **(B)** Horizontal well model 2017. **(C)** Vertical well model 2020. **(D)** Horizontal well model 2020.

$$\mathbf{F}^{\theta} = -\overline{k_{\theta}}\nabla T + f_{\sigma}\sigma_0\nabla T^4 + \sum_{\beta\equiv A,G} h_{\beta}\mathbf{F}_{\beta} \tag{4}$$

where $\overline{k_{\theta}}$ is composite thermal conductivity of the medium/fluid ensemble, $W\cdot m^{-1}\cdot K^{-1}$; h_{β} is specific enthalpy of phase $\beta \equiv A, G$, $J\cdot kg^{-1}$; f_{σ} is radiance emittance factor, dimensionless; σ_0 is Stefan-Boltzmann constant, Stefan-Boltzmann constant, $5.6687\times10^{-8}\ J\cdot m^{-2}\cdot K^{-4}$.

Under equilibrium conditions, the rate of heat removal or addition includes contributions of the heat associated with fluid removal or addition, as well as direct heat inputs or withdrawals, and is described by Equation 5.

$$q^{\theta} = q_d + \sum_{\kappa\equiv A,G} h_{\beta}q_{\beta} \tag{5}$$

where q_{β} is the production rate of the phase β, $kg\cdot m^{-3}$. For a prescribed production rate, the phase flow rates q_{β} are determined internally according to the general different options available in the TOUGH+ code.

Under different temperature and pressure conditions, hydrate systems are in different phase states. When the equilibrium state is broken, the state of the system will change. For the phase equilibrium relationship between hydrate decomposition and formation, Moridis (2023) has established a regression equation based on data from several researchers reported by Sloan:

$$\ln(p_e) = \begin{cases} -1.941\times10^5 + 3.310\times10^3 T - 2.255\times10^1 T^2 \\ +7.675\times10^{-2}T^3 - 1.304\times10^{-4}T^4 + 8.861\times10^{-8}T^5 \\ (T \geq 273,2K) \\ -4.389\times10^1 + 7.763\times10^{-1}T - 7.273\times10^{-3}T^2 \\ +3.854\times10^{-5}T^3 - 1.037\times10^{-7}T^4 + 1.099\times10^{-10}T^5 \\ (T < 273.2K) \end{cases} \tag{6}$$

The effect of salinity on the dissociation equilibrium pressure-temperature relationship is described by

$$T_e = T + \Delta T_D \tag{7}$$

where:

$$\Delta T_D = \Delta T_{D,r}\frac{\ln\left(1 - X^c_{mol,A}\right)}{\ln\left(1 - X^c_{mol,A,r}\right)} \tag{8}$$

In Equations 6–8, T is temperature, K; p_e is equilibrium pressure at temperature T, Pa; T_e is equivalent equilibrium temperature in the presence of inhibitor, K; ΔT_D is inhibitor-induced temperature depression, K; $\Delta T_{D,r}$ is temperature depression at the reference mole fraction $X^c_{mol,A}$, K; $X^c_{mol,A}$ is mole fraction of the inhibitor in the aqueous phase; $X^c_{mol,A,r}$ is reference mole fraction of the inhibitor in the aqueous phase; The inhibitor studied in this article is NaCl.

3 Geological setting and model construction

3.1 Geological setting

In 2015 and 2016, the China Geological Survey identified eight hydrate deposits containing underlying free gas in the Shenhu area, located on the northern slope of the Baiyun Sag within the Pearl River Mouth Basin in the northern South China Sea, as depicted in Figure 2A. Among these, the W11 and W17 deposits were selected as the optimal targets for production testing. The W17 site, situated in the Baiyun Sag of the Pearl River Mouth Basin, features a complex seabed terrain characterized by a higher north and lower south elevation, along with typical geological features such as seamounts, erosional channels, steep slopes, and reverse slopes.

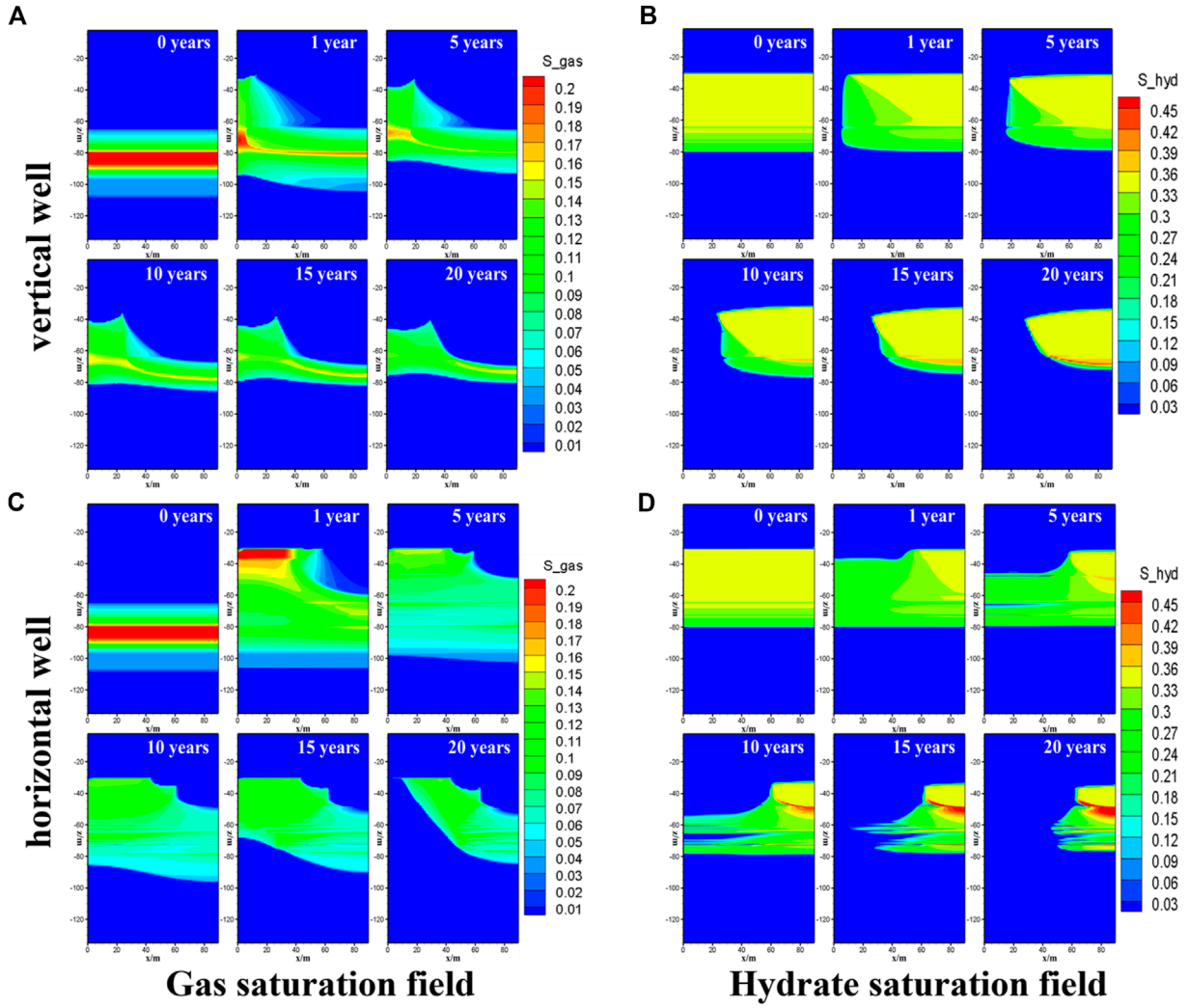

FIGURE 5
Temporal and spatial evolution of exploitation in different well types, 2017. **(A, C)** Gas saturation Field. **(B, D)** Hydrate Saturation field.

Geological and tectonic activities have resulted in the formation of a system of steeply inclined fractures and fault zones, providing favorable conditions for the formation and accumulation of natural gas hydrates. The first hydrate production test was conducted at Well SHSC-4 in the W17 site in 2017, followed by a second test at Well SHSC2-6, located approximately 500 m northwest of the first well, in 2020. The locations of the test wells are illustrated in Figure 2B. The simulated target reservoir is composed primarily of muddy silt with mineral composition mainly consisting of quartz feldspar, carbonate, and clay minerals, and its bound water saturation of the reservoir is 65% or higher. The hydrate reservoir at this station contains upper and lower capping layers, hydrate two-phase layer (water + hydrate), hydrate three-phase layer (water + hydrate + free gas), and underlying free gas layer (water + free gas), belonging to the Class1 hydrate reservoir (Li et al., 2018). It has been reported that the natural gas hydrates in the Shenhu Area of the South China Sea originate from thermogenic gas sources and occur in the form of structure I and structure II pore-filling types with methane content of over 99% (Qin et al., 2020; Ye et al., 2020; Yu et al., 2021).

3.2 Model construction

This study constructed a rectangular hydrate reservoir model (i.e., x-y-z coordinate system) for the first and second tests in the Shenhu Sea based on the field data obtained from the tests site, as illustrated in Figure 3. Figure 3A presents the geological model of the first test exploitation. From the reservoir characteristics shown in Table 1, it can be known that the marine hydrate reservoir at this site is located 200–278 m beneath the seafloor (mbsf) where the water depth is 1,266 m and the reservoir thickness is 78 m. Considering the symmetrical characteristic, only half of the reservoir model was taken into account. Furthermore, it was assumed that the reservoir properties were uniform along the y-coordinate, so only a planar reservoir model (i.e., xz coordinate system) was used as the simulation domain. This reservoir model had a length of 90 m and a height of 137 m. Along the z-coordinate, it was split into five layers from top to bottom: i) overburden (OB, 30 m); ii) hydrate-bearing layer (HBL, 35 m); iii) three-phase layer (TPL, 15 m); (iv) free gas layer (FGL, 27 m); and v) underburden (UB, 30 m). Figure 3B

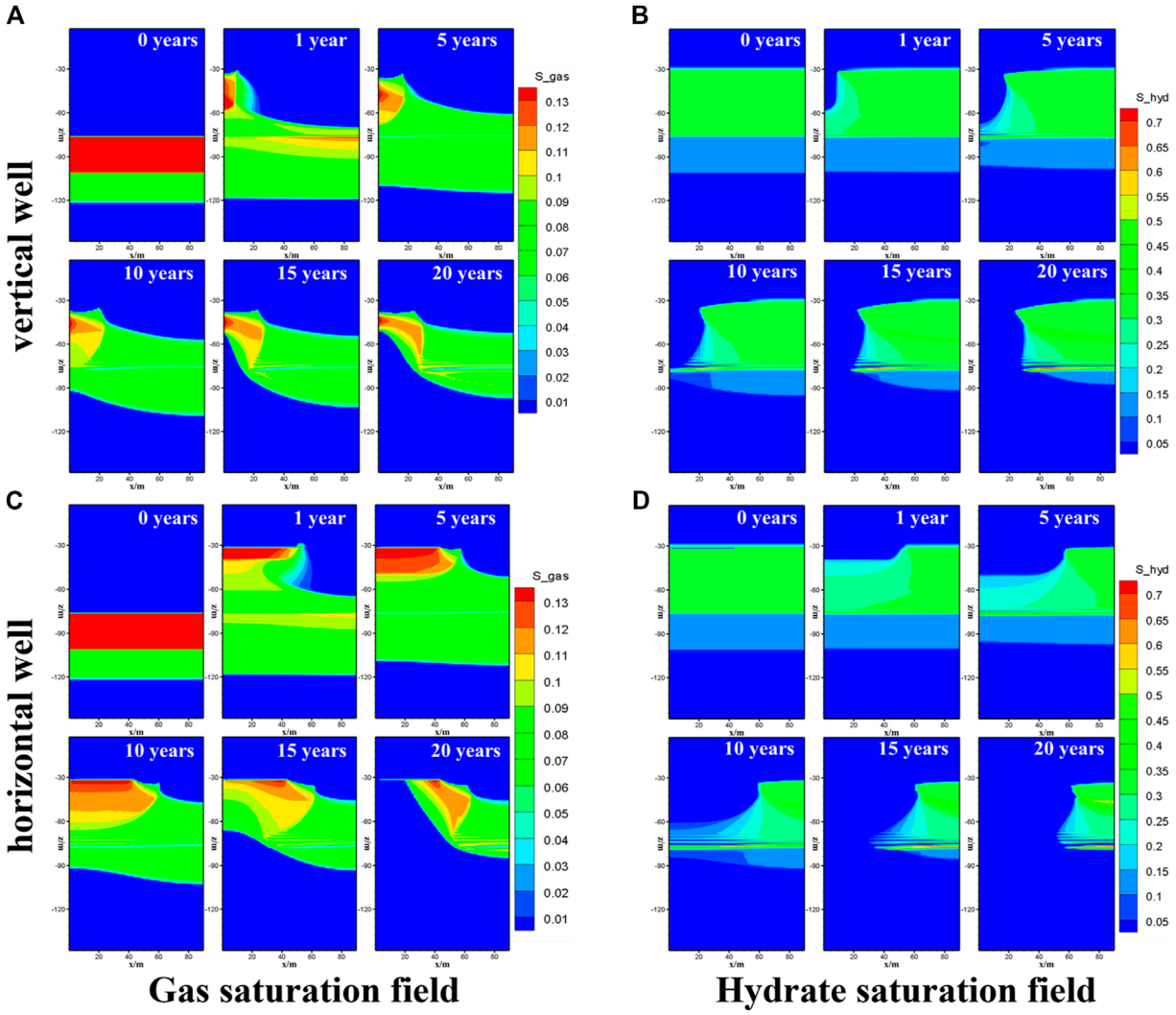

FIGURE 6
Temporal and spatial evolution of exploitation in different well types, 2020. **(A, C)** Gas saturation Field. **(B, D)** Hydrate Saturation field.

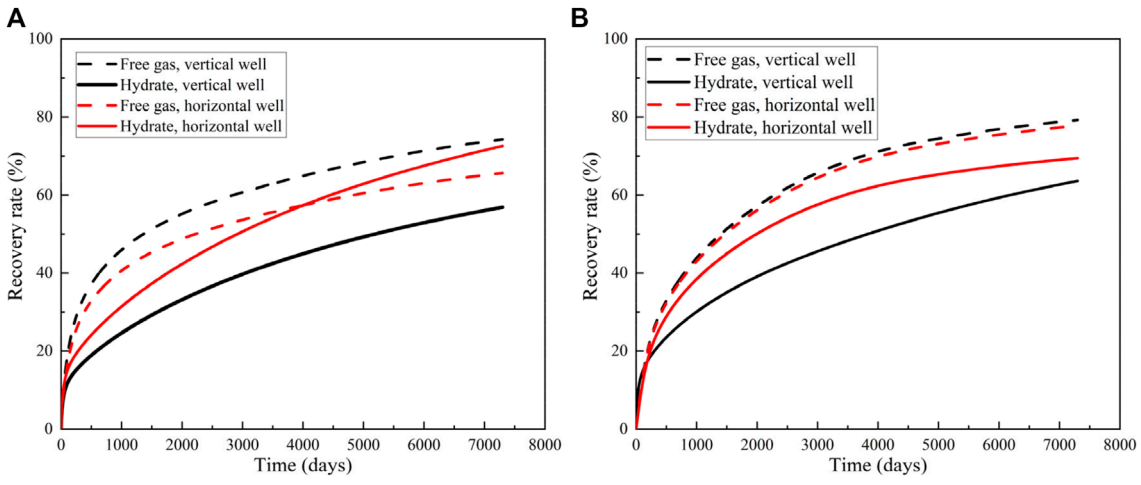

FIGURE 7
Recovery curves of free gas and hydrate from different well types in 2017 and 2020. **(A)** 2017 **(B)** 2020.

TABLE 2 Production well design of different well types and exploitation layers.

Cases	Design	Remarks
Case 1	Vertical well, HBL	Figure 8A
Case 2	Vertical well, HBL + TPL	Figure 8B
Case 3	Vertical well, HBL + TPL + FGL	Figure 8C
Case 4	Horizontal well, HBL	Figure 8D
Case 5	Horizontal well TPL	Figure 8E
Case 6	Horizontal well, FGL	Figure 8F

depicts the geological model of the second test exploitation. From the reservoir characteristics shown in Table 1, it can be known that the marine hydrate reservoir at this site is located 207–297 m beneath the seafloor (mbsf) where the water depth is 1,225 m and the reservoir thickness is 90 m. This reservoir model had a length of 90 m and a height of 150 m. Along the z-coordinate, it was split into five layers from top to bottom: i) overburden (OB, 30 m); ii) hydrate-bearing layer (HBL, 46 m); iii) three-phase layer (TPL, 25 m); iv) free gas layer (FGL, 19 m); and v) underburden (UB, 30 m).

The initial conditions and boundary conditions of the reservoir for this numerical simulation are from the public data of two tests in the Shenhu Sea, South China Sea, and the specific data are shown in Table 1. The survey shows that the seafloor temperature in the Shenhu sea area is 3.3–3.7°C, the heat flux is 74–78 mW/m^2, and the geothermal gradient is 4.3–6.77°C/100 m.30,31 Therefore, we set the initial temperature at the bottom of TPL for the first and second tests models to 15.12°C and 16.15°C the initial pressure at the bottom of TPL to 15.05 MPa and 15.95 MPa, and the geothermal gradient was set to 5.4°C/100 m. The OB and UB only contained liquid water without any free gas or hydrates, and since the corresponding reservoir conditions (i.e., average porosity and permeability) have not been reported in the literature, they were assumed to be identical with those of the HBL and FGL. In addition, the gas that formed the natural gas hydrates in the reservoir model was assumed to be 100% methane.

4 Results and discussion

4.1 Effect of well type

According to publicly available information, the second test recovery yielded 5.57 times the daily gas production of the first test recovery. To investigate whether the significant increase in gas production was due to the well type factor, numerical simulations of vertical and horizontal well extraction were carried out using the geological parameters of the first and second test production, respectively. The physical models established are illustrated in Figure 4.

Figure 5 display the spatial and temporal evolution of the gas phase saturation field and hydrate saturation field during the first test exploitation, while Figure 6 illustrate the spatial and temporal evolution of the second test exploitation. The left two panels of the figure depict the changes in gas saturation during the production process, while the right two panels show the corresponding changes in hydrate saturation. As seen in Figure 5A, initially, there are significant differences in gas saturation and pressure gradients between layers, allowing free gas to rapidly disperse near the well. However, after 20 years, the dispersion becomes limited to the immediate vicinity of the well. Figure 5C reveals that during the early stages of gas production, the exploitation of the two-phase hydrate layer using a horizontal well results in significant migration of free gas into this layer. After 20 years of gas production, all free gas in the free gas layer near the well is recovered, yet a considerable amount of free gas remains in the two-phase hydrate layer. Figures 5B–D indicate that hydrate decomposition initiates near the wellbore during the initial stages of production using both vertical and horizontal wells. In the case of vertical well production, hydrates surrounding the well are initially extracted by disrupting their equilibrium state, leading to a significantly larger area of undecomposed hydrates remaining after 20 years of gas production compared to that observed in horizontal well production.

Figure 6 show that the spatial and temporal evolution patterns of the gas phase saturation field and hydrate saturation field during both vertical and horizontal well exploitation observed in 2020 are comparable to those in 2017. Thus, we will not discuss them further here. Nonetheless, it is worth noting that the final remaining areas of free gas and undecomposed hydrate zone differ significantly due to the distinct geological conditions.

In addition, Figure 7 shows the variation of the recovery rate over a 20-year mining period for both tests. Figure 7A illustrates the recovery rates of hydrate and free gas from vertical and horizontal wells during the first test in 2017. The recovery rate initially increases rapidly during the early stage of depressurized extraction, followed by a slower growth rate. After 20 years of depressurized extraction, the free gas recovery rate and hydrate recovery rate are 74.52% and 56.88%, respectively, for vertical wells, and 65.65% and 72.57%, respectively, for horizontal wells. The recovery rate of free gas from vertical wells is 8.87% higher than that from horizontal wells, while the recovery rate of hydrate from vertical wells is 15.69% lower than that from horizontal wells. In Figure 7B, the recovery rates of hydrate and free gas from vertical and horizontal wells during the second test in 2020 are presented. After 20 years of reduced pressure extraction, the free gas recovery rate is 79.22% and the hydrate recovery rate is 63.62% for vertical wells, while the free gas recovery rate is 77.77% and the hydrate recovery rate is 69.44% for horizontal wells. The recovery rate of free gas from vertical wells is 1.45% higher than that from horizontal wells, and the recovery rate of hydrate from vertical wells is 5.82% lower than that from horizontal wells. Based on these results, we can conclude that extracting the hydrate layer is more economically efficient as the hydrate saturation is much higher than the free gas saturation. Therefore, we recommend using horizontal wells for the exploitation of the Class 1 hydrate reservoir under depressurization.

4.2 Effect of exploitation layer

Due to the abundance of numerical simulations on the first trial production in 2017, there are relatively fewer numerical simulations for the second trial production in 2020. Starting from this section, numerical simulations will be conducted for the second

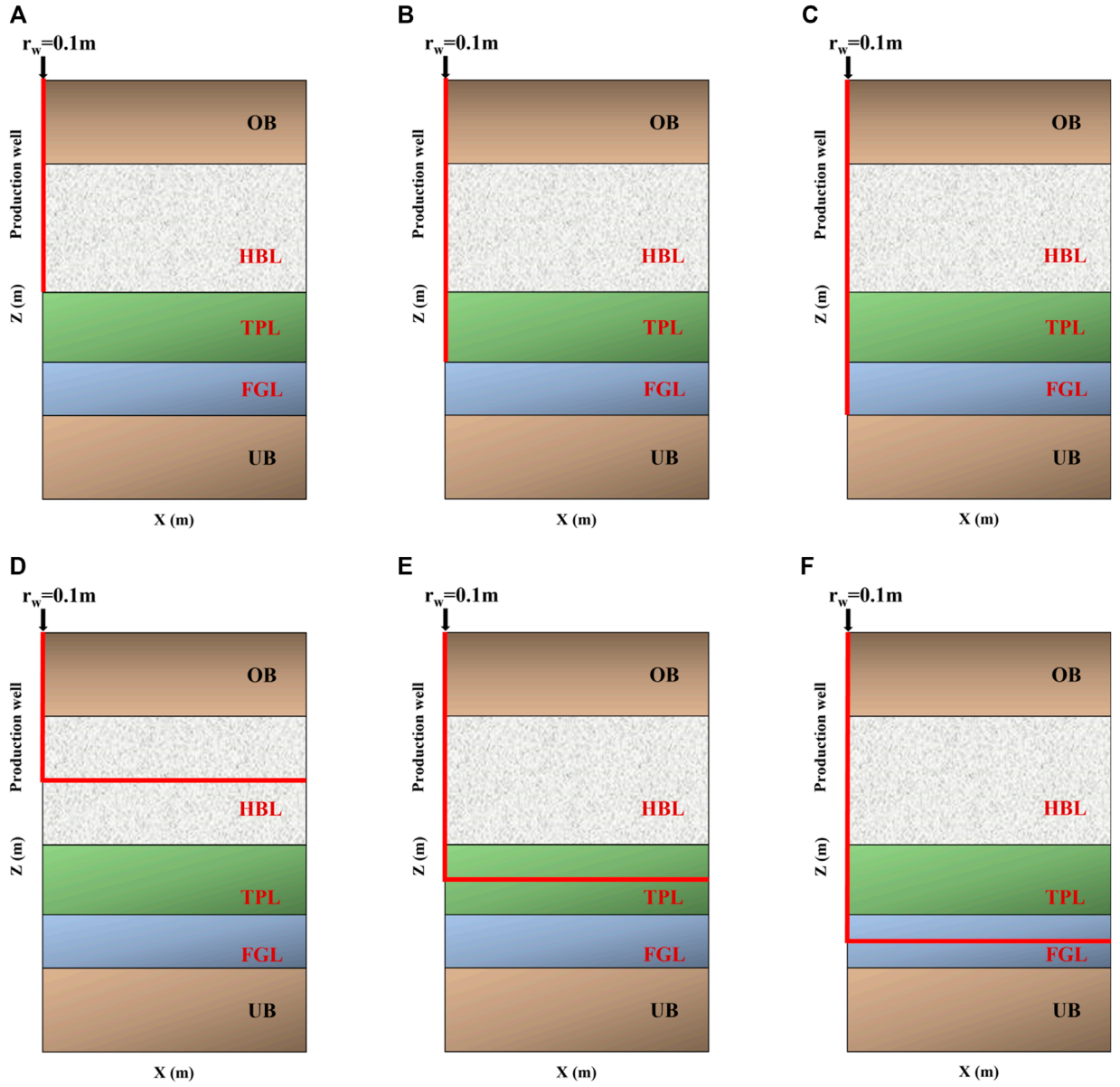

FIGURE 8
Schematic diagram of production well design of different well types and exploitation horizon. **(A)** Class 1, **(B)** Class 2 **(C)** Class 3 **(D)** Class 4. **(E)** Class 5. **(F)** Class 6.

trial production in 2020. In order to investigate the effects of different well types and different production layers on the recovery rate of hydrate and free gas, this section establishes a depressurization production model with different well types and different production layers and analyzes the changes in the recovery rate of hydrate and free gas. The design of the scheme is shown in Table 2, and the model is shown in Figure 8.

The recovery rates of different scenarios over a 20-year period of exploitation are presented in Figure 9. As can be seen from Figure 9A, Case 1 results in a recovery rate of 48.35% for free gas and 38.96% for hydrate. In Case 2, the recovery rates increase to 76.55% and 58.40% for free gas and hydrate, respectively. Case 3 yields even higher recovery rates of 79.22% and 63.62% for free gas and hydrate, respectively. The recovery rates of free gas and hydrate are the highest when the straight wells are exploited to the free gas layer, while the recovery rates of free gas and hydrate are the lowest when the hydrate two-phase layer is exploited. Therefore, direct wells are recommended to reach the free gas layer. From Figure 9B, it is evident that after 20 years of exploiting horizontal wells, Case 4, which exploits the hydrate two-phase layer, results in the highest hydrate recovery rate of 74.55%, but the lowest free gas recovery rate of 57.63%. This is because the reservoir permeability is low, and the horizontal wells are not directly in contact with the free gas layer, making it difficult for the free gas to flow upward. Therefore, the gas produced by exploiting the hydrate two-phase layer is mainly hydrate decomposed gas. Case 5, on the other hand, exploits the free gas layer, resulting in the highest free gas recovery rate of 84.61%, but the lowest hydrate recovery rate of 42.26%. This

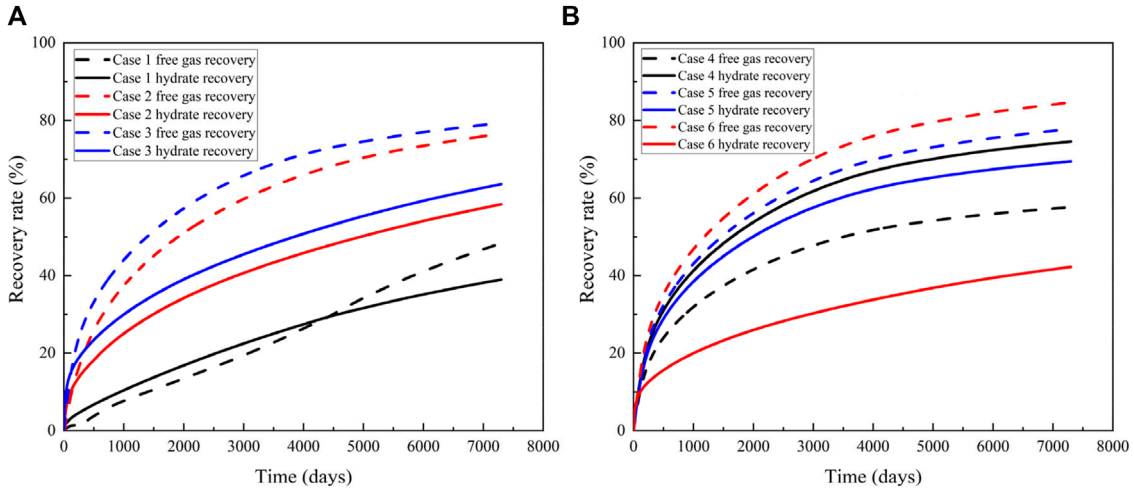

FIGURE 9
Recovery curves of free gas and hydrate from Cases 1–6. **(A)** Vertical well. **(B)** Horizontal well.

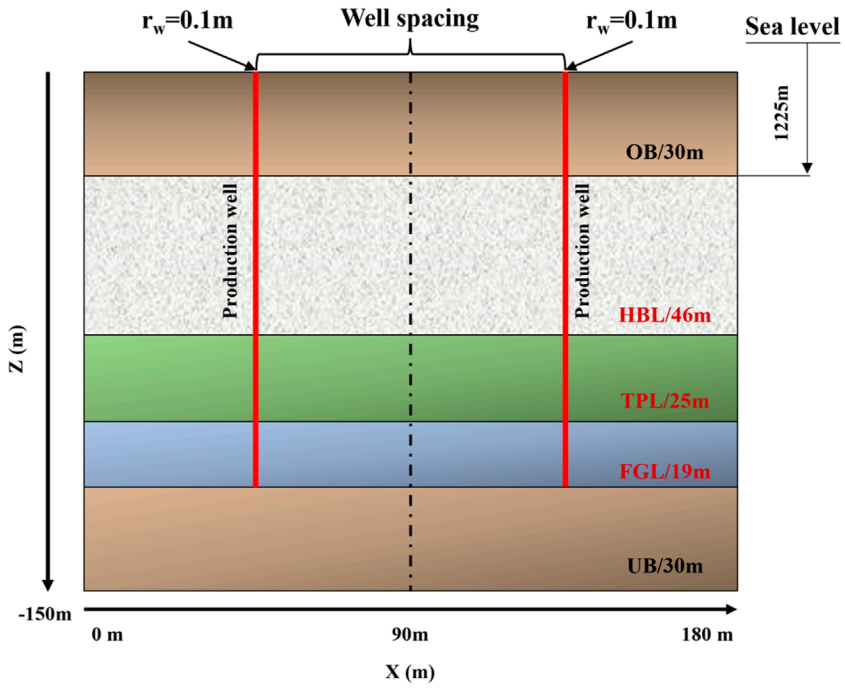

FIGURE 10
Schematic diagram of vertical wells with different well spacing for depressurization exploitation.

extraction effect is opposite to that of the hydrate two-phase layer, increasing the extraction range of the free gas layer but not directly contacting the upper hydrate layer. As a result, it only relies on the pressure drop transfer of the free gas layer to promote hydrate decomposition, which has a limited effect. The recovery rate of hydrate is 69.44%, and the recovery rate of free gas is 77.77%. The horizontal well arrangement can effectively connect the upper and lower layers, which can increase the decomposition area of hydrate and communicate with the lower free gas layer. Therefore, for long-term exploitation, it is recommended to drill horizontal wells to exploit the hydrate triple-phase layer, which can simultaneously exploit hydrate and free gas. Hence, the optimal option for straight well extraction is Case 3, and the optimal option for horizontal well extraction is Case 5.

4.3 Effect of well spacing

This section examines the impact of various vertical well spacing configurations on the recovery of hydrate and free gas. To illustrate, we select a symmetric cross section (x = 190 m) with a width of

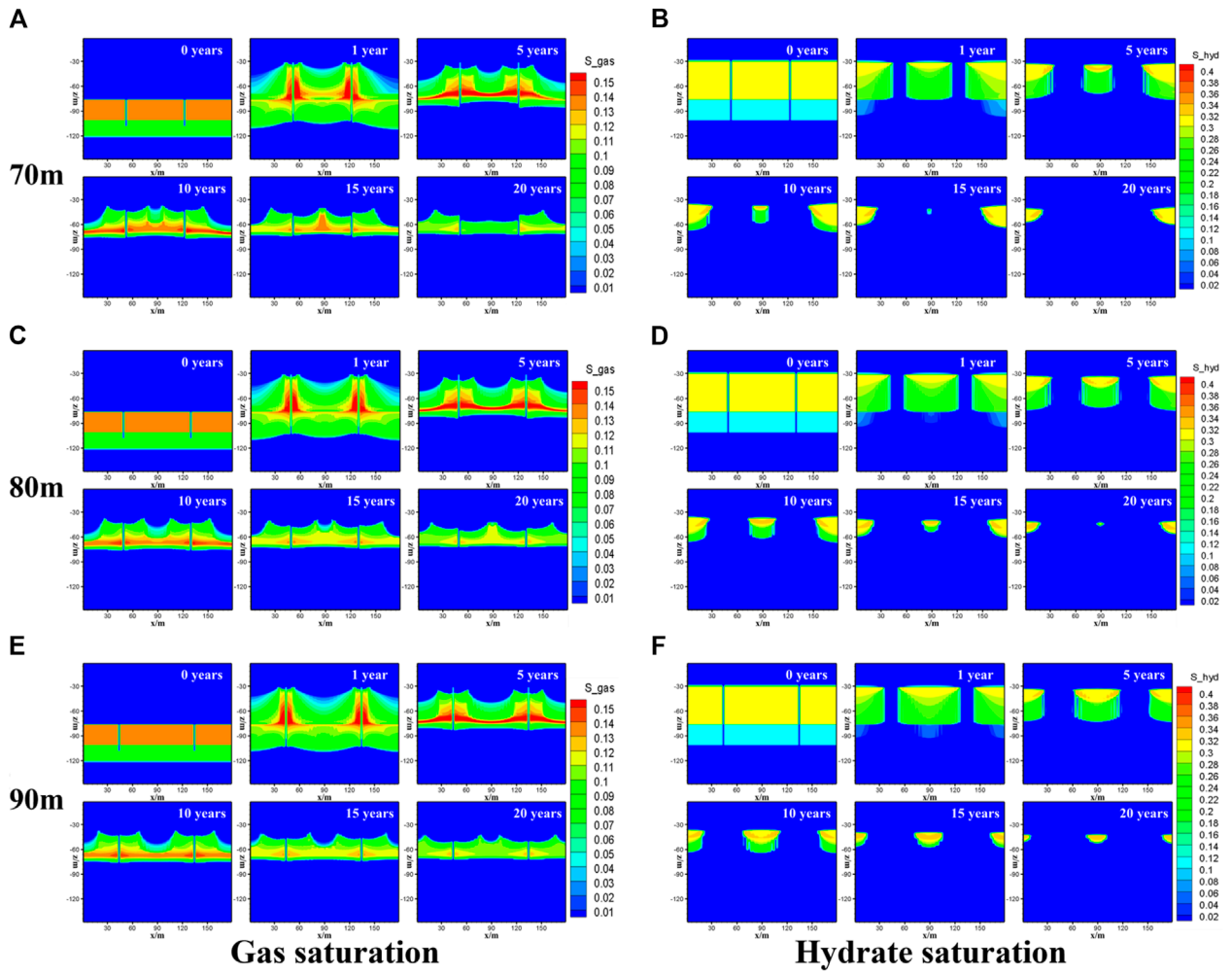

FIGURE 11
Spatiotemporal evolution of gas saturation field and hydrate saturation field, well spacing of 70–90 m. **(A, C, E)** Gas saturation Field. **(B, D, F)** Hydrate Saturation field.

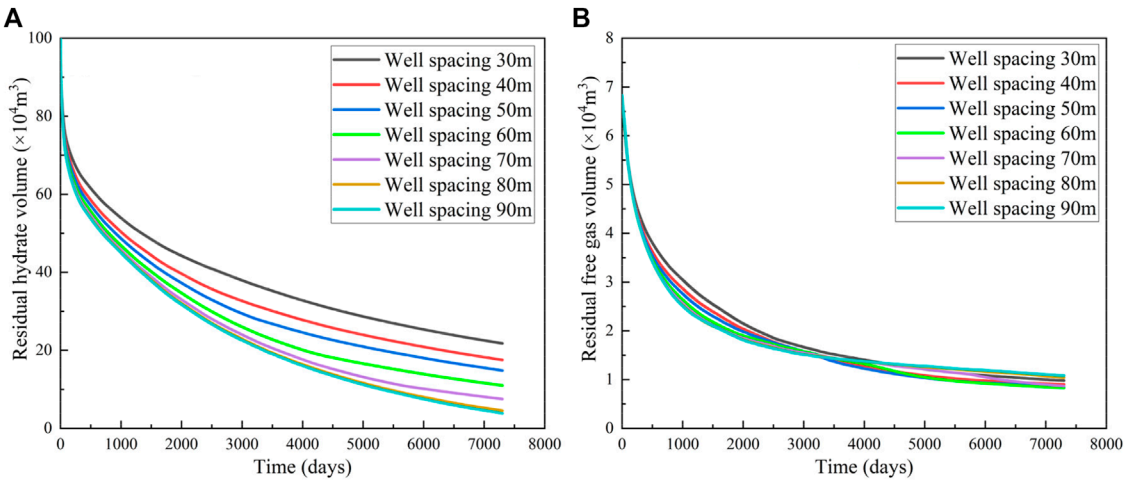

FIGURE 12
Variation trends of the residual hydrate volume and the residual free gas volume in depressurization exploitation with different well spacing for 20 years. **(A)** Residual hydrate volume. **(B)** Residual free volume.

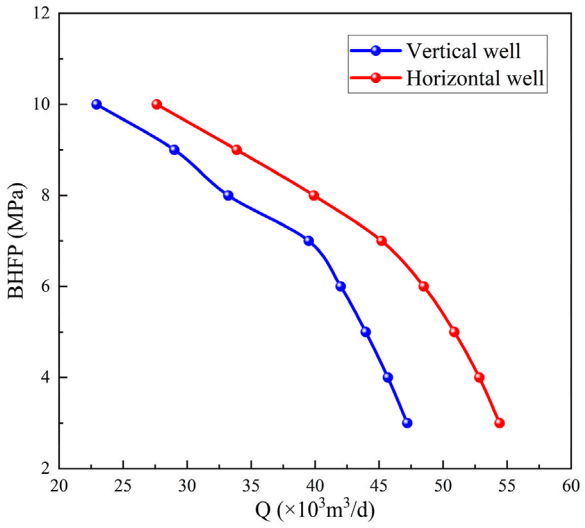

FIGURE 13
Inflow performance relationship curve.

1 m from the diameter of the model, as shown in Figure 10. The center of symmetry is positioned at x = 90 m, and we conduct depressurization exploitation simulations using vertical spacing of 30, 40, 50, 60, 70, 80, and 90 m to compare the variations of hydrate and free gas recovery rates under different vertical spacing configurations.

The spatial and temporal evolution of hydrate and free gas saturation extracted using depressurization at a well spacing of 30–60 m is shown in Supplementary Figures S1-S4. Figure 11 exhibit the spatial and temporal characteristics of hydrate and free gas saturation extracted using depressurization at a well spacing of 70–90 m. Figure 12 shows the variation trends of residual hydrate volume and residual free volume in 20 years of depressurized exploitation with different well spacing. As indicated in Figure 12A, the amount of residual hydrate extracted using double wells decreases gradually over time. The larger the spacing between double wells, the less residual hydrate is extracted after 20 years of operation. When the spacing between wells is 80 m and 90 m, the difference in the amount of residual hydrate is minimal. Combining the observations from Figure 11, it can be deduced that when the well spacing is 80 m, the undecomposed hydrate area between two wells is small, whereas when the well spacing is 90 m, the undecomposed hydrate area between two wells is larger. On the other hand, Figure 12B shows that the amount of residual free gas decreases rapidly initially, followed by a slower decline over time. However, the impact of different well spacing on the amount of residual free gas is not significant. To minimize the waste of hydrate resources, it is recommended to use double wells for hydrate exploitation in vertical wells with a well spacing of approximately 80 m.

4.4 Effect of bottom hole flowing pressure

The flow pressure at the bottom of the well is the most critical anthropogenic factor during pressure-reduction mining. Figure 13 displays the IPR (inflow performance relationship) curves for 20 years of vertical and horizontal well mining. Production capacity gradually declines as the bottom flow pressure rises, and at the same bottom flow pressure, the production capacity of horizontal wells is greater than that of vertical wells.

5 Conclusion

The specific purpose of this work is to conduct a numerical simulation study on depressurization exploitation for the class 1 hydrate reservoirs in the Shenhu sea of the South China Sea considering different development factors. In addition, the effects of different well types and different exploitation layers on the recovery rate of hydrate and free gas were analyzed. The effects of well spacing on enhanced hydrate recovery from vertical wells were also thoroughly investigated. Some important conclusions were drawn from the simulation results as below:

(1) For the first type of hydrate reservoir, under the same geological conditions, the highest hydrate and free gas recovery rates are achieved when mining to the free gas layer in a vertical well, which is the most effective approach. After 20 years of pressure-reduced extraction, the recovery rates of free gas and hydrate are 79.22% and 63.62%, respectively. The most effective approach is that the horizontal wells can extract hydrate and free gas at the same time when exploiting the hydrate three-phase layer. In the 2020 field test, the recovery efficiency of free gas from the optimal horizontal well is inferior to that from the optimal vertical well by 1.45%, but the recovery efficiency of hydrate is 5.82% higher than that from the vertical well. Since hydrate is more valuable to be extracted, the horizontal well is more effective.

(2) The best exploration efficiency is achieved when the spacing between two wells in a straight well is 80 m. In horizontal wells, the best recovery performance is achieved in the hydrate triple-phase layer. The recovery rates of free gas and hydrate were 77.77% and 69.44%, respectively, after 20 years of depressurization.

(3) The lower the flow pressure at the bottom of the well, the higher the production rate, but its influence is limited. Excessively low pressure will result in the hydrate layer freezing, so the bottomhole flow pressure should not be lower than the “four-phase point” of the hydrate phase equilibrium curve.

Data availability statement

The original contributions presented in the study are included in the article/Supplementary Material, further inquiries can be directed to the corresponding authors.

Author contributions

NW: Writing–review and editing, Funding acquisition, Resources. CL: Conceptualization, Data curation, Formal Analysis, Methodology, Software, Validation, Visualization, Writing–original draft, Writing–review and editing. XZ: Conceptualization, Data

curation, Formal Analysis, Methodology, Software, Validation, Visualization, Writing–original draft, Writing–review and editing. HL: Investigation, Writing–review and editing. LZ: Investigation, Writing–original draft, Writing–review and editing. JZ: Investigation, Writing–review and editing. BK: Funding acquisition, Project administration, Supervision, Writing–review and editing. RC: Funding acquisition, Methodology, Project administration, Supervision, Writing–review and editing.

Funding

The author(s) declare that financial support was received for the research, authorship, and/or publication of this article. This work was financially supported by the National Key Research and Development Program (Number 2021YFC2800903, 2023YFC2811002), National Natural Science Foundation of China (Number U20B6005-05), 111 Project (Number D21025), Open Fund Project of State Key Laboratory of Oil and Gas Reservoir Geology and Exploitation (Number PLN2021-01), and High-end Foreign Expert Introduction Program (Number G2021036005L).

Conflict of interest

The authors declare that the research was conducted in the absence of any commercial or financial relationships that could be construed as a potential conflict of interest.

Publisher's note

Supplementary material

The Supplementary Material for this article can be found online at: https://www.frontiersin.org/articles/10.3389/feart.2024.1444690/full#supplementary-material

References

Anderson, B. J., Kurihara, M., White, M. D., Moridis, G. J., Wilson, S. J., Pooladi-Darvish, M., et al. (2011). Regional long-term production modeling from a single well test, mount elbert gas hydrate stratigraphic test well, alaska north slope. *Mar. Pet. Geol.* 28, 493–501. doi:10.1016/j.marpetgeo.2010.01.015

Chen, L., Feng, Y. C., Okajima, J., Komiya, A., and Maruyama, S. (2018). Production behavior and numerical analysis for 2017 methane hydrate extraction test of Shenhu, south China sea. *J. Nat. Gas. Sci. Eng.* 53, 55–66. doi:10.1016/j.jngse.2018.02.029

Chibura, P. E., Zhang, W., Luo, A., and Wang, J. (2022). A review on gas hydrate production feasibility for permafrost and marine hydrates. *J. Nat. Gas. Sci. Eng.* 100, 104441. doi:10.1016/j.jngse.2022.104441

Cranganu, C. (2009). *In-situ* thermal stimulation of gas hydrates. *J. Pet. Sci. Eng.* 65, 76–80. doi:10.1016/j.petrol.2008.12.028

Fan, S. S., Yang, S. W., Wen, Y. G., Wang, Y. H., and Lang, X.-M. (2013). A simulation study of class III hydrate production with a high efficiency through the depressurization recovery and thermal stimulation in horizontal wells. *Nat. Gas. Ind.* 33, 36–42. (In Chinese). doi:10.3787/j.issn.1000-0976.2013.07.006

Feng, J. C., Wang, Y., Li, X. S., Li, G., Zhang, Y., and Chen, Z. Y. (2015). Production performance of gas hydrate accumulation at the GMGS2-site 16 of the pearl river mouth basin in the South China sea. *J. Nat. Gas. Sci. Eng.* 27, 306–320. doi:10.1016/j.jngse.2015.08.071

Gamwo, I. K., and Liu, Y. (2010). Mathematical modeling and numerical simulation of methane production in a hydrate reservoir. *Ind. Eng. Chem. Res.* 49, 5231–5245. doi:10.1021/ie901452v

Goel, N. (2006). *In situ* methane hydrate dissociation with carbon dioxide sequestration: current knowledge and issues. *J. Pet. Sci. Eng.* 51, 169–184. doi:10.1016/j.petrol.2006.01.005

Guo, X., Zhang, N., and Kong, B. (2022). Numerical simulation of depressurization production of natural gas hydrate in different well types. *Pet. Sci. Technol.* 41 (10), 1060–1080. doi:10.1080/10916466.2022.2072331

Hong, H. N., and Pooladi-Darvish, M. (2003) "A numerical study on gas production from formations containing gas hydrates," in *Proceeding of the Canadian international Petroleum Conference, PETSOC-2003-060, June 10–12, 2003, Calgary, Alberta, Canada; Canadian international petroleum conference*. Calgary, Alberta, Canada. doi:10.2118/2003-060

Konno, Y., Fujii, T., Sato, A., Akamine, K., Naiki, M., Masuda, Y., et al. (2017). Key findings of the world's first offshore methane hydrate production test off the Coast of Japan: toward future commercial production. *Energy fuels.* 31, 2607–2616. doi:10.1021/acs.energyfuels.6b03143

Kurihara, M., Sato, A., Ouchi, H., Narita, H., Masuda, Y., Saeki, T., et al. (2009). Prediction of gas productivity from Eastern Nankai Trough methane-hydrate reservoirs. *SPE Reserv. Eval. Eng.* 12, 477–499. doi:10.2118/125481-PA

Li, G., Li, X. S., Tang, L. G., and Zhang, Y. (2007). Experimental investigation of production behavior of methane hydrate under ethylene glycol injection in unconsolidated sediment. *Energy fuels.* 21, 3388–3393. doi:10.1021/ef060644d

Li, G., Li, X. S., Zhang, K., and Moridis, G. J. (2011). Numerical simulation of gas production from hydrate accumulations using a single horizontal well in Shenhu area, south China sea. *Chin. J. Geophys.* 54 (9), 2325–2337. (in Chinese). doi:10.3969/j.issn.0001-5733.2011.09.016

Li, J. F., Ye, J. L., Qin, X. W., Qiu, H. J., Wu, N. Y., Lu, H. L., et al. (2018). The first offshore natural gas hydrate production test in south China sea. *China Geol.* 1, 5–16. doi:10.31035/cg2018003

Lin, T. K., Dahyar, M., Lee, M. J., and Hsieh, B. Z. (2020). Study of the formation mechanisms of CO_2 hydrates from matching the experimental data with a porous media setting by multiphase flow-geochemical-thermal reservoir simulator. *J. Taiwan Inst. Chem. Eng.* 114, 115–124. doi:10.1016/j.jtice.2020.09.015

Makogon, Y. F., and Omelchenko, R. Y. (2013). Commercial gas production from messoyakha deposit in hydrate conditions. *J. Nat. Gas. Sci. Eng.* 11, 1–6. doi:10.1016/j.jngse.2012.08.002

Masuda, Y., Konno, Y., Iwama, H., Kawamura, T., Kurihara, M., and Ouchi, H. (2008) "Improvement of near wellbore permeability by methanol stimulation in a methane hydrate production well," in *Proceeding of the offshore Technology Conference, OTC-19433-MS, may 5–8, Houston, TX, USA; offshore Technology Conference*. Houston, TX, USA. doi:10.4043/19433-MS

McMullan, R. K., and Jeffrey, G. A. (1965). Polyhedral clathrate hydrates. IX. Structure of Ethylene Oxide hydrate. *J. Chem. Phys.* 42, 2725–2732. doi:10.1063/1.1703228

Merey, S., and Sinayuc, C. (2017). Numerical simulations for short-term depressurization production test of two gas hydrate sections in the black sea. *J. Nat. Gas. Sci. Eng.* 44, 77–95. doi:10.1016/j.jngse.2017.04.011

Moridis, G. J. (2003). Numerical studies of gas production from methane hydrates. *SPE J.* 8, 359–370. doi:10.2118/87330-PA

Moridis, G. J., and Collett, T. S. (2003) "Strategies for gas production from hydrate accumulations under various geologic conditions," in *Proceedings, TOUGH Symposium 2003*. Berkeley, CA, USA: Lawrence Berkeley national laboratory. May 12–14, 200.

Moridis, G. J., Kowalsky, M. B., and Pruess, K. (2007). Depressurization-induced gas production from class 1 hydrate deposits. *SPE Reserv. Eval. Eng.* 10, 458–481. doi:10.2118/97266-PA

Moridis, G. J., and Reagan, M. T. (2007a) "Gas production from oceanic class 2 hydrate accumulations," in *Proceeding of the offshore Technology Conference, OTC-18866-MS, April 30–may 3, Houston, TX, USA; offshore technology conference*. Houston, TX, USA. doi:10.4043/18866-MS

Moridis, G. J., and Reagan, M. T. (2007b) "Strategies for gas production from oceanic class 3 hydrate accumulations," in *Proceeding of the offshore Technology Conference, OTC-18865-MS, April 30–may 3, Houston, TX, USA; offshore technology conference: houston, TX, USA*. doi:10.4043/18865-MS

Moridis, G. J., and Reagan, M. T. (2011a). Estimating the upper Limit of gas production from class 2 hydrate accumulations in the permafrost: 1. Concepts, system Description, and the production Base case. *J. Pet. Sci. Eng.* 76, 194–204. doi:10.1016/j.petrol.2010.11.023

Moridis, G. J., and Reagan, M. T. (2011b). Estimating the upper limit of gas production from class 2 hydrate accumulations in the permafrost: 2. alternative well designs and sensitivity analysis. *J. Pet. Sci. Eng.* 76 (3-4), 124–137. doi:10.1016/j.petrol.2010.12.001

Moridis, G. J., Reagan, M. T., Boyle, K. L., and Zhang, K. (2011). Evaluation of the gas production potential of some particularly challenging types of oceanic hydrate deposits. *Porous Media* 90, 269–299. doi:10.1007/s11242-011-9762-5

Moridis, G. J., and Sloan, E. D. (2007). Gas production potential of disperse low-saturation hydrate accumulations in oceanic sediments. *Energy Conv. Manag.* 48, 1834–1849. doi:10.1016/j.enconman.2007.01.023

Myshakin, E. M., Gaddipati, M., Rose, K., and Anderson, B. J. (2012). Numerical simulations of depressurization-induced gas production from gas hydrate reservoirs at the walker ridge 313 site, northern Gulf of Mexico. *Mar. Pet. Geol.* 34, 169–185. doi:10.1016/j.marpetgeo.2011.09.001

Nair, V. C., Ramesh, S., Ramadass, G. A., and Sangwai, J. S. (2016). Influence of thermal stimulation on the methane hydrate dissociation in porous media under confined reservoir. *J. Pet. Sci. Eng.* 147, 547–559. doi:10.1016/j.petrol.2016.09.017

Ohgaki, K., Takano, K., Sangawa, H., Matsubara, T., and Nakano, S. (1996). Methane exploitation by carbon dioxide from gas hydrates—phase equilibria for CO_2-CH4 mixed hydrate system. *J. Chem. Eng. Jpn.* 29, 478–483. doi:10.1252/jcej.29.478

Qin, X. W., Liang, Q. Y., Ye, J. L., Yang, L., Qiu, H. J., Xie, W. W., et al. (2020). The response of temperature and pressure of hydrate reservoirs in the first gas hydrate production test in south China sea. *Appl. Energy.* 278, 115649. doi:10.1016/j.apenergy.2020.115649

Sloan, E. D., and Koh, C. A. (2007). *Clathrate hydrates of natural gases*. 3rd ed. New York: CRC Press. doi:10.1201/9781420008494

Su, Z., Moridis, G. J., Zhang, K., and Wu, N. Y. (2012). A huff-and-puff production of gas hydrate deposits in Shenhu area of south China sea through a vertical well. *J. Pet. Sci. Eng.* 86 (87), 54–61. doi:10.1016/j.petrol.2012.03.020

Sun, J. X., Qin, F. F., Ning, F. L., Gu, Y. H., Li, Y. L., Cao, X. X., et al. (2023). Gas recovery from silty hydrate reservoirs by using vertical and horizontal well patterns in the South China sea: effect of well spacing and its optimization. *Energy* 275, 127440. doi:10.1016/j.energy.2023.127440

Sun, Y. H., Ma, X. L., Guo, W., Jia, R., and Li, B. (2019). Numerical simulation of the short- and long-term production behavior of the first offshore gas hydrate production test in the south China sea. *J. Pet. Sci. Eng.* 181, 106196. doi:10.1016/j.petrol.2019.106196

Terzariol, M., and Santamarina, J. C. (2021). Multi-well strategy for gas production by depressurization from methane hydrate-bearing sediments. *Energy* 220, 119710. doi:10.1016/j.energy.2020.119710

Villano, L. D., Kommedal, R., Fijten, M. W. M., Schubert, U. S., Hoogenboom, R., and Kelland, M. A. (2009). A study of the kinetic hydrate inhibitor performance and seawater biodegradability of a series of Poly(2-alkyl-2-oxazoline)s. *Energy fuels.* 23, 3665–3673. doi:10.1021/ef900172f

Wang, D. Y., Ma, X. J., and Qiao, J. (2013). Impact factors of natural gas hydrate dissociation by depressurization: a review. *Adv. Mat. Res.* 868, 564–567. doi:10.4028/www.scientific.net/amr.868.564

Wei, N., Bai, R. L., Zhao, J. Z., Zhang, Y., and Xue, J. (2021). The prospect of natural gas hydrate (NGH) under the vision of peak carbon dioxide emissions in China. *Petroleum* 7, 357–363. doi:10.1016/j.petlm.2021.11.001

Wei, N., Pei, J., Zhao, J. Z., Zhang, L. H., Zhou, S. W., Luo, P. Y., et al. (2022). A state-of-the-art review and prospect of gas hydrate reservoir drilling techniques. *Front. Earth Sci.* 10. doi:10.3389/feart.2022.997337

Wei, N., Sun, W. T., Meng, Y. F., Liu, A. Q., Zhao, J. Z., Zhou, S. W., et al. (2018). Multiphase non equilibrium pipe flow behaviors in the solid fluidization exploitation of marine natural gas hydrate reservoir. *Energy Sci. Eng.* 6, 760–782. doi:10.1002/ese3.251

Xia, Z. Z., Wang, X. W., and Zhang, X. H. (2019). Investigation of the hydrate reservoir production under different depressurization modes. *Mar. Geores. Geotechnol.* 38 (8), 1002–1012. doi:10.1080/1064119X.2019.1646845

Xu, C. G., and Li, X. S. (2015). Research progress on methane production from natural gas hydrates. *RSC Adv.* 5, 54672–54699. doi:10.1039/c4ra10248g

Xu, C. G., Li, X. S., Yan, K. F., Ruan, X. K., Chen, Z. Y., and Xia, Z. M. (2019). Research progress in hydrate-based technologies and processes in China: a review. *Chin. J. Chem. Eng.* 27, 1998–2013. doi:10.1016/j.cjche.2018.12.002

Yamamoto, K. (2015). Overview and introduction: pressure core-sampling and analyses in the 2012-2013 MH21 offshore test of gas production from methane hydrates in the eastern nankai trough. *Mar. Pet. Geol.* 66, 296–309. doi:10.1016/j.marpetgeo.2015.02.024

Ye, J. L., Qin, X. W., Xie, W. W., Lu, H. L., Ma, B. J., Qiu, H. J., et al. (2020). The second natural gas hydrate production test in the South China sea. *China Geol.* 3, 197–209. doi:10.31035/cg2020043

Yu, T., Guan, G. Q., Abudula, A., Yoshida, A., Wang, D. Y., and Song, Y. (2019). Application of horizontal wells to the oceanic methane hydrate production in the nankai trough, Japan. *Jpn. J. Nat. Gas. Sci. Eng.* 62, 113–131. doi:10.1016/j.jngse.2018.11.027

Yu, T., Guan, G. Q., Wang, D. Y., Song, Y. C., and Abudula, A. (2021). Numerical evaluation on the effect of horizontal-well systems on the long-term gas hydrate production behavior at the second Shenhu test site. *J. Nat. Gas. Sci. Eng.* 95, 104200. doi:10.1016/j.jngse.2021.104200

Zhao, J., Song, Y., Lim, X. L., and Lam, W. H. (2017). Opportunities and challenges of gas hydrate policies with consideration of environmental impacts. *Renew. Sust. Energ. Rev.* 70, 875–885. doi:10.1016/j.rser.2016.11.269

Zhao, J. F., Yu, T., Song, Y. C., Liu, D., Liu, W. G., Liu, Y., et al. (2013). Numerical simulation of gas production from hydrate deposits using a single vertical well by depressurization in the Qilian Mountain permafrost, qinghai-tibet plateau, China. *Energy.* 52, 308–319. doi:10.1016/j.energy.2013.01.066

Zhao, J. F., Zhu, Z. H., Song, Y. C., Liu, W. G., Zhang, Y., and Wang, D. Y. (2015). Analyzing the process of gas production for natural gas hydrate using depressurization. *Appl. Energy.* 142, 125–134. doi:10.1016/j.apenergy.2014.12.071

Zhou, S. W., Chen, W., and Li, Q. P. (2014). The green solid fluidization development principle of natural gas hydrate stored in shallow layers of deep water. *China Offshore Oil Gas.* 26, 1–7. (In Chinese).

Zhou, S. W., Chen, W., Li, Q. P., Zhou, J. L., and Shi, H. S. (2017). Research on the solid fluidization well testing and production for shallow non-diagenetic natural gas hydrate in deep water area. *China Offshore Oil Gas.* 29, 1–8. (In Chinese). doi:10.11935/j.issn.1673-1506.2017.04.001

Zhou, S. W., Zhao, J. Z., Li, Q. P., Chen, W., Zhou, J. L., Wei, N., et al. (2018). Optimal design of the engineering parameters for the first global trial production of marine natural gas hydrates through solid fluidization. *Nat. Gas. Ind. B* 5, 118–131. doi:10.1016/j.ngib.2018.01.004

frontiers | Frontiers in Earth Science

TYPE Original Research
PUBLISHED 08 October 2024
DOI 10.3389/feart.2024.1454449

OPEN ACCESS

EDITED BY
Shida Chen,
China University of Geosciences, China

REVIEWED BY
Chen Qiusong,
Central South University, China
Qingquan Liu,
China University of Mining and Technology, China
Dongti Zhang,
University of New South Wales, Australia

*CORRESPONDENCE
Dongming Zhang,
zhangdm@cqu.edu.cn

RECEIVED 25 June 2024
ACCEPTED 16 September 2024
PUBLISHED 08 October 2024

CITATION
Li H, Yu G, Fang Y, Chen Y, Sun K, Liu Y, Chen Y and Zhang D (2024) Uncertainty prediction of conventional gas production in Sichuan Basin under multi factor control. *Front. Earth Sci.* 12:1454449. doi: 10.3389/feart.2024.1454449

Uncertainty prediction of conventional gas production in Sichuan Basin under multi factor control

Haitao Li[1], Guo Yu[2], Yizhu Fang[1], Yanru Chen[1], Kaijun Sun[3], Yang Liu[1], Yu Chen[4] and Dongming Zhang[4]*

[1]Exploration and Development Research Institute of PetroChina Southwest Oil and Gas Field Company, Chengdu, China, [2]PetroChina Southwest Oil and Gas Field Company Planning Department, Chengdu, Sichuan, China, [3]Southwest Oil and Gas Field Branch Chongqing Gas Mine, Chongqing, China, [4]College of Resources and Security, Chongqing University, Chongqing, China

The establishment of a natural gas production model under multi factor control provides support for the formulation of planning schemes and exploration deployment decisions, and is of great significance for the rapid development of natural gas. Especially the growth rate and decline rate of production can be regulated in the planning process to increase natural gas production. The exploration and development of conventional gas in the Sichuan Basin has a long history. Firstly, based on the development of conventional gas production, the influencing factors of production are determined and a production model under multi factor control is established. Then, single factor analysis and sensitivity analysis are conducted, and multi factor analysis is conducted based on Bayesian networks. Finally, combining the multivariate Gaussian mixture model and production sensitivity analysis, a production planning model is established to predict production uncertainty under the influence of multiple factors. The results show that: 1) the production is positively correlated with the five influencing factors, and the degree of influence is in descending order: recovery rate, proven rate, growth rate, decline rate, and recovery degree. After being influenced by multiple factors, the fluctuation range of production increases and the probability of realization decreases. 2) The growth rate controls the amplitude of the growth stage, the exploration rate and recovery rate control the amplitude of the stable production stage, the recovery degree controls the amplitude of the transition from the stable production stage to the decreasing stage, and the decreasing rate controls the amplitude of the decreasing stage. 3)The article innovatively combines multiple research methods to further obtain the probability of achieving production under the influence of multiple factors, providing a reference for the formulation of production planning goals.

KEYWORDS

Bayesian network, multivariate Gaussian mixture model, analysis of influencing factors, sensitivity analysis, production probability calculation, production planning model

1 Introduction

Carbon peaking and carbon neutrality are major national strategies aimed at promoting high-quality economic and social development through the transformation of the energy

system, and promoting the transformation of the energy system from fossil energy to renewable energy. Natural gas belongs to low-carbon fossil energy, with a strong development foundation and huge development potential. Moderately leveraging the unique advantages of clean, low-carbon, efficient, and stable natural gas is of great significance for the high-quality development of China's natural gas industry and the smooth realization of carbon peak and carbon neutrality goals (Song et al., 2023; Nuo et al., 2022; Jian et al., 2018; Jun et al., 2024; Wang et al., 2024; Arun Kumar et al., 2020). In addition, the development of natural gas production is highly uncertain due to various factors such as reserve utilization efficiency, economic factors, geological factors, and development factors (Hongbing and Han, 2023; Haitao et al., 2021; Jianliang and Nu, 2020). Reasonable production target planning is of great significance to the exploration and development of natural gas and can promote the rapid development of natural gas. Therefore, establishing a natural gas production prediction model under multi factor control provides support for the preparation of planning schemes and exploration deployment decisions, and is of great significance for the rapid development of natural gas.

There has been some research on methods and models for predicting natural gas production, and they have been well applied both domestically and internationally. Tongfei and Yanrui, 2022 proposed a new discrete fractional nonlinear grey Bernoulli model with power terms, which has the advantages of most grey prediction models, such as fractional order cumulative operation and time power terms. Then, taking the consumption and production of natural gas in China from 2003 to 2020 as an example, the feasibility and effectiveness of the model were verified. The results indicate that the predictive ability of this model is superior to other models. Chong et al., 2022 established an optimized grey system model with weighted score accumulation, which has good predictive performance. Then, taking the natural gas production of Germany, Italy, and Canada as examples, the feasibility of the model was confirmed through comparison with the competitive model, and the model was used to study China's natural gas production. The results indicate that this model is very suitable for predicting and analyzing China's natural gas production. Yingying et al., 2022 established a semi analytical shale gas constant pressure production capacity prediction model and verified it with actual production data. Research has shown that this method has certain theoretical reference value in reducing the risk of production prediction during the production process of shale gas wells and guiding the optimization of development plans. In addition, many scholars have applied algorithms to predict energy sources such as natural gas. Durmuş and Safa, 2022 proposed a new improved Artificial bee colony (M-ABC) method, which adaptively selects the optimal search equation to estimate energy consumption in Turkey more accurately. The results show that the model based on M-ABC algorithm is more successful in estimating energy demand. Durmuş Özdemir (Özdemir et al., 2022) developed a new adaptive artificial bee colony algorithm, which can adaptively select the appropriate search equation to estimate the transportation energy demand more accurately. The results show that the error of this algorithm is lower. (Bilici et al., 2023) compared the performance of four different meta-heuristic algorithms used to estimate gas demand in Turkey. The results show that PSO-Quadratic model is the most successful in predicting observed gas consumption. The research of these scholars has brought some inspiration, and suitable models or algorithms can be used to predict natural gas production.

Although domestic and foreign scholars have optimized production prediction models, these methods all combine models and historical data to predict the development trend of production, without considering factors that affect natural gas production, such as proven rate, recovery rate, decline rate, etc., and are not suitable for environments with multi factor control (Marta et al., 2020; Erick et al., 2022; Palanisamy et al., 2021). Therefore, it is necessary to establish a production target prediction model that considers various influencing factors. Guo et al., 2021 used Monte Carlo probability method to obtain the probability distribution and growth curve of various production risk factors and production of the Carboniferous gas reservoir in eastern Sichuan. In addition, the sensitivity analysis of risk factors was conducted using the fuzzy comprehensive evaluation method, and the natural gas production and realization probability under different risk factors were obtained. Jianzhong et al., 2016 used a gas field in the Ordos Basin as an example to construct an optimal extraction model for natural gas resources. They analyzed the impact of factors such as the extraction scale of the gas field, recovery rate, discount rate, and gas well depletion period on the optimal exploration path of the gas field. Since these studies only consider the impact of a single factor on production, they cannot reflect the coupling effect of multiple factors on production in actual production. Therefore, it is necessary to combine multiple influencing factors and calculate the multivariate probability of production realization. In view of many factors affecting natural gas production, this paper comprehensively considers the change rule and realization probability of production under the influence of different factors, which makes up for the shortcomings of current research. Due to the need to simultaneously consider multiple factors for mixed probability calculation and establish a multi factor prediction model, Bayesian networks and Gaussian mixture models are needed.

Bayesian networks are developed by J Pearl was proposed in the 1980s as a powerful tool for representing, manipulating, and inferring beliefs about the real world. They are used to demonstrate the probability relationships between random variables and serve as models for the joint probability distribution of these variables (Duygu and Derya, 2019; Yaser et al., 2021; Haoran et al., 2022; Jiří et al., 2023; Qi et al., 2018 proposed a fuzzy probability Bayesian network method for dynamic risk assessment. FPBN has been established to analyze and predict the propagation of network security risks, and an approximate dynamic inference algorithm has been proposed for dynamic assessment of ICS network security risks. Yang et al., 2021 proposed a system level fatigue reliability assessment model based on Bayesian networks, treating bridge decks as a parallel system. A fatigue probability reliability model was derived using the main S-N curve. Kyung et al., 2024 realized Bayesian inference of all conditional probabilities within the network at low power and low energy consumption, and achieved a normalized mean squared error of ~7.5×10^{-4} through division feedback logic with variational learning rate to suppress the inherent variation of the memristor. Therefore, Bayesian networks can be used to solve the calculation problem of mixed probabilities of multiple factors.

Gaussian Mixture Model (GMM) is a special type of finite mixture model that assumes that the basic distribution of data

is composed of a mixture of multiple Gaussian distributions. GMM has been widely applied in various scientific fields, including computer vision, pattern recognition, and supervised and unsupervised learning (Luca, 2023; Cangqi et al., 2020; Maruf, 2021; Joachim et al., 2024; Zhe et al., 2020 used a Gaussian mixture model to estimate the probability density function of wave height in the context of second-order random wave theory. Two methods were used to construct a Gaussian mixture probability distribution, and three sets of observation data were applied to further validate the accuracy and effectiveness of the Gaussian mixture model; Chunsheng et al., 2020 proposed a variational autoencoder that optimizes Gaussian mixture model prior. This method utilizes a Gaussian mixture model to construct a prior distribution, and utilizes the KL distance between the posterior distribution and the prior distribution to achieve iterative optimization of the prior distribution based on data. (Chen et al., 2024) reconstructed the probability density function of input random variables by using a Gaussian mixture model, proposed a K-value criterion for the selection of segmentation direction considering both nonlinearity and variance, and then divided the components of input random variables into a Gaussian mixture model, which has a small variance along the direction determined by the k value. Therefore, a Gaussian mixture model can be used to stack the distribution results of multiple probability calculations to obtain a mixed model that considers multiple factors.

Based on the development of conventional gas production in the Sichuan Basin, this article first determines the influencing factors of production by combining production planning models, and establishes a production prediction model under multi factor control. Then, based on the analysis of various factors, the variation patterns of production and realization probability under the influence of single factors were obtained. Combined with sensitivity analysis, the sensitivity degree of different factors was obtained, and the impact range of each factor was preliminarily determined. In addition, a multi factor analysis was conducted based on Bayesian networks, using the detection rate and recovery rate as prior probabilities to obtain binary distribution probabilities and implementation probabilities of other factors, as well as production variation graphs under the influence of multiple factors. Finally, combining the weight results of the multivariate Gaussian mixture model and sensitivity analysis, a production planning model is established to predict production uncertainty under the influence of multiple factors.

2 Production uncertainty prediction theory

2.1 Bayesian network

Bayesian networks are directional graphs that combine network structures, covering knowledge from multiple fields such as artificial intelligence, probability theory, and decision theory. Bayesian networks use directed acyclic graphs to represent the correlation and degree of influence of each information element. Among them, nodes are used to represent each feature attribute, directional arrows connecting nodes represent the correlation of each feature attribute, conditional probability represents the degree of influence between each feature attribute, and combines prior probability with sample information, correlation relationships, and probability tables (Deyan et al., 2022; Li et al., 2022; Dongfeng et al., 2020; Jianliang and Nu, 2020; David et al., 2022).

Bayesian networks have an important and commonly used characteristic. After the preceding nodes are determined, each subsequent node is independent of each other and directly related to the preceding node. Therefore, the probability of the preceding node can be used as a prior probability, and the probability of each subsequent independent node can be calculated. The existence of this feature also proves that Bayesian networks can conveniently calculate joint probability distributions, using Formula 1 to calculate multivariate non independent joint conditional probability distributions.

$$P(x_1, x_2, ..., x_n) = P(x_1)P(x_2|x_1)P(x_3|x_1, x_2)...P(x_n|x_1, x_2, ..., x_{n-1}) \tag{1}$$

In Formula 1, $P(x_n|x_1, x_2, ..., x_{n-1})$ represents the probability of node x_n under the probability of other nodes. In this case, other nodes are not independent, but x_n is independent.

In Bayesian networks, due to the above properties, the joint conditional probability distribution of any combination of random variables is shown in Formula 2, where *Parents* represents the joint probability of the preceding nodes of x_i.

$$P(x_1, x_2, ..., x_n) = \prod_{i=1}^{n} P(x_i|Parents(x_i)) \tag{2}$$

In Bayesian network, there can be multiple directed paths between nodes, meaning that there may be multiple subsequent nodes after a preceding node, and all subsequent nodes may be affected by the preceding node. There may be correlation or independence between subsequent nodes. Therefore, after determining the prior probability of the preceding node, the corresponding probability of the subsequent nodes can be obtained, which provides a good idea for the research of natural gas production prediction affected by multiple factors. Some factors that are bound to have an impact can be used as pre nodes to calculate their prior probabilities, and then study the implementation probabilities of other factors and their impact on production.

Based on the research approach described above, a Bayesian network with conditional probability distribution can be established to calculate the probability of factors affecting gas production in the gas field. As shown in Formula 3, both A and B_i represent various influencing factors that occur when predicting production in a certain gas region. $P(A)$ is a prior probability, which is the probability of being selected as a leading node. $P(B_i|A)$ is the probability of other factors calculated after the prior probability is known. $P(A|B_i)$ is the binary probability obtained by considering both A and B_i. To study the impact of multiple factors on natural gas production, it is necessary to calculate the production prediction results and realization probabilities under multiple factors. Therefore, it is necessary to take some factors as prior probabilities and then calculate the probabilities of other factors. Currently, it is necessary to adopt the research method of Bayesian network.

$$P(A|B_i) = \frac{P(B_i|A)P(A)}{\sum_{i=1}^{n} P(B_i|A)P(A)} \tag{3}$$

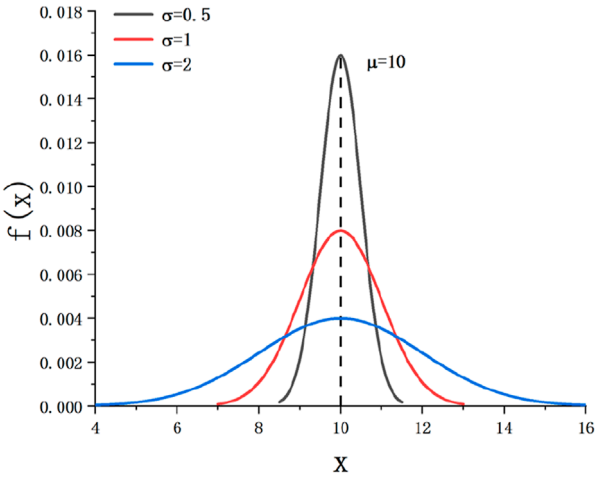

FIGURE 1
Univariate normal distribution function diagram.

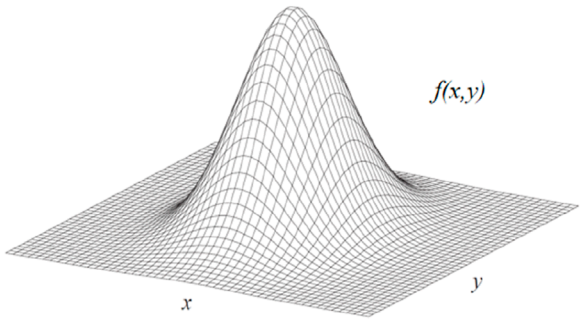

FIGURE 2
Binary normal distribution function diagram.

2.2 Multivariate Gaussian mixture model

The Gaussian mixture model can be seen as a model composed of multiple Gaussian models, which are hidden variables of the mixture model. A mixed model can use any probability distribution, and the Gaussian mixed model is used here because the Gaussian distribution has good mathematical properties and good computational performance, which can better analyze the trend of data changes. There is interference between different Gaussian models that changes the distribution shape of the mixed model, and the combined model is affected by the shape of other sub models (Andreas, 2021; Adriana and Martha, 2021; Julie and Agnes, 2020). Below is a detailed explanation of this.

The Gaussian distribution can be regarded as a normal distribution, and the distribution function of a single Gaussian model is shown in Formula 4. Figure 1 shows the univariate normal distribution function.

$$f(x) = \frac{1}{\sqrt{2\pi}\sigma} e^{-\frac{(x-\mu)^2}{2\sigma^2}} \tag{4}$$

Among them, μ is the mean, σ is the standard deviation.

When considering two Gaussian models simultaneously, the combined bivariate Gaussian model distribution function is shown in Formula 5, and Figure 2 shows the bivariate normal distribution function.

$$f(x_1,x_2) = \frac{1}{2\pi\sigma_1\sigma_2\sqrt{1-p^2}} \exp\left(-\frac{1}{2(1-p^2)}\left(\frac{(x_1-\mu_1)^2}{\sigma_1^2} + \frac{(x_2-\mu_2)^2}{\sigma_2^2} - \frac{2p(x_1-\mu_1)(x_2-\mu_2)}{\sigma_1\sigma_2}\right)\right) \tag{5}$$

Among them, x_1 satisfies the normal distribution $N(\mu_1,\sigma_1^2)$, x_2 satisfies the normal distribution $N(\mu_2,\sigma_2^2)$, p is the correlation coefficient, $p = \frac{C_{12}}{\sigma_1\sigma_2}$, C_{12} is the covariance, $C_{12} = E - \mu_1\mu_2$, and E is the expected value of the binary Gaussian model.

The distribution function of the multivariate Gaussian model is derived analogously, as shown in Formula 6.

$$f(x_1,x_2,\ldots,x_n) = \frac{1}{\sqrt{(2\pi)^n|\Sigma|^{1/2}}} \exp\left(-\frac{1}{2}(x-\mu)^T\Sigma^{-1}(x-\mu)\right) \tag{6}$$

Among them, Σ is the covariance matrix, T is the transposed symbol, μ is the mean.

After analyzing the influencing factors of natural gas production, this article uses a multivariate Gaussian mixture model to establish a production planning model. Firstly, establish a single Gaussian model based on each factor, and then use the superposition approach to combine the five Gaussian models together to form a production planning model under multi factor control.

2.3 Production uncertainty prediction model

From the historical production of natural gas, the development of production will go through multiple cycles, with each cycle showing three stages of growth, stability, and decline. Currently, natural gas in the Sichuan Basin is undergoing the fourth production cycle of development. According to the requirements of production planning, under a certain ultimate recoverable reserve URR, the production goes through a growth period, a stable production period, and a decreasing period, with a stable production period of 20 years. Finally, a production planning chart is generated. As shown in Figure 3, based on the historical production data of conventional gas in the Sichuan Basin, boundary conditions are set to predict the development trend of production. From the figure, using the data from 1953 to 2023 as historical data, predictions will be made after 2023, with a production growth period from 2023 to 2032, a stable production period from 2032 to 2051, and a production decline period after 2051. The area of the entire curve is equal to the ultimate recoverable reserve URR.

When planning production, it is necessary to consider factors that may affect changes in production. To reasonably screen the influencing factors of production, combined with the production planning chart, starting from different stages of production development, determine the influencing factors. Firstly, during the production growth stage, the production will show different

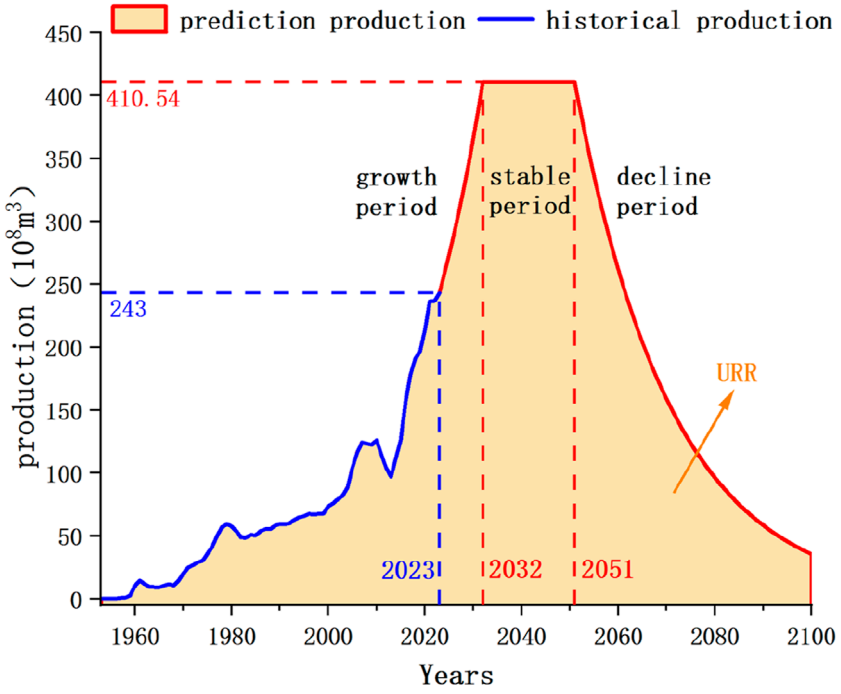

FIGURE 3
Historical development and production planning curve of conventional gas in Sichuan Basin.

growth rates with changes in the growth rate. Secondly, during the stable production stage, the degree of extraction will also affect the production during the stable production period. Finally, in the stage of production decline, production will show different degrees of decline with changes in the decline rate. In addition, the development of the entire production is also controlled by the ultimate recoverable reserve URR, which is also influenced by the proven rate and recovery rate. In summary, the factors that affect the development of production include the proven rate, recovery rate, growth rate, degree of recovery at the end of stable production period, and decline rate.

By constraining the production and time during the stable production period through these five influencing factors, multiple equations are established, as shown below.

$$\left[Q_{ls} + (Q + Q_0) * \frac{t_m - t_0}{2}\right] + t * Q * c_c + dj * Q = URR \quad (7)$$

$$\frac{Q - Q_0}{t_m - t_0} = k * Q_0 \quad (8)$$

$$\mathrm{dj} = \sum_{i=1}^{n} (e^{-m})^i \quad (9)$$

$$\mathrm{URR} = Q_r * tml * csl \quad (10)$$

Among them, Q is the production during the stable production period, and t_m is the time to enter the stable production period. These two variables need to be determined.

Q_{ls} is the historical cumulative production, Q_0 is the initial production (predicted from 2024, production in 2023 is Q_0), t_0 is the time corresponding to the initial production, t is the stable production period years (stable production period of 20 years, t is 20), i is the decreasing period years (decreasing by 50 years, i is 50), Q_r is the resource quantity, all of which are known quantities.

Among them, tml is the proven rate, csl is the recovery rate, c_c is the recovery degree control coefficient, k is the growth rate, and m is the decline rate. These five variables, as risk factors, have an impact on the stable production period Q and the time to enter the stable production period t_m in the production planning model. The final production uncertainty prediction model obtained is as follows.

$$Q(\mathrm{t}) = \begin{cases} Q_0 * (1+k)^{(t-t_0)} & (t_0 \le t \le t_m) \\ Q & (t_m \le t \le t_m + 19) \\ Q * (e^{-m})^{t-t_m-19} & (t \ge t_m + 19) \end{cases} \quad (11)$$

$$\sum Q(t) + Q_{ls} = URR \quad (12)$$

Formula 11 is a production prediction model, where $Q(\mathrm{t})$ is the production prediction result, t is the prediction time, t_0 is the last year of historical production, t_m is the time of entering the stable production period, Q_0 is the production of the last year of historical data, Q is the stable production period production, k is the growth rate, and m is the decreasing rate.

Formula 12 is the model boundary condition, $\sum Q(t)$ is the cumulative value of production prediction results, and URR is the ultimate recoverable reserves.

3 Analysis of factors affecting production prediction

3.1 Single factor analysis

Based on the historical production data and exploration and development parameters of conventional gas in the Sichuan Basin, an analysis is conducted on five influencing factors: proven rate, recovery rate, growth rate, stable production end recovery degree, and decline rate. The quantitative analysis of production influencing factors requires objective and accurate evaluation of different factors, and requires the generation and calculation of a large amount of factor data. Therefore, the Monte Carlo method is suitable for quantitative research of production influencing factors.

When estimating production probability based on the principle of Monte Carlo method, the problem to be solved must first be transformed into the expected value of a certain probability model. Then, the model is randomly sampled and simulated on a computer to extract sufficient random numbers and perform statistical analysis on the problem to be solved (Li et al., 2022; Simone et al., 2023).

Assuming the distribution density of the known random variable $f(x)$ is $\psi(x)$. The mathematical expectation of variable $f(x)$ is:

$$E = \int_{x_0}^{x_1} f(x)\psi(x)dx \tag{13}$$

In the formula, E is the expectation, $[x_0, x_1]$ is the interval of random sampling, and $f(x)$ is the random variable, $\psi(x)$ The density function of a random variable.

According to the distribution density function $\psi(x)$ Randomly select N sample points x_i, and use the arithmetic mean of the function value $f(x_i)$ corresponding to the sample points as the integral estimation value.

$$\overline{E_N} = \frac{1}{N}\sum_{i=1}^{N} f(x_i) \tag{14}$$

In the formula, $\overline{E_N}$ is the estimated integral value, x_i is the extracted sample, $f(x_i)$ is the function value of the extracted sample, and N is the number of samples.

Randomly extract variable values based on the probability distribution density function of the variables. After many independent simulations of the variable values, the probability density distribution of the objective function can be obtained. Monte Carlo simulation can achieve the calculation process of variable random sampling.

In subsequent research, it is necessary to calculate the prediction results and implementation probability of production under different factors, which requires random sampling. Taking the exploration rate as an example, the range of exploration rates is obtained based on actual production, and then a random sampling that conforms to a normal distribution is carried out within the range. 1,000 exploration rates are selected, and the remaining four factors are kept as the average to calculate the production and probability of achievement.

Firstly, the exploration rate and recovery rate are analyzed, both of which directly affect the ultimate recoverable reserve URR of natural gas, thereby affecting the overall amplitude of the production planning model, as shown in Figure 4. As shown in the figure, when other conditions are constant, the larger the ultimate recoverable reserve URR, the greater the production during the stable production period, and the later the time to reach the stable production period. As can be seen from Formulas 7–12, URR is the boundary condition for production prediction, and the result is controlled. Therefore, URR should first be used to study the influence of proved rate and recovery efficiency, and then take them as prior conditions to study other factors by using Bayesian network, to obtain the production prediction results under multi-factor control. In addition, the distribution probability density is calculated by Formulas 13, 14, as shown in the orange bar chart in Figure 5.

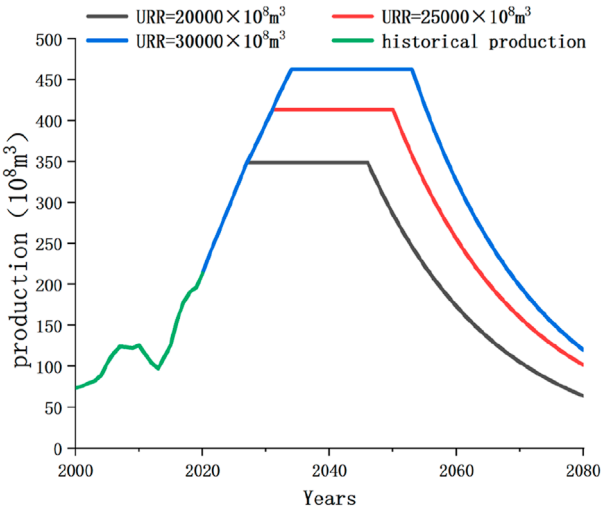

FIGURE 4
Prediction curves of conventional gas production under different URR conditions.

The proven rate of conventional gas in the Sichuan Basin is 40%–60%, and the recovery rate is 40%–50%. Under the separate influence of these two factors, the variation of stable production period production with factors and the probability of achievement are shown in Figure 5. From the figure, the production during the stable production period increases with the increase of the proven rate (or recovery rate), but the increase amplitude is inconsistent. The change in production shows a relatively gentle trend in the middle and a sharp change at both ends. This is because after using a normal distribution for Monte Carlo random sampling, within the range of proven rates (or recovery rates), the probability of sampling in the middle is high, while the probability of sampling at both ends is low, resulting in a denser production result in the middle and a looser production result on both sides.

Among them, under the influence of the proven rate, the range of stable production period production is 360–440 $\times 10^8 m^3$, and the production is concentrated in 380–420 $\times 10^8 m^3$. Under the influence of recovery rate, the range of stable production period production is 355–455 $\times 10^8 m^3$, and the production is concentrated in 390–430 $\times 10^8 m^3$.

Then analyze the three factors of growth rate, stable production at the end of the period, and decline rate. The trend of changes in the production planning curve and production development

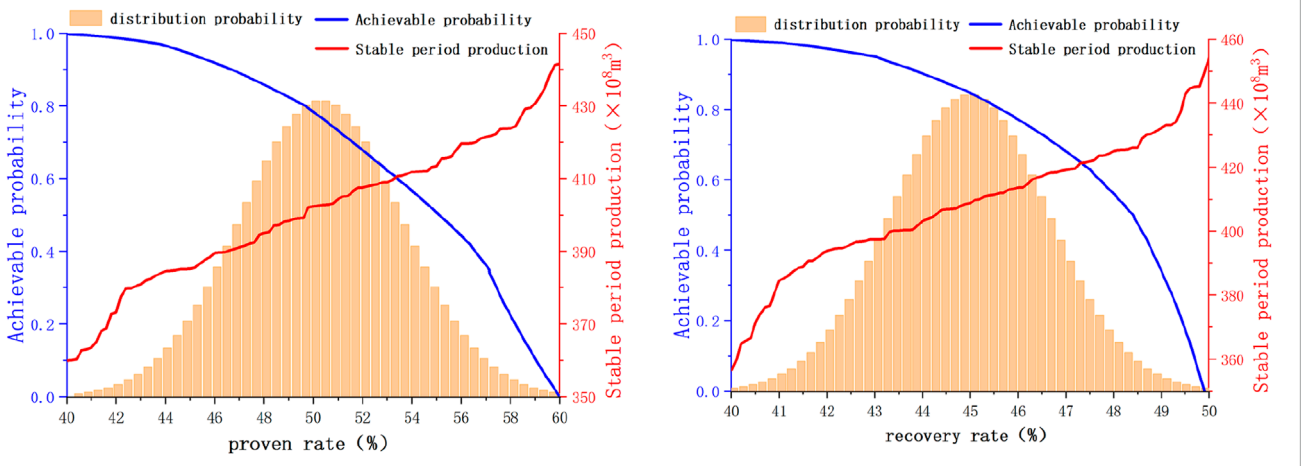

FIGURE 5
Production probability plots at different proved rates and recovery rates.

probability curve under the separate influence of three factors is shown in Figure 6.

From Figures 6A1, B1, as the growth rate increases, the increase in production before entering the stable production period increases, and the production will enter the stable production period earlier, and the production during the stable production period is larger. The growth rate of conventional gas is between 5%–15%, and a normal distribution is used for random sampling with a mean of 10%. The range of stable production period production is 380–440 $\times 10^8 m^3$, and the production is concentrated in 400–430 $\times 10^8 m^3$.

From Figures 6A2, B2, as the degree of recovery at the end of the stable production period increases, the cumulative production at the end of the stable production period is greater, and the production will enter the stable production period later, and the production during the stable production period is greater. The recovery rate at the end of the stable production period is between 60%–70%, and a normal distribution is used for random sampling, with a mean of 65%. The range of production during the stable production period is 385–430 $\times 10^8 m^3$, and the production is concentrated in 395–420 $\times 10^8 m^3$.

From Figures 6A3, B3, as the decline rate increases, the decrease in production after entering the decline period is greater. Therefore, under other conditions that remain unchanged, the cumulative production before entering the decline period is greater, and the production will enter the stable production period later, and the production during the stable production period is greater. The conventional gas decline rate is around 5%–20%, and a normal distribution is used for random sampling, with an average of 12.5%. The range of stable production period production is 380–430 $\times 10^8 m^3$, and the production is concentrated in 390–420 $\times 10^8 m^3$.

3.2 Single factor sensitivity analysis

From the content of Section 3.1, different factors have varying degrees of impact on production. Therefore, in subsequent research, it is necessary to first determine the degree of impact of each factor, which requires sensitivity analysis to study the degree of impact of each factor on the production prediction results during the stable production period (Endong et al., 2023; Shuai-hua and Huang, 2020).

Anton Sysoev (Anton, 2023) proposed an alternative method based on finite fluctuation analysis, which obtained a set of sensitivity measures for each input through sensitivity analysis. And the described method was compared with the Sobol index calculation method, proving the consistency of the proposed method. This is a very good sensitivity analysis method, but this article adopts different perspectives for research. This article analyzes the factors that affect production and needs to combine with actual production conditions to study the probability of achieving predicted production. Therefore, the article takes the probability of achieving production as the boundary and studies the maximum and minimum values that can be achieved by a single factor in the range of 0%–100%. The larger the fluctuation range of production, the greater the amplitude and possibility of changes in the actual production process, indicating that production is most sensitive to this factor.

In this section, sensitivity analysis of production prediction results under single factor is carried out, and the research results are as follows. The stable production period production and probability of achievement under different influencing factors are shown in Figure 7. From the perspective of fluctuation range, the proven rate and recovery rate have the greatest impact on the production during the stable production period. The curve changes in the figure show a trend of flat in the middle and steep at both ends, which is also because all factors are randomly sampled using a normal distribution, resulting in concentrated values in the middle and scattered values at both ends.

Sensitivity analysis is conducted based on the production probability graph results of five factors. Since the range of probability of realization is all 0%–100%, the maximum and minimum values of probability are taken to obtain the minimum and maximum production under each influencing factor. Subtraction results in production fluctuations. The larger the fluctuation value, the greater the impact of this factor and the greater its weight. Finally, normalize

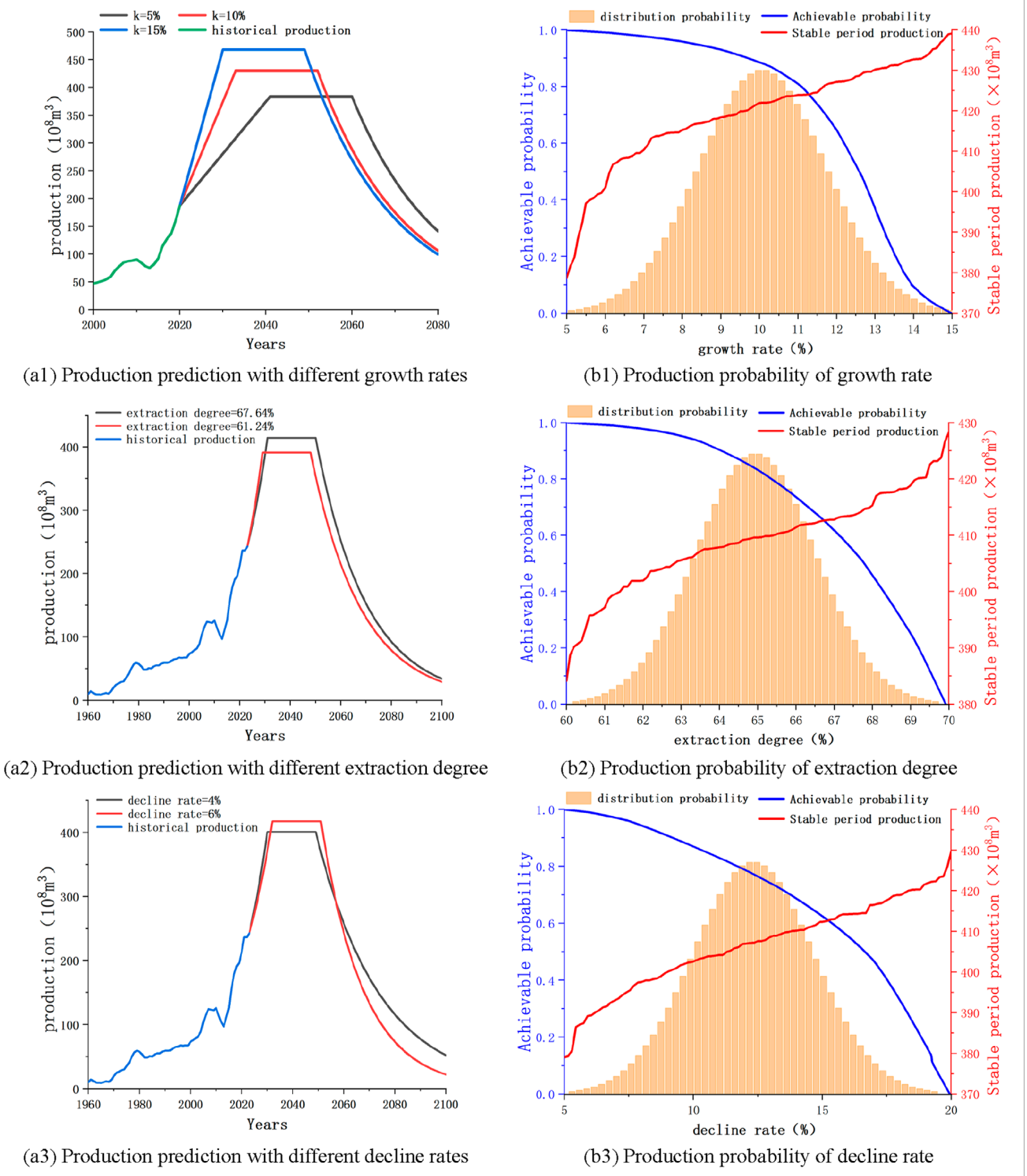

FIGURE 6
Production prediction curve and Production probability graph under different factors. **(A1)** Production prediction with different growth rates. **(A2)** Production prediction with different extraction degree. **(A3)** Production prediction with different decline rates. **(B1)** Production probability of growth rate. **(B2)** Production probability of extraction degree. **(B3)** Production probability of decline rate.

the production fluctuation value, calculate the weight value, and convert it into a percentage, which is the sensitivity level of the influencing factors, as shown in Table 1.

The sensitivity level of influencing factors is shown in Figure 8. From the figure, the factors that have a significant impact on the stable production period production are the proven rate, recovery

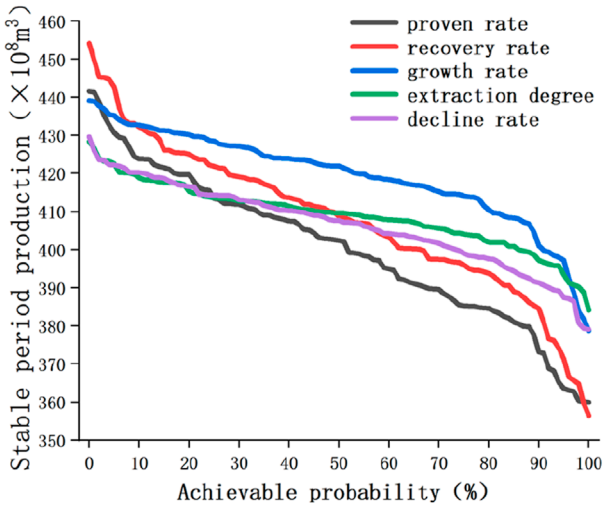

FIGURE 7
Production probability diagram under different factors.

rate, and growth rate, while the factors that have a smaller impact are the extraction degree and decline rate. The sensitivity and weight values of the influencing factors will serve as the basis for subsequent calculations.

Based on the analysis of production planning, the target for stable production period production planning of conventional gas is 390 $\times 10^8 m^3$. By benchmarking the planned production to the production probability diagram, the predicted range of achievement probability is obtained, as shown in Figure 9. As shown in the figure, the probability range for achieving a stable production period of 390 $\times 10^8 m^3$ under five factors is 70%–98%, with a probability greater than 70%, indicating a high possibility of achieving the production planning goal.

3.3 Multifactor analysis

After completing the single factor analysis of production, a multi factor analysis of production is carried out by combining Bayesian networks and binary Gaussian models. The specific research ideas are as follows. When conducting multi factor analysis, it is not possible to simultaneously consider the data calculation and graphic drawing of the five factors, therefore, the ultimate recoverable reserve URR is used as the entry point. Firstly, study the impact of the binary probability of proven rate and recovery rate on ultimate recoverable reserve URR and production. Further study the impact of the binary probability generated by the proven rate and recovery rate on production based on the remaining three factors.

In the actual production process, there are many factors that affect natural gas, so it is necessary to study the probability of achieving production during different stable production periods when considering multiple factors at the same time, and develop extraction plans based on the relationship between production and probability. For example, first determine the impact and probability of exploration rate and recovery rate on production, and then combine Bayesian networks to calculate the impact and probability of growth rate, exploration rate and recovery rate on production under the combined effect. Based on the results, determine the appropriate range of growth rate in actual production.

The conventional gas exploration rate in the Sichuan Basin is between 40%–60%, and the recovery rate is between 40%–50%. Due to the normal distribution used for random sampling, the combination of proven rate and recovery rate is also a normal distribution value, with a range of 16%–30%, which means the average is 23%. The conventional gas resource quantity $Q_r = 122300 \times 10^8 m^3$, the range of ultimate recoverable reserve URR is calculated using Formula 9, and the trend of production during stable production period is predicted based on ultimate recoverable reserve URR. The results are shown in Figure 10.

From Figure 10A, ultimate recoverable reserve URR increases with the increase of proven rate and recovery rate, and the amplitude of change in proven rate has a more significant impact on ultimate recoverable reserve URR. The ultimate recoverable reserve URR range of conventional gas is $19568 - 36690 \times 10^8 m^3$. From Figure 10B, the production shows a curved trend with the increase of proved rate and recovery rate, and the overall trend also increases with the increase of proved rate and recovery rate. Under the influence of proven rate and recovery rate, the range of stable production period production is 339–502 $\times 10^8 m^3$.

The probability of determining the distribution of proven rate and recovery rate is a normal distribution, with a mean of 23% and a value range of 16%–30%. Using it as a prior probability and other influencing factors as subsequent nodes, establish a Bayesian network and use a binary Gaussian model to calculate the probability of influencing factors.

Take the growth rate as an example to illustrate. The distribution probability of the growth rate is a normal distribution with a mean of 10% and a value range of 5%–15%. As these variables all follow a normal distribution, the Bayesian distribution probability of the growth rate follows a binary normal distribution. Then, the distribution probability is converted into a cumulative probability to obtain the Bayesian implementation probability diagram of the growth rate, as shown in Figure 11. From the figure, when the growth rate, proven rate, and recovery rate are small, the probability of realization is relatively high. As the influencing factors increase, the probability of realization gradually decreases. The probability map of implementation under Bayesian networks will also serve as the basis for the subsequent establishment of multivariate Gaussian mixture models.

Maintain the other influencing factors unchanged, and use Formula 6 to calculate the trend of production changes during the stable production period under the mixed influence of three factors, as shown in Figure 12. From Figure 12A, the trend of production change is an irregular surface graph, and production does not completely increase with the increase of growth rate. It is only a monotonic increasing relationship between production and growth rate within a specific range of proven rate and recovery rate. This pattern can be clearly seen from Figure 12B. Compared with the red and blue lines, when the exploration rate and recovery rate are high, even if the growth rate is low, the stable production period production is relatively high. This is because the production is influenced by a mixture of three factors. In actual production, the range of each factor should be determined based on the production situation, to reasonably control the production. Under the influence

TABLE 1 Influencing factors sensitivity analysis results table.

Achievable probability (%)	Production ($10^8 m^3$)	Proven rate	Recovery rate	Growth rate	Extraction degree	Decline rate
100	Minimum production	359.96	356.43	378.74	384.1	379.05
0	Maximum production	441.55	454.18	439.14	428.33	429.65
Production fluctuation value		81.59	97.75	60.4	44.23	50.6
Sensitivity level		24.39%	29.22%	18.05%	13.22%	15.12%

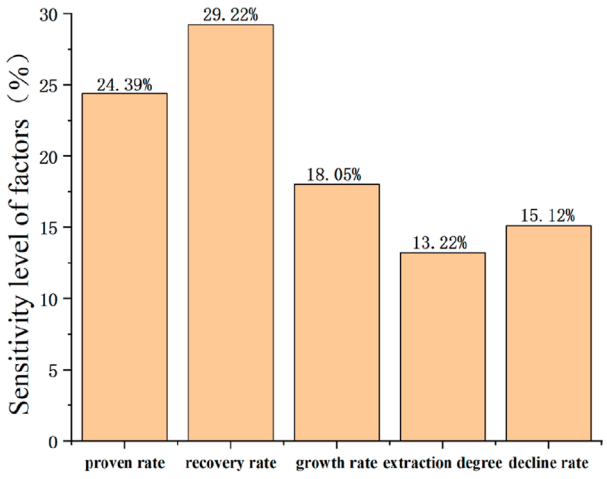

FIGURE 8
Sensitivity degree diagram of influencing factors.

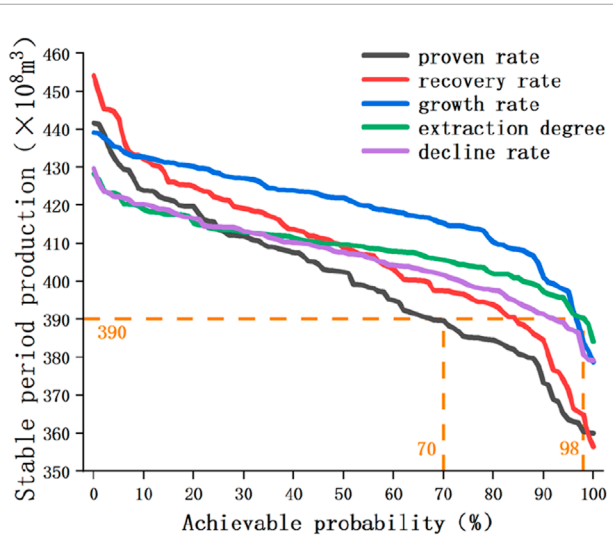

FIGURE 9
Production probability diagram under different factors.

of proven rate, recovery rate, and growth rate, the range of stable production period production is 352–500 $\times 10^8 m^3$.

Project the three-dimensional production map on the production growth rate surface and combine it with the calculation results of the implementation probability to obtain the production probability map under the Bayesian network. From Figure 12B, the results are shown in the blue curve at the lowest proved recovery rate and the red curve at the highest recovery rate. In the figure, when the stable production period production is about 390 $\times 10^8 m^3$, the corresponding probability of achievement is about 70%, while in single factor analysis, the corresponding probability of achievement is 90%. This is because the prior probabilities of proven rate and recovery rate are considered. Currently, under the Bayesian network, the impact of growth rate on production changes, and the probability of achievement decreases, reducing the likelihood of achieving production planning goals.

Similarly, the analysis of extraction degree and decline rate is consistent with the analysis process of growth rate. Using the proven rate and recovery rate as known probabilities, calculate the binary distribution probability of the recovery degree, and then obtain the probability of achieving the recovery degree, as shown in Figure 13A. Finally, combine Formula 6 to calculate the trend of production with the recovery degree, as shown in Figure 13B. The trend of change is an irregular surface graph, which shows that the production does not increase completely with the increase of recovery degree, but only shows a monotonic increasing relationship between production and recovery degree in a specific proved rate recovery rate interval. Under the influence of proven rate, recovery rate, and recovery degree, the range of stable production period production is 376–490 $\times 10^8 m^3$.

Using the proven rate and recovery rate as known probabilities, calculate the binary distribution probability of the decline rate, and then obtain the probability of achieving the decline rate, as shown in Figure 14A. Finally, combine Formula 6 to calculate the trend of production change with the decline rate, as shown in Figure 14B. The trend of change is an irregular surface graph, which shows that production does not increase completely with the increase of decline rate, but only shows a monotonic increasing relationship between production and decline rate in a specific proved rate recovery interval. Under the influence of proven rate, recovery rate, and decline rate, the range of stable production period production is 374–483 $\times 10^8 m^3$.

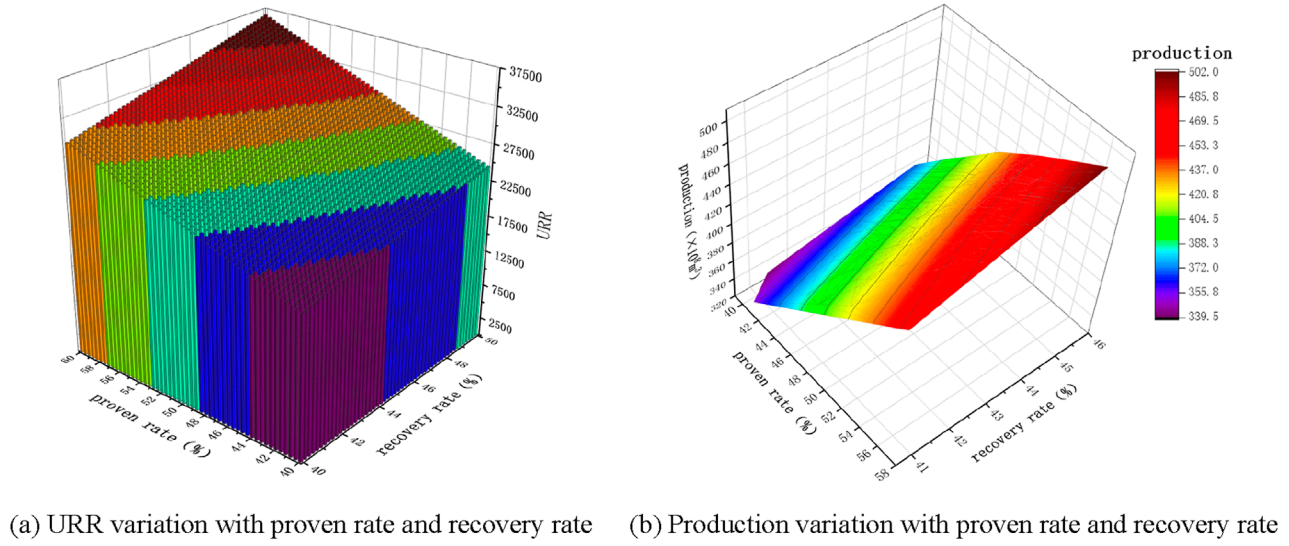

(a) URR variation with proven rate and recovery rate (b) Production variation with proven rate and recovery rate

FIGURE 10
URR and production change trend chart. **(A)** URR variation with proven rate and recovery rate. **(B)** Production variation with proven rate and recovery rate.

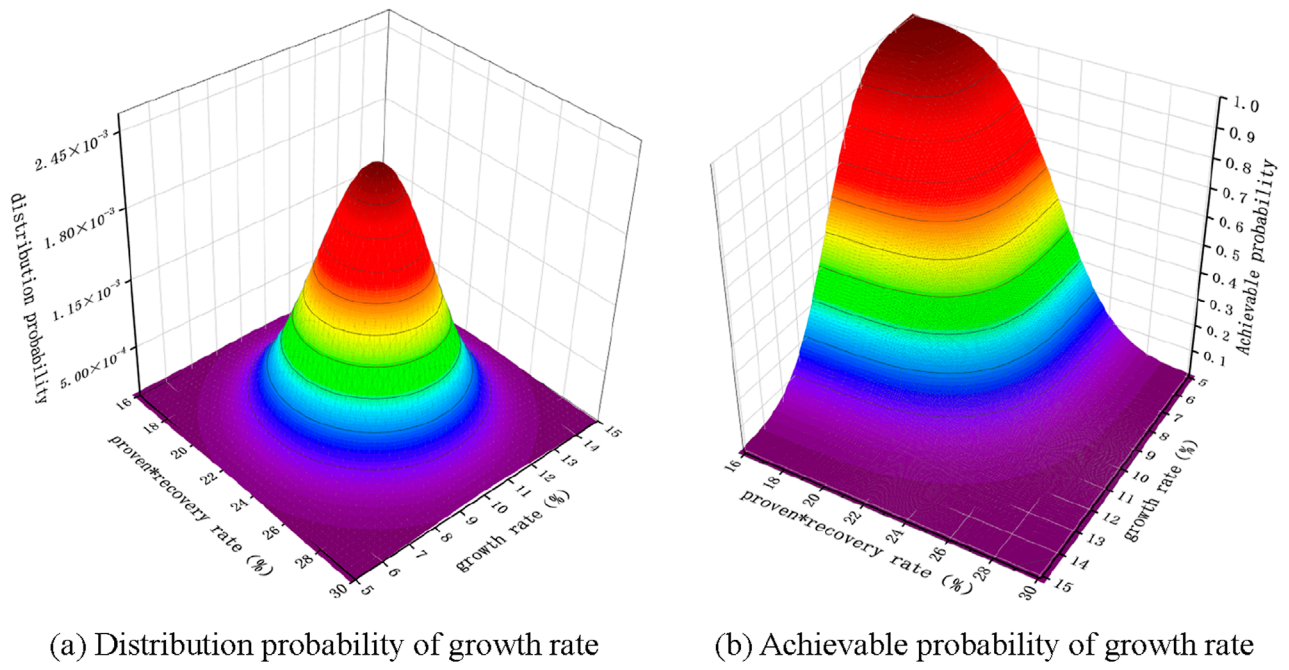

(a) Distribution probability of growth rate (b) Achievable probability of growth rate

FIGURE 11
Binary probability plot of growth rate. **(A)** Distribution probability of growth rate. **(B)** Achievable probability of growth rate.

3.4 Summary of factor analysis

By conducting a single factor analysis of production, the fluctuation range of influencing factors was determined, and it was clarified that under the influence of a single factor, the stable production period production increased with the increase of influencing factor values. Under the influence of the proven rate, the range of stable production period production is 359.96–441.55 $\times 10^8 m^3$; Under the influence of recovery rate, the range of stable production during the production period is 356.43–454.18 $\times 10^8 m^3$; Under the influence of growth rate, the range of stable production period production is 378.74–439.14 $\times 10^8 m^3$; Under the influence of extraction degree, the range of stable production period production is 384.1–428.33 $\times 10^8 m^3$; Under the influence of the decline rate, the range of stable production period production is 379.05–429.65 $\times 10^8 m^3$. As shown in Table 2, the recovery rate has the greatest impact

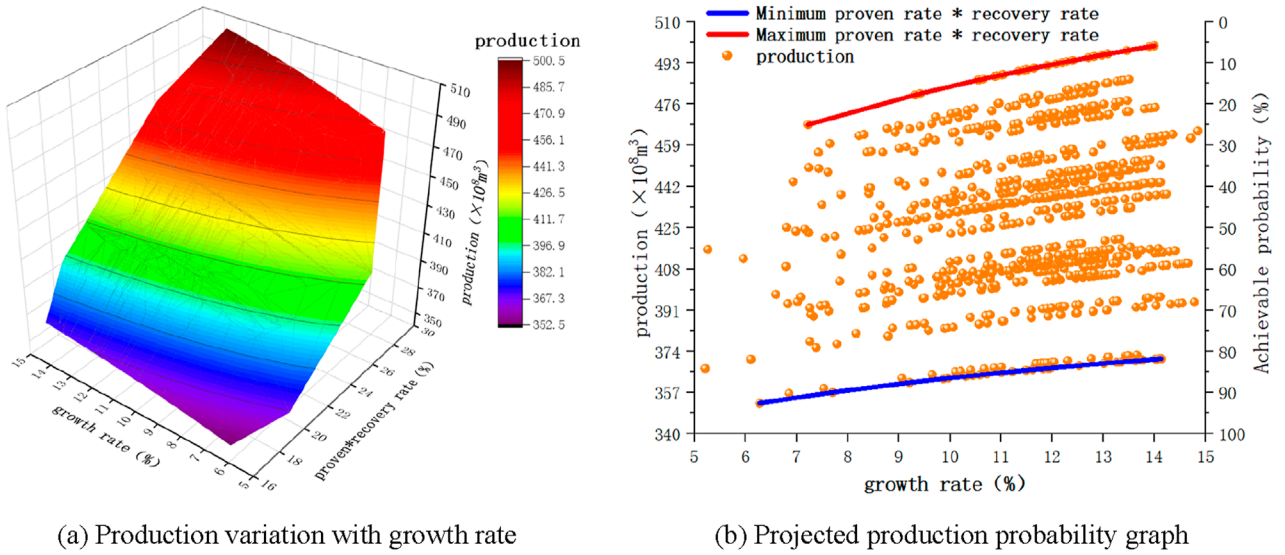

FIGURE 12
Calculation results under the influence of growth rate. **(A)** Production variation with growth rate. **(B)** Projected production probability graph.

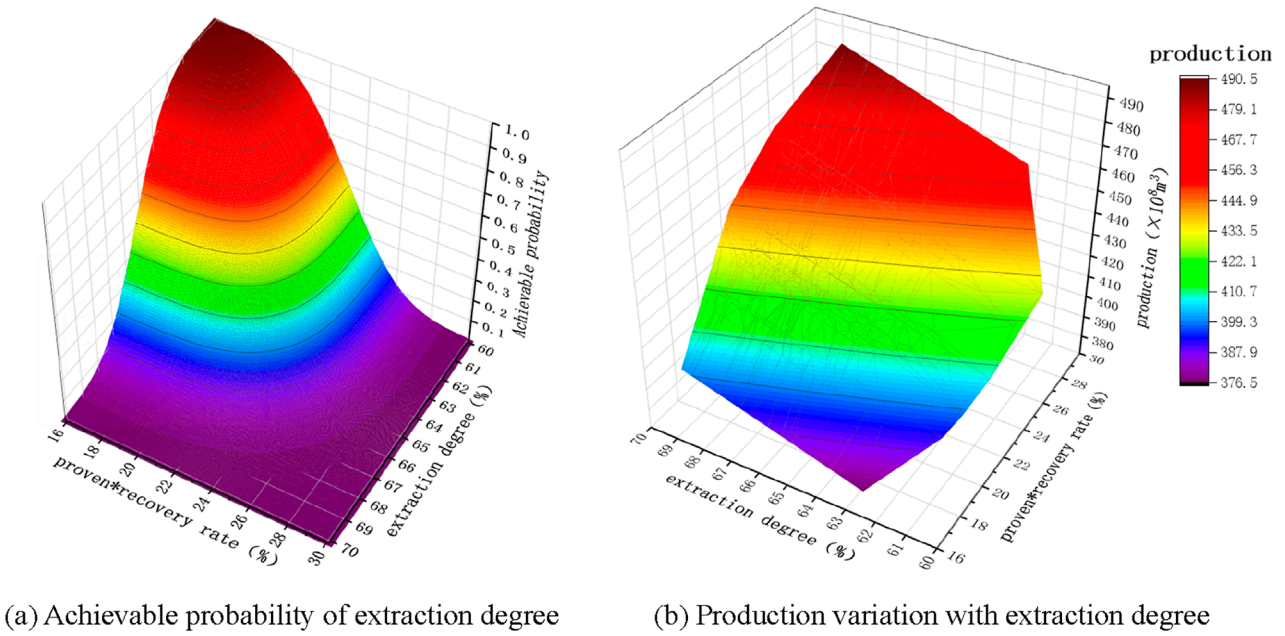

FIGURE 13
Calculation results under the influence of extraction degree. **(A)** Achievable probability of extraction degree. **(B)** Production variation with extraction degree.

on the production, and the degree of recovery has the least impact on the production.

By conducting sensitivity analysis on the factors affecting production, the sensitivity levels of five factors were obtained and converted into weight values for the establishment of subsequent multi factor production planning models. When the production planning target is determined to be 390 $\times 10^8 m^3$, the probability of achieving it under the influence of a single factor will exceed 70%, indicating a high possibility of achieving the target production.

By conducting a multifactor analysis of production, the distribution probability of the proven rate and recovery rate was used as a prior probability. The binary distribution probability and implementation probability of the other three factors were calculated, and the trend of stable production period production under the mixed action of multiple factors was predicted. The

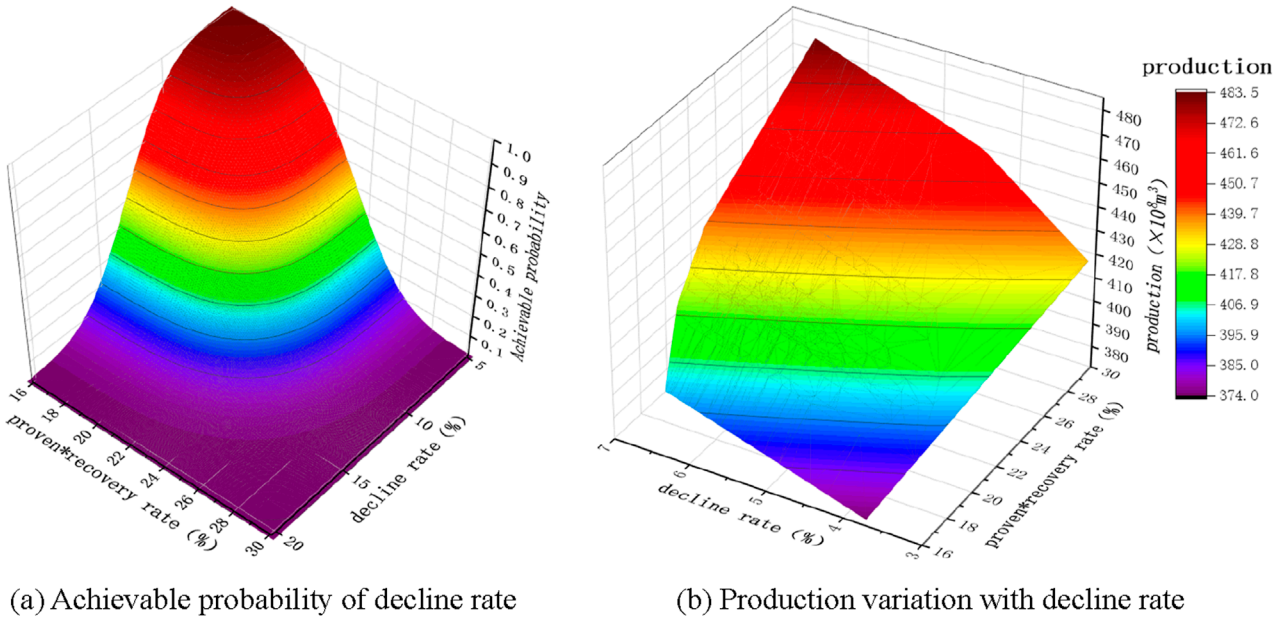

FIGURE 14
Calculation results under the influence of decline rate. **(A)** Achievable probability of decline rate. **(B)** Production variation with decline rate.

TABLE 2 Production prediction results table under different factors.

Influencing factor	Proven rate	Recovery rate	Growth rate	Extraction degree	Decline rate
Minimum production (10^8m^3)	359.96	356.43	378.74	384.1	379.05
Maximum production (10^8m^3)	441.55	454.18	439.14	428.33	429.65
Production fluctuation value (10^8m^3)	81.59	97.75	60.4	44.23	50.6

production during the stable production period does not increase entirely with the increase of influencing factor values, and only within a certain range can this law be met. In addition, taking the production probability projection diagram of growth rate as an example, the variation of stable production period production and its corresponding realization probability under the mixed effects of multiple factors was analyzed. The results showed that compared to the influence of single factors, the probability of achieving production targets under multiple factors decreased. In actual planning, it is necessary to consider the combined effects of multiple factors to more accurately carry out production planning.

4 Establishment of production planning model

Through the previous calculations, the influence law and sensitivity level of a single factor, as well as the probability of achieving mixed effects of multiple factors and the trend of production changes were obtained. Then, based on the sensitivity of a single factor, weight values are assigned to obtain a single factor production planning model. The impact of each factor on production planning is preliminarily analyzed. Finally, a multivariate Gaussian model is used to overlay and combine the single factor production model to obtain a multi factor production planning model.

When establishing a production planning model, it is considered that the greater the impact of a certain factor on production, the higher the proportion of that factor in the model. Therefore, the results of the sensitivity analysis in the previous section are used as weights in the production planning model. According to the sensitivity analysis results in Section 3.2, the sensitivity degree of the influencing factors is converted into weight, and the weight matrix of the five factors, namely, the proven rate, recovery rate, growth rate, recovery degree, and decline rate, is R= [0.25,0.29,0.18,0.13,0.15]. Based on historical data of conventional gas production, allocation is made according to weights, and production planning models are established based on different factors to obtain production prediction curves with different proportions, as shown in Figure 15.

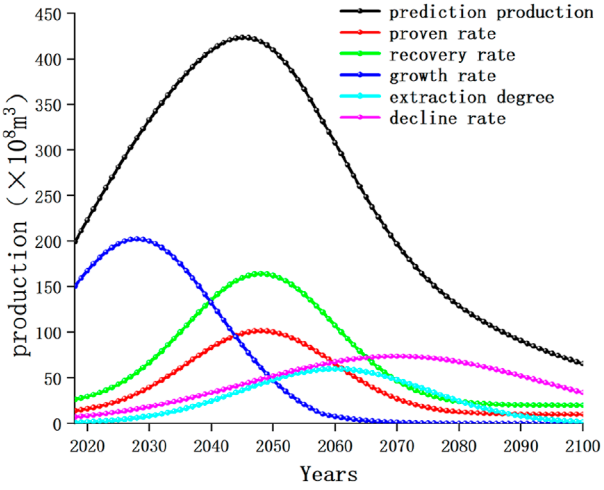

FIGURE 15
Production prediction curves for different factors.

The black curve in the figure represents the conventional gas production prediction curve, which is composed of five other curves stacked together. The remaining curves represent the production planning model after assigning weights to each of the five factors individually. As shown in the figure, the production curve of growth rate is concentrated in the growth period, the production curve of proven rate and recovery rate is concentrated in the stable production period, and the production curve of recovery degree and decline rate is concentrated in the decline period.

From this, the growth rate affects the trend of production changes during the growth period by controlling the amplitude of growth, and the proven rate and recovery rate affect the overall size of the production prediction curve by controlling the size of ultimate recoverable reserve URR, thereby affecting the trend of production changes throughout the entire life cycle. The most significant impact is the size of production during the stable production period, and the degree of recovery affects the trend of production changes before and after the decline period by controlling the cumulative production at the end of the stable production period, The decline rate affects the trend of production during the decline period by controlling the magnitude of the decline.

Figure 16 shows the trend of production changes under the mixed influence of five factors since 2020, namely, the multi factor production planning chart. The influencing factors of the coordinate axis represent five different factors, from 1 to 5, which are the proven rate, recovery rate, growth rate, extraction degree, and decline rate. As the value of the coordinate axis increases, the factors also overlap and have an impact on the production prediction results. As shown in the figure, the production prediction curve gradually becomes complete with the superposition of influencing factors, and finally forms a production planning curve that includes growth period, stable production period, and decreasing period.

From the graph, it can be seen that various factors have an impact on the production planning model. The growth rate controls the amplitude of the production growth stage, the proven rate and recovery rate control the amplitude of the stable production stage, the extraction degree controls the amplitude of the transition from the stable production stage to the decreasing stage, and the decline rate controls the amplitude of the decreasing production stage. Under the combined influence of five factors, the production will reach a peak of 423 $\times 10^8 m^3$ in 2045, with a stable production period of 2038–2051. The production planning model can study the forecast results of the production change over time under the influence of different factors, and obtain the influence of each factor on the production at different stages, to better adjust the factors according to the demand in the actual production and achieve the production target.

5 Conclusion

This article establishes a production uncertainty prediction model under multi factor control based on the development of conventional gas production in the Sichuan Basin. By analyzing the factors affecting production, the variation patterns of production and probability of achievement under the influence of single factors were obtained, and the sensitivity levels of different factors were obtained through sensitivity analysis. In addition, a multi factor analysis was conducted based on Bayesian networks, using the detection rate and recovery rate as prior probabilities to obtain binary distribution probabilities and implementation probabilities of other factors, as well as production variation graphs under the influence of multiple factors. A production planning model was established by combining the weight results of the multivariate Gaussian mixture model and sensitivity analysis. The conclusion is as follows.

1) The established production uncertainty model can effectively predict the development trend of production under the control of multiple factors. From the prediction results, production is positively correlated with the five influencing factors of proven rate, recovery rate, growth rate, extraction degree, and decline rate. During the stable production period, production will increase with the increase of the value of the influencing factors, and the degree of influence of the factors from large to small is: recovery rate, recovery rate, growth rate, decline rate, and extraction degree. When the impact of production changes from single factor to multiple factors, the fluctuation range of stable production increases, and the probability of achieving the target production decreases.
2) Based on the weight values of the degree of influence of factors, establish single factor and multi factor production planning models. From the perspective of production development trends, the growth rate controls the amplitude of the production growth stage, the proven rate and recovery rate control the amplitude of the stable production stage, the extraction degree controls the amplitude of the transition from the stable production stage to the decreasing stage, and the decline rate controls the amplitude of the decreasing production stage. These conclusions provide reference for the formulation of production planning goals.
3) Unlike conventional research that considers the impact of a single factor on production, this article comprehensively considers multiple influencing factors, studies the changes in

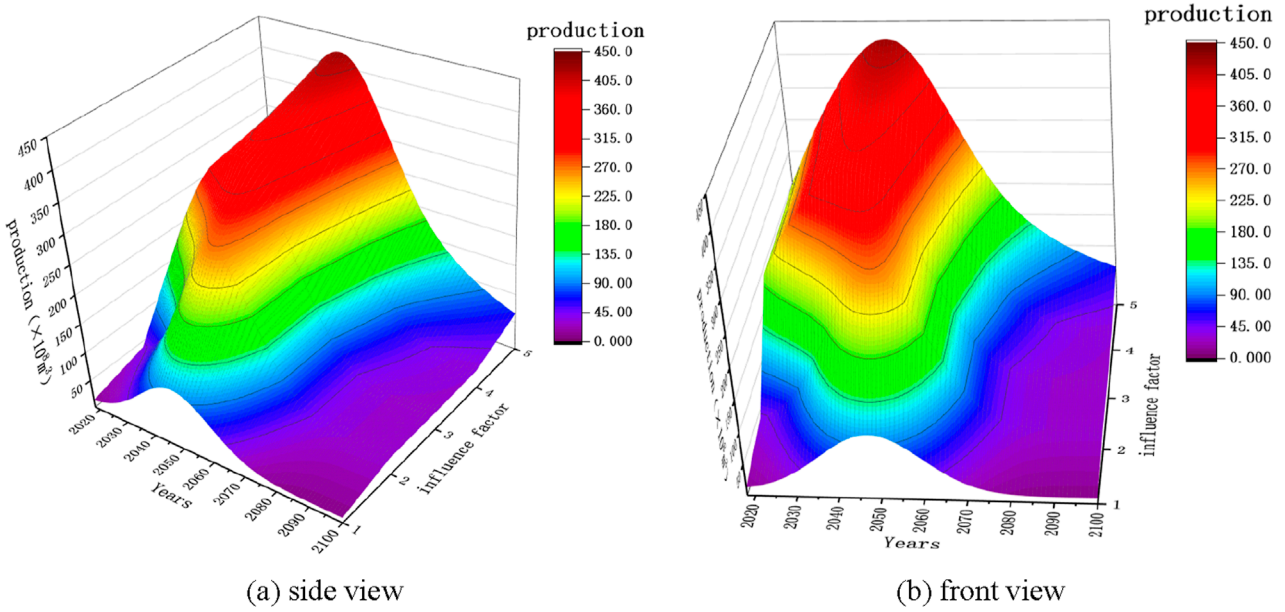

FIGURE 16
Production planning model under the influence of multiple factors. **(A)** side view. **(B)** front view.

natural gas production, calculates the probability of achieving production, and provides a reference for the formulation of production planning goals. In addition, the article establishes an uncertainty prediction model (Formulas 11, 12), which can effectively combine multiple factors to predict natural gas production.

4) The article analyzes the five main influencing factors of natural gas production, and comprehensive research has certain innovation. However, the influencing factors involved in the research are all those involved in the exploration and development process, and there are also some economic factors (such as investment and cost) that have not been considered. Therefore, more factors can be further considered to analyze the trend of production changes, to develop more suitable production planning schemes.

Data availability statement

The raw data supporting the conclusions of this article will be made available by the authors, without undue reservation.

Author contributions

HL: Conceptualization, Supervision, Writing–original draft, Writing–review and editing. GY: Data curation, Methodology, Supervision, Writing–review and editing. YF: Methodology, Validation, Writing–original draft. YaC: Supervision, Validation, Writing–original draft. KS: Investigation, Methodology, Writing–review and editing. YL: Methodology, Validation, Writing–review and editing. YuC: Investigation, Methodology, Validation, Writing–original draft. DZ: Methodology, Supervision, Validation, Writing–original draft, Writing–review and editing.

Funding

The author(s) declare that no financial support was received for the research, authorship, and/or publication of this article.

Conflict of interest

Authors HL, YF, YaC, and YL were employed by Exploration and Development Research Institute of PetroChina Southwest Oil and Gas Field Company.

Author GY was employed by PetroChina Southwest Oil and Gas Field Company Planning Department.

The remaining authors declare that the research was conducted in the absence of any commercial or financial relationships that could be construed as a potential conflict of interest.

Publisher's note

References

Adriana, L.L.-L., and Martha, L. (2021). Fitting a Gaussian mixture model through the gini index. *Int. J. Appl. Math. Comput. Sci.* 31, 487–500. doi:10.34768/amcs-2021-0033

Andreas, W. (2021). Quantum-like Gaussian mixture model. *Soft Comput.* 25, 10067–10081. doi:10.1007/s00500-021-05941-9

Anton, S. (2023). Sensitivity analysis of mathematical models. *Computation* 11, 159. doi:10.3390/computation11080159

Arun Kumar, S., Erfan, B. T., Alireza, G., and Dehnavi-Arani, S. (2020). Robust optimization and mixed-integer linear programming model for LNG supply chain planning problem. *Soft Comput.* 24, 7885–7905. doi:10.1007/s00500-019-04010-6

Bilici, Z., Özdemir, D., and Temurtaş, H. (2023). Comparative analysis of metaheuristic algorithms for natural gas demand forecasting based on meteorological indicators. *J. Eng. Res.* 11, 259–265. doi:10.1016/j.jer.2023.100127

Cangqi, Z., Hao, B., Jing, Z., Li, Q., and Zhang, Y. (2020). Gaussian mixture variational autoencoder for semi-supervised topic modeling. *IEEE ACCESS* 8, 106843–106854. doi:10.1109/access.2020.3001184

Chen., Q., Zhang., Z., Chunming, F., Hu, D., and Jiang, C. (2024). Enhanced Gaussian-mixture-model-based nonlinear probabilistic uncertainty propagation using Gaussian splitting approach. *Struct. Multidiscip. Optim.* 67, 49. doi:10.1007/s00158-023-03733-3

Chong, L., Tongfei, L., Wen-Ze, W., Xie, W., and Zhu, H. (2022). An optimized nonlinear grey Bernoulli prediction model and its application in natural gas production. *Expert Syst. Appl.* 194, 116448. doi:10.1016/j.eswa.2021.116448

Chunsheng, G., Jialuo, Z., Huahua, C., Ying, N., Zhang, J., and Zhou, D. (2020). Variational autoencoder with optimizing Gaussian mixture model priors. *IEEE ACCESS* 8, 43992–44005. doi:10.1109/access.2020.2977671

David, A., Concha, B., and Pedro, L. (2022). Semiparametric bayesian networks. *Inf. Sci.* 584, 564–582. doi:10.1016/j.ins.2021.10.074

Deyan, W., Adam, A. J., and Ying, X. (2020). Dynamic knowledge inference based on bayesian network learning. *Math. Problems Eng.* 2020, 6613896. doi:10.1155/2020/6613896

Dongfeng, L., Heng, F., Wang, R., Yang, S., Zhao, Y., and Yan, X. (2022). Prediction of casing collapse strength based on bayesian neural network. *Processes* 10, 1327. doi:10.3390/pr10071327

Durmuş, Ö., Safa, D., Doğan, A., et al. (2022). A new modified artificial bee colony algorithm for energy demand forecasting problem. *Neural Comput. Appl.* 34, 17455–17471. doi:10.1007/s00521-022-07675-7

Duygu, I., and Derya, E. (2019). A new approach for probability calculation of fuzzy events in Bayesian Networks. *Int. J. Approx. Reason.* 108, 76–88. doi:10.1016/j.ijar.2019.03.004

Endong, W., Lianjun, Z., Hong, C., and Zhang, X. (2023). Collinearity-oriented sensitivity analysis for patterning energy factor significance in buildings. *J. Build. Eng.* 73, 106685. doi:10.1016/j.jobe.2023.106685

Erick, M., Fernando, L. C. O., and de Menezes, L. M. (2022). Forecasting natural gas consumption using Bagging and modified regularization techniques. *Energy Econ.* 106, 105760. doi:10.1016/j.eneco.2021.105760

Guo, Yu., Haitao, Li., Yanru, C., Liu, L., Wang, C., Chen, Y., et al. (2021). Quantitative study on natural gas production risk of Carboniferous gas reservoir in eastern Sichuan. *J. Petroleum Explor. Prod. Technol.* 11, 3841–3857. doi:10.1007/s13202-021-01261-8

Haitao, L., Guo, Y., Chen, Y., and Zhang, D. (2021). Research on quantitative evaluation methods and influencing factors of natural gas reservoir development. *Shock Vib.* 2021, 1684178. doi:10.1155/2021/1684178

Haoran, L., Shaopeng, C., Sheng, L., Wang, N., Shi, Q., Cai, Y., et al. (2022). A bayesian network structure learning algorithm based on probabilistic incremental analysis and constraint. *IEEE ACCESS* 10, 130719–130732. doi:10.1109/access.2022.3229128

Hongbing, L., and Han, M. (2023). Forecast of China's natural gas demand based on the double-logarithmic model with stepwise regression method. *Energy Policy* 45, 8491–8506. doi:10.1080/15567036.2023.2227584

Jian, C., Ting, L., Lai, K. K., Zhang, Z. G., and Wang, S. (2018). The future natural gas consumption in China: based on the LMDI-STIRPAT-PLSR framework and scenario analysis. *Energy Policy* 119, 215–225. doi:10.1016/j.enpol.2018.04.049

Jianliang, W., and Nu, L. (2020). Influencing factors and future trends of natural gas demand in the eastern, central and western areas of China based on the grey model. *Nat. Gas. Ind. B* 7, 473–483. doi:10.1016/j.ngib.2020.09.005

Jianzhong, X., Xiaolin, W., and Wang, R. (2016). Research on factors affecting the optimal exploitation of natural gas resources in China. *Sustainability* 8, 435. doi:10.3390/su8050435

Jiří, V., Václav, K., and Kratochvíl, F. (2023). Structural learning of mixed noisy-OR Bayesian networks. *Int. J. Approx. Reason.* 161, 108990. doi:10.1016/j.ijar.2023.108990

Joachim, G., Philipp, L., Linda, P., Schmalwasser, L., and Lawonn, K. (2024). The whole and its parts: visualizing Gaussian mixture models. *Vis. Inf.* 8, 67–79. doi:10.1016/j.visinf.2024.04.005

Julie, D., and Agnes, D. (2020). A wasserstein-type distance in the space of Gaussian mixture models. *SIAM J. Imaging Sci.* 13, 936–970. doi:10.1137/19m1301047

Jun, L., Yan-Bin, Y., and Derek, E. (2024). Morphological complexity and azimuthal disorder of evolving pore space in low-maturity oil shale during *in-situ* thermal upgrading and impacts on permeability. *Petroleum Sci.* doi:10.1016/j.petsci.2024.03.020

Kyung, B., Soo, H. L., Yoon, H. J., Park, H., Kim, J., Cheong, S., et al. (2024). Implementation of Bayesian networks and Bayesian inference using a $Cu_{0.1}Te_{0.9}/HfO_2/Pt$ threshold switching memristor. *Nanoscale Adv.* 6, 2892–2902. doi:10.1039/d3na01166f

Li, H., Yu, G., Fang, Y., Chen, Y., and Zhang, D. (2022). Studies of natural gas production prediction and risk assessment for tight gas in Sichuan Basin. *Front. Earth Sci.* 10, 1059832. doi:10.3389/feart.2022.1059832

Luca, S. (2023). Entropy-based anomaly detection for Gaussian mixture modeling. *Algorithms* 16, 195. doi:10.3390/a16040195

Marta, M., Gregorio, F. V., Alicja, K., Wodarski, K., and Riesgo Fernández, P. (2020). Optimizing predictor variables in artificial neural networks when forecasting raw material prices for energy production. *Energies* 13, 2017. doi:10.3390/en13082017

Maruf, G. (2021). A novel approach for Gaussian mixture model clustering based on soft computing method. *IEEE ACCESS* 9, 159987–160003. doi:10.1109/access.2021.3130066

Nuo, W., Yuxiang, Z., Tao, S., Zou, X., Wang, E., and Du, S. (2022). Accounting for China's net carbon emissions and research on the realization path of carbon neutralization based on ecosystem carbon sinks. *Sustainability* 14, 14750. doi:10.3390/su142214750

Özdemir, D., Dörterler, S., and AydinDo, D. (2022). An adaptive search equation-based artificial bee colony algorithm for transportation energy demand forecasting. *Turkish J. Electr. Eng. Comput. Sci.* 30, 1251–1268. doi:10.55730/1300-0632.3847

Palanisamy, M., Md, S. A., Majed, A., Khan, U., Alagirisamy, K., Pachiyappan, D., et al. (2021). Forecasting natural gas production and consumption in United States-evidence from SARIMA and SARIMAX models. *Energies* 14, 6021. doi:10.3390/en14196021

Qi, Z., Chunjie, Z., Yu-Chu, T., Xiong, N., Qin, Y., and Hu, B. (2018). A fuzzy probability bayesian network approach for dynamic cybersecurity risk assessment in industrial control systems. *IEEE Trans. INDUSTRIAL Inf.* 14, 2497–2506. doi:10.1109/tii.2017.2768998

Shuai-hua, Ye., and Huang, A. (2020). Sensitivity analysis of factors affecting stability of cut and fill multistage slope based on improved grey incidence model. *Soil Mech. Found. Eng.* 57, 8–17. doi:10.1007/s11204-020-09631-w

Simone, C., Jeanne, T., Martin, W., and Zamponi, F. (2023). Machine-learning-assisted Monte Carlo fails at sampling computationally hard problems. *Mach. Learn. Sci. Technol.* 4, 010501. doi:10.1088/2632-2153/acbe91

Song, Y., Dongzhao, Y., Wei, S., Deng, C., Chen, C., and Feng, S. (2023). Global evaluation of carbon neutrality and peak carbon dioxide emissions: current challenges and future outlook. *Environ. Sci. Pollut. Res.* 30, 81725–81744. doi:10.1007/s11356-022-19764-0

Tongfei, L., and Yanrui, S. (2022). Predicting the production and consumption of natural gas in China by using a new grey forecasting method. *Math. Comput. Simul.* 202, 295–315. doi:10.1016/j.matcom.2022.05.023

Wang, Y., Chen, Q., Dai, B., and Wang, D. (2024). Guidance and review: advancing mining technology for enhanced production and supply of strategic minerals in China, Green and Smart Mining. *Engineering* 1, 2–11. doi:10.1016/j.gsme.2024.03.005

Yang, D., Jingliang, D., Tonglin, Y., Zhou, S., and Wei, Y. (2021). Failure evaluation of bridge deck based on parallel connection bayesian network: analytical model. *Materials* 14, 1411. doi:10.3390/ma14061411

Yaser, S., Parvin, N., Iraj, M., and Azam, K. (2021). Predicting the probability of occupational fall incidents: a Bayesian network model for the oil industry. *Int. J. Occup. Saf. Ergonomics* 27, 654–663. doi:10.1080/10803548.2019.1607052

Yingying, X., Xiangui, L., Zhiming, H., Shao, N., Duan, X., and Chang, J. (2022). Production effect evaluation of shale gas fractured horizontal well under variable production and variable pressure. *J. Nat. Gas Sci. Eng.* 97, 104344. doi:10.1016/j.jngse.2021.104344

Zhe, G., Zhaochen, S., and Shuxiu, L. (2020). Probability density function for wave elevation based on Gaussian mixture models. *Ocean. Eng.* 213, 107815. doi:10.1016/j.oceaneng.2020.107815

frontiers | Frontiers in Earth Science

TYPE Original Research
PUBLISHED 30 October 2024
DOI 10.3389/feart.2024.1487433

OPEN ACCESS

EDITED BY
Amer A. Shehata,
Texas A&M University Corpus Christi,
United States

REVIEWED BY
Sen Wang,
China University of Petroleum (East China), China
Mohammad Abdelfattah Sarhan,
Damietta University, Egypt

*CORRESPONDENCE
Jingang Fu,
fujgupc@gmail.com
Jingchen Ding,
dingjch.hbsj@sinopec.com

RECEIVED 28 August 2024
ACCEPTED 30 September 2024
PUBLISHED 30 October 2024

CITATION
Li Y, Fu J, Yan W, Chen K, Ding J and Wu J (2024) Experimental study on the dynamic threshold pressure gradient of high water-bearing tight sandstone gas reservoir. *Front. Earth Sci.* 12:1487433. doi: 10.3389/feart.2024.1487433

Experimental study on the dynamic threshold pressure gradient of high water-bearing tight sandstone gas reservoir

Yahui Li[1], Jingang Fu[2]*, Wenxin Yan[3], Kui Chen[1], Jingchen Ding[1]* and Jianbiao Wu[1]

[1]Sinopec North China Petroleum Bureau, Zhengzhou, China, [2]School of Petroleum and Natural Gas Engineering, Chongqing University of Science and Technology, Chongqing, China, [3]School of Petroleum Engineering, China University of Petroleum (East China), Qingdao, China

Tight sandstone water-bearing gas reservoirs typically exhibit low porosity and low permeability, with reservoir rocks characterized by complex pore structures, often featuring micron-scale or smaller pore throats. This intricate reservoir structure significantly restricts fluid flow within the reservoir, necessitating a certain threshold pressure gradient (TPG) to be overcome before flow can commence. This study focuses on the Ordos Basin and explores the influence of high water content tight sandstone gas reservoirs on TPG under different water saturation and formation pressure conditions through experiments. A mathematical model of TPG is established using multiple linear regression method. The results show that TPG is primarily affected by water saturation, followed by formation pressure. As the water saturation increases, the TPG of the core decreases, and the change becomes more pronounced when the water saturation exceeds 50%. As formation pressure increases, the weakening of the slippage effect in gas molecules leads to TPG stabilization, especially when local pressure exceeds 25.0 MPa. The research also shows that low-permeability cores exhibit greater TPG variation with pressure changes, while high-permeability cores remain more stable. A mathematical model was developed and validated to predict TPG based on permeability, water saturation, and formation pressure. These findings highlight the need to monitor formation water content during tight sandstone gas reservoir development to optimize production strategies, providing valuable insights for improving reservoir management and guiding future research.

KEYWORDS

tight sandstone gas reservoir, threshold pressure gradient, mathematical model, water saturation, formation pressure

Abbreviations: β, Dimensionless constant; τ_0, Yield stress of oil, MPa; K_a, Absolute permeability, mD; μ, Viscosity, mPa·s; S_w, Water saturation; S_{wi}, Initial water saturation; S_{wc}, Bound water saturation; P, Formation Pressure, MPa.

1 Introduction

Tight sandstone gas reservoirs possess vast reserves and significant development potential, with their proportion in oil and gas exploration and development steadily increasing, making them a crucial unconventional oil and gas resource (Civan, 2017; Sun et al., 2017; Zhang et al., 2019; Wang S et al., 2022; Farouk et al., 2024a; Farouk et al., 2024b). It is expected that the annual production of low-permeability tight gas reservoirs in China will reach about 600 × 10 m^3 by 2030 (Zhang et al., 2020; Ren et al., 2022). For example, the Ordos Basin in China contains large gas reserves and hosts some of the most developed gas fields. The reservoirs in this basin are characterized by low porosity, low permeability, and strong heterogeneity, which present significant challenges for gas reservoir development (Zhang et al., 2021; Wang R. et al., 2022). Additionally, the gas reservoirs contain a significant amount of water, which negatively impacts the production capacity of gas wells. This is due to poor natural productivity, complex seepage mechanisms, and the scattered distribution of remaining gas (Lan et al., 2014; Zheng et al., 2020; Fu et al., 2020; Fu et al., 2021). This accelerates reservoir damage and further reduces the development efficiency of gas reservoirs, making it challenging to achieve long-term stable production in the tight and complex water-bearing gas reservoirs of the Ordos Basin.

The geological conditions of tight gas reservoirs are complex, characterized by poor reservoir properties, strong heterogeneity, low porosity, low permeability, and high water saturation. Additionally, under water-bearing conditions, complex interactions between water and gas occur within the reservoir, contributing to the complexity of fluid flow mechanisms. Research has shown that in low-permeability gas reservoirs, the flow paths of gas and water are extremely narrow, which facilitates the formation of water films at the pore throats (Tian et al., 2020; Chen et al., 2023; Tian et al., 2023). These water films significantly hinder gas flow, requiring the gas to overcome the resistance of the film before it can start moving (Zeng et al., 2011; Li et al., 2016; Tian et al., 2018). The minimum pressure difference required to overcome this resistance is commonly referred to as the threshold pressure gradient (TPG). Under ideal conditions, gas flow follows Darcy's law, where the flow rate and pressure gradient curve exhibit a linear relationship, intersecting at the origin (Tian et al., 2014; Dong et al., 2019). However, in low-permeability porous media, gas flow deviates from Darcy's law, and the flow rate and pressure gradient curve display a partially nonlinear relationship (Zeng et al., 2011; Wang and Sheng, 2017; Liu, 2019; Liu et al., 2019). The intersection point of the nonlinear curve with the x-axis represents the TPG. At higher pressures, the flow rate and pressure gradient become approximately linear, and the extension of this linear curve intersects the x-axis to form the pseudo TPG. Extensive research has confirmed the presence of TPG in tight gas reservoirs, which leads to nonlinear fluid flow characteristics (Feng et al., 2024). The existence of a TPG implies that gas will only start to flow when the pressure difference within the reservoir reaches or exceeds this critical value. Moreover, a continuous pressure gradient must be maintained during gas flow to prevent the reformation of the water film; otherwise, the flow may be interrupted (Amann-Hildenbrand et al., 2012; Hu et al., 2018). Therefore, the TPG is a critical factor influencing the development efficiency of low-permeability gas reservoirs (Civan, 2017). In the development process, it is essential to fully consider the impact of TPG on gas flow and optimize the development strategy accordingly to enhance the recovery rate (Shanley et al., 2004; Hu et al., 2018).

TABLE 1 The TPG prediction models.

Prediction formula	Reservoir type	Scholar
$G = \frac{\beta\tau_0}{\sqrt{k_a}}$	Oil Reservoir	Pascal (1981)
$G = \alpha\left(\frac{k_a}{\mu}\right)^{\beta}$	Porous medium	Prada and Civan (1999)
$G = \alpha k_a^{\beta}$	Low permeability reservoir	Zeng et al. (2010)
$G = \alpha S_w^{\beta} k_a^{\gamma S_w^{\sigma}}$	Tight gas reservoir	Yang et al. (2015)
$G = \alpha k_a^{-\beta}(S_{wi} - S_{wc})^{\gamma}$	Tight gas reservoir	Liu (2023)

Research indicates that the productivity of gas wells diminishes as the TPG increases. A higher TPG requires a greater production pressure differential for fluid to start flowing, directly resulting in reduced production. To enhance production capacity, it is necessary to adopt measures that lower the TPG, such as enhancing reservoir permeability via techniques like hydraulic fracturing. Simultaneously, it is crucial to carefully manage the production pressure differential to prevent a decline in gas production efficiency due to excessive pressure differences. Hence, exploring the TPG of tight sandstone is of utmost importance (Cao et al., 2017; Song et al., 2015).Laboratory testing methods for determining the TPG can be broadly categorized into steady-state and unsteady-state approaches. The steady-state method is particularly effective for directly measuring the TPG, as it involves observing the minimum pressure required to maintain a constant flow rate through the sample. This approach provides a direct assessment of the TPG. In contrast, unsteady-state methods are often quicker to implement and are valuable for capturing dynamic flow behaviors and transient effects associated with the TPG. Although unsteady-state methods may not offer as direct a measurement of the TPG as the steady-state approach, they can provide insights into time-dependent flow phenomena (Bai et al., 1993).

Laboratory experiments have not only confirmed the existence of a TPG in tight reservoirs but have also revealed a significant correlation between this gradient and key physical properties of the reservoirs. Specifically, the experimental data demonstrate a clear inverse relationship between the TPG and reservoir permeability: the lower the permeability, the higher the required TPG. Additionally, there is a positive correlation between the TPG and water saturation in the reservoir, indicating that an increase in water saturation directly leads to a corresponding increase in the TPG (Miller and Low, 1963; Boukadi et al., 1998). For example, Zhu et al. observed that in low-permeability gas reservoirs, the TPG increases as permeability decreases or water saturation increases (Zhu et al., 2011). However, they did not establish a definitive correlation between these parameters. Dong et al., through core experiments, found that the TPG increases with the rise in effective stress and developed dynamic

TABLE 2 Parameters of natural core samples.

Layer	Sample	Diameter, cm	Length, cm	Porosity %	Permeability, mD
J30H1	1#	2.5	5.61	3.057	0.069
	2#	2.5	5.64	11.356	0.352
	3#	2.5	5.21	11.311	0.679
	4#	2.5	5.79	12.699	1.135
J30S2	5#	2.5	5.73	4.482	0.063
	6#	2.5	5.12	6.852	0.236
	7#	2.5	5.66	7.311	0.809
	8#	2.5	6.12	2.239	1.280
J58H1	9#	2.5	5.39	3.933	0.049
	10#	2.5	5.76	5.231	0.183
	11#	2.5	5.96	9.943	0.684
	12#	2.5	5.61	11.921	1.054
	Average	2.5	5.63	7.533	0.549

TABLE 3 Composition of the synthesized formation water.

Layer	Concentration, mg/L							Salinity, mg/L	Water type	pH
	K^++Na^+	Ca^{2+}	Mg^{2+}	Ba^{2+}	SO_4^{2-}	HCO_3^-	Cl^-			
J30H1	8,050	9,906	195.1	158.7	46.2	214	28,679	48,126	$CaCl_2$	6.27
J30S2	8,577	9,170	283.9	106.2	37.5	333.9	29,451	47,603	$CaCl_2$	6.20
J58H1	6,957	8,191	184.8	145.1	39	184	23,840	40,326	$CaCl_2$	6.32

TPG models for cores with different permeability. However, their study did not take into account the influence of water content on the TPG (Dong et al., 2019). Ding et al. conducted a TPG test under reservoir conditions and concluded that the start-up pressure gradient increases with the decrease of pore pressure (Ding et al., 2017). Under reservoir conditions, as core permeability decreases and water saturation increases, the TPG becomes greater. However, no starting pressure model has been constructed to account for these factors. Atif Zafar et al. considered the effects of water saturation, permeability, and pore pressure on the TPG. However, they only constructed separate models for the influence of water saturation, pore pressure, and permeability on the TPG, without comprehensively considering the relationship among the three factors. This limitation reduces the practical applicability of their findings for production guidance (Zafar et al., 2020).

Many scholars have conducted studies on the mathematical description models of the initiating pressure gradient across different reservoir types, as summarized in Table 1. Pascal H. et al. Utilized the finite difference method to investigate the threshold pressure in linear reservoirs, taking into account low-speed flow, and proposed a mathematical model for the TPG that incorporates rock shear stress and permeability. However, their model only considers the properties of the rock itself and lacks consideration of the fluid's influence on the TPG (Pascal, 1981). Prada A. et al. applied the TPG to correct Darcy's law for low-speed flow. They determined that fluid can only pass through the porous medium when the flow force is sufficient to overcome the TPG. A mathematical model for the TPG was developed, taking into account the fluid properties. (Prada and Civan, 1999). Zeng et al. (2010) studied the influence of different fluid components on the TPG of rocks and proposed a mathematical model for the TPG. However, their model only considers fluid properties and lacks consideration of rock properties. Liu, (2023) suggested that as production time increases, the gas flow space expands, and flow resistance decreases. They improved the formula for the TPG

TABLE 4 Fitting result of dynamic TPG of cores with different permeabilities.

Layer	Sample	Permeability/mD	Formula
J30H1	1#	0.069	$G = 0.357 \times 10^{-3} S_w^{.42} P^{-0.33}$
	2#	0.352	$G = 0.316 \times 10^{-3} S_w^{.39} P^{-0.24}$
	3#	0.679	$G = 0.293 \times 10^{-3} S_w^{0.37} P^{-0.21}$
	4#	1.135	$G = 0.264 \times 10^{-3} S_w^{0.28} P^{-0.19}$
J30S2	5#	0.063	$G = 0.56 \times 10^{-3} S_w^{0.382} P^{-0.95}$
	6#	0.236	$G = 0.32 \times 10^{-3} S_w^{0.28} P^{-0.69}$
	7#	0.809	$G = 0.31 \times 10^{-3} S_w^{0.25} P^{-0.54}$
	8#	1.280	$G = 0.29 \times 10^{-3} S_w^{0.11} P^{-0.34}$
J58H1	9#	0.049	$G = 0.48 \times 10^{-3} S_w^{0.72} P^{-0.93}$
	10#	0.183	$G = 0.42 \times 10^{-3} S_w^{.62} P^{-0.55}$
	11#	0.684	$G = 0.38 \times 10^{-3} S_w^{.54} P^{-0.47}$
	12#	1.054	$G = 0.31 \times 10^{-3} S_w^{0.38} P^{-0.31}$

and developed a calculation formula that considers the effects of permeability, initial water saturation, and bound water saturation. However, in actual production, it is challenging to accurately determine bound water saturation, which limits the practical significance of their model. Yang et al. (2015) conducted research on the threshold pressure effect in low-permeability tight gas reservoirs and quantitatively characterized the TPG of Sulige low-permeability tight gas reservoirs using a formula that incorporates the absolute permeability and water saturation of the reservoir. All the above theoretical models were developed under normal pressure conditions, neglecting the influence of formation pressure on the TPG.

To address this, this article first establishes a dynamic TPG testing device for tight gas reservoirs under water-bearing conditions by constructing a high-precision back pressure control system. We conducted tests on the dynamic TPG of tight gas reservoirs with varying water saturation levels across different reservoirs and analyzed the effects of permeability, water saturation, and formation pressure on the TPG. Finally, mathematical models for the TPG in various reservoirs were developed. This research provides a reference and foundation for accurately understanding the TPG characteristics of tight gas reservoirs and for formulating reasonable development plans.

2 Experimental material and procedures

2.1 Experimental materials

The experimental cores were taken from four samples, each with different permeability, from the J30S1, J30S2, and J58H1 layers of tight gas reservoirs in the Ordos Basin. The porosity and permeability of these cores were measured using the single chamber method based on Boyle's Law and the pulse decay method, respectively. The parameters of the natural core samples are listed in Table 2. The injection fluids used were synthesized formation water and nitrogen. The properties of the synthesized formation water are listed in Table 3, and the water was prepared based on the actual properties of the formation water from the study block. The temperature was set to 85°C, reflecting the actual gas reservoir temperature of the study block.

2.2 Experimental procedures

The experiment utilized a combination of the improved bubble method and the flow velocity pressure difference method, with the flowchart shown in Figure 1. First, the rock core is cleaned and dried for 48 h to determine its dry weight. Then, the rock core is placed in an intermediate container and vacuumed for 12 h. Water is pumped into the container and pressurized to 5 MPa for 24 h to fully saturate the core's pores. The saturated water mass of the rock core is then measured. The saturated core is placed into a core holder, and a confining pressure of 5 MPa is applied using a confining pressure pump. After the pressure stabilizes, nitrogen gas is used to displace the core at a constant pressure while continuously weighing it. Displacement is stopped when the core's water saturation reaches 70%. The confining pressure is then set to 40 MPa, and the back pressure is adjusted to the specified level. After the fluid pressure within the core stabilizes, the inlet pressure is gradually increased. At each pressure point, once the flow stabilizes, the gas flow rate, corresponding time, and pressure are measured until a complete flow curve is obtained. After completing the initial experiment, the core is re-saturated and displaced to water saturation levels of 60%, 50%, 40%, and 30%, with the experiment repeated for TPG testing.

To ensure the stability of the water saturation in the core during the experiment, a low-speed pressurization method was employed to prevent the water phase from flowing due to excessive pressurization speed. The weighing method was used to accurately determine the water saturation before and after the experiment. If the error in water saturation before and after the experiment remains within 2%, it can be concluded that only single-phase gas flow occurred during the experiment. Conversely, if the error exceeds this range, it is considered that gas-liquid two-phase flow occurred in the core, requiring the core to be cleaned and the experiment to be repeated.

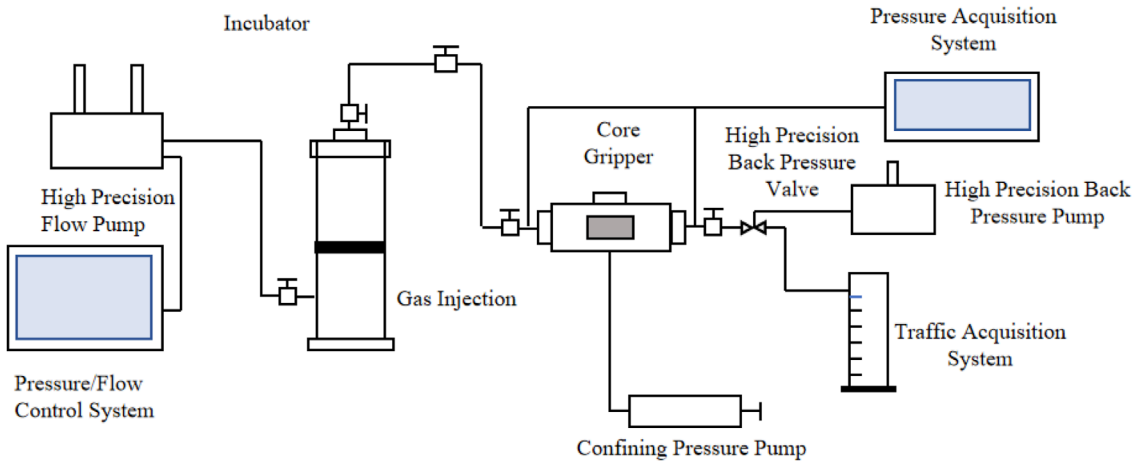

FIGURE 1
Apparatus of dynamic TPG test.

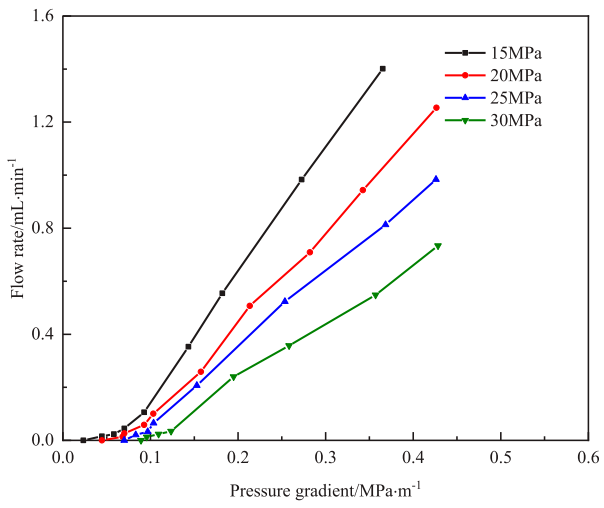

FIGURE 2
Schematic diagram of pressure gradient curve of non-Darcy flow.

3 Results

3.1 Effect of water saturation on TPG

Figure 2 shows the pressure gradient and flow rate curves for core 6# when the water saturation is 60% and the formation pressure are 15, 20, 25, and 30 MPa, respectively. It can be seen from the Figure 2 that when the pressure gradient are less than 0.092, 0.106, 0.114, and 0.123 MPa/m, the curve is nonlinear. This is because the pressure gradient in this area is low, and due to the Jamin effect, gas cannot pass through the core pores. As the pressure gradient gradually increases, the slope of the curve changes significantly, and the rate of increasing gas flow relative to the square of the pressure gradient is approximately linear. Extending the linear part of the curve to the *X*-axis, it will intersect with the *X*-axis at a point where the pressure gradient corresponding to that point is the TPG of the core.

The variation of TPG with water saturation was measured in three reservoirs at a formation pressure of 15MPa, as shown in Figure 3. The variation law of the TPG of three reservoirs was measured through experiments, as shown in Figure 3. The experimental results show that the TPG of the reservoir exhibits a clear regularity, generally increasing rapidly with the increase of the original water saturation. Under the same water saturation conditions, reservoirs with lower permeability correspond to more significant TPG. All three reservoir curves show that when the water saturation is greater than 50%, there is a significant turning point in the amplitude of the TPG change, and the TPG increases rapidly. Among them, J30S2 and J58H1 show more pronounced performance. This is because when the water saturation is high, the gas in the core is difficult to form a continuous phase flow, but is divided into many small bubbles. These tiny bubbles are subjected to capillary forces during their flow process, resulting in the so-called Jamin effect when passing through the core throat, which refers to the additional resistance caused by the shape change of the bubbles when passing through narrow channels. As the water saturation increases, the flow resistance caused by bubble segmentation and Jamin effect also increases accordingly, resulting in an increase in reservoir TPG at the macro level.

When the water saturation is 30%, the TPG of rock cores with permeability less than 0.1mD is 0.026 MPa/m, 0.086 MPa/m, and 0.048 MPa/m, respectively. J30S1 has the least impact on water saturation. When the water saturation increases from 30% to 70%, the TPG increases by 114.27%. J30S2 and J58H1 increase by 314.19% and 316.37%, respectively. The threshold pressure range for J30S1 is 0.026–0.036 MPa/m, J30S2 is 0.086–0.131 MPa/m, and J58H1 is 0.048–0.103 MPa/m. At the same water saturation, as the core permeability increases, the TPG decreases. When the water saturation is 30% and the permeability of the three layers increases from less than 0.1mD to greater than 1mD, the TPG decrease by 29.5%, 86.03%, and 75.83%, respectively. Similarly, when the water

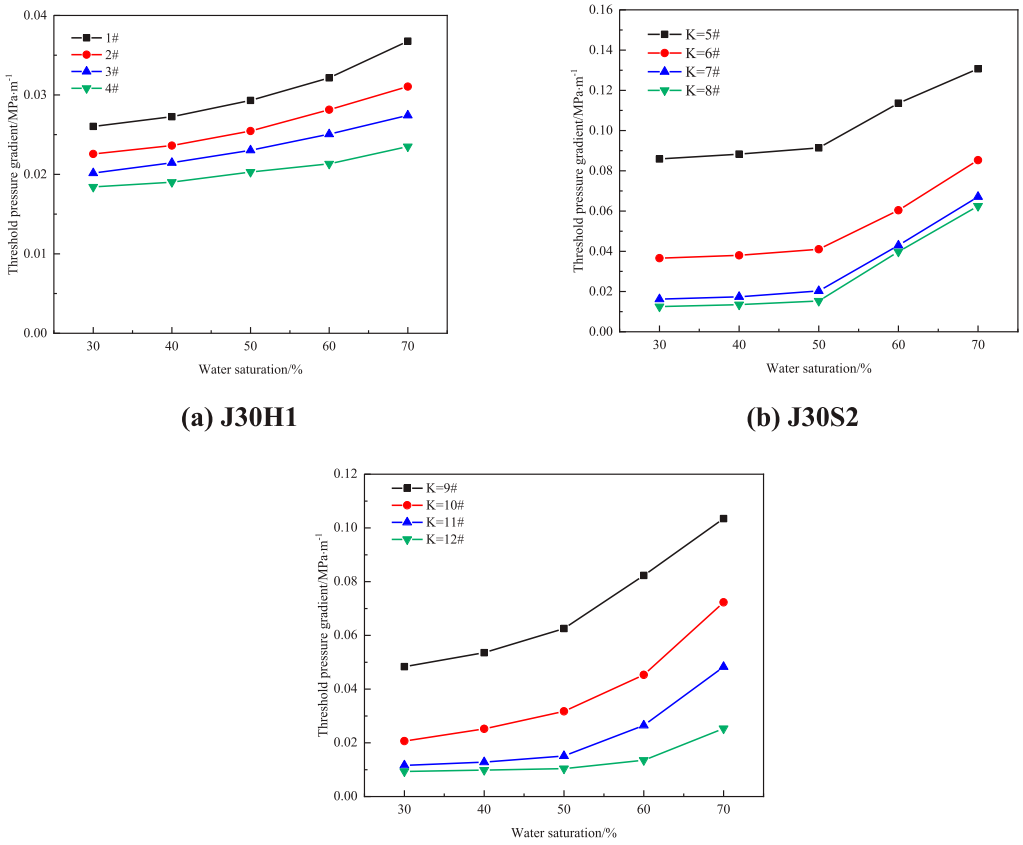

FIGURE 3
TPG of rock cores with different water saturation in three layers. **(A)** J30H1, **(B)** J30S2, **(C)** J58H1.

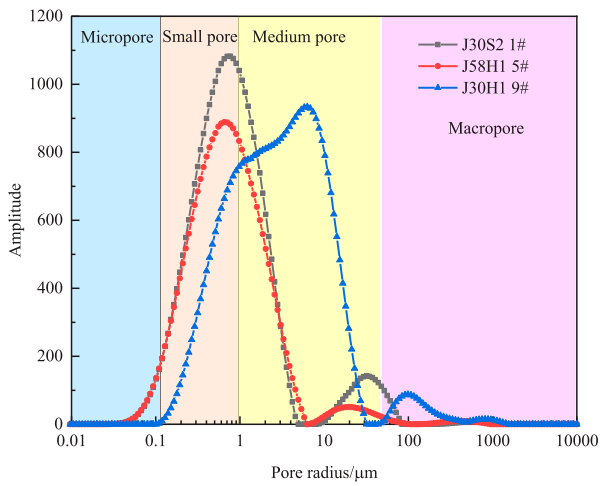

FIGURE 4
Comparison of NMR spectra of three layers.

saturation reaches 70%, the TPG decrease by 36.14%, 52.18%, and 75.54%, respectively. By conducting nuclear magnetic resonance analysis on three core layers with permeability less than 0.1mD, as shown in Figure 4, The pore distribution of J30S2 and J58H1 is mainly concentrated in micropores and small pores smaller than 1 μm. The proportion of mesopores and macropores in J30H1 accounts for 53.44% of the total pores, the smaller pore throats of J30S2 and J58H1 will result in greater capillary force, while J30S2 and J58H1 account for 23.57% and 20.13% of the total pores. The smaller pore throats in J30S2 and J58H1 need to overcome stronger capillary force to push gas through the pore throats, thus requiring higher pressure to initiate gas flow. On the contrary, the larger pore throat structure of J30H1 results in a smaller TPG.

3.2 Effect of formation pressure on TPG

To study the variation of the threshold pressure in dense experimental rock cores under different formation pressures, pore pressures were set at 15, 20, 25, and 30 MPa, respectively, with corresponding confining pressures set at 25, 30, 35, and 40 MPa. The difference between confining pressure and pore pressure was kept constant during the experiment to ensure the permeability of the rock core remained stable. When the water saturation is 30%, the relationship between formation pressure and TPG is shown in Figure 5.

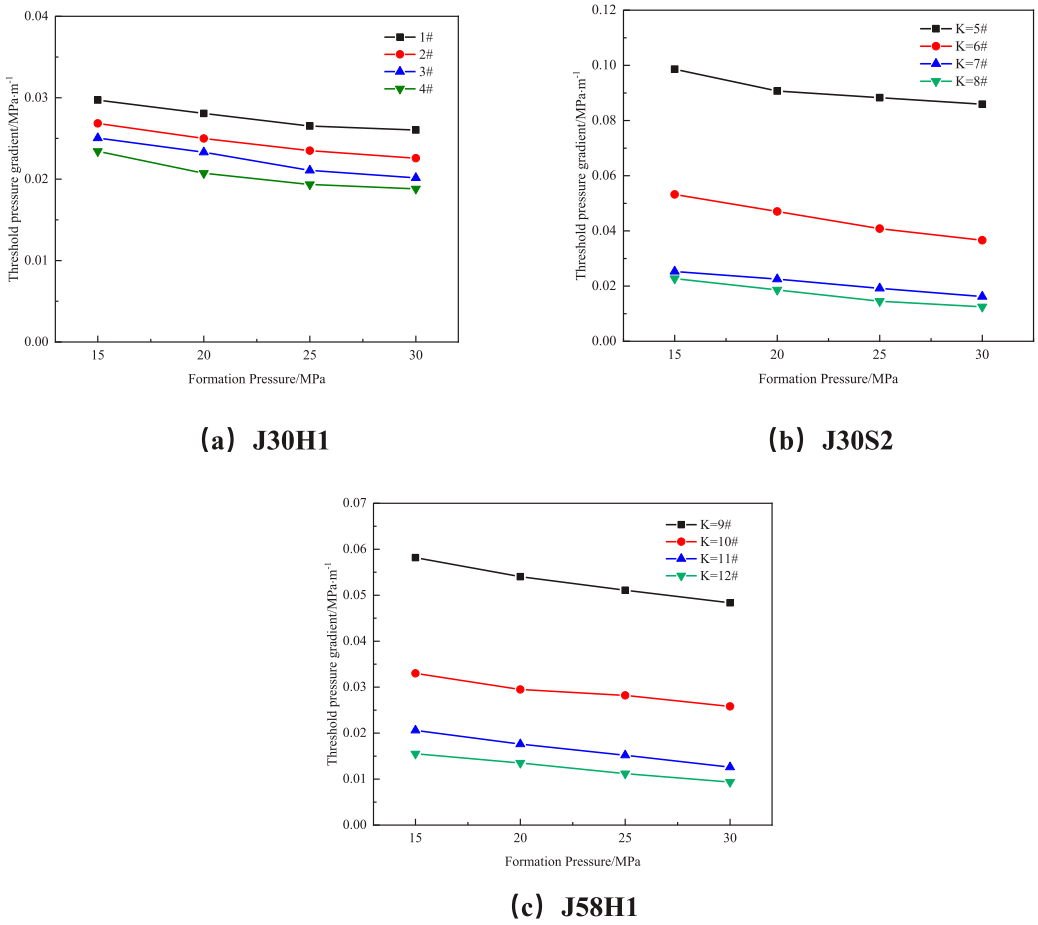

FIGURE 5
TPG of rock cores under different formation pressures in three layers. **(A)** J30H1, **(B)** J30S2, **(C)** J58H1.

Under low formation pressures, the TPG of tight gas reservoir cores decreases as pressure increases. However, once the local pressure exceeds 25.0 MPa, the rate of change in the TPG significantly diminishes and eventually stabilizes. The primary reason for this phenomenon is the significant impact of the slippage effect on gas permeation behavior in the cores of tight gas reservoirs. The slippage effect, also known as the Klinkenberg effect, refers to the phenomenon where gas flow in a porous medium at low pressure exhibits higher permeability compared to liquid permeability under the same conditions. This occurs because, at lower pressures, gas molecules have longer mean free paths and undergo slip at the pore walls, thereby increasing the apparent permeability and resulting in a lower measured TPG.

As formation pressure gradually increases, gas density rises, the mean free path between molecules shortens, and the frequency of collisions with pore walls decreases. Consequently, the slippage effect weakens, the increase in gas permeability becomes less pronounced, and the rate of change in the TPG decreases until it stabilizes. Once the local pressure exceeds 25 MPa, the gas density is sufficiently high, the influence of the slippage effect essentially disappears, and gas flow behavior begins to resemble conventional Darcy flow as described by Darcy's law. Thus, the TPG stabilizes.

When formation pressure changes, cores with lower permeability exhibit more significant variations in the TPG, while cores with higher permeability show a relatively smaller range of TPG changes. Specifically, for cores with permeability exceeding 1.0 mD, the TPG remains almost stable with changes in formation pressure, decreasing by 12.41%, 12.88%, and 16.91%, respectively. In contrast, for cores with permeability less than 0.1 mD, the TPG decreases by 19.68%, 44.93%, and 39.68%. This difference can be attributed to the varying influence of the slippage effect in cores with different permeabilities. At the same formation pressure, as the core permeability increases, TPG decreases. When the formation pressure is 15MPa, the permeability of the three layers increases from less than 0.1mD to greater than 1mD, and the TPG decreases by 21.21%, 85.45%, and 73.28%, respectively. Similarly, when the formation pressure is 30MPa, the TPG decreased by 27.69%, 76.98%, and 81.25%, respectively. In low-permeability cores, the pore channels are narrow, making the slippage effect more pronounced, which significantly increases gas permeability at low pressures and thus causes a substantial decrease in TPG. Conversely, in high-permeability cores, the pore channels are relatively wide, and the slippage effect is weaker, resulting in a more gradual and stable change in TPG.

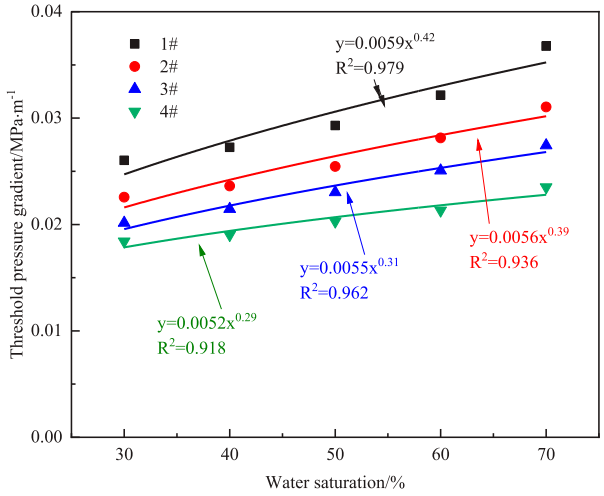

FIGURE 6
The fitting curve between TPG and water saturation.

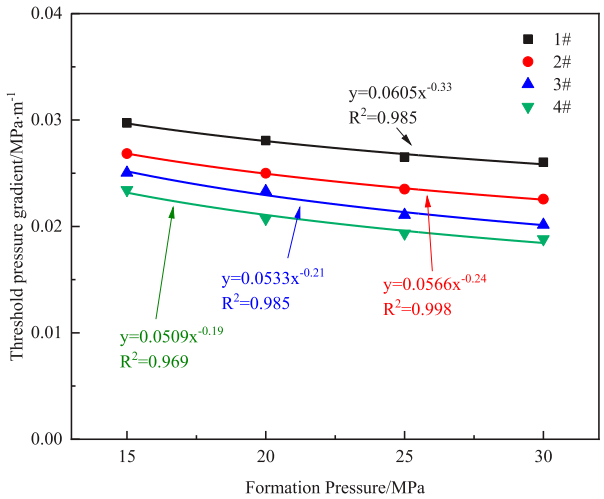

FIGURE 7
The fitting curve between TPG and formation pressure.

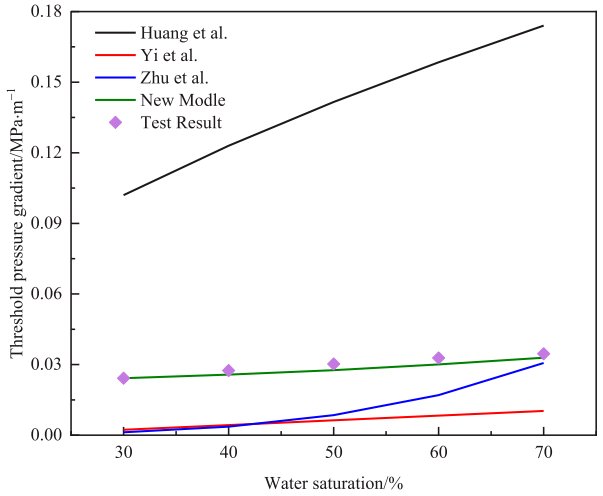

FIGURE 8
The comparison between the newly developed model and other models (Yi et al., 2006; Huang et al., 2016; Zhu et al., 2022).

4 Discussion

4.1 Establish of mathematical model for dynamic TPG

Through the study of the variation of TPG with water saturation and formation pressure, the relationship between TPG, water saturation, and formation pressure was statistically fitted, as shown in Figures 6, 7. The corresponding expression for a single factor was obtained as shown in Equation 1.

$$G = aS_w^{\ b}P^c \quad (1)$$

Where G is the TPG (MPa/m), P is the formation pressure (MPa), and S_w is the water saturation (%).The parameters a,b,and c are fitting coefficients. A total of 12 sets of coefficients a,b,and c were obtained through fitting,and the expressions for the TPG in cores with different permeabilities across the three layers were derived, as shown in Table 4. To explore the relationship between the TPG and core permeability, the coefficient a, b, and c was fitted to the core permeability. The detailed steps are outlined in the Appendix. Finally, the mathematical models for the TPG of the three layers are obtained as shown in Equations 1–3.

$$\text{J30H1:}G = 2.78\times10^{-4}K^{-0.09}S_W^{\ -0.13K+0.45}P^{-0.19K^{-0.19}} \quad (2)$$

$$\text{J30S2:}G = 3.02\times10^{-4}K^{-0.12}S_W^{\ -0.24K+0.37}P^{-0.37K^{-0.39}} \quad (3)$$

$$\text{J58H1:}G = 3.38\times10^{-4}K^{-0.14}S_W^{\ -0.27K+0.66}P^{-0.34K^{-0.22}} \quad (4)$$

4.2 Model validation

In order to verify the reliability of the model proposed in this article, different models were used to calculate the TPG using J30H1 as an example. The predicted results are shown in Figure 8. From the Figure 8, it is evident that there is a significant discrepancy between the theoretical calculation results of previous researchers and the measured values. However, the theoretical value of the TPG calculated using the new model bears little difference from the measured value, thus validating the rationality and accuracy of the new model. It can effectively describe and evaluate the TPG of tight sandstone gas reservoirs containing water.

The general formula for TPG can be effectively utilized to rapidly determine the TPG for reservoirs with varying permeability. For instance, by selecting three reservoirs with permeabilities ranging from 0.1 mD to 1 mD, calculations can be performed to generate a graph depicting the relationship between TPG, formation pressures, and water saturation levels in the study area, as illustrated in Figure 9. The results presented in Figure 9 indicate that water

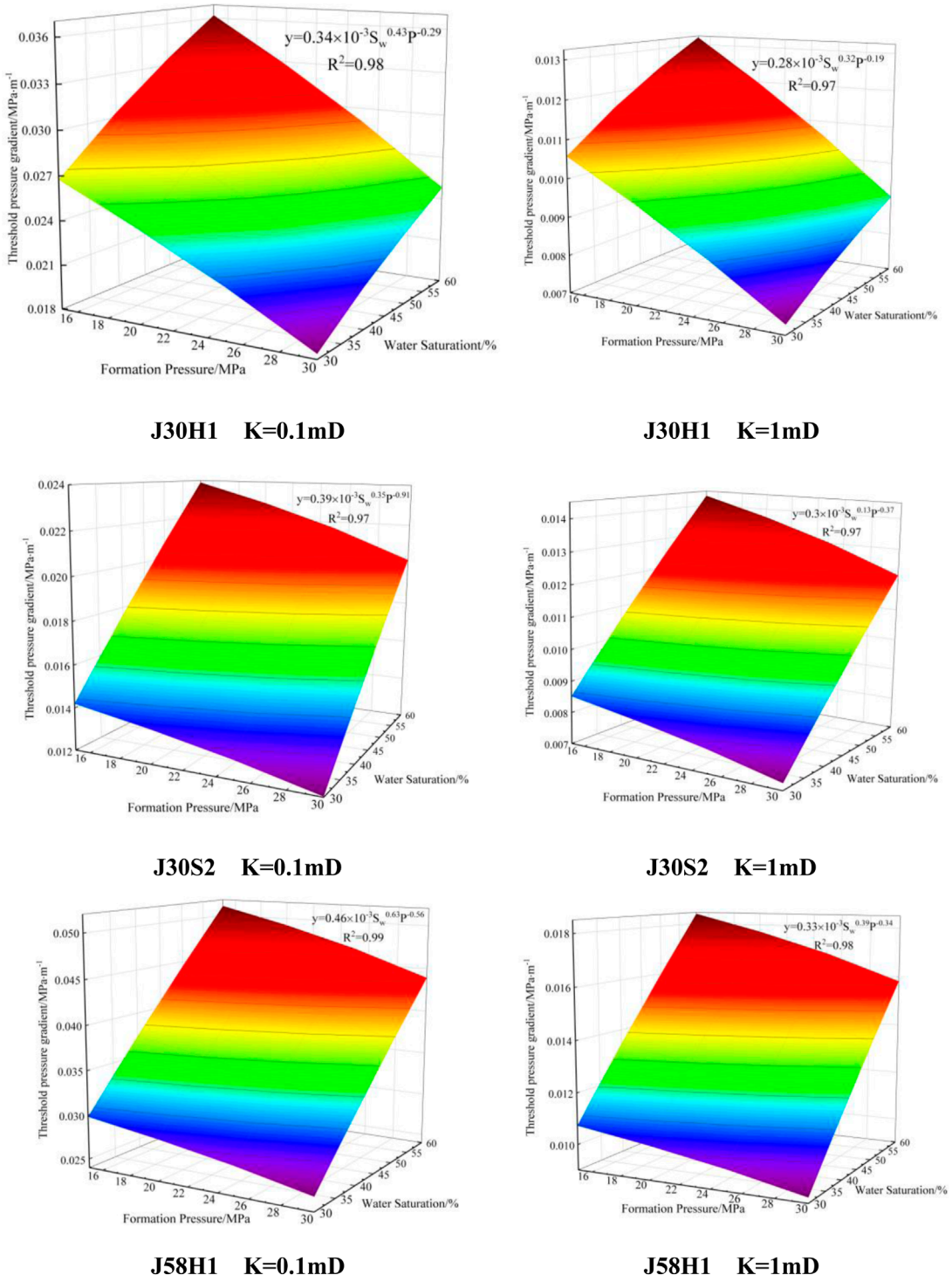

FIGURE 9
The TPG relationship diagram of three reservoirs under different formation pressures and water content conditions.

saturation exerts a more significant influence on TPG compared to formation pressure. This finding underscores the critical importance of closely monitoring changes in formation water content during the development of tight sandstone gas reservoirs to ensure optimal reservoir management and production efficiency.

5 Conclusion

This study conducted a comprehensive analysis of the variation in threshold pressure gradient (TPG) under different water saturation and formation pressure conditions for tight sandstone gas

reservoirs in the Ordos Basin, China, through experimental research and mathematical modeling. The key conclusions are as follows:

(1) The study revealed that TPG is closely related to both water saturation and formation pressure, with water saturation having a significantly greater impact on TPG compared to formation pressure.
(2) As formation pressure increases, the slippage effect of gas molecules gradually diminishes, resulting in a decrease in the rate of change of TPG, which eventually stabilizes. When the local pressure exceeds 25.0 MPa, the slippage effect almost disappears, and gas flow behavior approaches the conventional flow described by Darcy's law, leading to a stabilized TPG.
(3) The study also found that TPG in low-permeability cores exhibits greater variation with changes in formation pressure, whereas TPG in high-permeability cores remains relatively stable. In low-permeability cores, the slippage effect significantly enhances gas permeability, resulting in larger fluctuations in TPG.
(4) Based on the experimental data, a mathematical model was established to describe the relationship between TPG, permeability, water saturation, and formation pressure. The model's applicability was validated through case studies, providing a theoretical basis for predicting TPG in gas reservoirs with varying permeability.

In the development of tight sandstone gas reservoirs, special attention should be paid to changes in formation water content, as it has a more pronounced impact on TPG. This insight is crucial for formulating effective development strategies. Future research should integrate actual production data to further optimize and refine the model, enhancing its applicability and predictive accuracy under complex geological conditions.

Data availability statement

The original contributions presented in the study are included in the article; further inquiries can be directed to the corresponding author. The NMR data can be accessed via the following link: https://figshare.com/s/a82b60f719dc6b08eae6.

Author contributions

YL: Conceptualization, Supervision, Writing–original draft, Writing–review and editing. JF: Conceptualization, Formal Analysis, Funding acquisition, Methodology, Supervision, Writing–original draft, Writing–review and editing. WY: Conceptualization, Data curation, Formal Analysis, Methodology, Writing–original draft, Writing–review and editing. KC: Investigation, Methodology, Writing–original draft, Writing–review and editing. JD: Formal Analysis, Funding acquisition, Writing–original draft, Writing–review and editing. JW: Data curation, Investigation, Methodology, Resources, Writing–original draft, Writing–review and editing.

Funding

The author(s) declare that financial support was received for the research, authorship, and/or publication of this article. The authors gratefully acknowledge the support from the National Science Foundation Projects of China (52104022), Project Supported by the Science and Technology Research Program of Chongqing Municipal Education Commission (Grant No. KJQN202401509), Project supported by the Key Laboratory of the Ministry of Education on Safe Mining of Deep Metal Mines (DM 2023B06).

Conflict of interest

Authors YL, KC, JD, JW were employed by Sinopec North China Petroleum Bureau.

The remaining authors declare that the research was conducted in the absence of any commercial or financial relationships that could be construed as a potential conflict of interest.

Publisher's note

References

Amann-Hildenbrand, A., Ghanizadeh, A., and Krooss, B. M. (2012). Transport properties of unconventional gas systems. *Mar. and Petroleum Geol.* 31, 90–99. doi:10.1016/j.marpetgeo.2011.11.009

Bai, M., Elsworth, D., and Roegiers, J. C. (1993). Multiporosity/multipermeability approach to the simulation of naturally fractured reservoirs. *Water Resoures. Res.* 29 (6), 1621–1633. doi:10.1029/92wr02746

Boukadi, F., Bemani, A., Rumhy, M., and Kalbani, M. (1998). Threshold pressure as a measure of degree of rock wettability and diagenesis in consolidated Omani limestone cores. *Mar. and Petroleum Geol.* 15 (1), 33–39. doi:10.1016/s0264-8172(97)00059-7

Cao, Y., Ye, L., Lei, Q., Chen, X., Ma, Y. Z. Z., and Huang, X. (2017). Gas-water flow behavior in water-bearing tight gas reservoirs. *Geofluids* 2017, 1–16. doi:10.1155/2017/9745795

Chen, F., Wang, Z., Fu, S., Li, A., and Zhong, J. (2023). Research on transformation of connate water to movable water in water-bearing tight gas reservoirs. *Energies* 16 (19), 6961. doi:10.3390/en16196961

Civan, F. (2017). Effect of poroelasticity, pore confinement, molecular-to-inertial transport, and threshold pressure on flow of gas through hydraulically-fractured shale-gas reservoirs. *SPE Annu. Tech. Conf. Exhib.* doi:10.2118/187056-MS

Ding, J., Yang, S., Shi, Q., Yan, J., and Zheng, C. (2017). Experimental study on dynamic threshold pressure gradient of tight gas reservoir. *Pet. Geol. Recovery Effic.* 24 (5), 64–69. doi:10.13673/j.cnki.cn37-1359/te.2017.05.010

Dong, M., Shi, X., Ling, S., Zhang, B., and Li, X. (2019). Effect of dynamic pseudo threshold pressure gradient on well production performance in low-permeability and tight oil reservoirs. *J. Pet. Sci. Eng.* 173, 69–76. doi:10.1016/j.petrol.2018.09.096

Farouk, S., Qteishat, A., Sen, S., Ahmad, F., El-Kahtany, K., Collier, R., et al. (2024b). Characterization of the gas-bearing tight paleozoic sandstone reservoirs of the risha field, Jordan: inferences on reservoir quality and productivity. *Arabian J. Sci. Eng.*, 1–21. doi:10.1007/s13369-024-09000-x

Farouk, S., Sarhan, M. A., Sen, S., Ahmad, F., El-Kahtany, K., and Reda, M. M. (2024a). Evaluation of the lower cretaceous alam el bueib sandstone reservoirs in shushan basin, Egypt-implications for tight hydrocarbon reservoir potential. *J. Afr. Earth Sci.* 218, 105386. doi:10.1016/j.jafrearsci.2024.105386

Feng, Q., Xing, X., Wang, S., Liu, G., Qin, Y., and Zhang, J. (2024). CO_2 diffusion in shale oil based on molecular simulation and pore network model. *Fuel* 359, 130332. doi:10.1016/j.fuel.2023.130332

Fu, J., Su, Y., Li, L., Hao, Y., and Wang, W. (2020). Predicted model of relative permeability considering water distribution characteristics in tight sandstone gas reservoirs. *Fractals* 28 (01), 2050012. doi:10.1142/S0218348X20500127

Fu, J., Su, Y., Li, L., Wang, W., and Wang, C. (2021). Productivity model with mechanisms of multiple seepage in tight gas reservoir. *J. Petroleum Sci. Eng.* 209 (01), 109825. doi:10.1016/j.petrol.2021.109825

Hu, W., Wei, Y., and Bao, J. (2018). Development of the theory and technology for low permeability reservoirs in China. *Pet. Explor. Dev.* 45, 685–697. doi:10.1016/S1876-3804(18)30072-7

Huang, L., Shi, J., Yang, L., Zang, J., Zhang, L., and Yu, P. (2016). Experimental research and analysis on threshold pressure gradient in low-permeability gas reservoir. *Fault-Block Oil Gas. Field* 23, 610–614. doi:10.6056/dkyqt201605015

Lan, Y., Deng, X., Cheng, D., and Huang, J. (2014). Diagenetic facies and reservoir quality evaluation of Chang 6 sandstone reservoir in the upper Triassic Yanchang Formation of Huaqing area, Ordos Basin. *Acta Petrol. Min.* 33 (1), 51–63. doi:10.1016/j.marpetgeo.2020.104360

Li, Y., Dong, P., He, Z., Lei, G., Cao, N., and Wu, Z. (2016). Stress sensitivity analysis of permeability and threshold pressure gradient in low-permeability reservoir. *Pet. Geol. Recovery Effic.* 23 (6), 57–63. doi:10.13673/j.cnki.cn37-1359/te.2016.06.010

Liu, W. (2019). Analytical study on a moving boundary problem of semispherical centripetal seepage flow of Bingham fluid with threshold pressure gradient. *Int. J. Non-Linear Mech.* 113, 17–30. doi:10.1016/j.ijnonlinmec.2019.03.011

Liu, W., Zhang, Q., and Zhu, W. (2019). Numerical simulation of multi-stage fractured horizontal well in low-permeable oil reservoir with threshold pressure gradient with moving boundary. *J. Pet. Sci. Eng.* 178, 1112–1127. doi:10.1016/j.petrol.2019.04.033

Liu, Y. (2023). Research on the two phase flow mechanism and mathematical model of seepage in dense gas reservoirs with water content. *Beijing Univ. Sci. Technol.* doi:10.26945/d.cnki.gbjku.2023.000452

Miller, R. J., and Low, P. F. (1963). Threshold gradient for water flow in clay systems. *Soil Sci. Soc. Am. J.* 27 (6), 605–609. doi:10.2136/sssaj1963.03615995002700060013x

Pascal, H. (1981). Nonsteady flow through porous media in the presence of a threshold gradient. *Acta Mech.* 39 (3), 207–224. doi:10.1007/BF01170343

Prada, Á., and Civan, F. (1999). Modification of Darcy's law for the threshold pressure gradient. *J. Pet. Sci. Eng.* 22, 237–240. doi:10.1016/S0920-4105(98)00083-7

Ren, X., Li, A., and Memon, A. (2022). Experimental study on gas–water relative permeability characteristics of tight sandstone reservoir in Ordos Basin. *Geofluids* 2022, 1–8. doi:10.1155/2022/1521837

Shanley, K. W., Cluff, R. M., and Robinson, J. W. (2004). Factors controlling prolific gas production from low-permeability sandstone reservoirs: implications for resource assessment, prospect development, and risk analysis. *AAPG Bull.* 88 (8), 1083–1121. doi:10.1306/03250403051

Song, H., Cao, Y., Yu, M., Wang, Y., John, K., and Juliana, L. (2015). Impact of permeability heterogeneity on production characteristics in water-bearing tight gas reservoirs with threshold pressure gradient. *J. Nat. Gas Sci. and Eng.* 22, 172–181. doi:10.1016/j.jngse.2014.11.028

Sun, F., Yao, Y., Li, X., Yu, P., Zhao, L., and Zhang, Y. (2017). A numerical approach for obtaining type curves of superheated multi-component thermal fluid flow in concentric dual-tubing wells. *Int. J. Heat. Mass Transf.* 111, 41–53. doi:10.1016/j.ijheatmasstransfer.2017.03.103

Tian, J., Kang, Y., Jia, N., Luo, P., and You, L. (2020). Investigation of the controlling rock petrophysical factors on water phase trapping damage in tight gas reservoirs. *Energy Sci. Eng.* 8 (3), 647–660. doi:10.1002/ese3.539

Tian, J., Qin, C., Kang, Y., You, L., Jia, N., and Song, J. (2023). Reasons for low flowback behaviors of water-based fluids in tight sandstone gas reservoirs. *J. Pet. Sci. Eng. 220 Part A* 220, 111152. doi:10.1016/j.petrol.2022.111152

Tian, W., Li, A., Ren, X., and Josephine, Y. (2018). The threshold pressure gradient effect in the tight sandstone gas reservoirs with high water saturation. *Fuel* 226, 221–229. doi:10.1016/j.fuel.2018.03.192

Tian, W., Zhu, W., and Zhu, H. (2014). Influencing factors of threshold pressure gradient value for tight sandstone. *Fault-Block Oil Gas. Field* 21 (05), 611–614. doi:10.6056/dkyqt201405016

Wang, R., Liu, K., Shi, W., Qin, S., Zhang, W., Qi, R., et al. (2022). Reservoir densification, pressure evolution, and natural gas accumulation in the upper paleozoic tight sandstones in the north Ordos Basin, China. *Energies* 15, 1990. doi:10.3390/en15061990

Wang, S., Liang, Y., Feng, Q., and Javadpour, F. (2022). Sticky layers affect oil transport through the nanopores of realistic shale kerogen. *Fuel* 310, 122480. doi:10.1016/j.fuel.2021.122480

Wang, X., and Sheng, J. (2017). Effect of low-velocity non-Darcy flow on well production performance in shale and tight oil reservoirs. *Fuel* 190, 41–46. doi:10.1016/j.fuel.2016.11.040

Yang, C., Li, X., Liu, S., Gao, S., Ye, L., and Liu, J. (2015). Threshold pressure effect of Sulige low-permeability tight gas reservoir. *Acta Pet. Sin.* 36, 347–354. doi:10.7623/syxb201503009

Yi, G., Tang, H., and Lü, D. (2006). The study and analysis of starting pressure gradient in low permeability gas reservoirs. *Offshore oil.* 26, 51–54. doi:10.3969/j.issn.1008-2336.2006.03.010

Zafar, A., Su, Y., Li, L., Fu, J., Mehmood, A., Ouyang, W., et al. (2020). Tight gas production model considering TPG as a function of pore pressure, permeability and water saturation. *Pet. Sci.* 17, 1356–1369. doi:10.1007/s12182-020-00430-4

Zeng, B., Cheng, L., and Li, C. (2011). Low velocity non-linear flow in ultra-low permeability reservoir. *J. Pet. Sci. Eng.* 80 (1), 1–6. doi:10.1016/j.petrol.2011.10.006

Zeng, B., Cheng, S., and Hao, F. (2010). Experiment and mechanism analysis on threshold pressure gradient with different fluids. *Niger. Annu. Int. Conf. Exhib.* Nigeria, July 2010. doi:10.2118/140678-MS

Zhang, F., Jiang, Z., Sun, W., Zhang, X., Zhu, L., Li, X., et al. (2020). Effect of microscopic pore-throat heterogeneity on gas-phase percolation capacity of tight sandstone reservoirs. *Energy fuels.* 34 (10), 12399–12416. doi:10.1021/acs.energyfuels.0c02393

Zhang, L., Zhou, F., Zhang, S., Li, Z., Wang, J., and Wang, Y. (2019). Evaluation of permeability damage caused by drilling and fracturing fluids in tight low permeability sandstone reservoirs. *J. Pet. Sci. Eng.* 175, 1122–1135. doi:10.1016/j.petrol.2019.01.031

Zhang, Y., Shu, J., He, Z., Wang, Y., Guo, M., Zhu, G., et al. (2021). Characteristics of heterogeneous diagenesis and modification to physical properties of Upper Paleozoic tight gas reservoir in eastern Ordos Basin. *J. Pet. Sci. Eng. 208 Part E*, 109243. doi:10.1016/j.petrol.2021.109243

Zheng, D., Pang, X., Jiang, F., Liu, T., Shao, X., and Huyan, Y. (2020). Characteristics and controlling factors of tight sandstone gas reservoirs in the Upper Paleozoic strata of Linxing area in the Ordos Basin, China. *J. Nat. Gas. Sci. Eng.* 75, 103135. doi:10.1016/j.jngse.2019.103135

Zhu, W., Song, H., Huang, X., Liu, X., He, D., and Ran, Q. (2011). Pressure characteristics and effective deployment in a water-bearing tight gas reservoir with low-velocity non-Darcy flow. *Energy fuels.* 25, 1111–1117. doi:10.1021/EF1014633

Zhu, W., Zou, G., Liu, Y., Liu, W., and Pan, B. (2022). The influence of movable water on the gas-phase threshold pressure gradient in tight gas reservoirs. *Energies* 15, 5309. doi:10.3390/en15145309

Appendix

According to studies 3.1 and 3.2, it is known that the TPG is influenced by the permeability of the rock core. To investigate the influence of different reservoir permeability on the TPG, the relationship between the coefficients *a*, *b*, and *c* and permeability in Equation 1 was fitted, using J30H1 as an example, as shown in Figure A1. The coefficients *a*, b and *c* exhibit a linear or exponential relationship with permeability. By substituting the relationship between the coefficients and permeability into Equation 1, the mathematical model for the TPG as a function of permeability, water saturation, and formation pressure for J30H1 was obtained, as shown in Equation 2. Similarly, mathematical models for J30S2 and J58H1 were established, as shown in Equations 3, 4.

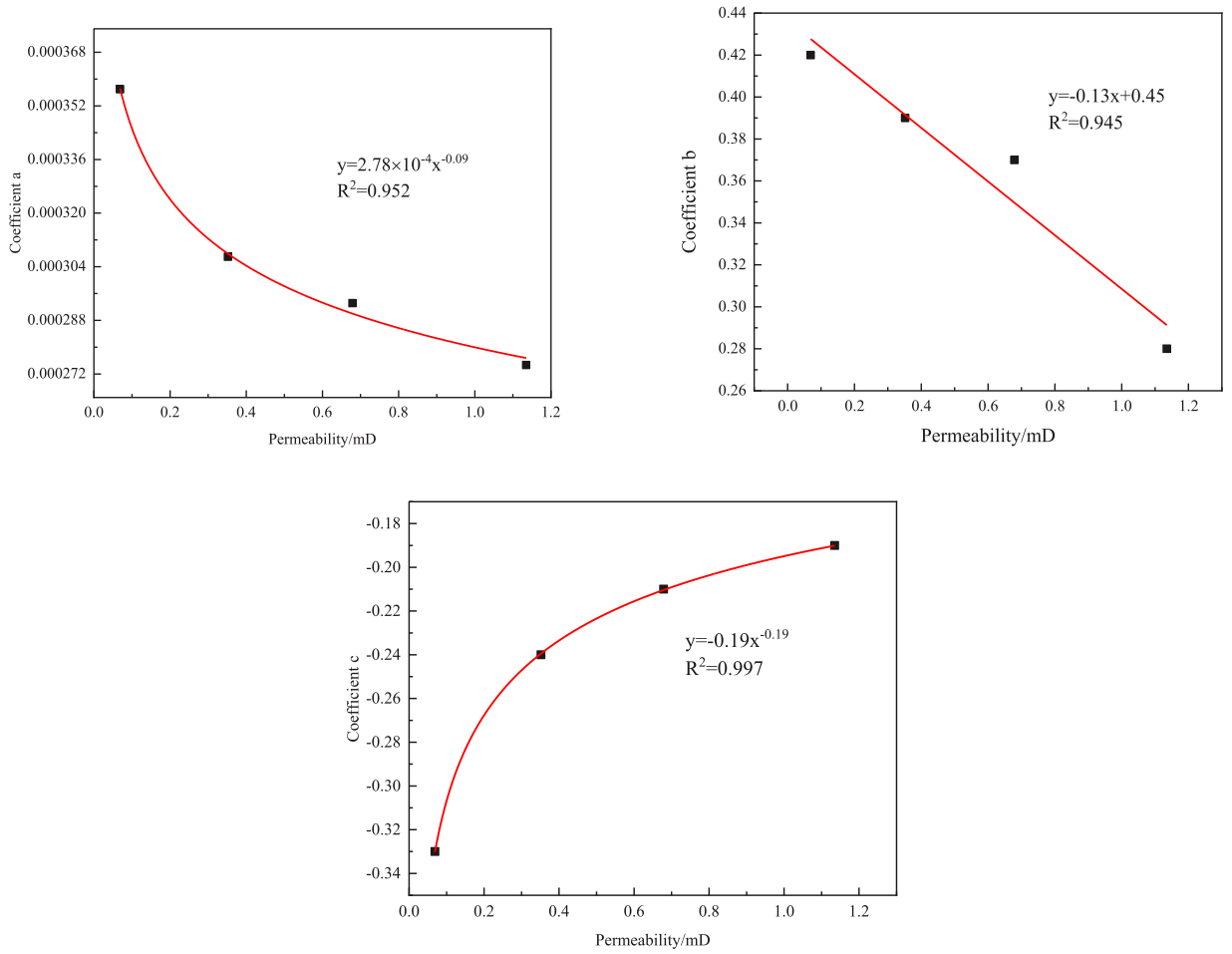

FIGURE A1
Coefficient and permeability fitting curve.

frontiers | Frontiers in Earth Science

TYPE Original Research
PUBLISHED 13 November 2024
DOI 10.3389/feart.2024.1480459

OPEN ACCESS

EDITED BY
Zhengguang Zhang,
General Prospecting Institute of China National Administration of Coal Geology, China

REVIEWED BY
Chaojun Fan,
Liaoning Technical University, China
Long Fan,
University of Alaska Fairbanks, United States

*CORRESPONDENCE
Bo Wang,
wangbo1230038@163.com

RECEIVED 14 August 2024
ACCEPTED 24 September 2024
PUBLISHED 13 November 2024

CITATION
Wu C, Wang B, Hu X, Jin X, Liang W, Shi M, Zhu X and Guo L (2024) Optimization method for predicting coal reservoir fractures in the Laochang area of Eastern Yunnan using paleotectonic stress inversion.
Front. Earth Sci. 12:1480459.
doi: 10.3389/feart.2024.1480459

Optimization method for predicting coal reservoir fractures in the Laochang area of Eastern Yunnan using paleotectonic stress inversion

Changwu Wu[1], Bo Wang[2]*, Xiong Hu[1], Xue Jin[3,4], Wei Liang[1], Mingjian Shi[2], Xueguang Zhu[1] and Liang Guo[5]

[1]China United Coalbed Methane National Engineering Research Center Company Limited, Beijing, China, [2]Information Institute of the Ministry of Emergency Management of PRC, Beijing, China, [3]Key Laboratory of Coalbed Methane Resources and Reservoir Formation Process of the Ministry of Education, China University of Mining and Technology, Xuzhou, China, [4]School of Resources and Geosciences, China University of Mining and Technology, Xuzhou, China, [5]Huayang New Material Technology Group Co., Ltd. No. 1 Coal Mine, Yangquan, China

Introduction: Coal reservoir fractures serve as critical storage spaces and migration pathways for coalbed methane (CBM), significantly influencing CBM enrichment. The characteristics of coal reservoir fracture development can be obtained using traditional simulation methods, but these still have shortcomings. This work presents an optimization approach for the traditional method.

Methods: This study introduces an optimization approach for traditional methods with two novel contributions. This study integrates the simulation of tectonic stress fields with fracture prediction, using surface sandstone fractures as constraints to reconstruct the paleostress field of the coal seam, while also accounting for the influence of coal thickness on fracture development to calculate fracture density.

Results: The predicted fracture density results were validated against measured values from the Bailongshan mine and Xiongdong coal mine with a relative error of approximately 12%, suggesting a reasonable degree of reliability.

Discussion: Based on the results of the fracture simulation predictions, it is believed that the coal seam fracture density in the study area is mostly 10–20 lines/m and that the sweet spot for CBM development is located in the Yuwang block.

KEYWORDS

coal reservoir, fracture, numerical simulation, quantitative prediction, tectonic stress

1 Introduction

In coal reservoirs, the storage spaces and migration pathways of coalbed methane (CBM) are jointly formed by the pore–fracture system, which is an important index that determines the success of CBM development projects (Moore, 2012; Li and Liu, 2022; Zhang et al., 2019). Most of the regional fractures are formed under the control of

tectonic stresses; hence, the characteristics of the tectonic stress field determine the spatial distribution, development, and evolution of these fractures (Zhou et al., 2006; Liu et al., 2023). Concurrently, most coal-bearing basins experience superimposed and reworked tectonic processes of varying magnitudes and phases, including compression, shearing, and extension (Liu et al., 2000). Tectonic movements control the formation and distribution of fractures and pores in coal reservoirs, reshaping their structural characteristics and ultimately altering the permeability of the coal reservoir (Ju et al., 2005; Pang et al., 2017). Accordingly, numerical simulations are used as feasible and practical approaches for restoring the paleo stress fields and predicting fractures in coal reservoirs.

In the 1990s, Qian et al. (1994) explored the use of numerical simulations to invert the stress field for fracture prediction, and this approach has been used in oil and gas fields. Numerical simulation of the tectonic stress field involves establishing a numerical model of the study area to simulate and calculate the stress field distribution using finite element software (Carminati and Vadacca, 2010; Zhou et al., 2021; Ren, 2019). Wu et al. (2011) used numerical simulation to study the fracture development in the Longmaxi formation; Wang et al. (2016) numerically simulated the low-permeability sandstone reservoirs of the Yanchang Formation using ANSYS software. Wang (2007) combined rock mechanics with numerical simulation to establish a quantitative relationship between the stress field and fracture parameters as well as realize quantitative fracture predictions; this method was successfully applied to the Dina gas field. Since then, numerical simulations have been widely used for quantitative predictions of reservoir fractures. Predicting reservoir fractures based on the paleo stress field is more accurate (Fang et al., 2005; Fang et al., 2017); however, this method has been primarily used on sandstone, carbonate, and shale formations, with relatively fewer studies on fracture prediction in coal reservoirs.

Studies have shown that fracture development is influenced by the thickness of the rock formation (Dixon, 1979). McQuillan (1973) and Ladeira and Price (1981) showed that fracture spacing has a linear relationship with layer thickness when the layer is less than 1.5 m thick or a nonlinear relationship when the layer thickness exceeds 1.5 m. Jiang and Wang (2015) noted that there is an exponential relationship between the fracture density of the rock layer and its thickness. However, most reservoir simulations are based on basic mechanical properties, such as Poisson's ratio and Young's modulus, and do not take into account the effects of reservoir thickness on the fractures.

Therefore, this paper introduces an optimized method for predicting fractures in CBM reservoirs. The proposed method uses surface fractures as boundary constraints to initially simulate the paleotectonic stress field during the critical period of fracture formation. Subsequently, by considering the influence of thickness on the evolution of the coal seam fractures, an optimized fracture prediction model is used to forecast fractures in the $9^{\#}$ coal seam of the established mining area. Finally, based on the fracture prediction outcomes, the sweet spots for CBM development are delineated, thereby establishing a foundation for further exploration and development.

2 Geological conditions and the key period of fracture formation

The geotectonic position of the Laochang area is in the Pu'an-Shizong depression of the Nanpanjiang-Youjiang basin. The Youjiang Basin (Figure 1) is along the southwestern margin of the Upper Yangzi landmass; it is connected to the North Vietnam landmass in the southwest, to the Yinzhi landmass through the Jinshajiang-Maoguishan Suture Belt and Majiang Suture Belt, and to the Qinzhou Suture Belt in the southeast. The basin is bounded by the Mile-Shizong Fault in the northwest and Ziyun-Luodian Fault in the northeast. Inside the basin, the northwest Baise-Longlin Fault and northeast Nanpanjiang Fault are developed.

2.1 Stratigraphy and coal-bearing strata of the study area

In the Laochang area, the strata exposed from oldest to youngest include the Permian system: Maokou Formation (P_2m), Longtan Formation (P_3l), and Changxing Formation (P_3c), the Triassic system: Kaiyuan Formation (T_1k), Feixianguan Formation (T_1f), Yongning Formation (T_1y), and Gejiu Formation (T_2g), as well as the Quaternary system (Q). The distribution of outcrops is controlled by the structural influences of the Laochang anticline, with the exposed strata becoming progressively older toward the core of the anticline. The Upper Triassic strata are missing, and only the Wailu Formation is in direct contact with the Quaternary unconformity in the area.

The coal-bearing strata in the Laochang area belong to the Upper Permian Longtan Formation (P_3l) and Changxing Formation (P_3c). The Longtan Formation is divided into upper and lower parts, with the main exploitable coal seam $9^{\#}$ being concentrated in the upper part; its thickness ranges from 0 to 17.53 m, and the total exploitable thickness is approximately 18.46 m. The lower part of the Longtan Formation is dominated by tuff, sandstone, shale, and coal seams. The Changxing Formation contains the main recoverable coal seam $6^{\#}$ with a single-layer thickness of 0–6.65 m and total recoverable thickness of approximately 8.97 m; it is in conformable contact with the base of the Longtan Formation. The present study focuses on the $9^{\#}$ coal seam of the Longtan Formation.

2.2 Tectonic features of the study area

The Laochang area is surrounded by the Baise-Longlin Fault, Nanpanjiang Fault, and Mile-Shizong Fault, which divide the South China landmass from the Yangzi landmass. Moreover, there are ancient uplifts between the fa zones located near the Laochang and Dashuijing areas. Owing to the ancient uplifts, the area surrounding Laochang has developed interspersed dome and basin structures; arcuate structures parallel to the boundaries of the uplift are also formed near the margins (Figure 2). For instance, an arcuate fault zone developed in the southern part of the Laochang area, while the northern and western parts formed the

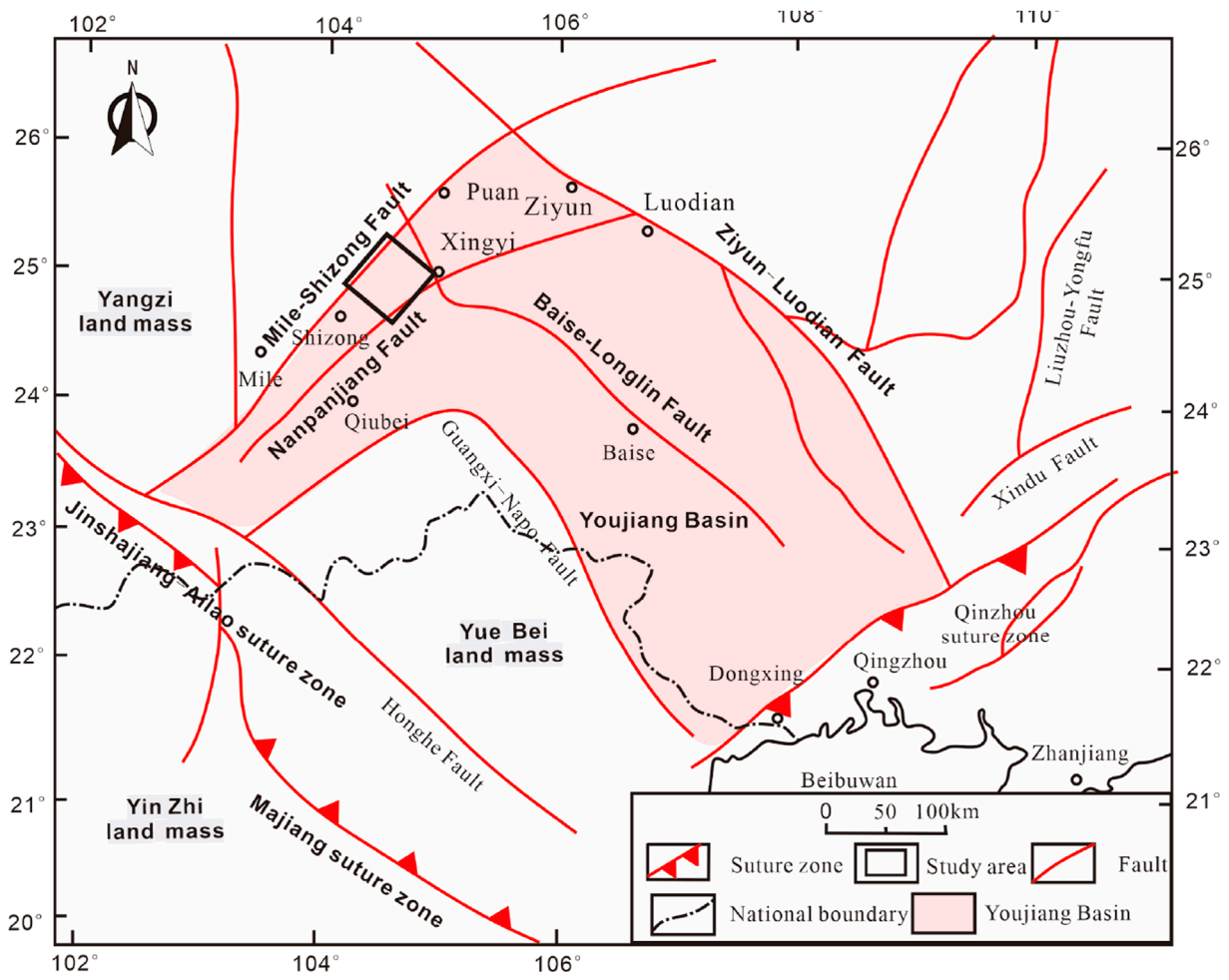

FIGURE 1
Tectonic outline of the Youjiang Basin (Gui and Wang, 2000).

Dehei-Qingkou arcuate compressional deformation belt. The central part features a rhombic dome, the eastern part has a clockwise rotating pivot structure, and the northern part has a series of extensional faults (Wang, 2007).

During the Indosinian movements, the southern part of the Nanpanjiang Fault was extruded by NNW-SSE stresses, and these stresses changed to NW-SE on the northern side of the fault. At the same time, owing to the existence of the Dashuijing ancient uplift, folds were formed parallel to the Nanpanjiang Fault and boundary of the Dashuijing ancient uplift, which then compounded to form the arcuate structures of the Tsuiyang Fault and Xiaolajia Fault. Thus far, the main tectonic framework of the study area was formed under the influence of the Indosinian stress field. During the Early and Middle Yanshanian periods, the study area was subjected to NE-SW compressive stress; during the Late Yanshanian period, the study area was in a NWW-SEE tensile environment; during the Himalayan period, the area was transformed into an EW extensional stress environment, which further modified the tectonics of the study area (Guo et al., 2004).

2.3 Characteristics of fracture development and the key period of formation

Owing to weak tectonic deformations in Yuwang and its surrounding area, the recovered paleo stress field based on the statistical fracture data is more credible. In addition, the fractures in the study area are predominantly conjugate shear joints, which are conducive to restoring the paleo stress field. Using the stereographic projection method, the original orientations of the structural fractures in the horizontal state of the rock layer were restored. Based on the corrected fracture data, a contoured equal-area projection map was drawn to determine the dominant orientations of the conjugate structural fractures.

To investigate the fracture development in the study area, we selected 19 outcrops to calculate the orientations and density of fractures from different formational episodes to reconstruct the principal stresses individually. The results show that the fractures in the study area experienced three stages of tectonics in different

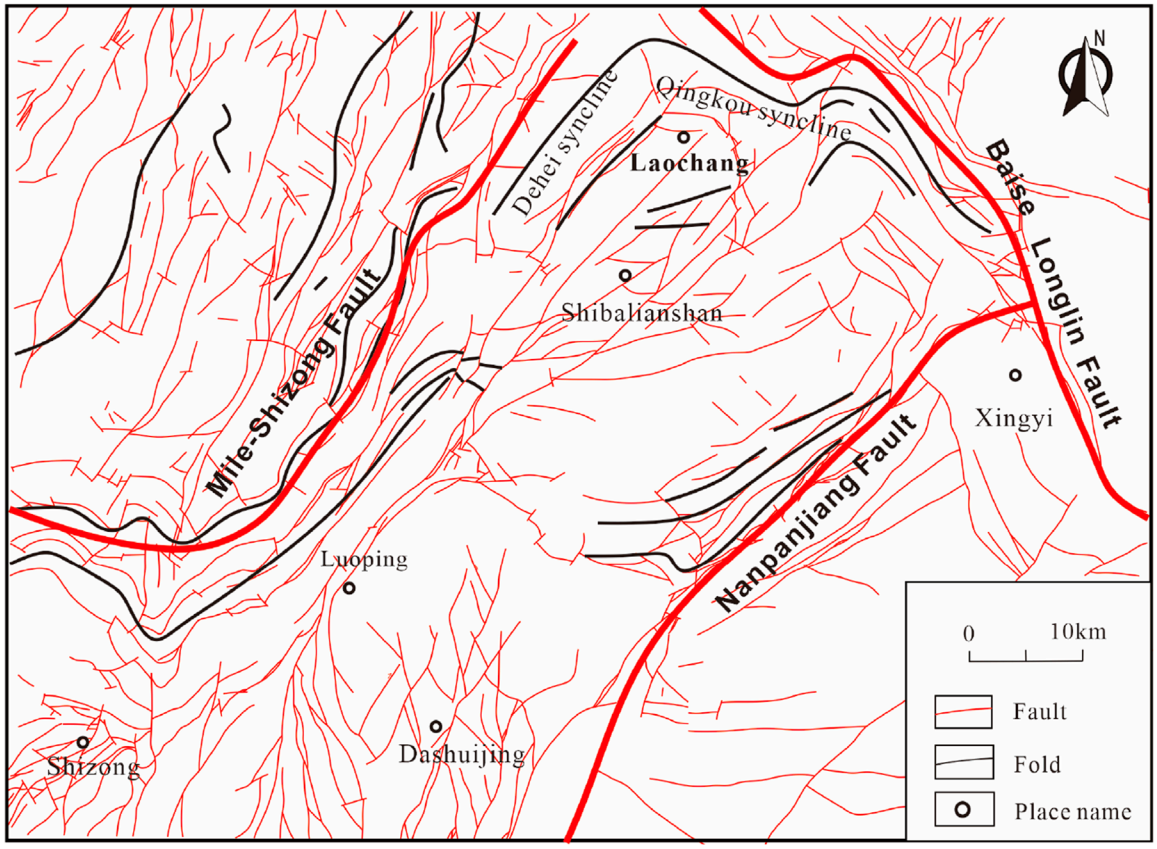

FIGURE 2
Tectonic outline of the Laochang area.

directions. The statistical results indicate that a total of 12 outcrop fracture measurement points predominantly show development of the NW-NNE fractures, and the maximum compressive stresses recovered in the NNW-SSE direction, which belongs to the Indosinian period (Figure 3). Three of the field outcrop fracture measurement points focus on the development of the NNW-NEE fractures, and the maximum compressive stresses are in the NW-SE direction, which belongs to the Early and Middle Yanshanian periods. Four of the fracture measurement points show dominant fractures developing in the NE-NWW direction, with the maximum compressive stresses being in the NEE-SWW direction, belonging to the Himalayan period (Figure 3). Obviously, the Indosinian fractures account for a higher proportion in the study area, and it is assumed that the tectonic stresses of the Indosinian movements have the greatest influence on fracture formation in the study area.

For instance, at the 92404 fracture point (Figure 4), the Feixianguan Formation is exposed with yellowish-brown thin-bedded silty fine sandstone. The strike and dip of this formation is 130°∠10°, indicating a relatively gentle stratification with the development of two sets of fracture systems. The fracture dip is significant and nearly perpendicular to the stratum. The first set of conjugate shear fractures trend NW and NNE, indicating NWW-SSE compressional stress from the Indosinian period; the second set of conjugate shear fractures trend SWW and NNW, indicating NW-SE compressional stress from the Yanshanian period.

3 Fracture prediction principles

In this paper, fracture development in the surface rock layers was taken as a constraint, and ANSYS finite element simulation software was used to invert the paleotectonic stress field during the critical period; then, the fracture density computation model was used to predict the density and orientation of the fractures by taking the rock layer thickness into account. Thus, it is necessary to first clarify the mathematical theoretical model of stress on the density and orientations of the fractures.

3.1 Relationship between fracture density and stress

Fractures are formed when the rock stress approaches or exceeds its ultimate strength, such that the internal binding force of the rock is damaged and the rock is no longer integral, thus producing deformations of various sizes. Accordingly, fracture deformations can be described as local responses of the rock to applied stress. According to the Mohr–Coulomb model of fracture strength, each rock variety has its own inherent shear strength τ_0. Under the premise that all other conditions remain unchanged, τ_0 is a constant. For a given cross section of the rock, when the applied shear stress reaches or exceeds τ_0, shear fractures may be formed along the

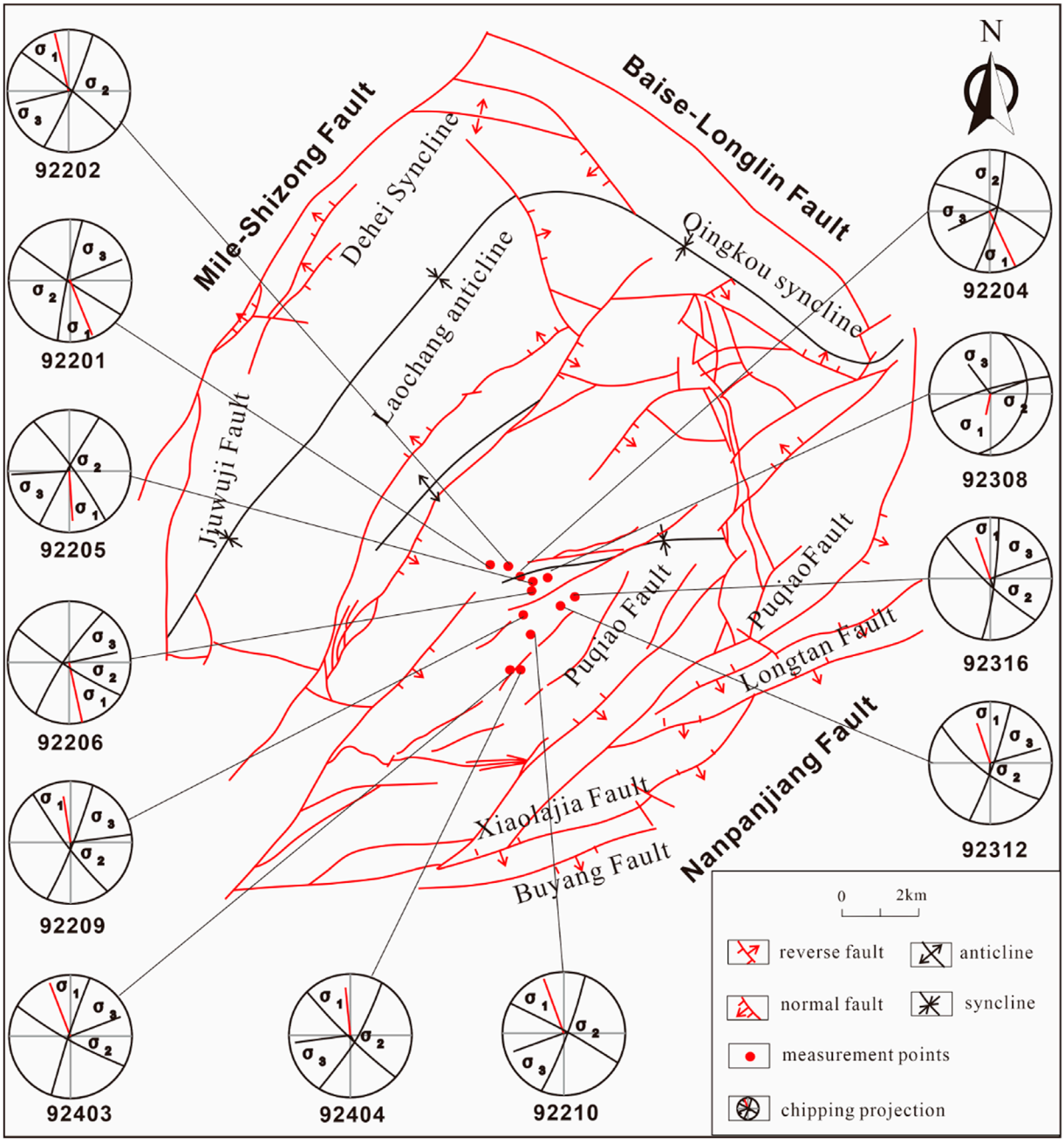

FIGURE 3
Tectonic outline and conjugate joint stress analysis diagram of the Laochang area.

section. Wang (2007) established the following equation set based on energy conservation (Figure 5):

$$\begin{cases} W_f = \dfrac{1}{2E}\left(\sigma_1^2 + \sigma_3^2 - 2\mu\sigma_1\sigma_3 - 0.85^2\sigma_p^2 + 2\mu\sigma_3 0.85\sigma_p\right) \\ \sigma_p = \dfrac{2C_0\cos\varphi + (1+\sin\varphi)\sigma_3}{1-\sin\varphi} \\ W_f = D_{vf}(J_0 + \sigma_3 b) \\ D'_{lf} = \dfrac{2D_{vf}L_1L_3\sin\theta\cos\theta - L_1\sin\theta - L_3\cos\theta}{L_1^2\sin^2\theta + L_3^2\cos^2\theta}, \end{cases} \quad (1)$$

where W_f is the energy dissipated during loading; considering that the energy dissipated as elastic waves is negligible, the loading energy denotes the power consumed during fracture formation (J/m^3). Furthermore, E is the elastic modulus of the rock stratum (GPa); σ_1, σ_2, and σ_3 are the external stress values (MPa); μ is the Poisson's ratio of the rock stratum; C_0 is the cohesive force representing the shear strength in the event that $C_0 = 0$ (Pa); φ is the internal friction angle (°); J_0 is the surface energy of the fractures when the corresponding confining pressure is zero (J/m^2) and is equivalent to the surface energy of the fractures obtained by uniaxial compression testing; D_{vf}

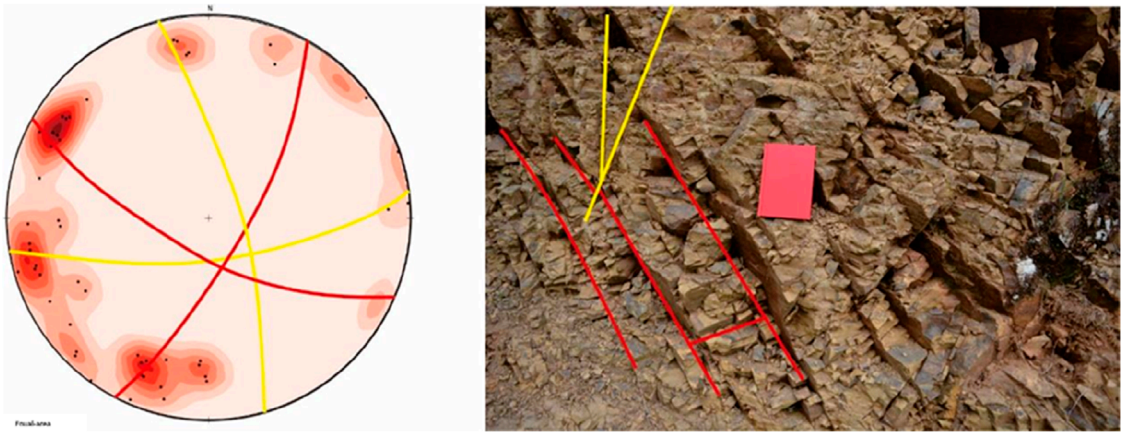

FIGURE 4
Equal density map of the 92404 fracture joint and its field development conditions.

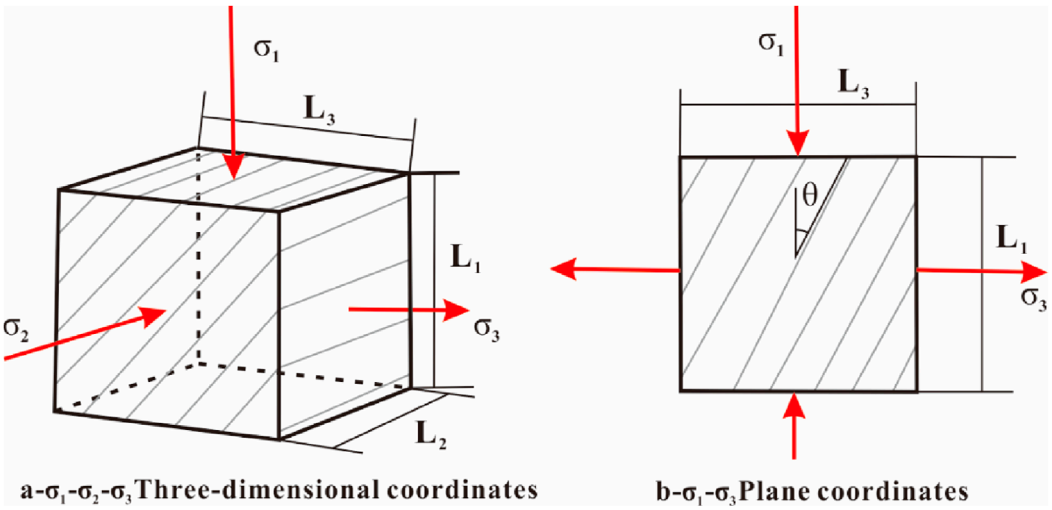

FIGURE 5
Relationships between the parameters and stress for fractures within the representative elementary volume (Wang, 2007).

is the ratio of the total surface area of the fractured rock mass to its representative elementary volume and represents the volume density of the fractures within the representative elementary volume; b is the fracture aperture; σ_p is the rock breakdown pressure (MPa); θ is the rupture angle of the rock fractures (°) and is defined as the angle included between the fracture surface and σ_1; L_1 and L_3 refer to the respective rock lengths in the directions of σ_1 and σ_3 (m).

The confining pressure impedes fracture formation as the energy accumulated in the rock needs to overcome the intrinsic cohesion due to the intermolecular forces as well as the confining pressure to experience lithological disruption and form a fracture. The surface energy of the fractures is a combination of the effects of the intrinsic properties of the rock and pressure impediments to fracture formation. According to the theory of maximum strain energy density and maximum tensile stress in brittle fracture mechanics, brittle materials like rocks fracture when the rate of release of the elastic strain energy accumulated in the material is equal to the amount of energy required to produce a unit area of the fracture surface. Therefore, the following energy equation is established:

$$W_f = D_{vf}(J_0 + \sigma_3 b) \tag{2}$$

Adopting the fracture bulk density to describe the fractures comprehensively reflects the fracture information and is less affected by the size of the unit; however, this is not conducive to the study of fractures in coal reservoirs. In fracture research, emphasis is placed on the fracture trace density (or fracture spacing), which refers to the number of fractures per unit length (with fracture spacing being the reciprocal of the fracture line density). Consequently, it is necessary to establish a formula for the fracture line density.

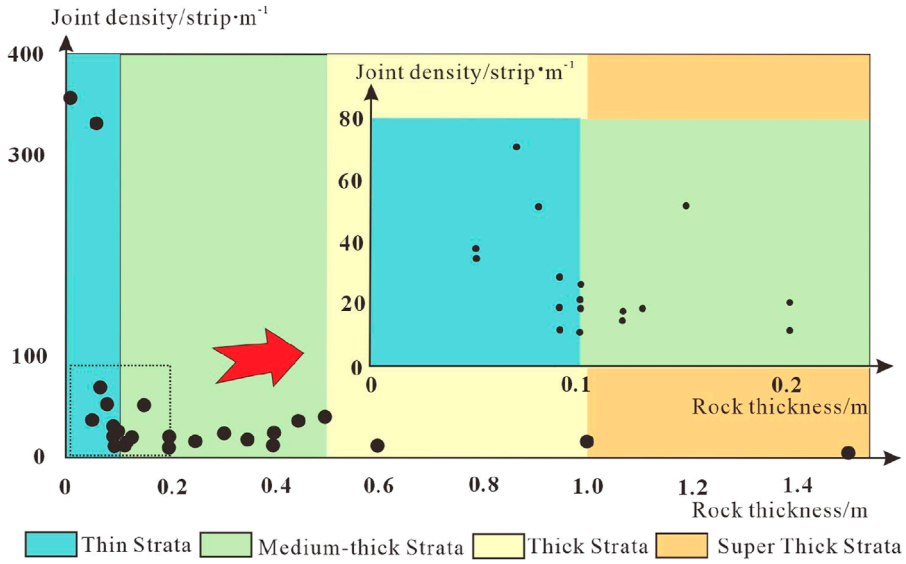

FIGURE 6
Relationship between stratum thickness and fracture density.

In particular, the volume and trace density of the fractures can be converted as follows:

$$D'_{lf} = \frac{2D_{vf}L_1L_3 \sin\theta\cos\theta - L_1\sin\theta - L_3\cos\theta}{L_1^2 sin^2\theta + L_3^2 cos^2\theta}. \quad (3)$$

According to Equation 3, there is no necessary relationship between the fracture line density and stratum thickness. However, Jing et al. (2014) and Wang (2014) believed that there is a negative power function relationship between the two variables. When the rock stratum is thin (thickness: <10 cm), the stratum thickness has the most significant influence on fracture line density. When the rock layer is medium-thick (thickness: 10–50 cm), the influence of the formation thickness on the stratum declines rapidly. In some areas, the fracture density may increase abnormally under the influence of tectonics. If the stratum is thick or superthick, the fracture line density is comparatively low and tends to be stable. The fracture data compiled from previous field outcrop observations show a similar negative power function relationship between the fracture line density and stratum thickness (Figure 6).

Wang (2007) proposed a model that does not consider the effect of thickness on the fracture line density; here, it was considered that the depth of the fracture formed under stress is greater than the rock thickness, i.e., the fractures extend throughout the model. However, during fracture formation, although some of the microfractures eventually extend throughout the model to form fractures, there are still numerous microfractures with depths less than the rock thickness that are unable to penetrate the entire model or can only form small fractures inside the rock. During actual measurements, such fractures are not counted, resulting in lower measured fracture line density values.

In addition, owing to the non-homogeneous nature of the rock, there are bound to be differences between the fractures in the homogeneous model and those in the actual rock. This means that under stress, the lengths of the fractures formed by interconnected microfractures in the direction of σ_2 will be different, resulting in some of the fractures failing to penetrate the model. To solve this problem, we consider that the non-homogeneous regions in the rock are distributed more randomly. In this case, the lengths of the fractures in the direction of σ_2 are normally distributed (Figure 7).

For rocks of thickness h, fractures with lengths greater than h in the σ_2 direction were successfully observed in the field. However, fracture lengths less than h are developed inside the rock, making it difficult to observe them visually. Therefore, the measured fracture density can be expressed by the following equation:

$$D_{lf} = D'_{lf} \times \int_h^{+\infty} \frac{1}{\sqrt{2\pi}\alpha} e^{-\frac{(l_2-l_0)^2}{2\alpha^2}} dl_2, \quad (4)$$

where l_0 is the fracture length along σ_2 under homogeneous conditions, and l_2 is the measured length in the same direction. Moreover, both α and l_0 are subjected to the actions of rock stratum lithology and stress, whose specific values should be determined according to the physical conditions of the specific areas. In this scenario, the relationship between the fracture line density and stress can be expressed by the following equation set:

$$\begin{cases} w_f = \frac{1}{2E}\left(\sigma_1^2 + \sigma_3^2 - 2\mu\sigma_1\sigma_3 - 0.85^2\sigma_p^2 + 2\mu\sigma_3 0.85\sigma_p\right) \\ \sigma_p = \frac{2C_0\cos\varphi + (1+\sin\varphi)\sigma_3}{1-\sin\varphi} \\ w_f = D_{vf}(J_0 + \sigma_3 b) \\ D'_{lf} = \frac{2D_{vf}L_1L_3\sin\theta\cos\theta - L_1\sin\theta - L_3\cos\theta}{L_1^2\sin^2\theta + L_3^2\cos^2\theta} \\ D_{lf} = D'_{lf} \times \int_h^{+\infty} \frac{1}{\sqrt{2\pi}\alpha} e^{-\frac{(l_2-l_0)^2}{2\alpha^2}} dl_2. \end{cases} \quad (5)$$

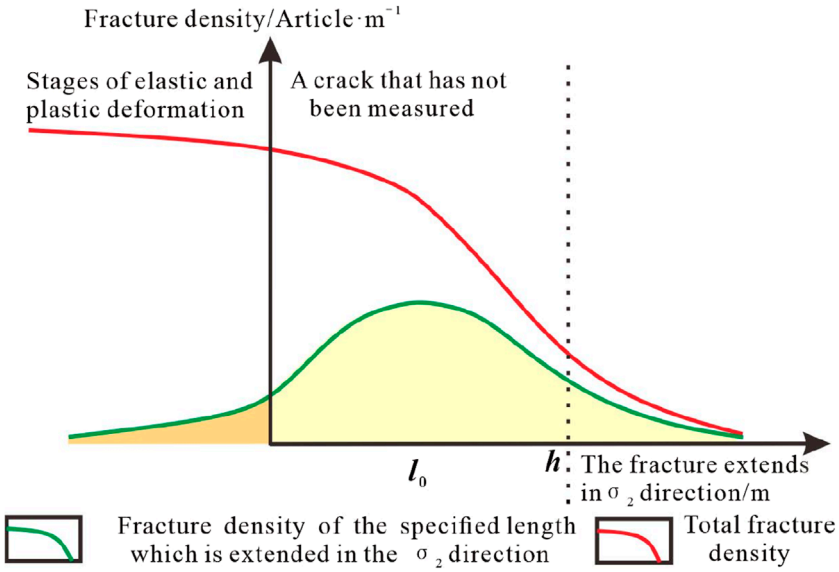

FIGURE 7
Schematic illustration of the fracture lengths.

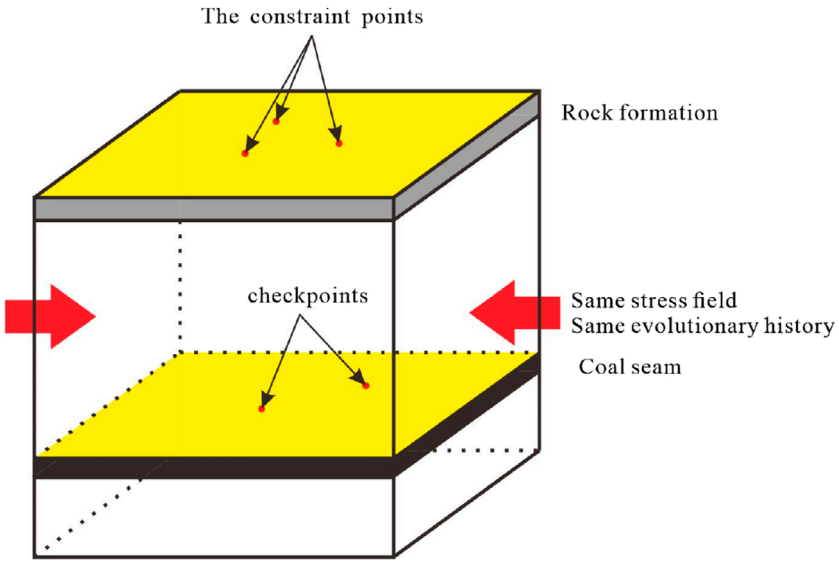

FIGURE 8
Fracture development prediction model for coal reservoirs.

Theoretical analysis results were compared with the field survey outcomes, and it was found that the expected value of the fracture length along σ_2 was rather small for fractures formed inside the rock. In actual field conditions, it is less likely for the rock thickness to be less than the corresponding expected value. Consequently, a relationship similar to the negative power function exists between the stratum thickness and measured fracture density. Thus, the expected fracture lengths may be set to 0 in the σ_2 direction.

3.2 Relationship between fracture orientation and stress

Based on the Mohr–Coulomb shear fracture criterion, an angular bisector of the conjugate fractures is in the stress direction. If the stress direction is known, we only need to acquire the rupture angles of the coalbed fractures under stress to roughly predict the orientations of the coal reservoir fractures. Based on long-term geological research, Ramsay (1980) proposed that the conjugate shear angle is variable, i.e., it can be less or more than 90°.

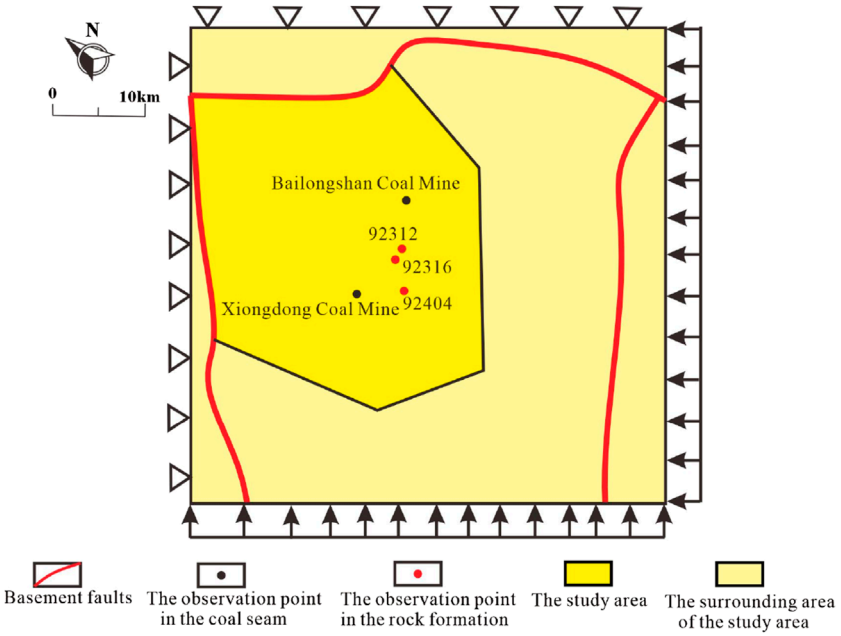

FIGURE 9
Schematic illustration of the coal reservoir fracture development prediction model for the Laochang area.

TABLE 1 Rock mechanical parameters of the Laochang area for numerical simulation.

Element name	Density (kg/m^3)	Young's modulus (GPa)	Poisson's ratio
Siltstone	2,800.00	4.00	0.30
Fault zone of the rock stratum	2,000.00	0.80	0.34
Coal seam	1,350.00	3.00	0.30
Fault zone of the coal seam	1,000.00	0.60	0.34

However, according to the Cullen–Moore rupture criterion, there are no rupture angles larger than 90° or that such angles larger than 90° cannot be expressed mathematically. Although the relationship between the conjugate shear angle and confining pressure can be expressed by envisioning the ultimate stress Moore envelope as a parabola, when the conjugate shear angle is close to 90°, the field measurement is at 0.5°, and the error of the derived pressure reaches several orders of magnitude. Later, Lin (1993) improved this method by replacing the parabola with an ellipse to better represent the relationship between the conjugate shear angle and confining pressure. Accordingly, Lin (1993) proposed an ellipse parameter t as follows:

$$t_0 = \arctan\left[sin\left(\frac{\varphi}{2}\right)\tan\left(90° - \varphi\right)\right], \tag{6}$$

$$t = \arctan\left[\sin\left(\frac{\varphi}{2}\right)\tan\left(V\right)\right]. \tag{7}$$

When $V = 90°$, $t = 90°$. Then, the shear strength of the rock can be expressed as

$$\tau = \left|\frac{4C_0 \sin\left(t\right)}{\sin\left(\varphi\right)\sin\left(t_0\right)}\right|. \tag{8}$$

By substituting Equations 6, 7 into Equation 8, i.e., the measured values of shear strength and cohesive force of the rock, the theoretical value of the rupture angle can be obtained. Thus, under the premise of a known stress direction, the fracture orientation can be clarified.

4 Coal reservoir fracture prediction

Fractures formed under the influence of tectonic stress exhibit a spatial distribution and an evolutionary development dictated by the regional tectonic stress field. Research on fracture formation and distribution in the Laochang area show that the fractures are formed under the control of lithology and tectonic stress as well as the influence of rock stratum thickness. The tectonic stresses exerted on rock strata and coal reservoirs are consistent to a certain

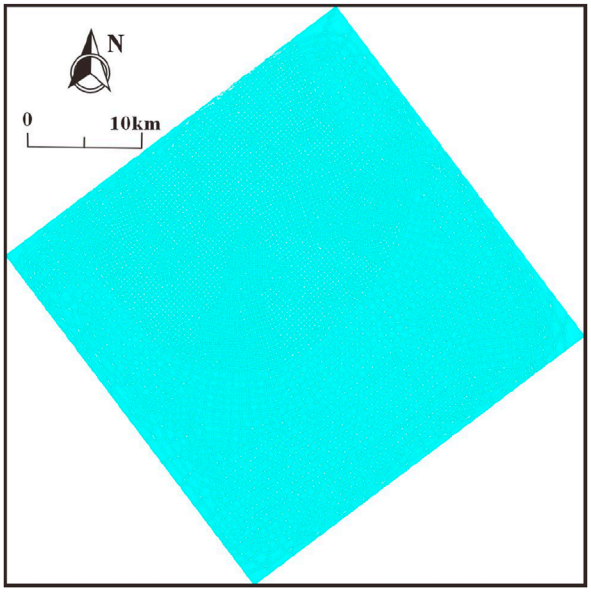

FIGURE 10
Mesh generation diagram for the Laochang area.

extent. Thus, ANSYS finite element numerical simulations were conducted to establish a prediction model by placing the coal reservoir and a certain thickness of the rock layer in the same stress field. Field measurements of the fracture density values of the outcrop rock layers and surface structural characteristics were adopted as constraints to fulfill the equivalent stress inversion during the critical period of fracture formation in the study area. Hence, the overall fracture development and distribution rules can be predicted for the coal reservoir in accordance with the distribution of the surface fractures. Subsequently, by incorporating the thickness of the simulated coal seam stratigraphy from the study area in the mathematical model, it is possible to obtain the predicted fracture density distribution within the coal reservoir that closely matches the actual measured fracture density (Figure 8).

4.1 Prediction model

The construction of the prediction model entails building a unified geometric model, building the model, and mesh generation.

4.1.1 Unified geometric model

Since the formation of the Permian coal measures, the Laochang area primarily experiences tectonic movements due to Indosinian, Yanshanian, and Himalayan influences. As observed from the field fracture measurement data and principal stress restoration results, the Indosinian period is the critical stage of fracture formation; therefore, we consider it as the target period for this simulation. However, stresses in the Laochang area during the Indosinian period vary in both direction and magnitude, which is not conducive to the establishment of the model. Hence, the model scope was extended to the southern district of the Laochang area. In this case, the entire model roughly covers places from the Laochang ancient uplift to the northeastern boundary of the Dashuijing ancient uplift. Based on the geological evolution of the Laochang area, the model is initially simplified by removing the structures formed during and after the Indosinian period while retaining only the basement structures that existed before. Finally, to facilitate stress loading, the model was rotated to generate a simulation model for the Laochang area (Figure 9).

The stresses should be applied so that they are maximally consistent with the actual scenarios. During the Indosinian period, the closure of the Mayang River and Qinzhou remnant troughs almost created a south–north stress, but the study area was influenced by the Nanpanjiang Fault such that the direction of stress shifted to NNW-SSE. This result is consistent with the stress recovery results from the fractures in the field. According to the tectonic framework surrounding the Laochang area, the Dashuijing ancient uplift and Nanpanjiang Fault are deemed to be located to the southwest and southeast of this area, respectively. In the actual process of tectonic evolution, different modes of stress attenuation produced different stress strengths and directions near the Laochang area. Based on the structural outline map of the Luoping area, it is inferred that stress along the southeastern boundary of Laochang area is in the northwest direction, and fault zones and folds are densely formed along the Nanpanjiang Fault by the stresses applied directly on it during the Indosinian period. Along the southwestern boundary of the Laochang area, the stresses are almost in the south–north and NNE directions, resulting in simple faults and wide but gentle folds; the reason for this is that the stresses from the Indosinian movements act on the Dashuijing ancient uplift via the Nanpanjiang Fault and finally affect the Laochang area, which could lead to stress attenuation to a certain extent. Basement faults were found at the northwest and northeast boundaries of Laochang area. Therefore, the stress status of the surroundings for the model is designed as follows. In addition to inward extrusion along the ancient uplift boundary, the southeastern stress is far greater than the southwestern component. Moreover, the displacements of the basement faults remain unchanged. The rock mechanical parameters of the Laochang area are obtained experimentally from the collected samples (Table 1).

4.1.2 Model construction

Transformation from a geometric to geological model was realized by attaching the rock mechanical parameters representing the properties of different units to the geometric model. In combination with the results of the field geological survey, the siltstone of the Feixianguan Formation exposed in the Laochang area was selected as the reference stratum. Based on the rock mechanical experiments, the Young's modulus and Poisson's ratio that represent the mechanical properties of the rock were included with the original model to establish the geological model for siltstone in the Laochang area.

Once the geological model is constructed, the unit model must be selected. Generally, for the 3D geological model, PLANE183 is selected as the basic unit in the finite element analysis.

4.1.3 Mesh generation

Given the complex geological conditions, the automatic mesh division methods available in simulation software cannot accurately

TABLE 2 Measured data processing to predict fracture density in the Laochang area.

Lithology	Measured fracture density (lines/m)	Thickness (m)	Predicted total fracture density (lines/m)	SD	Probability	Normal probability	Absolute difference
Siltstone	19.00	0.35	40.00	2.00	0.48	0.43	0.0445
	19.00	0.09	40.00	2.00	0.48	0.48	0.0071
	19.00	0.10	40.00	2.00	0.48	0.48	0.0051
	18.00	0.12	40.00	2.00	0.45	0.48	0.0261
Coal seam	78.00	1.20	290.00	1.36	0.27	0.19	0.0802
	30.00	1.70	290.00	1.36	0.10	0.11	0.002

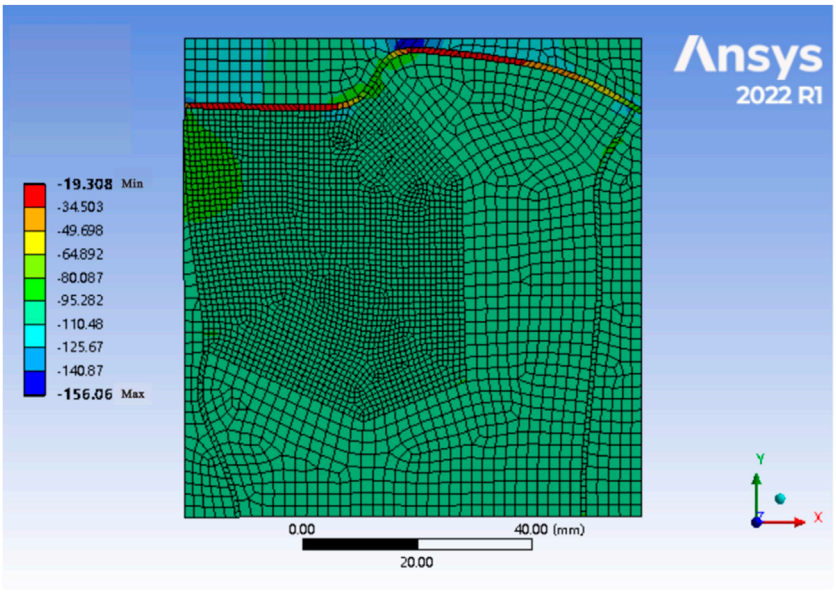

FIGURE 11
Simulation results of the maximum principal stress in the study area.

represent the complex geological structures and lithologies. However, manual mesh division can take into account different material properties. During mesh division, rock bodies with different material properties should be categorized with different units, and the parts wherein the rock properties vary should be refined using a denser mesh where appropriate. It is also important to avoid the use of obtuse angles within the units. Concurrently, the special characteristics of the strata and structures must be considered to determine the combination of units and specific division method to be employed. In accordance with mesh generation principles, quadrilateral meshes were primarily adopted in this work. Specifically, the geological model of the entire research area was divided into 5,609 elements and 18,925 nodes to reflect the geological tectonic characteristics of the main research area (Figure 10).

4.1.4 Data selection and processing

The data from field measurements are first screened, and the fracture points from the Indosinian period are selected and classified according to lithology. Then, the variance of the fracture density in the mathematical formula is calculated based on the relationship between the rock layer thickness and fracture density (Table 2).

4.1.5 Mechanical model

Using the generated mesh, the boundary conditions of the stress field were loaded for the study area to realize conversion from a geological model to a mechanical model. In addition to applying appropriate stresses along the bottom and right-side boundaries of the model, constraints were imposed on the model boundaries adjacent to the Mile-Shizong Fault and Baise-Longlin Fault to restrict displacement of the basement faults.

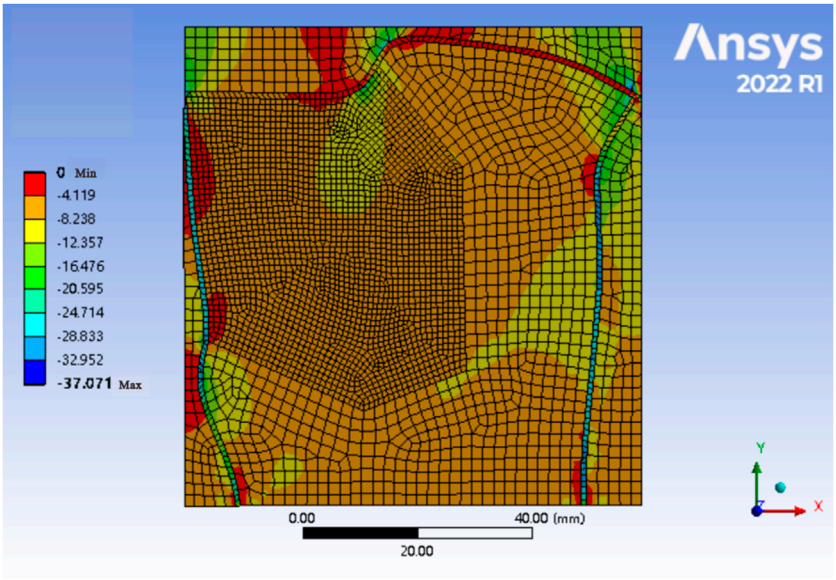

FIGURE 12
Simulation results of the minimum principal stress in the study area.

As seen from the previous paleo stress measurements from the vicinity of the research area, the corresponding differential stress was designed as approximately 100 MPa. By applying stresses to the boundaries along the sides of the model, the stress distribution was obtained for the research area, followed by calculation of the fracture density predicted using the constrained points. Then, the calculated and measured fracture density values were compared, and the errors between them were further analyzed. Finally, the stress magnitudes along the sides were adjusted according to the experimental findings. By ensuring that the differential stress magnitudes remained roughly unchanged, the above procedures were repeated until the predicted fracture density of the surface was maximally similar to its measured value.

Error analysis was performed based on the relative errors calculated as follows:

$$R = \frac{|\text{Measured Joint Density} - \text{Predicted Joint Density}|}{\text{Measured Joint Density}} \times 100\%, \quad (9)$$

where R is the relative error.

Considering that the fracture densities measured during the field survey may have errors, especially when the values at the observation points are rather low, the relative errors may greatly inconvenience the overall error analysis. Hence, absolute error is introduced to support the error analysis as follows:

$$r = |\text{Measured Joint Density} - \text{Predicted Joint Density}|, \quad (10)$$

where r is the absolute error.

The fracture density was calculated using the simulation results of the maximum and minimum principal stress values under varying stress conditions (Figures 11, 12). Under the condition that the extremal stress values are 8 MPa and 100 MPa, the predicted fracture density calculated by using Equation 5 is slightly different from the measured value with respect to the constraint points. Specifically, the relative errors are all below 9%, and the absolute errors are less than 2 fractures per meter, which are calculated by using Equations 9, 10.

4.2 Prediction results

By modifying the mechanical parameters of the surface geometric model as well as lithological parameters used in the calculations, it is possible to perform a forward modeling of the structural evolution of the coal reservoir by substituting the thickness of the coal seam at each point in Equation 4. This allows the simulation and prediction of the fracture density as well as fracture orientations within the coal reservoir.

4.2.1 Fracture density distribution prediction

Using the self-programmed command flow, all node coordinates and stress values of the paleo stress field simulation results were extracted, and the fracture density prediction was calculated using Equations 1–3. Finally, the node coordinates and predicted fracture density were imported into Surfer to draw the contour map of the overall fracture density of the coal reservoir (Figure 13). Xiao (2017) reported that the overall fracture density in the Laochang area is mainly controlled by large-scale boundary faults and ancient uplifts, while the local fracture density anomalies are influenced by different tectonic combinations in the area. Based on the current results from the paleo stress field study on the key period of fracture formation in the study area, we note that Laochang and its surrounding areas were subjected to NNW-SSE stresses during the Indosinian period, which resulted in bidirectional lateral extrusion stresses perpendicular to the boundaries of the Nanpanjiang Fault and Dashuijing ancient uplift. Thus, the fracture density in the study area gradually decreases from the southeast to northwest direction.

The findings of previous studies regarding the thickness of the 9# coal seam in the study area (Figure 14) were applied as the thickness

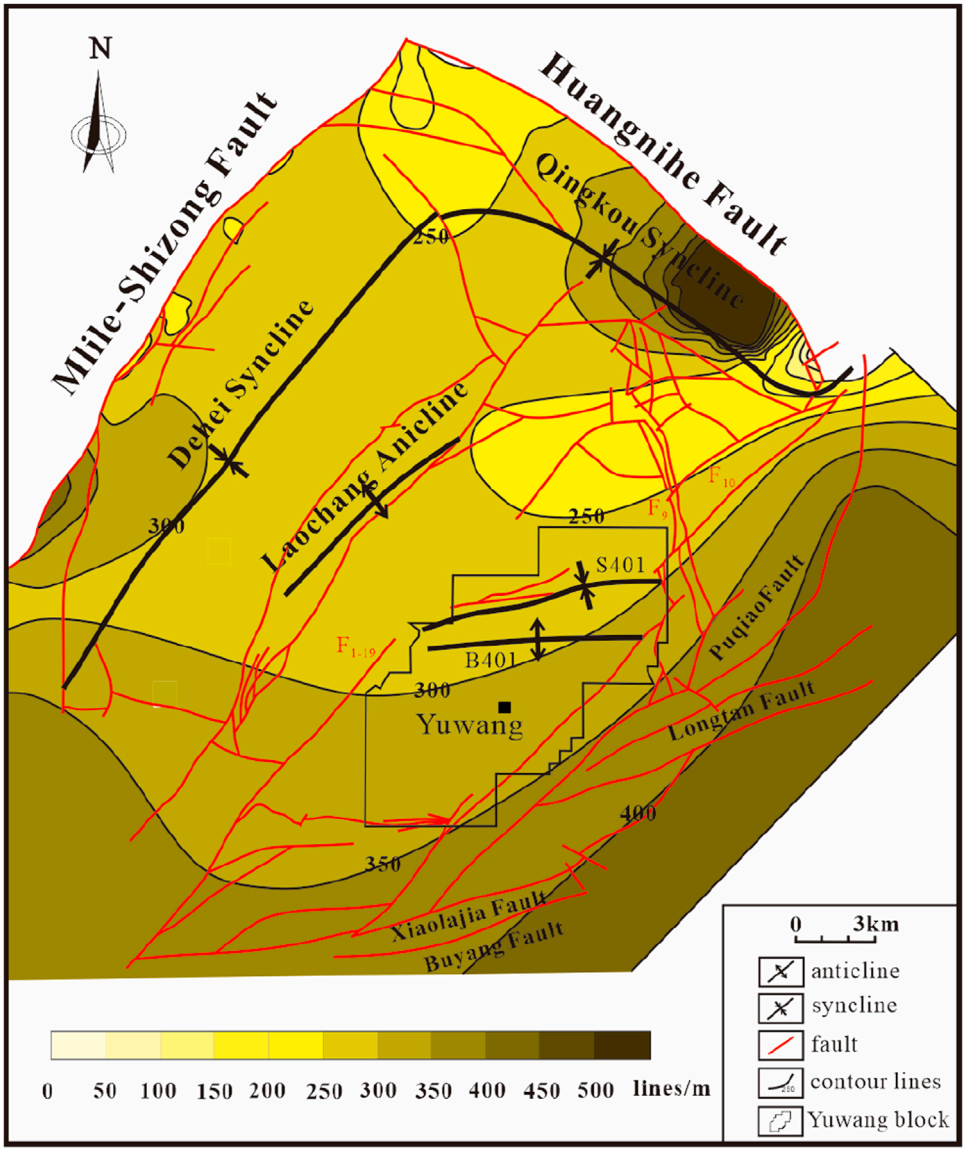

FIGURE 13
Contour map of the predicted fracture density for coal reservoirs in the Laochang area without considering stratum thickness.

parameter values in the fracture mathematical model to calculate the fracture density using Equation 4; then, the measured fracture density contour map of the coal reservoir was obtained using the contour map of its total fracture density as well as the contour map of the thickness of the 9# coal seam (Figure 15). Comparing the measured and calculated fracture densities after considering the effects of thickness, the relative error in fracture density is less than 13% (Table 3), which indicates that the predicted results have a certain degree of confidence. According to the results, the number of fractures measured in the coal reservoir in the Laochang area mostly ranges from 10 to 20 per meter, while some regions may have up to 80 fractures per meter or above. Under tectonic influence, the fractures in the Laochang area have a higher distribution density in the south than in the north as well as higher density in the west than in the east. Owing to the impact of thickness, fractures are mainly developed in the east of F_{1-19} as well as other places next to B_{401}, F_9, and F_{10}, where the coal seams are rather thin. The fracture density of the coal reservoir in the Yuwang block is generally high. In the northern part of the Laochang anticline, rapid increases in the coal seam thickness cause the fracture density to decline rapidly. In some zones, the number of fractures is even as low as 1 per meter.

4.2.2 Fracture orientation prediction

The coordinates of all the nodes and directions of the stress values were extracted using the self-programmed command flow. After simple calculations, the data were imported into Surfer to obtain the statistical results. The predicted stress direction of the coal reservoir in the Laochang area is mostly between 150° and

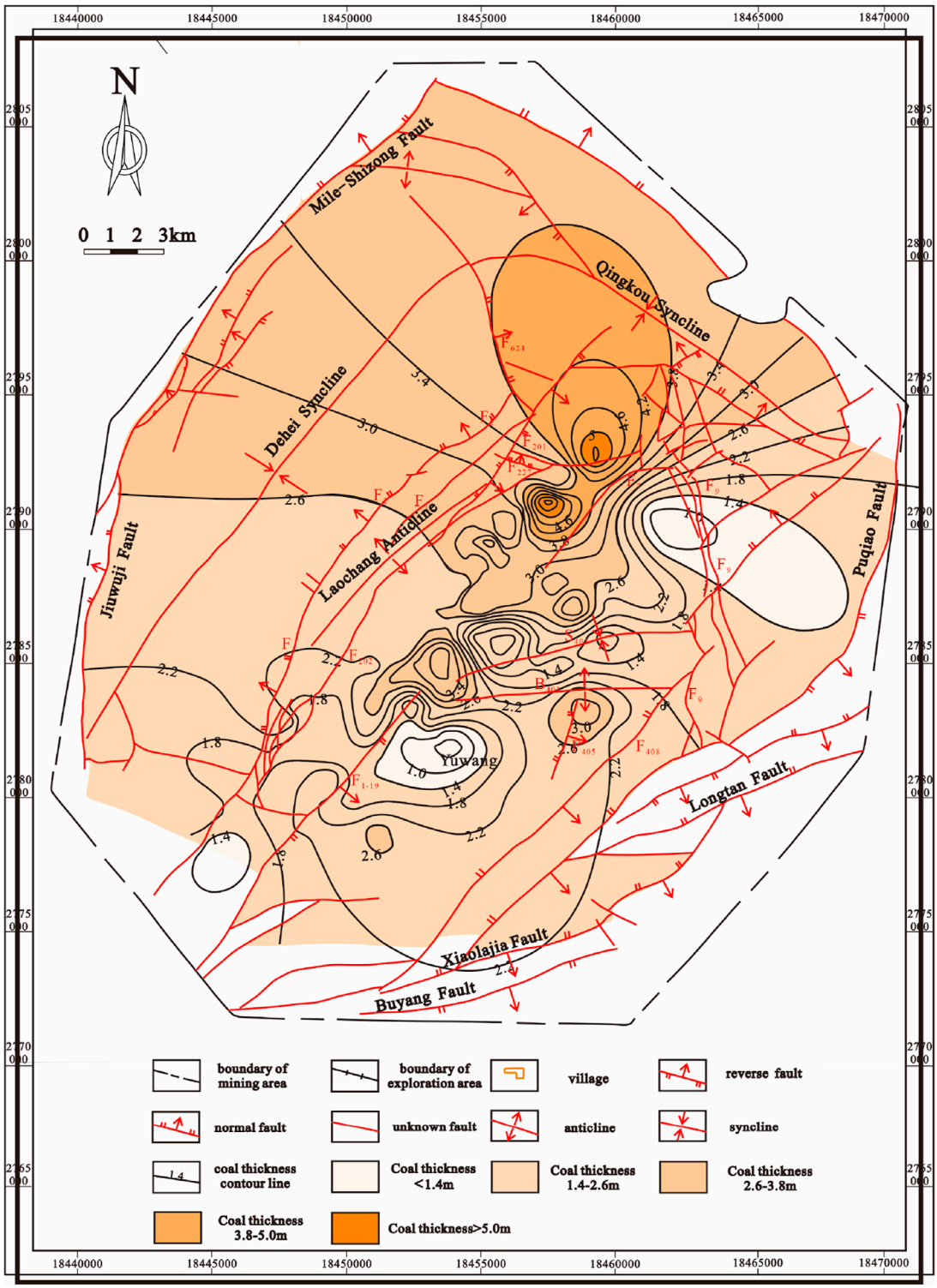

FIGURE 14
The Thickness contour map of the 9# coal seam in the Laochang area (Wang, 2007).

155°. The stress direction is roughly NNW and perpendicular to the Nanpanjiang Fault. Given the presence of basement faults, the stress directions may change perpendicular to such faults. Along the east side of the Mile-Shizong Fault, the stresses move gradually downward from 152° to 150°; in contrast, the stresses near the Baise-Longlin Fault move upward from 152° to 155°.

Based on the stress directions obtained from the simulations and theoretical rupture angles obtained by calculations, the following

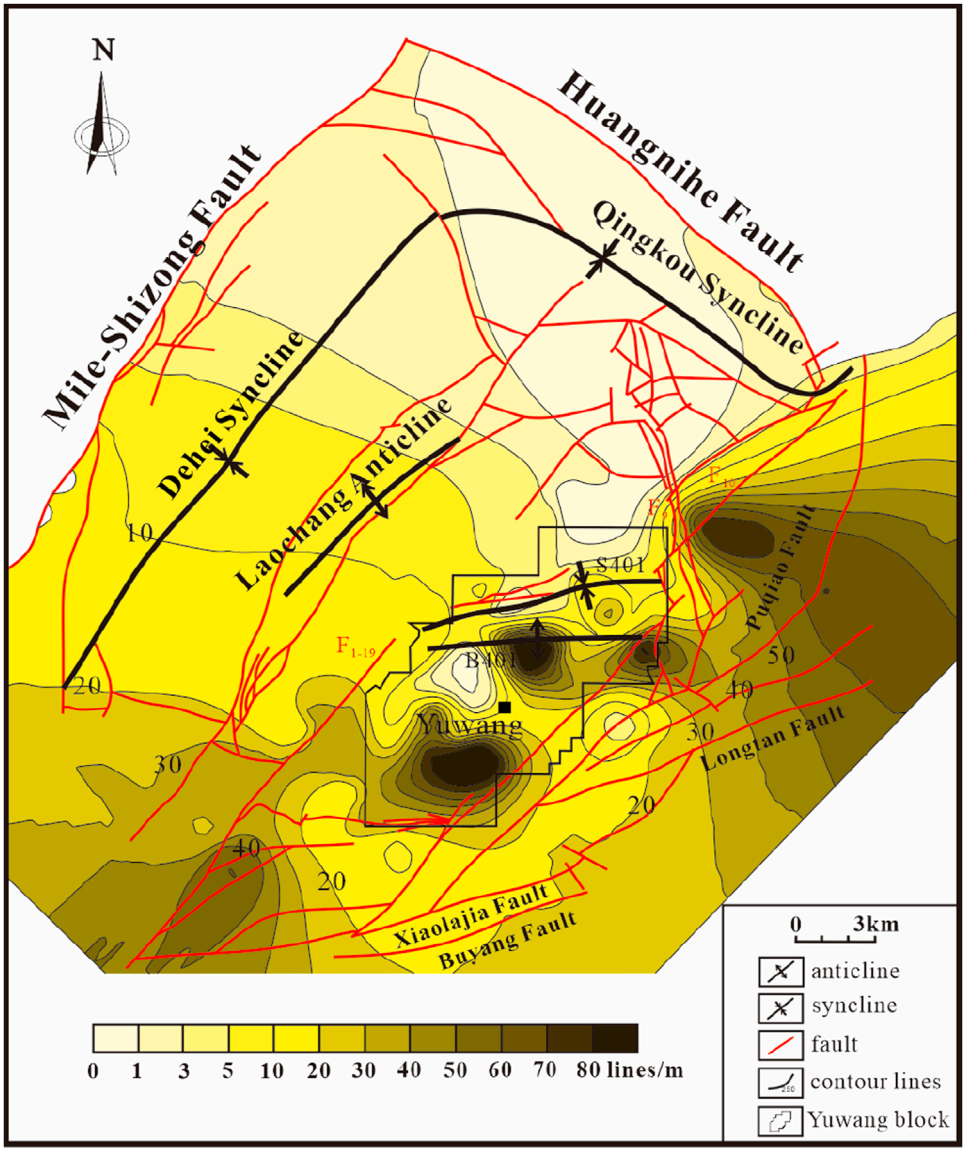

FIGURE 15
Contour map for the predicted fracture density of coal reservoirs in the Laochang area considering stratum thickness.

TABLE 3 Error analysis of the fracture density prediction considering stratum thickness for coal reservoirs in the Laochang area.

Observation point	Thickness of coal seam (m)	Measured fracture density (lines/m)	Predicted fracture density (lines/m)	Relative error (%)	Absolute error (lines/m)
Bailong Mountain coal mine	1.70	30.00	33.81	12.71	2.81
Xiongdong coal mine	1.20	78.00	68.00	12.27	9.57

conclusions can be drawn (Table 4). When the fracture formation in the coal reservoir does not change with progressive deformation or preliminary rupture, two major sets of fractures are developed in the coal reservoir; the fracture strikes from one set are roughly at 193°, while those from the other set are at about 116°. In addition, unusual concentration or changes in the stress direction in the area due to inhomogeneities in the coal and rock can lead to abnormal changes in the direction and density of the fractures. However, the overall tendency for variation should generally be similar to the corresponding predicted outcomes.

TABLE 4 Rupture angles for coal reservoirs in the Laochang area.

Observation point	Fracture set 1	Fracture set 2	Rupture angle	Calculated value of rupture angle	Relative error (%)	Absolute error
Bailong Mountain coal mine	29.00°∠82.00°	315.00°∠81.00°	106.00°	103.19°	1.73	1.81
Xiongdong coal mine	210.00°∠85.00°	135.00°∠81.00°	105.00°	103.19°	2.65	2.81

4.2.3 Sweet spot area optimization

Permeability and gas content are the factors that directly control CBM accumulation (Fang et al., 2005). Although the permeability generally decreases with increasing burial depth, the development of fracture systems in deep coal reservoirs can enhance permeability (Sun et al., 2014); therefore, cleat density is crucial for CBM development. Based on the simulation results presented herein, thicker coal seams tend to have lower cleat densities and lower permeability. The Yuwang Block is characterized by relatively thin coal seams with well-developed cleats and good connectivity, resulting in high permeability. However, excess tectonic stresses can lead to significant deformation of the coal seams and the formation of mylonitic coal, which would reduce permeability (Jiang et al., 2005). The Yuwang Block exhibits a simple geological structure and lacks major faults and folds, suggesting a high potential for CBM. Furthermore, the coal seam thickness is correlated with the gas content, with thicker seams generally exhibiting lower gas content (Qin et al., 2000). Although the Yuwang Block generally has thin coal seams, the presence of small-scale folds in the northern region, particularly within the synclinal structures, has resulted in locally thicker coal seams with well-developed cleats; these represent the areas with the highest potential for CBM development.

Based on previous studies of the present-day *in situ* stress in the Yuwang region, the maximum horizontal principal stress in the Yuwang Block is approximately in the south–north direction (Ju et al., 2020). Previously reported fracture prediction results for the Laochang area within the region indicate that the dominant joint sets are oriented NNE and NEE. One of these joint sets forms a smaller angle with the present-day SHmax orientation. Consequently, this joint set exhibits higher effectiveness under the influence of the current stress regime, leading to increased coal seam permeability and enhanced CBM migration. Therefore, the most suitable areas for CBM exploitation would be the middle and southern parts of the Yuwang block. This conclusion is also consistent with the previously reported sweet spot for coalbed gas development in the Laochang area.

5 Conclusion

This paper entails recovery and evaluation of the paleotectonic stress field in a study area using numerical simulations by taking the Laochang area as an example and drawing on the development of fractures in the adjacent layers of the coal seam. Accordingly, the method for calculating the reservoir fracture density is optimized to the study area to realize prediction of the coal reservoir fracture density and direction. The main findings of this study are as follows:

1) Traditional approaches of simulating tectonic stresses are often limited by their reliance on experimental stress parameters without incorporating geological constraints such as faults. This study introduces a method to integrate tectonic stress field simulation with fracture prediction by using surface sandstone faults as the constraints for stress inversion. The sandstone layer, which is geographically aligned with the coal reservoir, provides a natural dataset for analyzing the stress history influencing both the sandstone layer and coal reservoir. This integration is expected to improve the accuracy of stress predictions and enhance our understanding of the geological structures in the study area.
2) The fracture density calculation model was improved by specifically considering the effect of the rock layer thickness on the fracture density. The fracture density calculation formula previously summarized by researchers does not account for the influence of stratum thickness on fracture density. In the Laochang area, there is an inverse power function relationship between the fracture density and stratum thickness. Owing to the heterogeneity of the rock layer, there are variations in the fracture lengths in the σ_2 direction. In this study, we consider that the heterogeneous regions in the rock are distributed randomly and that the fracture lengths in the σ_2 direction follow a normal distribution. Thus, fractures are observed in the field only when their lengths exceed the rock layer thickness.
3) According to the prediction results of the fracture simulations, it is believed that the fracture density of the coal reservoir in the study area is mostly 10–20 per meter. Overall, the fracture density distribution in the coal reservoir trends high in the south to low in the north and high in the east to low in the west. Ultimately, through integrated analysis of the fracture density and orientation, coal seam thickness, structural complexity, and the present-day stress field within the study area, the Yuwang block is determined as the sweet spot for CBM development in the Laochang area.

Data availability statement

The raw data supporting the conclusions of this article will be made available by the authors without undue reservation.

Author contributions

CW: conceptualization, methodology, and writing–review and editing. BW: methodology, resources, and writing–review and editing. XH: investigation and writing–review and editing. XJ: software and writing–original draft. WL: supervision and writing–original draft. MS: writing–original draft. XZ: writing–original draft. LG: Visualization and writing–review and editing.

Conflict of interest

Authors CW, XH, WL, and XZ were employed by China United Coalbed Methane National Engineering Research Center Company Limited.

Author LG was employed by Huayang New Material Technology Group Co., Ltd. No. 1 Coal Mine.

The remaining authors declare that the research was conducted in the absence of any commercial or financial relationships that could be construed as a potential conflict of interest.

Funding

The authors declare that financial support was received for the research, authorship, and/or publication of this article. This study was supported by the Jiangsu Province Carbon Peak Carbon Neutral Technology Innovation Project in China (Grant no. BE2022034-1).

Publisher's note

All claims expressed in this article are solely those of the authors and do not necessarily represent those of their affiliated organizations, or those of the publisher, the editors, and the reviewers. Any product that may be evaluated in this article, or claim that may be made by its manufacturer, is not guaranteed or endorsed by the publisher.

References

Carminati, E., and Vadacca, L. Two- and three-dimensional numerical simulations of the stress field at the thrust front of the Northern Apennines, Italy. *J. Geophys. Res. Solid Earth*, 2010, 115 doi:10.1029/2010jb007870B12).

Ding, Z., Qian, X., Huo, H., and Yang, Y.(1998). A new method for quantitative prediction of tectonic fractures—two-factor method. *Oil & Gas Geology* 19(1), 1–7. doi:10.11743/ogg19980101

Dixon, J. M. (1979). *Techniques and tests for measuring shearing fracture intensity [D]*. Morgantown: West Virginia University.

Fang, A., Hou, Q., Ju, Y., Bu, Y., and Lu, J. (2005). A study on control action of tectonic activity on CBM pool from various hierarchies. *Coal Geol. China*, 17 (04):15–20. doi:10.3969/j.issn.1674-1803.2005.04.006

Fang, H., Sang, S., Wang, J., Liu, S., and Ju, W. (2017). Simulation of paleotectonic stress fields and distribution prediction of tectonic fractures at the Hudi coal mine, Qinshui Basin. *Acta Geol. Sin. Ed.*, 91 (06). doi:10.1111/1755-6724.13447

Gui, B., and Wang, C. (2000). Tectonic characteristics of coalbed methane in the east Yunnan-Qianxi area. *Yunnan Geol.*, 19 (04): 321–351.

Guo, X., Zhuang, D., Gui, B., and Kong, L. (2004). Hydrogeological characteristics of coal seams and coalbed methane reservoirs in Laofang mining area. *Yunnan Geol.*, 23 (04): 487–495. doi:10.3969/j.issn.1004-1885.2004.04.010

Jiang, Bo, and Wang, L. (2015). Structural kinematic evaluation and prediction method for fracture development in coal reservoirs. *Coal Sci. Technol.*, 43 (02): 16–20. doi:10.13199/j.cnki.Cst.2015.02.004

Jiang, B., Qin, Y., Ju, Y., and Wang, J. (2005). Research on tectonic stress field of generateand reservoir of coalbed M ethane *J. China Univ. Min. & Technol.*, 34 (05): 564–569. doi:10.3321/j.issn:1000-1964.2005.05.005

Jing, B., Wang, L., Wang, J., and Qu, Z. (2014). "Tectonic prediction and evaluation of non-homogeneity of coal reservoir rift development in Linfen area, East China [A]," in *2014 China geoscience joint academic conference–topic 57: basin dynamics and unconventional energy proceedings [C]*.

Ju, Y., Jiang, B., Wang, G., Hou, Q., et al. (2005). *Tectonic coal structure and reservoir physical properties [M]*. Xuzhou: China University of Mining and Technology Press.

Ju, W., Jiang, B., Qin, Y., Wu, C., Li, M., Xu, H. et al. (2020). Characteristics of present-day *in-situ* stress field under multi-seam conditions: implications for coalbed methane development. *J. China Coal Soc.*, 45 (10): 3492–3500. doi:10.13225/j.cnki.jccs.2019.1135

Ladeira, F. L., and Price, N. J. (1981). Relationship between fracture spacing and bed thickness. *J. Struct. Geol.*, 3 (2): 179–183. doi:10.1016/0191-8141(81)90013-4

Li, P., and Liu, Q. (2022). A dual porous and fractures medium CBM numerical model development and analysis. *J. Petroleum Sci. & Eng.*, 214. doi:10.1016/j.petrol.2022.110511

Lin, Y. (1993). Exploration of the relationship between the conjugate shear angle of rocks and the magnitude of peritectic pressure. *Adv. Geophys.* (04): 133–139.

Liu, C., Chongyuan, Z., and Xingke, Y. (2000). Strong activity and active deep action-two important features of sedimentary basins in China. *Oil Gas Geol.* 21 (1): 1–6.

Liu, H., Zuo, Y., Rodriguez-Dono, A., Wu, Z., Sun, W., Zheng, L., et al. (2023). Study on multi-period palaeotectonic stress fields simulation and fractures distribution prediction in Lannigou gold mine, Guizhou. *Geomechanics Geophys. Geo-Energy Geo-Resources*, 9, 92, doi:10.1007/s40948-023-00633-01).

McQuillan, H. (1973). Small-scale fracture density in Asmari Formation of southwest Iran and its relation to bed thickness and structural setting. *Bull. Am. Assoc. Petrolewn Geol.*, 57 (12): 2367–2385. doi:10.1306/83d9131c-16c7-11d7-8645000102c1865d

Moore, M. A. (2012). Coalbed methane: a review. *Int. J. Coal Geol.* 101, 36–81. doi:10.1016/j.coal.2012.05.011

Pang, Y., Chen, K., Zhang, P., He, K., Tang, J., Zhang, D., et al. (2024). Simulation study on the paleo-stress field of the Longmaxi formation in the wulong area, southeast chongqing [J/OL]. *Seismol. J.* 1-19. doi:10.11939/jass.20230137

Qian, X., Ding, Z., Zheng, Y., and Hou, G.(1994). Research on quantitative prediction technology of tectonic fracture, taking hilly oilfield as an example. China Petroleum and Natural Gas Corporation. Report on the research results of China's oil and gas reservoirs, a key scientific and technological research project of China National Petroleum Corporation.

Qin, Y., Ye, J., Lin, D., Jiao, S., and Li, G. (2000). Relationship of coal reservior thickness and its permeability and gas-bearing property. *Coal Geol. & Explor.*, 28 (01), 24–27. doi:10.3969/j.issn.1001-1986.2000.01.007

Ramsay, J. G. (1980). Shear zone geometry: a review. *J. Struct. Geol.*, 2 (1): 83–99. doi:10.1016/0191-8141(80)90038-3

Ren, Q., Jin, Q., Feng, J., and Li, M. (2019). Simulation of stress fields and quantitative prediction of fractures distribution in upper Ordovician biological limestone formation within Hetianhe field, Tarim Basin, NW China. *J. Petroleum Sci. & Eng.*, 173, 1236–1253. doi:10.1016/j.petrol.2018.10.081

Sun, F., Wang, B., Li, M., and Liang, H. (2014). Major geological factors controlling the enrichment and high yield of coalbed methane in the southern Qinshui Basin. *Acta Pet. Sin.*, 35 (06): 1070–1079. doi:10.7623/syxb201406004

Wang, B. (2007). *Tectonic fracture description and quantitative prediction of reservoirs [D]*. Qingdao: China University of Petroleum.

Wang, J., Ju, W., Shen, J., and Sun, W. (2016). Prediction of tectonic fracture distribution in chang7-1 reservoir of Yanchang Formation, dingbian area, ordos basin. *Geol. Explor.*, 52 (05): 966–973. doi:10.13712/j.cnki.dzykt.2016.05.019

Wang, L. (2014). *Tectonic dynamics method for evaluating the inhomogeneity of coal reservoir fracture development and its application - a case study in Linfen area, East China [D]*. Xuzhou: China University of Mining and Technology.

Wu, L., Ding, W., Jinchuan, Z., Yuxi, L., Song, Z., and Liangjun, H. (2011). Prediction of fracture distribution in organic-rich shale reservoirs of the Lower Silurian Longmaxi Formation in southeastern Chongqing. *J. Petroleum Nat. Gas*, 33 (9), 4. doi:10.3969/j.issn.1000-9752.2011.09.009

Xiao, W. (2017). *Geological characteristics of coalbed methane and dessert section preference in the Laofang mine area, east Yunnan*. Xuzhou: China University of Mining and Technology.

Zhang, B., Li, Y., Fantuzzi, N., Zhao, Y., Liu, Y. B., Peng, B., et al. (2019). Investigation of the flow properties of CBM based on stochastic fracture network modeling. *Materials*, 12 (15): 2387, doi:10.3390/ma12152387

Zhou, J., Jiang, T., Mou, H., Jiang, S., and Zhou, L. (2021). Effect of fault zone and natural fracture on hydraulic fracture propagation in deep carbonate reservoirs. *IOP Conf. Ser. Earth Environ. Sci.*, 861 (6): 062057, doi:10.1088/1755-1315/861/6/062057

Zhou, J., Tong, X., and Feng, Y. (2006). Characteristics and controlling factors of fracture development in the Chaiwopu anticline reservoir. *Acta Pet. Sin.*, 27 (3), 53–56. doi:10.3321/j.issn:0253-2697.2006.03.011

Frontiers in Earth Science

Investigates the processes operating within the major spheres of our planet

Advances our understanding across the earth sciences, providing a theoretical background for better use of our planet's resources and equipping us to face major environmental challenges.

Discover the latest Research Topics

See more →

Frontiers

Avenue du Tribunal-Fédéral 34
1005 Lausanne, Switzerland
frontiersin.org

Contact us

+41 (0)21 510 17 00
frontiersin.org/about/contact